

Martin Koch: Measurement of the Self-Diffusion Tensor of Water in the Human Brain. Leipzig: Max Planck Institute of Cognitive Neuroscience, 2000 (MPI Series in Cognitive Neuroscience; 14)

**Measurement of the Self-Diffusion Tensor
of Water in the Human Brain**

Die Deutsche Bibliothek - CIP-Einheitsaufnahme

Koch, Martin:

Measurement of the self-diffusion tensor of water in the human brain / Martin Koch.
[Max Planck Institute of Cognitive Neuroscience]. - Leipzig : MPI of Cognitive
Neuroscience, 2000

(MPI series in cognitive neuroscience ; 14)

Zugl.: Leipzig, Univ., Diss., 2000

ISBN 3-9807282-3-4

Druck: Sächsisches Digitaldruck Zentrum, Dresden

© Martin Koch, 2000

Measurement of the Self-Diffusion Tensor of Water in the Human Brain

Von der Fakultät für Physik und Geowissenschaften
der Universität Leipzig
genehmigte

D I S S E R T A T I O N

zur Erlangung des akademischen Grades
doctor rerum naturalium
Dr. rer. nat.
vorgelegt

von Diplom-Physiker Martin Koch
geboren am 21. Oktober 1968 in Dinslaken
Gutachter: Prof. Dr. rer. nat. J. Kärgner
Priv.-Doz. D. G. Norris PhD
D. Le Bihan MD, PhD
Prof. F. Ståhlberg PhD
Tag der Verleihung: 21. August 2000

Bibliographische Beschreibung

Koch, Martin

Measurement of the Self-Diffusion Tensor of Water in the Human Brain

Universität Leipzig, Dissertation, in englischer Sprache

159 Seiten, 224 Literaturangaben, 26 Abbildungen, davon 7 in Farbe, 8 Tabellen

Referat

Die kernspintomographische Bildgebung ermöglicht orts aufgelöste Messungen des Selbstdiffusionstensors von Wasser im lebenden menschlichen Gehirn. Da der Diffusionstensor von Wasser in biologischem Gewebe durch Zellmembranen beeinflusst wird, kann mit Hilfe der Diffusionstensorbildgebung (Diffusion Tensor Imaging, DTI) die Richtung von Faserbündeln bestimmt werden, die aus parallel verlaufenden Nervenzellfortsätzen bestehen.

Für DTI müssen schnelle Bildgebungsmethoden eingesetzt werden, um Störungen durch Bewegung zu vermeiden und um eine große Anzahl an Messungen in annehmbarer Zeit durchführen zu können. Bislang wurde DTI fast ausschließlich mit der Bildgebungssequenz EPI (Echo Planar Imaging) realisiert. Diese Methode gehört zwar zu den schnellsten Sequenzen in der NMR-Bildgebung, bringt aber Bildverzerrungen und -auslöschungen mit sich, und eine hohe räumliche Auflösung kann nur mit sehr starken und schnell schaltbaren Gradientenspulen erreicht werden. In dieser Arbeit wird deshalb neben EPI die Bildgebungsmethode U-FLARE (Ultra-Fast Low Angle Rapid Acquisition with Relaxation Enhancement) für die Diffusionstensorbildgebung verwendet.

Die Dissertation stellt zunächst die physikalischen Grundlagen der Messung und das Prinzip der NMR-Bildgebung dar. Es werden dann die verwendeten Bildgebungsmethoden und die Maßnahmen erläutert, die notwendig sind, um in Tensormessungen mit U-FLARE die gleiche Genauigkeit wie bei EPI und eine höhere Auflösung zu erreichen. Die Arbeit befasst sich im Weiteren mit einer Analyse der Fehlerquellen bei der Bestimmung des Diffusionstensors und mit Möglichkeiten der Abhilfe.

Die auf der U-FLARE-Sequenz beruhende Messmethode wurde auf eine Fragestellung aus der Neuroanatomie angewandt. Dieses Experiment wurde motiviert durch Veröffentlichungen, die zeigen, dass die Fluktuationen des T_2^* -gewichteten NMR-Signals aus dem rechten und linken motorischen Kortex zueinander zeitlich korreliert sind, auch wenn keine willkürliche Bewegung ausgeführt wird. Diese Korrelation beruht möglicherweise auf spontaner neuronaler Aktivität, die sich über interhemisphärische Fasern auf die Gegenseite überträgt. In dieser Arbeit wird die Hypothese untersucht, dass korrelierte Fluktuationen des T_2^* -gewichteten Signals immer zwischen solchen kortikalen Gebieten auftreten, die in der auf DTI beruhenden Faserkarte erkennbar miteinander verbunden sind. Dazu wurden mit Hilfe einer auf U-FLARE beruhenden Messung des Diffusionstensors von Wasser subkortikale Faserverbindungen abgebildet. Die Stärke der gemessenen Faserverbindungen zwischen verschiedenen Kortexarealen wurde durch einen Monte-Carlo-Algorithmus quantifiziert. Die Ergebnisse wurden verglichen mit der zeitlichen Korrelation zwischen den Signalverläufen dieser Areale aus einer Zeitreihe von T_2^* -gewichteten Bildern.

Contents

1	Introduction	1
1.1	Anisotropic motion of water in the brain	1
1.2	Aim of this thesis	2
2	Basics	5
2.1	Nuclear magnetic resonance	5
2.1.1	The basic NMR experiment	5
	The rotating frame of reference	8
	RF perturbation of the spin state	9
	Relaxation and Bloch equations	11
	Relaxation mechanisms	12
	The free induction decay	14
	The spin echo	15
	Coherence pathways	17
2.1.2	NMR imaging	20
	Slice selection	21
	Frequency encoding	21
	Phase encoding	22
	The concept of \mathbf{k} space	23
2.1.3	Fast imaging	24
	RARE — refocusing with RF pulses	25
	EPI — refocusing with gradient pulses	26
2.2	Diffusion	27
2.2.1	Transport and self-diffusion	29
2.2.2	Random walk model of diffusion	29
2.2.3	Restricted diffusion	30
2.2.4	Anisotropic diffusion	31
2.2.5	Microscopic definition of the diffusion tensor	31
2.2.6	Symmetry of the diffusion tensor	32
2.2.7	The eigenvector basis	33
2.2.8	The diffusion ellipsoid	36
2.2.9	Implications for diffusion measurements in biological systems	37
2.3	Tensors	38
3	NMR measurement of anisotropic self-diffusion	41
3.1	The Bloch equations including diffusion and flow	41
3.2	The Stejskal-Tanner experiment	43

3.2.1	Restricted diffusion	45
3.3	Diffusion tensor imaging (DTI)	45
3.3.1	Spatial localization	47
3.3.2	Measures of diffusion anisotropy	48
3.4	<i>In vivo</i> application	49
3.4.1	Determinants of water self-diffusion <i>in vivo</i>	49
	Pseudodiffusion	50
3.4.2	Applications of diffusion weighted imaging	51
	Stroke	51
	Isotropic diffusion weighting	52
3.4.3	Applications of diffusion tensor imaging	52
	Anisotropic diffusion in brain white matter	52
	Clinical application and application for functional neuroanatomy	54
	Application in MEG source localization	55
4	Implementation of diffusion tensor imaging	57
4.1	Instrumentation and subjects	57
4.2	Imaging sequences	58
4.2.1	Diffusion weighting	58
4.2.2	EPI	59
4.2.3	U-FLARE	60
	U-FLARE with improved SNR and resolution	62
4.3	Data processing for diffusion tensor imaging	65
4.3.1	Tensor calculation	65
4.3.2	Eigenvector calculation and display	66
5	Sources of systematic error and possible solutions	69
5.1	Influence of noise	71
5.2	Contribution of imaging gradients	72
5.3	Concomitant gradients	73
5.4	Miscalibration and non-orthogonality of gradients	74
5.5	Nonlinearity of gradient fields	77
5.6	Eddy currents	78
5.6.1	Strategies for avoiding eddy current effects	81
5.6.2	Assessment of strategies for avoiding eddy current effects	82
	Experimental	83
	Eddy current correction for EPI	84
	Results	85
	Conventional SE EPI	85
	Double-SE EPI	87
	U-FLARE	88
	Discussion	88
5.6.3	Consequences of eddy currents for DTI	90
5.7	Background gradients	91
5.8	Subject motion	93
5.9	Flow	97
5.10	Different fibre directions in a volume element	98

5.11 Conclusion	99
6 Investigating the connectivity hypothesis	101
6.1 Introduction	101
6.1.1 Definition of functional connectivity	101
6.1.2 Functional magnetic resonance imaging	101
6.1.3 Biswal's experiment	102
6.1.4 Interpretation of Biswal's results	103
6.1.5 The connectivity hypothesis	104
6.2 Measurement of functional connectivity	104
6.2.1 Experimental	105
6.2.2 Data Processing	105
6.3 Measurement of anatomical connectivity	105
6.3.1 Experimental	106
6.3.2 Quantification of fibre connections in DTI maps	107
6.4 Relations between anatomical and functional connectivity	108
6.4.1 The classes approach	109
Results	109
6.4.2 The region-of-interest approach	110
Results	113
7 Conclusion	117
A Colour figures	119
B Abbreviations	123
C Zusammenfassung der wissenschaftlichen Ergebnisse	125
C.1 Motivation und Einordnung	125
C.2 Methoden	127
C.3 Ergebnisse	129
C.4 Ausblick	130
References	131

Chapter 1

Introduction

1.1 Anisotropic motion of water in the brain

Despite over 100 years of brain research still relatively little is known about how the human brain works. Although we know much about the tissue microstructure and a fair amount concerning the subunits that mediate basic tasks like the control of skeletal muscles, vision, hearing *etc.* this is not true for more complex functions of the human brain. One reason for this lack of knowledge is certainly the brain's complexity: the human brain contains about 10^{11} neurons [1, p. 196], some of which have 10^5 possibilities to communicate with other neurons [2, p. 26]. Another reason is that the function of a region of brain tissue is by no means obvious: While the microscopic principles of communication between neurons are more or less the same in the whole brain the most important property that determines the function of a part of the brain is the way the neurons in it are connected with each other, and to which neurons in the rest of the brain they are connected. The histological properties only depend to a small degree on the function. The microscopic circuit diagram of the network, however, is beyond our reach. Moreover, the neurons performing a specific function may be distributed over a large portion of the brain — although we know this is not the case for a number of basic functions. Therefore an investigation of brain functions must rely on methods that provide information on a more macroscopic scale. Among the techniques that are available for obtaining *in vivo* anatomical images of internal parts of the body, magnetic resonance imaging (MRI) and X-ray computed tomography (CT) provide the highest spatial resolution (about 1 mm). MRI also benefits from not relying on potentially harmful ionizing radiation. Since the advent of functional MRI (fMRI) [3] it can also yield information on task-induced activation of a brain region [4, 5].

Neurons communicate with each other via extensions (axons) of the cell body whose length can be of the order of many centimeters. In the human central nervous system (CNS) the axons of different origins often converge to build macroscopic fibre bundles of many thousands of axons before they diverge again to their individual destinations. Thus the brain tissue separates into regions containing mainly neuronal cell bodies (grey matter, GM) and other regions mainly consisting of axons (white matter, WM). While a variety of techniques including fMRI allow the detection of activated regions in grey matter, measurements of activation in WM fibre tracts that interconnect different regions of GM lack sensitivity and have only very recently been reported [6]. Until 1994 neither conventional MRI nor any other imaging method was able to image the WM fibre tracts *in vivo*, due to insensitivity to the fibre direction. However, it was found in 1989 that the tissue structure in WM influences the self-diffusion of water molecules in brain WM: the mean square displacement of diffusing water molecules in WM is larger along the

fibre direction than perpendicular to it [7, 8, 9, 10]. This anisotropy was also observed in muscle tissue [11, 12]. Consequently the ability of MRI to measure diffusion coefficients non-invasively with high spatial resolution opens up the possibility of imaging the direction of fibre bundles in white matter. Spatially resolved measurements of the diffusion tensor of water can thus be used to image fibres in brain white matter [13, 14]. The technique has been termed diffusion tensor imaging (DTI) [15, 16, 17]. The fibre anatomy measured with DTI can be compared with the outcome of a psychological experiment or with the fMRI measurement of brain activity during such an experiment. It is subject to interindividual differences, as is the brain anatomy in general [18, p. 173]. One of the main concerns of neuroanatomy is to find anatomical criteria for the definition of functional units in the brain. Since a functional unit of the cortex¹ has been proposed to be defined by both intrinsic structure and as the target zone of fibres from other specific brain areas [19, p. 14], a measurement of the anatomy of afferent fibres may be used to delineate such functional units. In some cortical areas microscopic processing units (“macrocolumns”) of about 0.5 to 1 mm diameter have been identified [19, p. 37]. Histological definitions lead to considerably larger regions. However, the size of the cortical regions activated by a specific task in an fMRI experiment is typically in the intermediate range (about 1.5 cm). As DTI provides information on this “mesoscopic” level of description between the size of a macrocolumn and that of a histologically defined area, DTI measurements of fibre anatomy may contribute to an anatomical definition of a functional unit in the cortex.

Since DTI probes tissue microstructure, it can also be used as a tool for the investigation of diseases that affect this structure [20]. It is expected that DTI will contribute to the diagnosis and explanation of pathological processes involved in ventricular dysrhythmia [21], in multiple sclerosis [22], stroke [23, 24], cancer [25, 26], and possibly in mental disorders of organic origin [27, 28].

1.2 Aim of this thesis

This thesis is concerned with the imaging of human brain white matter fibre tracts by means of spatially resolved NMR measurements of the self-diffusion tensor of water (diffusion tensor imaging). The use of different imaging strategies in combination with diffusion tensor imaging shall be evaluated. The technique shall then be applied to investigate whether there is a direct relation between fibre anatomy as detected by DTI on the one hand, and results of fMRI experiments measuring brain function on the other. This introductory chapter will be followed by:

Chapter 2 which will give an introduction to nuclear magnetic resonance imaging and to the physics of diffusion. This chapter will also contain a short explanation of the term “tensor”.

Chapter 3 describes how diffusion coefficients can be measured by means of NMR, and how the complete diffusion tensor can be obtained.

Chapter 4 is dedicated to the implementation of diffusion tensor imaging experiments on a clinical magnetic resonance imaging system. It gives a description of the experimental setup.

¹The cortex is the outer 2 to 5 mm thick layer of grey matter that covers the cerebrum.

Chapter 5 contains a discussion of possible sources of measurement errors, along with strategies for avoiding them.

Chapter 6 reports on experiments that are designed to demonstrate whether two brain regions that are connected by a dominant WM fibre show a high correlation of neuronal activity.

Chapter 7 summarizes the results of this thesis.

Chapter 2

Basics

2.1 Nuclear magnetic resonance

With the discovery of X-rays in 1895 a type of electromagnetic radiation became available that was able to penetrate biological tissue. This made insights into the intact human body possible without the need for surgical operation. Biological tissue is also penetrated by sound with wavelengths above $100\text{ }\mu\text{m}$. This ultra-sound is also being used for medical imaging. Besides the wavelength region of X-rays ($\lambda \approx 1\text{ }\text{\AA}$), electromagnetic radiation with wavelengths above 1 m is also able to penetrate tissue. However, if radiation in this radio frequency “window” is to be used for medical imaging, the imaging principle that is used with X-rays would only allow a spatial resolution of about 1 m : the radiation wavelength sets a principal limit to the spatial resolution of any imaging method based upon attenuation.¹ Thus for imaging with radiation wavelengths in the region of 1 m a completely different principle must be applied. A basis for such a technique is supplied by the phenomenon of nuclear magnetic resonance (NMR) discovered in 1946 [30, 31]:

- The magnetization of a sample within a static magnetic field can be manipulated by high frequency radiation. After such an excitation the magnetization vector precesses about the magnetic field direction.
- The contributions of the atomic nuclei to the measurable magnetization are oscillating functions of time. The oscillation frequency is proportional to the magnetic field strength at the location of the nucleus.

NMR tomography methods are widely applied in medicine. Moreover, high resolution NMR spectroscopy has become an important tool for investigating molecular structure.

2.1.1 The basic NMR experiment

The total angular momentum, \mathbf{J} , of an atomic nucleus consists of the orbital angular momenta and the spins of the protons and neutrons forming the nucleus. \mathbf{J} is often referred to as the spin of the nucleus, although the nucleons’ orbital angular momenta also contribute to the total angular momentum. For simplicity, we restrict ourselves to hydrogen nuclei. In this case, there

¹The minimum half aperture that is required to observe the first minimum of the diffraction pattern of two point light sources separated by d can be calculated from $\sin \varphi = \lambda/d$. [29, p. 493] With $d < \lambda$ no φ satisfies this condition.

is no orbital angular momentum. The angular momentum of a nucleus gives rise to a magnetic dipole moment, $\boldsymbol{\mu}$. In the case of hydrogen where no coupling between angular momenta needs to be considered, spin and magnetic moment are parallel,²

$$\boldsymbol{\mu} = \gamma \mathbf{J}. \quad (2.1)$$

The proportionality constant, γ , is called the magnetogyric ratio. It is a property of the nucleus under consideration. A classical proton moving in a circular orbit with the angular momentum \mathbf{J} would have a magnetic moment corresponding to $\gamma = e/(2m_p)$.³ Actually this relation holds only for orbital angular momenta. In the case of spin we have to write $\gamma = g_s e/(2m_p)$. For protons we find experimentally $g_s = 5,5858$. A classical treatment would always yield $g_s = 1$.⁴

The observation that the angular momentum, and thus the magnetic dipole moment, of a nucleus in a magnetic field cannot be oriented arbitrarily is essential for an understanding of nuclear magnetic resonance. This behaviour of angular momenta is called quantization of orientation. In quantum mechanics it follows from the eigenvalue equation for the operator that represents the measurement of the component of the angular momentum along the magnetic field direction. If the z direction is chosen to be the magnetic field direction, this operator is denoted as \hat{J}_z . For convenience, $\hat{J}_x, \hat{J}_y, \hat{J}_z$ are often replaced by the dimensionless operators $\hat{I}_i = \hat{J}_i/\hbar$, with $i = x, y, z$ and $\hbar = h/(2\pi)$ where h is Planck's constant. The eigenvalue equations for \hat{I}_z and \hat{I}^2 are commonly written in the form

$$\hat{I}^2 |Im\rangle = I(I+1) |Im\rangle \quad (2.2)$$

$$\hat{I}_z |Im\rangle = m |Im\rangle. \quad (2.3)$$

The magnetic quantum number, m , can assume the values $-I, -I+1, \dots, I$. For hydrogen nuclei the angular momentum or “spin” quantum number is $I = \frac{1}{2}$, hence $m = \pm\frac{1}{2}$. This means that a measurement of the z component of the angular momentum, can only yield the results $\pm\frac{1}{2}\hbar$. These two possible results correspond to the two possible orientations of the angular momentum with respect to the direction of the magnetic field. In contrast to the direction of \mathbf{J} , recorded as a result of the measurement, the direction of the vector of *expectation* values of the components of \mathbf{J} is not quantized, *i.e.* it can point to any direction in space [33, p. 16].

The energy of a proton in a magnetic field is determined by the orientation of the magnetic moment relative to the magnetic field direction. The Hamilton operator which corresponds to a measurement of the energy is $\hat{H} = -\hat{\boldsymbol{\mu}} \cdot \mathbf{B}$. Assuming the field to be aligned along z and using equation (2.1) the Hamiltonian can be written as

$$\hat{H} = -\gamma \hbar \hat{I}_z B. \quad (2.4)$$

Thus, if the magnetic field vector points in z direction, the energy depends on the z component of the proton's angular momentum. The two states corresponding to $m = \pm\frac{1}{2}$ differ in energy

²If orbital angular momenta are present the situation is more complicated. However, the magnetic moment vector may still be defined in such a way that it is parallel or antiparallel to \mathbf{I} . [32, p. 58] The property of two quantum mechanical (vector) operators of being parallel is expressed in terms of their matrix elements. [33, p. 2]

³This coincides with the value we would calculate for a rotating charged sphere with angular momentum \mathbf{J} in the classical picture. m_p is the mass of a proton, e is the elementary charge.

⁴An explanation of why the classical expectation does not coincide with the experimental value requires quantum electrodynamics in the case of the electron. The anomalous magnetic moment of protons and neutrons can be explained by their substructure which is dealt with in the framework of the standard model [34, sections 2.2.4.1 and 2.4.5.2].

by $\Delta E = \hbar\omega$ where

$$\omega = \gamma B \quad (2.5)$$

is called the Larmor frequency. At $B = 3$ Tesla the Larmor frequency for hydrogen nuclei is $\omega = 2\pi \cdot 125.3$ MHz.

To derive the equation of motion for the magnetic moment, we use the equations of motion for the operators $\hat{I}_x, \hat{I}_y, \hat{I}_z$ which are not explicitly time-dependent,

$$\frac{d\hat{I}_x}{dt} = \frac{i}{\hbar} [\hat{H}, \hat{I}_x] \quad (\text{and cyclic permutations of } x, y, z). \quad (2.6)$$

By means of the commutation relations for angular momenta,

$$[\hat{I}_x, \hat{I}_y] = i\hat{I}_z \quad (\text{and cyclic permutations of } x, y, z), \quad (2.7)$$

and using equation (2.1) and the definition of the time derivative of operators, we obtain

$$\frac{d\langle\hat{\boldsymbol{\mu}}\rangle}{dt} = \langle\hat{\boldsymbol{\mu}}\rangle \times \gamma\mathbf{B} \quad (2.8)$$

where $\langle\hat{\boldsymbol{\mu}}\rangle$ is the vector composed of the expectation values of the components of $\hat{\boldsymbol{\mu}}$. Hence the expectation values $\langle\hat{\mu}_x\rangle$ and $\langle\hat{\mu}_y\rangle$ are time dependent. They behave as if $\boldsymbol{\mu}$ precessed about the magnetic field direction with the Larmor frequency ω . The classical description would also yield this result: in a magnetic field a body that carries a magnetic dipole moment is subjected to a torque $\mathbf{T} = \boldsymbol{\mu} \times \mathbf{B}$ that tries to align the magnetic moment with the direction of the external field. If the body possesses angular momentum due to a rotation about the direction of the magnetic moment then the magnetic moment is not simply flipped to the field direction but rather precesses about this axis.

In order to find out how the wave function of a spin is related to the time evolution of the expectation values of $\langle\boldsymbol{\mu}\rangle$, we realize that the state of a single spin (with $I = \frac{1}{2}$) can be expressed as a complex linear combination of the two eigenstates,

$$|\psi(t)\rangle = \sum_{m=-\frac{1}{2}}^{+\frac{1}{2}} a_m(t) |m\rangle \quad (2.9)$$

with

$$a_m(t) = c_m e^{-\frac{i}{\hbar} E_m t}, \quad E_m = -\gamma\hbar B m. \quad (2.10)$$

Equation (2.9) is the general solution of the stationary Schrödinger equation. If we express the c_m by

$$c_{+\frac{1}{2}} = a e^{i\alpha}, \quad c_{-\frac{1}{2}} = b e^{i\beta} \quad (a, b, \alpha, \beta \in \mathbb{R}, a, b \geq 0), \quad (2.11)$$

where due to normalization $a^2 + b^2 = 1$, it can be shown [33, section 2.2] that the expectation values $\langle\mu_i\rangle$ follow

$$\langle\hat{\mu}_x(t)\rangle = r \sin \theta \cos \phi(t) \quad (2.12a)$$

$$\langle\hat{\mu}_y(t)\rangle = r \sin \theta \sin \phi(t) \quad (2.12b)$$

$$\langle\hat{\mu}_z(t)\rangle = r \cos \theta \quad (2.12c)$$

$$\text{with } r = \frac{\gamma \hbar}{2}, \quad \phi(t) = \beta - \alpha - \omega_0 t, \quad \cos \theta = a^2 - b^2. \quad (2.13)$$

These functions satisfy the equations (2.8). a^2 and b^2 describe the probabilities of finding a spin in the eigenstates, and $\phi(t) = \beta - \alpha - \omega_0 t$ may be considered as the phase⁵ of the spin. Equations (2.12a)–(2.12c) can be interpreted as the equation of motion in polar coordinates for a vector of length r and azimuth θ that precesses with angular velocity $-\omega_0$ about the vertical axis. In accordance with (2.5) we define a vector $\boldsymbol{\omega} = -\gamma \mathbf{B}$ such that $\omega = |\boldsymbol{\omega}| > 0$.

So far, equation (2.8) only concerns the expectation values of the components of magnetic moment of a *single* spin. We now wish to measure the vector \mathbf{M} of macroscopic magnetization which is the magnetic dipole moment per unit volume. In order to calculate the magnetization of an *ensemble* of many spins, we have to average over these without knowing the exact wave functions of the individual spins. Equation (2.8) is also valid for the expectation values of the components of \mathbf{M} , provided that the spins in the ensemble do not interact with each other [33, section 2.3]:

$$\frac{d\langle \hat{\mathbf{M}} \rangle}{dt} = \langle \hat{\mathbf{M}} \rangle \times \gamma \mathbf{B}. \quad (2.14)$$

The vector $\langle \hat{\mathbf{M}} \rangle$ is an implicit average over the ensemble.⁶

The population of the two eigenstates in thermal equilibrium at the temperature T can be described by a Boltzmann distribution,

$$\frac{N_{-1/2}}{N_{+1/2}} = \exp \left[-\frac{\hbar \omega}{kT} \right] \quad (2.15)$$

where N_m is the probability of finding a spin in the eigenstate $|m\rangle$, averaged over the ensemble, and k is Boltzmann's constant. At the magnetic field strengths that can be produced in a laboratory the energy difference $\hbar \omega$ at room temperature is so small that the ratio of the population numbers deviates from unity by only approximately 10^{-5} . The difference in population gives rise to a macroscopic magnetization of the sample. In thermal equilibrium \mathbf{M} points in the direction of the external magnetic field because the dipole moments $\langle \hat{\boldsymbol{\mu}} \rangle$ of all protons do not precess in phase but all phases $\beta - \alpha$ between 0 and 2π occur with the same probability (hypothesis of random phases [33, section 5.4]).

The rotating frame of reference

Equation (2.14) remains valid if we replace $\langle \hat{\mathbf{M}} \rangle$ by the classical vector \mathbf{M} . Moreover, it is also valid for time varying \mathbf{B} fields [33, p. 19]. Therefore it can be used as a classical equation of motion for \mathbf{M} to study how a time dependent magnetic field influences the magnetization. In the presence of an oscillating magnetic field in the radio frequency range⁷ the main magnetic field, \mathbf{B}_0 , and the applied oscillating field, $\mathbf{B}_1(t)$, add to give an effective magnetic field, $\mathbf{B}_{\text{eff}}(t)$,

⁵or, to be more exact, the expectation value of the observable “phase”

⁶The state of the ensemble can be described with the statistical operator, $\hat{\rho}$. For the state of the ensemble after a measurement, cf. [35, section 3.7§3]. For the time evolution of the statistical operator, see [35, section 3.7§4] and [33].

⁷The oscillating field has to be dealt with in near field approximation, i.e. for the distance r to the source of the magnetic field, $r \ll \lambda$ may be assumed.

and the spins now precess about the time dependent direction of this effective field. Assume a circularly polarized magnetic field

$$\mathbf{B}_1(t) = B_1 \cos(\omega t) \mathbf{e}_x - B_1 \sin(\omega t) \mathbf{e}_y \quad (2.16)$$

that rotates in the xy plane in the same sense as the spin precession. In a coordinate system S' that rotates relative to the laboratory frame of reference, S , with frequency ω about the z axis, the situation can be described in a simple way. In the rotating frame \mathbf{B}_1 is stationary. The magnetic moments behave as if they experienced the effective field

$$\mathbf{B}'_{\text{eff}} = (B_0 - \frac{\omega}{\gamma}) \mathbf{e}_{z'} + B_1 \mathbf{e}_{x'}. \quad (2.17)$$

(The origin of time was chosen to be the time when the x axes of the two frames of reference are coincident.) If, moreover, $\omega = \omega_0$, the z' component of the effective field vanishes, and we remain with $\mathbf{B}'_{\text{eff}} = B_1 \mathbf{e}_{x'}$. In this case the magnetization vector simply precesses about the x' axis. Viewed from the laboratory frame of reference, \mathbf{M} simultaneously precesses about the directions of \mathbf{B}_0 and \mathbf{B}_1 [36, p. 36]:

$$\mathbf{M}(t) = M_0 (\sin \omega_1 t \sin \omega_0 t \mathbf{e}_x + \sin \omega_1 t \cos \omega_0 t \mathbf{e}_y + \cos \omega_1 t \mathbf{e}_z) \quad (2.18)$$

with the initial condition $\mathbf{M}(0) = M_0 \mathbf{e}_z$. The vectors \mathbf{e}_x , \mathbf{e}_y , \mathbf{e}_z are unit vectors along the x , y , and z axes of the laboratory frame, respectively, and $\omega_1 = \gamma B_1$. Since the precession about \mathbf{B}_0 is usually much faster, the vertex of the vector \mathbf{M} moves on a spiral-shaped trajectory on a spherical surface. If the oscillating field is applied in the form of a short high frequency pulse of duration Δt the magnetization precesses during this time period about the x' axis (according to the left-hand rule) through the angle

$$\theta = \gamma B_1 \Delta t. \quad (2.19)$$

This flip angle is an important property of such a radio frequency (RF) pulse. It depends on the amplitude and duration of the RF pulse, whereas the precession axis is determined by the phase of the rotating field $\mathbf{B}_1(t)$. A pulse with $\theta = \pi/2$ and $\mathbf{B}_1 = B_1 \mathbf{e}_{x'}$ is termed a 90_x pulse. While in thermal equilibrium \mathbf{B}_0 and \mathbf{M} are parallel, after the application of a 90° pulse the magnetization vector, \mathbf{M} , precesses within the xy plane about \mathbf{B}_0 . In an appropriately positioned receiver coil this induces an alternating voltage. This actual NMR signal decays over time and is termed the free induction decay⁸ (FID).

RF perturbation of the spin state

In quantum mechanical terms, the \mathbf{B}_1 field modifies the time dependency of the complex factors $a_m(t)$ in equation (2.9). In the rotating frame of reference the time dependency of the $a_m(t)$ that arises from the stationary magnetic field is removed. The presence of the oscillating \mathbf{B}_1 field reintroduces a time dependency. It can be shown [33, section 2.6] that the spin state in the rotating frame,

$$|\psi'(t)\rangle = \tilde{a}(t) |+\tfrac{1}{2}\rangle + \tilde{b}(t) |-\tfrac{1}{2}\rangle, \quad (2.20)$$

⁸The term *free* induction emphasizes the absence of a B_1 field.

with $\tilde{a}(t), \tilde{b}(t) \in \mathbb{C}$ evolves according to

$$\tilde{a}(t) = \tilde{a}(0) \cos(\omega_1 t/2) + i\tilde{b}(0) \sin(\omega_1 t/2) \quad (2.21)$$

$$\tilde{b}(t) = \tilde{b}(0) \cos(\omega_1 t/2) + i\tilde{a}(0) \sin(\omega_1 t/2), \quad (2.22)$$

still assuming that \mathbf{B}_1 is aligned with the x' axis. These equations allow the calculation of the spin phases after the application of a 90° pulse. For a time t that satisfies $\omega_1 t = \pi/2$ and that may be called $t_{\pi/2}$, they simplify to

$$\tilde{a}(t_{\pi/2}) = [\tilde{a}(0) + i\tilde{b}(0)]c \quad (2.23)$$

$$\tilde{b}(t_{\pi/2}) = [\tilde{b}(0) + i\tilde{a}(0)]c \quad (2.24)$$

with $c = \cos(\pi/4) = \sin(\pi/4)$. By recalling from equation (2.13) that in the rotating frame the phase of a spin is given by

$$\phi(t) = \arg[\tilde{b}(t)] - \arg[\tilde{a}(t)] = \arg[\tilde{b}(t)\tilde{a}^*(t)], \quad (2.25)$$

where $\arg[z] = \varphi$ if $z = re^{i\varphi}$ and $r, \varphi \in \mathbb{R}$, and by setting $\tilde{a}(0) = ae^{i\alpha}$, $\tilde{b}(0) = be^{i\beta}$ we obtain

$$\phi(t_{\pi/2}) = \arg[\tilde{b}(t_{\pi/2})] - \arg[\tilde{a}(t_{\pi/2})] \quad (2.26)$$

$$= \arg[\tilde{b}(0)\tilde{a}^*(0) - i|\tilde{b}(0)|^2 + i|\tilde{a}(0)|^2 + \tilde{b}^*(0)\tilde{a}(0)] \quad (2.27)$$

$$= \arg[(\tilde{b}(0)\tilde{a}^*(0)) + (\tilde{b}(0)\tilde{a}^*(0))^* + i(a^2 - b^2)] \quad (2.28)$$

$$= \arg[2 \operatorname{Re}(\tilde{b}(0)\tilde{a}^*(0)) + i(a^2 - b^2)] \quad (2.29)$$

$$= \arg[2ab \cos(\beta - \alpha) + i(a^2 - b^2)]. \quad (2.30)$$

If we further take into account that $a^2 > b^2$ due to (2.15), assume without loss of generality that $a, b \geq 0$, and rename $\phi(t_{\pi/2})$ to $g(\delta)$ to emphasize that it is a function of $\delta = \beta - \alpha$, we can write

$$g(\delta) = \phi(t_{\pi/2}) = \begin{cases} \arctan \frac{a^2 - b^2}{2ab \cos(\delta)} + \pi & \text{if } \cos(\delta) < 0 \\ \arctan \frac{a^2 - b^2}{2ab \cos(\delta)} & \text{otherwise} \end{cases}. \quad (2.31)$$

This function is symmetric about $\delta = \pi$ as can be seen by taking the complex conjugate of both $a(0)$ and $b(0)$. Through differentiation we further find its maximum and minimum at $\delta = 0$ and $\delta = \pi$, respectively:

$$\begin{aligned} \max_{\delta \in [0, 2\pi)} g(\delta) &= g(\pi) = \arctan \frac{a^2 - b^2}{-2ab} + \pi = \pi - \varepsilon \\ \min_{\delta \in [0, 2\pi)} g(\delta) &= g(0) = \arctan \frac{a^2 - b^2}{2ab} = \varepsilon \end{aligned}$$

with some small $\varepsilon > 0$. Hence, if the phases at $t = 0$ are evenly distributed over the interval $[0, 2\pi)$, then after the 90° pulse the phase distribution will be centred at $\delta = \pi/2$ and will cover only the range $[0 + \varepsilon, \pi - \varepsilon)$. The distribution width, $\pi - 2\varepsilon$, decreases with increasing $a^2 - b^2$. Thus the random distribution of phases in equilibrium is disturbed by the RF pulse.⁹ This

⁹The resulting phase distribution is in fact the probability distribution function of a random variable that is created by applying a deterministic function to another variable (the original phases). A method of calculation can be found in [37, section 3.8].

is the reason why the expectation values of the transversal magnetization components are not zero after the pulse. Finally we use the relation [38]

$$\frac{\pi}{2} - \arctan x = \arccos \frac{x}{\sqrt{1+x^2}} \quad (2.32)$$

to prove that

$$\varepsilon = \frac{\pi}{2} - \theta \quad (2.33)$$

with θ as defined in equation (2.13). Hence, the classical expectation agrees with the quantum mechanical calculation: in equilibrium, the vectors $\boldsymbol{\mu} = \langle \hat{\boldsymbol{\mu}} \rangle$ of the individual spins are equally distributed over a cone with aperture θ aligned with the z axis. After the 90° pulse the cone is tilted by 90° , now being aligned with the positive y axis, resulting in a phase range of $[\pi/2 - \theta, \pi/2 + \theta] = [0 + \varepsilon, \pi - \varepsilon]$. For the realistic estimate $a^2/b^2 \approx 1 + 10^{-5}$ at room temperature we obtain $\varepsilon \approx 5 \cdot 10^{-6}$.

Relaxation and Bloch equations

In thermal equilibrium \mathbf{M} is stationary and parallel to the direction of the magnetic field, $\mathbf{M} = M_0 \mathbf{e}_z$. (The magnetic field may be oriented along z again). The transverse components of \mathbf{M} that are measured in an NMR experiment decay when the system returns to equilibrium. To discuss the processes that reestablish the equilibrium, it is convenient to consider the vector components of \mathbf{M} separately. The process that returns M_z to M_0 is called spin-lattice or longitudinal relaxation whereas the attenuation of M_x and M_y is called spin-spin or transversal relaxation. The return to equilibrium is usually modelled by an exponential time course. The corresponding time constants are denoted by T_1 for M_z (longitudinal) relaxation and by T_2 for M_x and M_y (transversal) relaxation such that

$$\dot{M}_x = -\frac{M_x}{T_2}, \quad \dot{M}_y = -\frac{M_y}{T_2}, \quad \dot{M}_z = -\frac{M_z - M_0}{T_1}. \quad (2.34)$$

In MRI, the relaxation times T_1 and T_2 have an important influence on the signal-to-noise ratio (SNR) in the image and the signal contribution of a specific tissue type. T_1 relaxation involves a change in the population of the two eigenstates. This requires an exchange of energy between the spin system and its environment, the “lattice”. T_2 relaxation, in contrast, does generally not require an energy transfer to a reservoir [33, p. 34]. The reason for T_2 relaxation is that the spins exchange energy with each other, and phase differences between the spins arise. However, the transversal magnetization components are also reduced by the eigenstate populations returning to the equilibrium values. Therefore the mechanisms underlying T_1 and T_2 relaxation cannot strictly be separated. Apart from the dephasing due to spin-spin interaction, a further dephasing and consequent decrease of the M_x and M_y components occurs if the \mathbf{B}_0 field is not perfectly homogeneous. In this case (which is the normal situation encountered in medical imaging) the spins at different locations encounter a slightly different B_0 and will accumulate different phases over time. The total M_x and M_y of the sample will thus decay even faster than they would due to T_2 relaxation alone. The decay of transversal magnetization components that arises from both dephasing due to spin-spin interaction and dephasing due to magnetic field inhomogeneity is often described with the time constant T_2^* . It will later become apparent that in contrast to T_1 and T_2 relaxation, the dephasing due to B_0 inhomogeneities is reversible.

Once M_z has reached its equilibrium value M_0 , there are no remaining transverse components of \mathbf{M} . Thus in summary the time constants always satisfy

$$T_2^* \leq T_2 \leq T_1. \quad (2.35)$$

By combining the classical version of equation (2.14) with the phenomenological description (2.34) of the relaxation processes we obtain the classical Bloch equations [39]:

$$\begin{aligned} \frac{dM_x}{dt} &= \gamma(\mathbf{M} \times \mathbf{B})_x - \frac{M_x}{T_2} \\ \frac{dM_y}{dt} &= \gamma(\mathbf{M} \times \mathbf{B})_y - \frac{M_y}{T_2} \\ \frac{dM_z}{dt} &= \gamma(\mathbf{M} \times \mathbf{B})_z - \frac{M_z - M_0}{T_1}. \end{aligned} \quad (2.36)$$

The Bloch equations represent an equation of motion for \mathbf{M} including relaxation, on a phenomenological level of description. In the rotating frame of reference the effective field from equation (2.17) has to be used instead of \mathbf{B} . Flow and diffusion effects have been neglected in this formulation but may also be included in the description (see also section 3.1) [40].

All relaxation processes arise from the motion of molecules, atoms, nuclei, or electrons. Random motion of particles that carry electrical charge or magnetic moment produces fluctuating magnetic fields. These fields influence the spins because they exert a torque on them. The effect of fluctuating fields on the magnetization is described by equation (2.14). If we use the symbol \mathbf{b} for the fluctuating fields we find that dM_i/dt does not depend on b_i (with $i = x', y', z'$). Consequently, T_1 relaxation is only due to $b_{x'}$ and $b_{y'}$, whereas T_2 relaxation may arise from $b_{x'}$, $b_{y'}$, or $b_{z'}$. On this basis, another statement can be made concerning the frequencies of the field fluctuations (*i.e.* of molecular motion) responsible for each type of relaxation. In order to perturb \mathbf{M} , a torque has to be in effect over a period of time. fluctuations (*i.e.* of molecular motion) cause which type of relaxation. Thus components of \mathbf{b} that are static in the rotating frame of reference most effectively perturb \mathbf{M} . Static b_z components in the laboratory frame are also static in the rotating frame of reference. Hence the zero frequency in the motional spectrum contributes to T_2 relaxation. On the other hand, a static $b_{x'}$ or $b_{y'}$ component in the rotating coordinate system arises from a high (ω_0) frequency component in the laboratory system. Only the (laboratory) high frequency contributions lead to a static $b_{x'}$ or $b_{y'}$ in the rotating frame and consequently to T_1 relaxation. These qualitative results are summarized in Table 2.1. A more quantitative discussion can be found in [36, p. 59 ff.] and in [41, p. 46 ff.].

laboratory frame:	rotating frame:	
$\omega = 0$	\rightarrow static $b_{z'}$	$\rightarrow T_2$ relaxation
$\omega = \omega_0$	\rightarrow static $b_{x'}, b_{y'}$	$\rightarrow T_1, T_2$ relaxation.

Table 2.1: Contributions of different frequency components of molecular motion to relaxation (see text).

Relaxation mechanisms

We now briefly describe the most important mechanisms that can lead to relaxation. They rely upon some sort of interaction between a spin and its surroundings, and a fluctuating time dependency of either the interaction or some property of the environment.

magnetic dipole-dipole interaction. In many cases (especially for $I = 1/2$) this is the most important relaxation mechanism. Although the separation of nuclei is very large compared to their dimensions, the magnetic field produced by the magnetic moment of spins influences the neighbouring spins. The interaction Hamiltonian fluctuates due to molecular motion, leading to relaxation. The T_2 values in solids are only of the order of $10\ \mu\text{s}$ [36, p. 48] due to the zero-frequency contribution to transverse relaxation (see Table 2.1) [42, p. 93]. In liquids and in biological tissue T_2 is usually much longer (see Table 2.2).

electric quadrupole interaction. Nuclei with $I > 1/2$ can possess a nonspherical charge distribution. In this case they have an electrical quadrupole moment that interacts with local electrical field gradients produced by the electron shell of the molecule that contains the nucleus. Reorientation of the molecule changes the electrical field gradient at the location of the nucleus which establishes a relaxation mechanism.

chemical shift anisotropy. The electronic shells of atoms and molecules modify the magnetic field that is experienced by a nucleus. The reason is twofold [43, p. 175]: moving electric charges in a magnetic field are subjected to the Lorentz force such that circular electric currents arise in the electronic environment of a nucleus. These currents give rise to a small additional magnetic field \mathbf{B}_l . Furthermore, the electronic shells are polarized by the magnetic field. This distortion also produces an additional magnetic field, \mathbf{B}_p . The magnitude of both \mathbf{B}_l and \mathbf{B}_p is proportional to B_0 . The magnitude of the effective magnetic field at the location of a nucleus can be written as

$$\mathbf{B}_{\text{local}} = \mathbf{B}_0 + \mathbf{B}_l + \mathbf{B}_p = (1 - \sigma)\mathbf{B}_0 \quad (2.37)$$

where σ is called the shielding factor. The resulting resonance frequency offset from ω_0 is called the chemical shift. It is characteristic of the chemical environment of a nucleus which is used in NMR spectroscopy to identify chemical compounds. The shielding factor can depend on the orientation of the molecule relative to \mathbf{B}_0 . The additional field $-\mathbf{B}_0\sigma$ and \mathbf{B}_0 need not be parallel, such that σ is a rank 2 tensor¹⁰. If σ is anisotropic then random motion of molecules causes the tensor σ to fluctuate, modulating the magnetic field at the nucleus and thus providing a relaxation mechanism.

spin-spin interaction (scalar coupling, J coupling). Spin-spin interaction is an indirect interaction between nuclei in the same molecule. In contrast to the direct magnetic dipole-dipole interaction, it is mediated through covalent bonds: The nuclear magnetic moment causes a polarization of the molecular orbital. The resulting magnetic moment of the orbital influences some other nucleus in the molecule. A time dependence of the Hamiltonian is introduced if either the relative orientation of the magnetic moments of the nuclei or their interaction via the molecular orbital fluctuates. The spin-spin interaction is sometimes called scalar coupling since it is independent of the orientation of the molecule with respect to the external magnetic field. Scalar coupling can also occur between a nuclear and an electronic spin in paramagnetic substances and is then referred to as contact interaction.

¹⁰See section 2.3 for a definition of the term tensor.

spin-rotation. When a molecule rotates, its electrons give rise to a magnetic moment that produces a magnetic field at the location of a nucleus in the molecule. Collisions between molecules cause this local field to fluctuate, thereby generating a relaxation mechanism.

The relaxation time constants T_1 and T_2 depend both on the type of molecules that contain the nuclei in question, and on the molecular environment. Thus different types of biological tissue exhibit different relaxation rates while their proton densities are often very similar. In medical applications of NMR the relaxation properties of tissues are the major basis for a distinction between healthy and pathological tissue.

NMR measurements can yield information on a number of other parameters including pH, temperature, concentration of different chemical species, diffusion coefficients, level of blood supply within living tissue, and velocity or acceleration of flow.

	1.5 T [44]		3 T [45]	
	T_1/ms	T_2/ms	T_1/ms	T_2/ms
White matter	510	67	832	80
Grey matter	760	77	1331	110
CSF	2650	280		

Table 2.2: Typical relaxation times in brain tissue and cerebrospinal fluid at 1.5 T and 3 T magnetic field strength.

The free induction decay

We now consider the properties of an NMR signal following a single RF pulse, the free induction decay. It is often useful to write the transverse components of the magnetization vector, \mathbf{M} , as a complex number

$$M_{xy}(t) = M_x(t) + iM_y(t) \in \mathbb{C}. \quad (2.38)$$

The equations (2.36) imply that the transverse magnetization after a 90° pulse in a liquid can be written as

$$M_{xy}(t) = M_0 e^{i\omega t} e^{-t/T_2^*} \quad (2.39)$$

where T_2 was replaced by T_2^* to account for dephasing due to magnetic field inhomogeneities.¹¹ The magnetization for flip angles θ other than 90° can be obtained by multiplying the right hand side with $\sin \theta$. Commonly the voltage signal induced in the receiver coil by the precession of \mathbf{M} is mixed (multiplied) with a reference that oscillates with the frequency ω_0 . The remaining signal only contains the frequency offsets $\omega_\Delta = |\omega| - |\omega_0|$. Only these lower frequencies can be processed by digital-to-analog converters. In order to discriminate between positive and negative difference frequencies ω_Δ the voltage signal is usually mixed with two reference oscillations that are $\pi/2$ out of phase, which yields two signals that are proportional to M_x and M_y , respectively, due to (2.14) [46]. This process is called quadrature detection. The detected

¹¹In solids, the FID can be approximated by a Gaussian [36, section 2.4].

signal can thus also be thought of as a complex time-dependent quantity, $S(t) \sim M_{xy}(t)$. After the 90° pulse this signal may be written as

$$S(t) = S_0 e^{i\omega_\Delta t} e^{-t/T_2^*} e^{i\phi} \quad (2.40)$$

where ϕ is an arbitrary, adjustable parameter of the mixing process (receiver phase). In most applications of NMR, the frequency spectrum of $S(t)$,

$$\tilde{S}(\omega) = S_0 \left(\frac{(T_2^*)^{-1}}{(T_2^*)^{-2} + (\omega - \omega_\Delta)^2} - i \frac{\omega - \omega_\Delta}{(T_2^*)^{-2} + (\omega - \omega_\Delta)^2} \right) e^{i\phi}, \quad (2.41)$$

is to be investigated. For $\phi = 0$, the real part of $\tilde{S}(\omega)$ is a Lorentzian symmetrical lineshape of $2/T_2^*$ full width at half maximum (FWHM), centred at $\omega = \omega_\Delta$. It is called the absorption spectrum. The imaginary part in the case $\phi = 0$ is antisymmetric about $\omega = \omega_\Delta$. It is called the dispersion spectrum.¹² If $\phi \neq 0$ then real and imaginary parts of the spectrum are linear combinations of absorption and dispersion spectrum. However, pure absorptive and dispersion parts can be obtained by shifting the complex phase of $\tilde{S}(\omega)$. This process is known as “phasing” the spectrum. A time delay between the end of the RF pulse and the start of acquisition has the same effect as a deviation of ϕ from 0. Since nuclei with different resonance frequencies develop different phase shifts during this time, the phase shift necessary to separate absorption and dispersion part may depend on the frequency. In this case a phase correction that is proportional to frequency must be applied. Since the magnitude spectrum is broader than the purely absorptive Lorentzian part [48, section 3.4], in spectroscopy the real part of the phase corrected spectrum is generally preferred to the magnitude spectrum. T_2 relaxation and magnetic field inhomogeneity determine the observed angular frequency linewidth according to [41, p. 4]

$$\omega_{1/2} = \frac{1}{T_2^*} = \frac{1}{T_2} + \frac{\gamma}{2} \Delta B_0 \quad (2.42)$$

where ΔB_0 is the FWHM of the B_0 distribution.

The spin echo

It is technically impossible to produce an absolutely homogeneous magnetic field within the sample. This problem is particularly important in medical imaging where sample dimensions are large. To reduce the effects of main field inhomogeneity a second RF pulse after the excitation may be used. After the magnetization has been tipped away from its equilibrium orientation parallel to the main field axis, z , the magnetic moments of the protons precess in-phase. The phases of two protons that experience a slightly different magnetic field start to diverge immediately after the excitation. If at the time τ after excitation a 180° pulse is applied, then the spins precess after the pulse about \mathbf{B}_0 as before but their “order” has changed: now the spins with the higher Larmor frequency precess “behind” the spins with lower frequency, and the phase difference between them now decreases. After another time delay τ after the second RF pulse the phase difference will be zero. At this time point the transverse magnetization component and the detectable signal assume a maximum before they

¹²The absorption spectrum represents the absorption of energy by the nuclear spins as a function of angular frequency [47, section 7.6]. The term “dispersion” spectrum is based on an optical analogy.

decay with the time constant T_2^* again. This signal maximum is called the Hahn Spin Echo. The symbol TE is commonly used for the time 2τ between excitation and the signal maximum. In contrast to the reversible T_2^* decay, the T_2 decay is irreversible.

At the centre of a spin echo the phase shift due to magnetic field inhomogeneity is zero. At a time period Δt before or after the echo centre the phase of a spin at a location \mathbf{r} can be expressed as $\omega_0(t - \Delta t) - \varphi(\mathbf{r})$ or $\omega_0(t + \Delta t) + \varphi(\mathbf{r})$, respectively, where φ is the phase error due to field inhomogeneity. By choosing the origin of time at the echo centre (which is equivalent to applying a constant phase shift) we achieve that the complex signal of the spin echo is invariant under simultaneous conjugation and reflection about the echo centre since

$$e^{i(-\omega_0\Delta t - \varphi(\mathbf{r}_1))} + e^{i(-\omega_0\Delta t - \varphi(\mathbf{r}_2))} = \left(e^{i(\omega_0\Delta t + \varphi(\mathbf{r}_1))} + e^{i(\omega_0\Delta t + \varphi(\mathbf{r}_2))} \right)^* \quad (2.43)$$

holds for the superposition of signal contributions from different locations. Hence, provided that the centre of the spin echo is sampled in the middle of the acquisition window, the (inverse) Fourier transform of the data is a purely real Lorentzian, in contrast to the FID spectrum. A constant phase factor renders it complex but does not increase the linewidth of the magnitude spectrum: there is no necessity for “phasing” the spectrum.¹³

The full removal of field inhomogeneity effects is only possible if the protons do not move during the experiment. Moving spins experience different magnetic fields over time such that the phase differences cannot be refocused by applying an RF pulse. Hence, although the signal intensity at the spin echo centre is not directly affected by the T_2^* decay, it is affected by diffusional motion of spins if the magnetic field is not perfectly homogeneous. The signal amplitude at the echo centre depends on the gradient G of the magnetic field, according to (see section 3.2) [49, 50, 40]

$$S(2\tau) = S(0) \exp\left(-\frac{2\tau}{T_2}\right) \exp\left[-D\gamma^2 G^2 \frac{2}{3}\tau^3\right] \quad (2.44)$$

where G and the diffusion coefficient D are assumed to be stationary. In order to reduce the dependence on diffusion, Carr and Purcell [50] used a train of 180° pulses to repeatedly refocus the magnetization with a train of refocusing RF pulses, $90^\circ - \tau - 180^\circ - 2\tau - 180^\circ - 2\tau - \dots$. At times τ after each 180° pulse, a spin echo occurs. The signal amplitude at the centre of the echo at time t is [41, section 2.4]

$$S(t) = S(0) \exp\left(-\frac{t}{T_2}\right) \exp\left[-D\gamma^2 G^2 \frac{1}{3}t\tau^2\right]. \quad (2.45)$$

By adjustment of τ the diffusion term may in principle be made as small as desired. However, imperfections of the 180° pulses can render the refocusing in the experiment by Carr and Purcell incomplete. Phase errors due to deviations of the flip angle from 180° accumulate if the phase of 90° and 180° pulses are the same. This can be avoided if the precession axis of all refocusing pulses is chosen to be parallel to the current direction of the transverse magnetization that was created by the initial 90° pulse in the $x'y'$ plane. Hence 90° and 180° pulses have to be 90° out of phase. As this scheme was proposed by Meiboom and Gill [51] this requirement is called the CPMG condition.

Dephasing due to magnetic field inhomogeneities (either intra-voxel dephasing or diffusion effects) is significant if samples are investigated that have a strongly nonuniform distribution of magnetic susceptibility, χ . At the boundaries between tissue and air, for example, strong background gradients can occur, in particular at high magnetic field strengths (*cf.* p. 26).

¹³ T_2 relaxation and non-refocusable phase changes have been neglected in this consideration. See [36, p. 72 f.].

Coherence pathways

It is also possible to generate echoes by RF pulses with flip angles other than 180° . For example, a $90^\circ\text{--}\tau\text{--}90^\circ\text{--}\tau$ sequence can also generate an echo [49]. The echo that forms at the end of the sequence $90^\circ\text{--}\tau_1\text{--}90^\circ\text{--}\tau_2\text{--}90^\circ\text{--}\tau_1$ irrespective of the value of τ_2 is called a stimulated echo ($\tau_1 \neq \tau_2$) [49]. In principle all echoes that occur can be accounted for by considering the magnetization vectors of groups of nuclei that experience the same magnetic field (isochromats). If the number of pulses is large it is difficult to account for the echo formation using the isochromat approach. However, it is possible to predict time and amplitude of the echoes by means of a formalism that is based on the Bloch equations.

The effect of a large number of RF pulses on the magnetization can be derived by successive application of the Bloch equations in both the presence and absence of the rotating RF fields [52]. It may be assumed that the pulses have rectangular shape (constant amplitude during the pulse), and that the pulse duration t_w is small compared to T_1, T_2 , and $1/|\omega_0 - \omega|$, and that B_1 is large ($\omega \gg |\omega_0 - \omega|, 1/T_1, 1/T_2$). Equation (2.18) describes the effect of an RF pulse on the magnetization vector as a rotation of \mathbf{M} about the axis of the RF field such that in the rotating frame of reference¹⁴

$$\begin{aligned} M_{x'}(t + t_w) &= M_{x'}(t) \\ M_{y'}(t + t_w) &= M_{y'}(t) \cos \theta - M_{z'} \sin \theta \\ M_{z'}(t + t_w) &= M_{y'}(t) \sin \theta + M_{z'} \cos \theta \end{aligned} \quad (2.46)$$

with $\mathbf{B}_1 = B_1 \mathbf{e}_{x'}$, $B_1 > 0$ as in equation (2.16), and $\theta = \omega_1 t_w$. Relaxation effects have been neglected. With the definition $F(t) = M_{x'}(t) + iM_{y'}(t)$ as in (2.38) and using the identity $2 \cos^2 \theta = 1 + \cos(2\theta)$ we can rewrite this to

$$F(t + t_w) = F(t) \cos^2 \frac{\theta}{2} + F^*(t) \sin^2 \frac{\theta}{2} - iM_{z'}(t) \sin \theta \in \mathbb{C} \quad (2.47)$$

$$M_{z'}(t + t_w) = M_{z'}(t) \cos \theta + \text{Im } F(t) \sin \theta \in \mathbb{R}. \quad (2.48)$$

This is the basis for the “partition formalism” proposed by Woessner [52]. By successive application of these rules it is possible to calculate the echo amplitudes of complicated pulse trains with any refocusing flip angle [53, 54, 55].

Let us consider a pulse sequence $90^\circ\text{--}\tau\text{--}\theta\text{--}2\tau\text{--}\theta\text{--}2\tau\text{--}\theta\cdots$. The 90_x pulse is applied to the equilibrium situation with $\mathbf{M} = M_0 \mathbf{e}_{z'}$. After the subsequent dephasing in the presence of magnetic field inhomogeneities and applied gradients the magnetization is

$$F^{(0)} = M_{x'} + iM_{y'} = M_1, \quad M_{z'}^{(0)} = 0 \quad (2.49)$$

where we have introduced a new symbol M_1 . If we want to calculate the effect of a train of RF pulses we repeatedly have to apply equations (2.47) and (2.48). We always specify the magnetization in terms of F and $M_{z'}$ which may be combined to a vector in $\mathbb{C} \times \mathbb{R}$. The magnetization components after the n th pulse following the 90° pulse are denoted by $F^{(n)}$ and $M_{z'}^{(n)}$. After the first RF pulse with flip angle θ_1 we obtain

$$\begin{pmatrix} F^{(1)} \\ M_{z'}^{(1)} \end{pmatrix} = \begin{pmatrix} F^{(0)} \cos^2 \frac{\theta_1}{2} + F^{(0)*} \sin^2 \frac{\theta_1}{2} \\ \text{Im } F^{(0)} \sin \theta_1 \end{pmatrix} = \begin{pmatrix} M_{11} + M_{1-1} \\ M_{10} \end{pmatrix} \quad (2.50)$$

¹⁴For positive θ the equations (2.46) describe the result of a 90_x RF pulse as a rotation of \mathbf{M} about the x' axis according to the left-hand rule. \mathbf{B}_1 is oriented along the positive x' axis. If $\mathbf{R}(\theta)$ is a twodimensional matrix representing a mathematically positive rotation by θ about $\mathbf{e}_{x'}$ then the effect of the pulse is a mapping $\begin{pmatrix} M_{z'} \\ M_{y'} \end{pmatrix} \mapsto \mathbf{R}(-\theta) \begin{pmatrix} M_{z'} \\ M_{y'} \end{pmatrix}$, or $\begin{pmatrix} M_{y'} \\ M_{z'} \end{pmatrix} \mapsto \mathbf{R}(\theta) \begin{pmatrix} M_{y'} \\ M_{z'} \end{pmatrix}$.

where the last equal sign defines new symbols for $M_{z'}^{(1)}$ and the parts of $F^{(1)}$ (in the same order as before the equal sign). The symbols M_{11}, M_{1-1}, M_{10} can serve to predict the echoes occurring with the given pulse sequence. In Equation (2.50) two parts of the transverse magnetization are considered separately: M_{11} is proportional to $M_{x'} + iM_{y'}$, and M_{1-1} is proportional to $M_{x'} - iM_{y'}$. This latter part of the transverse magnetization is phase reversed relative to the situation immediately after the 90° pulse. It will be completely rephased at time τ after the θ_1 pulse which is equal to the duration of the dephasing period between the 90° and the θ pulse. For $\theta_1 = 180^\circ$, $M_{11} = 0$ and $|M_{1-1}| = |M_{x'} + iM_{y'}|$ which is the Hahn spin echo described above. For $\theta_1 \neq 180^\circ$ however, the echo amplitude will be reduced relative to the spin echo amplitude by the factor $\sin^2(\theta/2)$.

Let us now consider how the formalism works for n pulses. Through repetitive application of the transformation rules starting from $M_{z'}^{(1)} = \text{Im } F^{(0)} \sin \theta_1$ we can prove that any $M_{z'}^{(n)}$ can be expressed as

$$M_{z'}^{(n)} = \sum_{j=0}^{n-1} \text{Im } F^{(j)} c_j = \frac{i}{2} \sum_{j=0}^{n-1} (F^{(j)} - F^{(j)*}) c_j \quad (2.51)$$

with some $c_j \in \mathbb{R}$. Equation (2.47) yields for the transverse component after the n th pulse

$$F^{(n+1)} = F^{(n)} \cos^2 \frac{\theta_{n+1}}{2} + F^{(n)*} \sin^2 \frac{\theta_{n+1}}{2} - i \sin \theta_{n+1} M_{z'}^{(n)}. \quad (2.52)$$

With the expression for $M_{z'}^{(n)}$ from equation (2.51) we can rewrite this as a linear combination of the $F^{(0)}, \dots, F^{(n)}$ and their complex conjugates,

$$F^{(n+1)} = \sum_{j=0}^n F^{(j)} c_j + \sum_{j=0}^n F^{(j)*} d_j, \quad \text{with some } c_j, d_j \in \mathbb{R}. \quad (2.53)$$

Thus $F^{(n+1)}$ is a linear combination of $F^{(0)}, \dots, F^{(n)}, F^{(0)*}, \dots, F^{(n)*}$. Since this holds for all n we conclude that $F^{(n+1)}$ must also be a linear combination of $F^{(0)}$ and $F^{(0)*}$. Hence we can assume that any $F^{(n)}$ may be written in the form¹⁵

$$F^{(n)} = \sum_i M_{q_0^i \dots q_{n-1}^i, 1} + \sum_i M_{q_0^i \dots q_{n-1}^i, -1} \quad (2.54)$$

$$M_{z'}^{(n)} = \sum_i M_{q_0^i \dots q_{n-1}^i, 0} \quad (2.55)$$

$$\text{with } M_{q_0^i \dots q_{n-1}^i, 1} = u F^{(0)} \quad \text{and} \quad M_{q_0^i \dots q_{n-1}^i, -1} = v F^{(0)*} \quad (2.56)$$

where $u, v \in \mathbb{R}$ and $q_j^i \in \{0, 1, -1\}$. Using this nomenclature, the magnetization after an RF pulse can be expressed in terms of the magnetization before the pulse. We assume that $F^{(n)}$ and $M_{z'}^{(n)}$ are expressed in the form (2.54) and (2.55) and aim at expressing $F^{(n+1)}$ and $M_{z'}^{(n+1)}$ in the same form. From equation (2.48) we can infer that

$$M_{z'}^{(n+1)} = \sum_i M_{q_0^i \dots q_{n-1}^i, 0} \cos \theta_{n+1} + \text{Im} \left[\sum_i M_{q_0^i \dots q_{n-1}^i, 1} + \sum_i M_{q_0^i \dots q_{n-1}^i, -1} \right] \sin \theta_{n+1} \quad (2.57)$$

¹⁵The symbols $q_0^i \dots q_n^i$ etc. represent *any* train of indices. If q_j^i occurs in different equations it can represent different values.

for which we define (in the same order) the symbols

$$\sum_i M_{q_0^i \dots q_{n-1}^i, 0, 0} + \sum_i M_{q_0^i \dots q_{n-1}^i, 1, 0} + \sum_i M_{q_0^i \dots q_{n-1}^i, -1, 0} \quad (2.58)$$

such that $M_{z'}^{(n+1)}$ assumes the form (2.55). In order to express the transverse component, $F^{(n+1)}$, in the form (2.54), we have to reform the last term in equation (2.52). Using again that all $F^{(n)}$ can be expressed as a linear combination of $F^{(0)}$, $F^{(0)*}$, we can express the $F^{(j)}$ in equation (2.51) by $F^{(0)}$, $F^{(0)*}$ and obtain by reordering

$$M_{z'}^{(n)} = \frac{i}{2} \sum_i (F^{(0)} + F^{(0)*}) d_i, \quad d_i \in \mathbb{R}. \quad (2.59)$$

Due to this relation we can write equation (2.52) in the form

$$F^{(n+1)} = F^{(n)} \cos^2 \frac{\theta_{n+1}}{2} + F^{(n)*} \sin^2 \frac{\theta_{n+1}}{2} + \sum_i M_{q_0^i \dots q_{n-1}^i, 0, 1} + \sum_i M_{q_0^i \dots q_{n-1}^i, 0, -1} \quad (2.60)$$

where $M_{q_0^i \dots q_{n-1}^i, 0, 1}$ and $M_{q_0^i \dots q_{n-1}^i, 0, -1}$ satisfy (2.56), with real proportionality constants. The first two terms in this equation can be expressed as

$$\begin{aligned} F^{(n)} \cos^2 \frac{\theta_{n+1}}{2} + F^{(n)*} \sin^2 \frac{\theta_{n+1}}{2} &= \\ &= \left[\sum_i M_{q_0^i \dots q_{n-1}^i, 1, 1} + \sum_i M_{q_0^i \dots q_{n-1}^i, -1, -1} \right] \cos^2 \frac{\theta_{n+1}}{2} + \left[\sum_i M_{q_0^i \dots q_{n-1}^i, 1, -1} + \sum_i M_{q_0^i \dots q_{n-1}^i, -1, 1} \right] \sin^2 \frac{\theta_{n+1}}{2} \\ &= \sum_i M_{q_0^i \dots q_{n-1}^i, 1, 1} + \sum_i M_{q_0^i \dots q_{n-1}^i, -1, -1} + \sum_i M_{q_0^i \dots q_{n-1}^i, 1, -1} + \sum_i M_{q_0^i \dots q_{n-1}^i, -1, 1} \end{aligned} \quad (2.61)$$

where the last line is a definition that corresponds to the summands in the preceding line in the same order. Combining (2.60) and (2.61) we can finally rewrite equation (2.52) as

$$F^{(n+1)} = \sum_i M_{q_0^i \dots q_n^i, 1} + \sum_i M_{q_0^i \dots q_n^i, -1} \quad (2.62)$$

such that $F^{(n+1)}$ has the same form as $F^{(n)}$ in equation (2.54).

We can successively express the magnetization after the n th pulse following the 90° pulse in terms of the $M_{q_0 \dots q_{n-1}}$ that describe the magnetization before the pulse, and then introduce new symbols $M_{q_0 \dots q_n}$ for the rephasing and dephasing parts of \mathbf{M} after the pulse. The history of a magnetization part $M_{q_0 \dots q_n}$ can then be derived by inspection of its indices. The train of indices 1, 0, -1 for example characterizes a magnetization part that can be thought of as being first in the transverse plane, after θ_1 parallel to z' , and after θ_2 transversal again and rephasing. This is the mechanism that leads to the stimulated echo. If the RF pulses are assumed to be infinitesimally short and if the θ_n pulse occurs at the time $t = t_n$, the term $M_{q_0 \dots q_n}$ will give rise to an echo at $t = t_n + T$ if

$$q_0 \tau + \sum_{i=1}^{n-1} q_i 2\tau + q_n T = 0 \quad \text{and} \quad q_n \neq 0. \quad (2.63)$$

This condition is equivalent to requiring that the accumulated phase of a spin is zero at $t = t_n + T$ irrespective of its position. The echo amplitude will be determined by the sum of all $|M_{q_0 \dots q_n}|$ that satisfy the condition (2.63). Each (q_0, \dots, q_n) represents a “coherence pathway”, *i.e.* a part of the magnetization with a common history in the sense described above.

Woessner [52] gives a physical interpretation of equations (2.47) and (2.48). The probability of finding a spin at the time $t + t_w$ in the state $|+\frac{1}{2}\rangle$ if it was in the state $|-\frac{1}{2}\rangle$ at time t (and vice versa) is $\sin^2(\theta/2)$, and it is $\cos^2(\theta/2)$ of finding it in the same state as before (transition probability) [56]. He describes the effect of an RF pulse as follows [52]: If $\theta \neq \pi$ the RF pulse separates the transverse magnetization into two parts. The first is proportional to $F^{(n)*}$ and due to nuclei that have “undergone a quantum transition”. The second is proportional to $F^{(n)}$ and due to those nuclei of which the state is untouched by the pulse. However, this would be in contradiction with the discussion on page 9 where we have seen that every spin state is modified by the RF pulse. Woessner’s interpretation is hence incompatible with our quantum mechanical description of the NMR experiment.

The effect of pulsed magnetic field gradients can be incorporated in the formalism. During a time period $[a, b]$ they impose an additional position-dependent phase shift

$$L_{a,b} = \int_a^b \gamma \mathbf{r} \cdot \mathbf{G}(t) dt \quad (2.64)$$

on the spins. The condition (2.63) for echo formation then assumes the form

$$q_0 L_{0,\tau} + \sum_{i=1}^{n-1} q_i L_{(2i-1)\tau, (2i+1)\tau} + q_n L_{(2n-1)\tau, (2n-1)\tau+T} = 0 \quad \text{and} \quad q_n \neq 0 \quad (2.65)$$

which is identical with (2.63) for a constant gradient. By appropriate application of gradient pulses it is therefore possible to suppress unwanted coherence pathways. This is sometimes desired to avoid interference between echoes that are due to different pathways. In a spin echo experiment for example signal contributions due to transverse magnetization created by an imperfect 180° pulse can be removed by applying two identical gradient pulses before and after the 180° pulse, respectively. Such gradients are generally called spoiler gradients.

2.1.2 NMR imaging

For the investigation of large inhomogeneous samples it is often important to obtain the spatial distribution of a measured parameter in the object. Due to the large abundance of water in biological tissues, such imaging experiments are most widely applied in the field of ^1H NMR. In NMR imaging the dependence of the resonance frequency on the magnetic field is used to localize the protons that give rise to an NMR signal. By means of a DC current in a coil the magnetic field may deliberately be rendered inhomogeneous. If the coil is suitably designed the magnetic field strength depends (at least within a certain volume) linearly on the spatial coordinate in the direction of the applied field gradient, or in other words, $\mathbf{G} = \nabla B(\mathbf{r})$ is independent of \mathbf{r} :

$$\mathbf{B}(\mathbf{r}) = (B_0 + \mathbf{r} \cdot \mathbf{G})\mathbf{e}_z, \quad \omega(\mathbf{r}) = \gamma(B_0 + \mathbf{r} \cdot \mathbf{G}). \quad (2.66)$$

The additional magnetic field is chosen to be much larger than magnetic field inhomogeneities and field shifts caused by the chemical environment of the spins. By using pulsed field gradients in three orthogonal directions instead of a constant gradient in one direction, the spatial

localization in three directions can be achieved. Slice-selective excitation, frequency and phase encoding are the main concepts used today to this purpose. The imaging principle (“back-projection”) that was applied in the first imaging experiments [57] was largely replaced by the two-dimensional Fourier transform or “spin-warp” method [58] that is presented below.

Slice selection

Due to the finite duration of an RF pulse, its spectrum contains more than one frequency. Let us denote the full width at half maximum of the angular frequency profile by $\Delta\omega_1$. Only protons with a Larmor frequency that matches one of these frequencies can be excited by the RF pulse. A spatially constant field gradient during the application of an RF pulse means that only protons within a slice of the sample are excited. The slice will be perpendicular to the direction of the field gradient, and its width will be proportional to the width of the frequency spectrum of the RF pulse. For the purpose of the following discussion the slice will be considered as oriented perpendicular to the z axis. If we denote the centre frequency of the pulse profile and the centre of the slice with ω_1^{cent} and z^{cent} , respectively, and the RF bandwidth and the slice thickness with $\Delta\omega_1$ and Δz , respectively, Δz and z^{cent} may be calculated by

$$\omega_1^{\text{cent}} = \gamma(B_0 + Gz^{\text{cent}}) \quad (2.67)$$

$$\Delta\omega_1 = \gamma G \Delta z. \quad (2.68)$$

For small tip angles ($\theta < 60^\circ$) the amplitude of transverse magnetization as a function of the resonance frequency (*i.e.* as a function of z) can be approximated by the Fourier transform of $B_1(t)$ [36, p. 105]. This function is called the slice profile.

Since the protons within a slice of finite thickness have different resonance frequencies, they will have different phases after the excitation. To avoid signal loss due to this intra-slice dephasing, we have to rephase the spins with a further gradient pulse with inverted amplitude. On the simplifying assumption that the spins are tipped instantaneously after half the duration of the RF pulse, the spins will be completely refocused if the rephasing gradient has half the duration of the slice excitation gradient pulse [36, p. 105]. For a refocusing RF pulse this rephasing gradient pulse is not necessary because the magnetization will dephase during the first half of the RF pulse, and rephase during the second half.

Frequency encoding

The protons within a selectively excited slice can also be distinguished by using the linear spatial variation of the Larmor frequency in the presence of a magnetic field gradient. If the slice is oriented perpendicular to z and a gradient $\mathbf{G} = G\mathbf{e}_x$ is applied,

$$\omega(\mathbf{r}) = \gamma(B_0 + xG). \quad (2.69)$$

If this field gradient is present during signal detection, the different frequencies in the detected signal can be unravelled using Fourier analysis (see below). The number of spins in the selected slice that have x coordinates in the range $x + dx$ then is proportional to the magnitude of the signal found in the corresponding frequency range $\omega + d\omega$. The gradient used for frequency encoding is often called the readout gradient.

To avoid the necessity of phasing (see p. 15) the signal is usually acquired in the form of a spin echo or a gradient echo: In the gradient echo alternative the readout gradient is preceded by

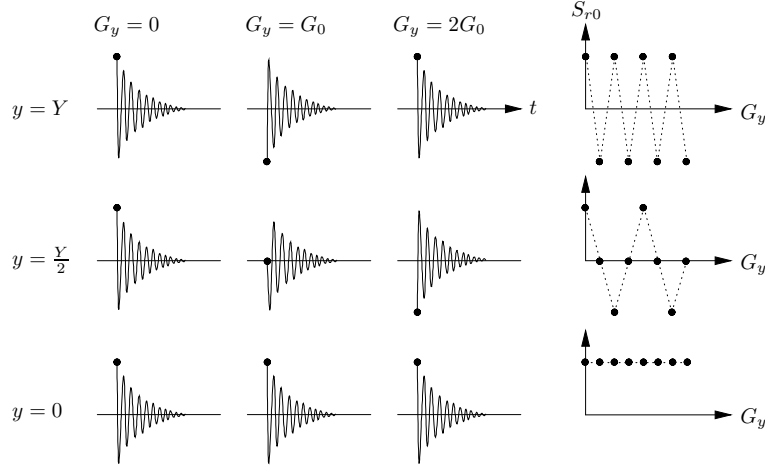


Figure 2.1: Principle of phase encoding. The real part of the signal arising from nuclei at different y positions is shown on the left. On the right, the real part of the initial signal, S_{r0} , is shown as a function of the strength of the phase encoding gradient. The frequency at which S_{r0} oscillates is proportional to the y coordinate of the nucleus. Figure after [47].

a gradient pulse in the readout direction but with inverted amplitude (read dephase gradient). This has the effect that the first part of the readout gradient neutralizes the dephasing effect of the inverted gradient, and the signal maximum occurs when $\int_0^t G(t') dt' = 0$. The signal acquired in this way is called a gradient echo. If a spin echo is to be measured the same gradient scheme can be used, adjusting the read dephase in such a way that gradient and spin echo coincide, *i.e.* $\int_0^t G(t') dt' = 0$ at the time of the spin echo centre. With the spin echo, instead of the inverted gradient immediately before the readout gradient a gradient pulse of the same polarity as the readout can be used before the 180° RF pulse.

Phase encoding

To resolve the spatial locations also along the y axis within the sample slice, the frequency encoding mechanism cannot be used. A gradient perpendicular to the readout gradient would superimpose on the readout gradient, and the precession frequency would be proportional to the sum of the x and y coordinates. Nevertheless the fundamental relation (2.5) can be used. The relative phase of a spin can be manipulated by switching to a higher or lower precession frequency for a short period of time. If this is realized through a magnetic field gradient pulse with $\mathbf{G} = G_y \mathbf{e}_y$, then after the pulse the spins will have acquired a phase shift proportional to their y position. This experiment is repeated with many different, equally spaced gradient strength values. The phase shift changes linearly with G_y , and the transverse magnetization components of a contributing spin as a function of G_y oscillate with a frequency that is proportional to the y coordinate of the spin. This behaviour is shown schematically in Fig. 2.1. A Fourier analysis of the data acquired after this phase manipulation, using the y gradient strength as the independent variable, can reveal the density of spins at a certain y position.

The concept of \mathbf{k} space

Using slice selection, frequency encoding, and phase encoding, a two-dimensional image of a sample slice can be produced. A complete three-dimensional representation of the sample can be attained by frequency encoding in one and phase encoding in two other perpendicular directions, or by phase encoding in all three directions. We now put the concepts of frequency and phase encoding in a more mathematical form.

If we use the Bloch equations (2.36), neglect the relaxation terms, and denote by $\rho(\mathbf{r})$ the proton density at the position \mathbf{r} , then the signal originating from an infinitely small volume dV in complex notation is

$$dS(\mathbf{r}, t) = \rho(\mathbf{r}) dV e^{i\phi(\mathbf{r}, t)}. \quad (2.70)$$

The time t may be measured from the centre of the excitation pulse. The exponent can be written as

$$i\phi(\mathbf{r}, t) = i\gamma \left[B_0 t + \int_0^t \mathbf{r} \cdot \mathbf{G}(t') dt' \right]. \quad (2.71)$$

We may henceforth neglect the B_0 term by considering only the quadrature signal after mixing with the ω_0 reference, such that only the offset frequencies $\omega - \omega_0$ appear in the signal. By integration of (2.70) over the sample volume we obtain the total received signal,

$$S(t) = \iiint \rho(\mathbf{r}) e^{i\gamma \mathbf{r} \cdot \int_0^t \mathbf{G}(t') dt'} d^3r. \quad (2.72)$$

With the definition

$$\mathbf{k} = \frac{\gamma}{2\pi} \int_0^t \mathbf{G}(t') dt' \in \mathbb{R}^3 \quad (2.73)$$

this equation assumes the form

$$\tilde{S}(\mathbf{k}) = \iiint \rho(\mathbf{r}) e^{i2\pi \mathbf{k} \cdot \mathbf{r}} d^3r. \quad (2.74)$$

Realizing that the right hand side is the Fourier transform of $\rho(\mathbf{r})$, we can obtain $\rho(\mathbf{r})$ by inverse Fourier transformation of $\tilde{S}(\mathbf{k})$,

$$\rho(\mathbf{r}) = \iiint \tilde{S}(\mathbf{k}) e^{-i2\pi \mathbf{k} \cdot \mathbf{r}} d^3k. \quad (2.75)$$

The equations (2.74) and (2.75) are fundamental to NMR imaging. They state that the detected signal, $\tilde{S}(\mathbf{k})$, is the Fourier transform of the proton density, $\rho(\mathbf{r})$. This is the mathematical representation of the principle of frequency and phase encoding. It helps to understand the effect of complicated trains of gradient pulses in imaging experiments and to compare the properties of imaging sequences [59]. The domain of definition of \tilde{S} is called “ \mathbf{k} space”. In two-dimensional Fourier imaging the term only refers to the $k_x k_y$ plane.

Let us assume that the frequency encoding, phase encoding, and slice selection gradients are aligned along the x , y , and z axis, respectively, and that the gradient pulses have rectangular

shapes. Then the components of the vector \mathbf{k} are

$$\begin{aligned} k_x &= \frac{\gamma}{2\pi} \int_0^t B_x(t') dt' \\ k_y &= \frac{\gamma}{2\pi} \int_0^t B_y(t') dt' = \frac{\gamma}{2\pi} G_y^a \tau \\ k_z &= 0 \end{aligned}$$

where τ and G_y^a denote the duration and amplitude, respectively, of the phase encode gradient pulse. The z component of \mathbf{k} is zero since the time integral over the slice selection gradient pulses vanishes if we have correctly refocused the slice gradients. The measurement yields the complex values of $\tilde{S}(\mathbf{k})$ for a finite range of discrete \mathbf{k} values that are accessed through variation of t and G_y^a . The signal is sampled at different times t during the readout gradient, and for different values of G_y^a where both t and G_y^a values are usually equidistant. To avoid aliasing, the G_y^a increment, $G_{y,\text{inc}}^a$, is chosen such that the phase increment between successive phase encoding steps does not exceed π at the furthest edges of the region to be imaged (the field of view, FOV). This requirement leads to

$$G_{y,\text{inc}}^a = \frac{2\pi}{\gamma\tau \text{FOV}} \quad \text{and} \quad k_{y,\text{inc}} = \frac{1}{\text{FOV}}. \quad (2.76)$$

The starting value of G_y^a must be such that $G_y^a = 0$ is included. The order in which the k_x and k_y values are accessed during the measurement can be represented as a graph in \mathbf{k} space called the \mathbf{k} -space trajectory. By means of a two-dimensional inverse Fourier transform according to equation (2.75) the measured $\tilde{S}(\mathbf{k})$ values may be converted into an image of the proton density distribution in the selected slice, $\rho(\mathbf{r})$. Since phase shifts can render the inverse Fourier transform of $\tilde{S}(\mathbf{k})$ complex, its magnitude is usually displayed.

2.1.3 Fast imaging

The time required to image a slice of the human body can be of the order of minutes. In particular the phase encoding steps require much time, for after each phase encoding step it takes the magnetization several T_1 periods to recover before the sample can be re-excited for the next phase encoding step. The number of phase encoding steps is typically about 256 in medical applications. Given an experiment that contains a single θ_x pulse which is repeated with TR , the longitudinal magnetization immediately before the RF pulse is given by [36, p. 65]

$$M_z = M_0 \frac{1 - \exp(-TR/T_1)}{1 - \cos\theta \exp(-TR/T_1)}. \quad (2.77)$$

Long acquisition times are a serious drawback in human applications. There are three main reasons why short acquisition times are desirable:

1. Subject motion between successive phase encoding steps causes image artefacts. Physiological motion due to respiration or cardiac activity can also induce artefacts. Particularly in diffusion weighted imaging the effects of motion can be devastating (see section 5.8).
2. Experiments that require the acquisition of many images may take unacceptably long for the subject, or patient. This problem is encountered for example in diffusion tensor imaging since here averaging is crucial for an acceptable signal-to-noise ratio, and images under different conditions have to be acquired.

3. In some applications a train of images is acquired to sample the evolution of a time dependent quantity. Often a subsecond temporal resolution is required. Examples are the measurement of haemodynamic changes due to brain activity (see ch. 6), or the observation of the passage of a contrast-agent bolus through a vascular network.

Different approaches have been proposed to minimize the acquisition time in MR imaging. In most cases their application is a trade-off between scan time and image quality or spatial resolution. Fast imaging techniques can be grouped into two categories.

1. Imaging sequences that minimize the time required for the spin system to recover from an excitation. This can be achieved by excitation with small flip angles. In this case the longitudinal magnetization has recovered shortly after each excitation such that the time between the excitations can be minimized. The FLASH method [60, 61] is the most common method in this category.
2. Sequences which try to minimize the number of excitations. Sequences that contain only one excitation are called single-shot techniques. The complete image information is then collected during the lifetime of transverse magnetization. In general, more than one line of k space needs to be sampled per excitation. After a single excitation the transverse magnetization is repeatedly refocused, and each echo is phase encoded independently. The echo train can either be generated by a train of successive RF pulses (*e.g.* RARE), or by magnetic field gradients that induce a train of gradient echoes (EPI).

As sequences in the first category have not been used for this thesis the following paragraphs will be restricted to the principles and properties of sequences in the second category.

RARE — refocusing with RF pulses

In the RARE (rapid acquisition with relaxation enhancement) sequence [62], a train of spin echoes is generated by means of 180° RF pulses. Each echo is phase encoded differently. This is achieved by application of a phase encoding gradient pulse before each echo and variation of the pulse amplitude from echo to echo. After the acquisition of an individual echo a gradient pulse called “rewinder” brings $\int_0^t G_{\text{ph}}(t')dt$ back to zero such that for each echo $\int_0^t G_{\text{ph}}(t')dt$ is solely determined by the gradient pulse directly preceding the echo. The k -space trajectory consists in this case of straight¹⁶ lines in the two-dimensional k space, the order of which can be determined at will.

The contrast in the image largely depends on TE_{eff} which is the time between the excitation and the centre of the echo with $\int_0^t G_{\text{ph}}(t')dt = 0$, *i.e.* $k_{\text{ph}} = 0$. This is generally true for most sequences and objects because low spatial frequencies largely determine the overall image intensity whereas high k values are responsible for sharp edges and fine details in the image. The acquisition order of the lines of k space determines TE_{eff} and thus the contrast properties of the image. Since at the centre of each spin echo any dephasing due to B_0 inhomogeneities is refocused, the image contrast is determined by T_2 rather than by T_2^* . An image where the intensity of a pixel largely depends on the T_2 value at that location is said to be T_2 weighted. Long effective echo times produce strong T_2 contrast whereas T_1 weighting can be achieved by short repetition times between excitations.

To increase the sensitivity it is possible, and common practice to use more than one excitation and to sample only a part of k space after each excitation. By such k -space segmentation

¹⁶provided that the readout gradient pulse is rectangular in shape

the echo train length per excitation is reduced. RARE provides images of high resolution and with a low artefact level. However, its applicability suffers from the large amount of energy the RF pulses deposit in the tissue. To avoid heating up the tissue long echo times have to be used. Since the resulting echo train length is incompatible with the limited relaxation times found in tissue RARE, is usually applied with k-space segmentation.

This drawback led to the development of RARE variants that employ refocusing angles below 180° (*e.g.* U-FLARE, see ch. 4). In these sequences a problem becomes crucial which is apparent in the RARE sequence to a lesser degree: if the flip angle of the refocusing pulses is not exactly 180° then stimulated echoes appear that can interfere with the spin echoes. If the CPMG condition (see section 2.1.1) is not fulfilled this can lead to severe artefacts. A contravention of the CPMG condition can occur for example in diffusion weighted imaging (see section 4.2.3). Due to equation (2.45) RARE sequences are less sensitive to diffusion than sequences that contain less refocusing pulses. However, diffusion sensitization can be deliberately introduced (see ch. 3) by means of a preparation experiment.

EPI — refocusing with gradient pulses

In the EPI (echo planar imaging) sequence [63] the magnetization is refocused by gradient pulses instead of by RF pulses. The magnetization is alternately dephased and rephased by an oscillating read gradient. Phase encoding of the train of gradient echoes thus generated can be accomplished in different ways. With a very weak, constant phase gradient the k-space trajectory is a zig-zag curve [63]. With weak, short phase gradient pulses (“blips”) simultaneous with the sign changes of the read gradient, the k space is sampled in a rectangular grid [64]. A further alternative is “spiral” EPI with oscillating read and phase gradients resulting in a spiral-shaped k-space trajectory. The echo train length is limited by the T_2^* decay but the spatial resolution can be increased by k-space segmentation. However, this renders the sequence sensitive to motion, in particular if diffusion weighting is involved (see section 5.8).

The major disadvantage of EPI is that dephasing due to magnetic field inhomogeneities is not refocused which can cause serious image artefacts [65]. In *in vivo* NMR main field inhomogeneity can arise from the different magnetic susceptibilities of air, muscle tissue, brain parenchyma, and CSF. The magnetic field \mathbf{B} in a (non-ferromagnetic) material with the (dimensionless) magnetic susceptibility χ is given by [29, p. 361]

$$\mathbf{B} = \mu_0(1 + \chi)\mathbf{H} \quad (2.78)$$

where μ_0 is the vacuum permeability and \mathbf{H} is the “macroscopic” magnetic field [66, p. 18]. The term $\chi\mathbf{H}$ is the magnetization, *i.e.* the magnetic moment per unit volume. The magnetized sample itself gives rise to a field \mathbf{H}_s within the sample and in the environment that is superimposed on the externally applied field \mathbf{H} and depends on the sample geometry. This additional field is responsible for the fact that the magnetic field at some location \mathbf{r} in an inhomogeneous sample is not simply determined by $\chi(\mathbf{r})$. On account of the resulting magnetic field gradients (susceptibility gradients) echo planar images of biological samples are often distorted near tissue borders: a field offset B_χ causes a phase evolution between successive phase encoding steps (the phase evolution between successive sampling points during echo acquisition is negligible since the time between sampling points is much shorter than the time between phase encoding steps). The resulting phase ramp over the data in phase encode direction appears after Fourier transformation as a bulk shift in this direction. This can be concluded from the shift theorem of the Fourier transform ([67, p. 104], *cf.* 95) or from the expression for the signal phase at the

centre of the n th echo acquisition,

$$\phi = \gamma \int_0^t B_z(\mathbf{r}, t) dt = \gamma y G_y \tau_{\text{ramp}} n + B_\chi \tau_{\text{pe}} n = \gamma \left(y + \frac{B_\chi \tau_{\text{pe}}}{G_y \tau_{\text{ramp}}} \right) G_y \tau_{\text{ramp}} n, \quad (2.79)$$

which was derived from 2.66 assuming triangular phase blips with ramp time τ_{ramp} and amplitude G_y , and where τ_{pe} is the time between successive phase encoding steps. In addition, intravoxel dephasing can lead to complete extinction in regions of low main field homogeneity (short T_2^* values). The inhomogeneity problem can be reduced by image correction algorithms that are based on field mapping techniques [68]. It is most prominent at high magnetic field strengths where susceptibility differences cause large background gradients, rendering T_2^* considerably shorter than the echo train length. Since high resolution requires a long echo train, the T_2^* decay limits the achievable resolution.

The influence of main field inhomogeneity can be reduced by incorporating a second RF pulse with a flip angle of 180° in the sequence and acquiring the train of gradient echoes during the time when the spin echo forms. This variant is called spin-echo EPI (SE-EPI) as opposed to gradient-echo EPI which has only an excitation RF pulse. The sequence timing is usually adjusted in such a way that the spin echo centre and the phase encoding step with $\mathbf{k} = 0$ coincide. In this case the image contrast is mainly determined by T_2 . The phase difference between spins at different locations is zero at $\mathbf{k} = 0$ but the phase difference between successive phase encoding steps remains the same. Therefore SE-EPI is also prone to image distortions although the extinction problem is mitigated.

The implementation of EPI requires strong and rapidly switchable magnetic field gradients and a high level of sequence adjustment, and it must include the implementation of a correction algorithm that takes account of slight differences between the echoes acquired with a positive read gradient (odd echoes) and the echoes acquired with a negative read gradient (even echoes). A phase correction needs to be applied before the actual images are formed by two-dimensional Fourier transform. Without correction the difference between odd and even echoes causes a shifted image of reduced intensity to be added to the image of the object [69, 70]. The shift occurs in the phase encode direction and is always equal to half the field-of-view. The signal intensity in the ghost can be space-dependent and is often accompanied by signal variations or extinctions in the object image. This artefact is known as Nyquist or $N/2$ ghost. The correction parameters can be determined from a separate reference scan which in comparison to the image scan only lacks the phase encoding gradient.

Since chemical shift dephasing is not refocused in EPI, the long time between the gradient echoes causes the frequency shift of fat protons in biological tissue to be translated into a spatial shift in the image in the phase encode direction. RF pulses tuned to the fat frequency are often used before the EPI sequence to saturate the fat protons and thus to suppress their signal in the image. In spite of its technical and fundamental disadvantages, EPI is widely used in imaging studies for psychological research since it can supply images within 30–100 ms. It is one of the fastest MR imaging techniques that are currently available.

2.2 Diffusion

Diffusion is the process by which matter is transported from one part of a system to another as a result of random molecular motion [71]. Consider for example a fluid system which consists of two types of molecules, denoted A and B, that are nonuniformly distributed. The concentrations

of A and B change with time until they have reached the equilibrium situation where both concentrations have the same value throughout the system — although they may be different from each other. The mechanism underlying this process is the random translational motion of molecules which is commonly called Brownian motion. A particle in the system has a mean kinetic energy $\frac{3}{2}kT$ of irregular “thermal” motion, regardless of its mass (only the velocity depends on the particle’s mass).¹⁷ This energy manifests itself in rotations and translations of the particle. The transport of molecules of type A, say, can be described by the flux density \mathbf{j} . If $\mathbf{v}(\mathbf{r})$ is the velocity at position \mathbf{r} , and c the concentration in terms of particles per unit volume, then the flux density is defined by $\mathbf{j} = c\mathbf{v}$. The number of particles crossing a surface S per unit time is given by the flux $\Phi_S = \int_S \mathbf{j} \cdot d\mathbf{s}$. Since the particle flux density is proportional to the concentration gradient, we can define by [72]

$$\mathbf{j} = -D\nabla c \quad (2.80)$$

a positive real quantity D which is called the diffusion coefficient. Equation (2.80) is called Fick’s first law. If the surface A encloses a volume V , we can use the divergence theorem to write the flux through the closed surface out of the volume V as

$$\Phi_A = \oint_A \mathbf{j} \cdot d\mathbf{s} = \int_V \nabla \cdot \mathbf{j} dV. \quad (2.81)$$

The surface element vectors $d\mathbf{s}$ are by convention oriented towards the outside of the volume. If the number N of particles contained in V changes during the time interval Δt by $\Delta N = N(t + \Delta t) - N(t)$, we can equate the loss of particles in V to the flux of particles through the surface of V ,

$$\frac{\Delta N}{\Delta t} = -\Phi_A = -\int_V \nabla \cdot \mathbf{j} dV. \quad (2.82)$$

For an infinitesimally small volume V we may approximate the right hand side by $-\nabla \cdot \mathbf{j}V$. Division by V yields

$$\frac{\Delta c}{\Delta t} = -\nabla \cdot \mathbf{j}. \quad (2.83)$$

In the limit of an infinitesimally short time period Δt and by means of equation (2.80) we obtain

$$\frac{dc}{dt} = \lim_{\Delta t \rightarrow 0} \frac{\Delta N}{\Delta t} = -\nabla \cdot \mathbf{j} = \nabla \cdot (D\nabla c) \quad (2.84)$$

and consequently, if the diffusion coefficient is independent of the concentration,

$$\dot{c} = D \operatorname{div} \operatorname{grad} c. \quad (2.85)$$

This relation is Fick’s second law [72]. It is also called the diffusion equation [71, p. 5].

¹⁷ k is Boltzmann’s constant, and T is the temperature in Kelvin.

2.2.1 Transport and self-diffusion

Random motion of molecules also takes place in a fluid containing only one type of molecule. It is termed self-diffusion [73] as opposed to transport diffusion as described above. For self-diffusion the above equations remain valid if we think of a part of the molecules as being labelled. The quantities \mathbf{j} and c have to be replaced by flux and fraction, respectively, of the labelled molecules, \mathbf{j}^* and c^* . The self-diffusivity can be defined by equation (2.80). The question of how the labelling is accomplished is irrelevant. However, while the self-diffusivity can depend on the total concentration of the molecules considered, it cannot depend on the fraction of labelled molecules, c^* , which is arbitrary and assumed not to affect molecular motion. Although self-diffusion and transport diffusion rely on the same mechanism, the corresponding diffusion coefficients are not necessarily the same.¹⁸ We shall be dealing with self-diffusion throughout the rest of this thesis and will denote the corresponding coefficient by D .

2.2.2 Random walk model of diffusion

At this point we should introduce a more microscopic view of the self-diffusion process. Einstein [76] related diffusion processes to Brownian motion by modelling the path of a single diffusing molecule as a “random walk”. The molecule is thought of as performing a large number of small jumps, each in a random direction. The direction of each jump is independent of the preceding jump.¹⁹ The probability density of finding at a time t a particle at the position \mathbf{r} is given by

$$P(\mathbf{r}, t) = \int P(\mathbf{r}_0, 0) P_s(\mathbf{r}, t | \mathbf{r}_0) d^3 r_0, \quad (2.86)$$

in terms of $P_s(\mathbf{r}, t | \mathbf{r}_0)$ which is the conditional probability density to find a particle at the time t at the position \mathbf{r} provided that it (the same particle) was at position \mathbf{r}_0 at $t = 0$. The function $P(\mathbf{r}, t)$ satisfies equation (2.80) with the concentration c replaced by $P(\mathbf{r}, t)$. As the spatial derivatives in (2.80) refer to the coordinates \mathbf{r} we can conclude that $P_s(\mathbf{r}, t | \mathbf{r}_0)$ satisfies an analogous equation. In this equation \mathbf{j} must be interpreted as the flux of conditional probability [36, section 6.2]. The continuity equation for conditional probability then leads to $\dot{P}_s = D \operatorname{div}_{\mathbf{r}} \operatorname{grad}_{\mathbf{r}} P_s$ which is analogous to the diffusion equation (2.85). With the boundary conditions $P_s(\mathbf{r}, 0 | \mathbf{r}_0) = \delta(\mathbf{r} - \mathbf{r}_0)$ and $P_s(\mathbf{r}, t | \mathbf{r}_0) \rightarrow 0$ as $|\mathbf{r} - \mathbf{r}_0| \rightarrow \infty$ this equation has the solution [36, 77]

$$P_s(\mathbf{r}, t | \mathbf{r}_0) = (4\pi Dt)^{-3/2} \exp \left[-\frac{(\mathbf{r} - \mathbf{r}_0)^2}{4Dt} \right]. \quad (2.87)$$

The function $P_s(\mathbf{r}, t | \mathbf{r}_0)$ is called the propagator. In homogeneous systems it has Gaussian form as in equation (2.87), and its FWHM increases linearly with \sqrt{t} . The probability density for any particle to have a displacement $\mathbf{s} = \mathbf{r} - \mathbf{r}_0$ after the time t ,

$$\overline{P}_s(\mathbf{s}, t) = \int P_s(\mathbf{r}_0 + \mathbf{s}, t | \mathbf{r}_0) \rho(\mathbf{r}_0) d^3 r_0, \quad (2.88)$$

¹⁸The Darken equation [74] relates transport and self-diffusivity to each other by means of the activity coefficient [75, p. 280].

¹⁹In fact Brownian motion must be modelled as a Markoff process [73, p. 577], *i.e.* the probability for the direction of a jump does not depend on the complete history but it can be determined from the direction of a jump at some earlier time. The “loss of memory” is characterized by the correlation time τ_c [36, p. 335].

where $\rho(\mathbf{r})$ is the particle density, is called the “average propagator” [78]. If P_s does not depend on the starting position \mathbf{r}_0 then $\overline{P}_s(\mathbf{s}, t) = P_s(\mathbf{s}, t|0)$. The ensemble average over $\mathbf{s}^2(t)$ is [36, section 6.2]

$$\langle \mathbf{s}^2(t) \rangle = \int \mathbf{s}^2 \overline{P}_s(\mathbf{s}, t) d^3s. \quad (2.89)$$

In the case of free diffusion described by the propagator given in (2.87) this leads to

$$\langle \mathbf{s}^2(t) \rangle = 6Dt. \quad (2.90)$$

This important relation means that the root mean square displacement of a particle is proportional to \sqrt{t} in the isotropic case. It is generally referred to as Einstein’s equation, and it can serve as an alternative definition of the diffusion coefficient D .

The function P_s in equation (2.87) has a maximum at $\mathbf{r} = \mathbf{r}_0$ for all times t . However, this does not mean that the majority of the particles have no net displacement since the probability of finding a particle within a sphere of radius $\sqrt{\varepsilon}$ centred about $\mathbf{r} = 0$ is

$$P(\mathbf{r}^2 \leq \varepsilon) = \int_0^{2\pi} \int_0^\pi \int_0^{\sqrt{\varepsilon}} P_s(\mathbf{r}, t|0) r^2 dr \sin \vartheta d\vartheta d\varphi < \int_0^{2\pi} \int_0^\pi \int_{\sqrt{\varepsilon}}^\infty P_s(\mathbf{r}, t|0) r^2 dr \sin \vartheta d\vartheta d\varphi = P(\mathbf{r}^2 > \varepsilon) \quad (2.91)$$

for sufficiently large t . Note further that $\langle \mathbf{r}^2 \rangle > 0$, and that $\langle \mathbf{r} \rangle = 0$ due to symmetry.

2.2.3 Restricted diffusion

In inhomogeneous media the time dependence of the mean square displacement can deviate from Einstein’s equation (2.90). This is important for example in biological tissues where cell membranes obstruct the motion of molecules. In a system consisting of small compartments that are divided by impermeable membranes, the displacement will follow (2.90) as long as t is small since only very few molecules collide with the wall of the compartment. But the displacement cannot increase beyond the cell size, l . The displacement will thus approximate a constant value for long times, $|\mathbf{s}| \rightarrow l$ as $t \rightarrow \infty$.

If we define the diffusion coefficient by (2.90), we can account for this behaviour by making D a function of time, $D(t)$. Since diffusion coefficients are often (as in NMR) measured by observing how far the molecules have travelled within a fixed observation time an effective diffusion coefficient is frequently defined by

$$D_{\text{eff}}(\tau) = \frac{\langle \mathbf{s}^2(\tau) \rangle}{6\tau} \quad (2.92)$$

where τ is the time of observation [74, section 7.2]. $D_{\text{eff}}(\tau) = D$ for small τ while for $\tau \rightarrow \infty$ the mean displacement $\sqrt{\langle \mathbf{s}^2(\tau) \rangle}$ approaches the compartment size l such that $D_{\text{eff}}(\tau) = l^2/(6\tau)$, *i.e.* $D_{\text{eff}}(\tau) \rightarrow 0$ as $\tau \rightarrow \infty$. Unless we know the compartment size, these two domains are indistinguishable from a measurement of $\langle \mathbf{s}^2(\tau) \rangle$ at a fixed τ . The propagator can be approximated to have the Gaussian shape in (2.87) with D replaced by D_{eff} [74, section 7.2].

2.2.4 Anisotropic diffusion

If diffusion is restricted by an *anisotropic* arrangement of barriers then the mean square displacement $\langle (\mathbf{s}(t) \cdot \hat{\mathbf{r}})^2 \rangle$ along a certain direction $\hat{\mathbf{r}}$ will depend on this direction ($|\hat{\mathbf{r}}| = 1$). Consider for example a situation where molecular motion is free (or even facilitated by additional forces) in a certain direction and obstructed in the perpendicular directions. A concentration gradient which is oblique to these directions will elicit a flux that is not parallel to the concentration gradient. Instead the flux will be diverted along the privileged direction. To account for \mathbf{j} and $-\nabla c$ not being parallel we have to introduce instead of D a tensor²⁰ \mathbf{D} of rank two such that Fick's law (2.80) assumes the form

$$\mathbf{j} = -\mathbf{D} \nabla c \quad \text{or} \quad j_i = - \sum_{k=1}^3 D_{ik} \frac{\partial c}{\partial r_k} \quad (2.93)$$

which can be understood as a matrix equation (*cf.* equation (2.134) below). Equation (2.93) implies that a concentration gradient in some direction can lead to a flux density in another direction: flux and concentration gradient are not necessarily parallel. The tensor element D_{ik} determines the contribution of the k th component of ∇c to the i th component of \mathbf{j} . If the diffusion is anisotropic, the equations (2.87) and (2.90) have to be replaced by [79]

$$P_s(\mathbf{r}, t | \mathbf{r}_0) = (4\pi t)^{-3/2} (\det \mathbf{D})^{-1/2} \exp \left[-\frac{(\mathbf{r} - \mathbf{r}_0)^T \mathbf{D}^{-1} (\mathbf{r} - \mathbf{r}_0)}{4t} \right] \quad \text{and} \quad (2.94)$$

$$\langle s^2 \rangle = 2t \operatorname{Tr} \mathbf{D}, \quad (2.95)$$

where \mathbf{D}^{-1} is the inverse of the matrix \mathbf{D} , and $\operatorname{Tr} \mathbf{D}$ is the sum of the diagonal elements of \mathbf{D} . We will later show that \mathbf{D}^{-1} exists (see p. 2.2.7). Based on the comparison of (2.90) and (2.95), one-third of the trace of the diffusion tensor can be interpreted as the mean of the diffusion coefficient over all directions. In addition, the relation

$$\langle s_i s_j \rangle = 2t D_{ij} \quad (2.96)$$

holds, and the diffusion equation (2.85) assumes the form

$$\dot{c} = \operatorname{div}(\mathbf{D} \operatorname{grad} c). \quad (2.97)$$

The diffusion tensor \mathbf{D} is said to be isotropic if it is proportional to the identity matrix.

2.2.5 Microscopic definition of the diffusion tensor

The diffusion tensor can also be defined in terms of microscopic quantities [36, p. 335]. This definition is based on the consideration of velocity correlations and will help us to understand why the diffusion tensor is symmetric.

The cross correlation function of velocity components is defined as

$$\kappa_{ij}(t) = \int_0^\infty v_i(t') v_j^*(t' + t) dt' / \int_0^\infty v_i(t') v_j^*(t') dt' \quad (2.98)$$

²⁰See section 2.3 for a definition of the term tensor.

where the complex conjugation may be omitted since \mathbf{v} is real. Using the ergodic hypothesis that in a stationary system a time average can be replaced by an ensemble average, and using that $\langle v_i(t)v_j(t+\tau) \rangle$ is independent of t , we can write the correlation function as [80, p. 53]

$$\kappa_{ij}(t) = \langle v_i(0)v_j(t) \rangle / \langle v_i(0)v_j(0) \rangle \quad (2.99)$$

where $\langle \dots \rangle$ denotes an ensemble average. The relationship between the diffusion tensor and the velocity correlation functions can be derived from equation (2.96),²¹

$$2tD_{ij} = \langle s_i(t)s_j(t) \rangle = \left\langle \int_0^t v_i(t_1) dt_1 \int_0^t v_j(t_2) dt_2 \right\rangle = \left\langle \int_0^t v_i(t_1) \int_0^t v_j(t_2) dt_2 dt_1 \right\rangle. \quad (2.100)$$

By substitution of t_2 by $\tau = t_2 - t_1$ we obtain

$$2tD_{ij} = \left\langle \int_0^t v_i(t_1) \int_{-t_1}^{t-t_1} v_j(\tau + t_1) d\tau dt_1 \right\rangle = \int_0^t \int_{-t_1}^{t-t_1} \langle v_i(t_1)v_j(\tau + t_1) \rangle d\tau dt_1 = \int_0^t \int_{-t_1}^{t-t_1} \langle v_i(0)v_j(\tau) \rangle d\tau dt_1 \quad (2.101)$$

where we have used the linearity of the ensemble average and the stationary character of the ensemble. Since the velocity correlation, $\langle v_i(0)v_j(\tau) \rangle$, tends to zero as $\tau \rightarrow \infty$ (*i.e.* it is very small if τ is much larger than the velocity correlation time [36]) we introduce a negligible error by expanding the limits of the τ integral to $\pm\infty$ [74, p. 53],

$$2tD_{ij} = \int_0^t \int_{-\infty}^{+\infty} \langle v_i(0)v_j(\tau) \rangle d\tau dt_1 = \int_0^t dt_1 \int_{-\infty}^{+\infty} \langle v_i(0)v_j(\tau) \rangle d\tau = 2t \int_0^\infty \langle v_i(0)v_j(\tau) \rangle d\tau \quad (2.102)$$

since the velocity correlation function is even (which is shown in the following section). Therefore the elements of the diffusion tensor and the velocity correlation function are related by

$$D_{ij} = \int_0^\infty \langle v_i(0)v_j(\tau) \rangle d\tau. \quad (2.103)$$

which is in fact the spectrum of the correlation function $\kappa_{ij}(t)$ without normalization evaluated at zero frequency.²²

2.2.6 Symmetry of the diffusion tensor

We have already mentioned that the diffusion tensor is symmetric, *i.e.* $D_{ij} = D_{ji}$. This property is a consequence of the microscopic reversibility of the particle trajectories [79]. For its derivation [73, p. 598] we use the definition (2.103) of \mathbf{D} in terms of particle velocities.

In equilibrium $\langle v_i(t)v_j(t+\tau) \rangle$ can only depend on τ rather than on t itself. Thus it is invariant under the translations of the origin of time, $t \mapsto t - \tau$. Therefore

$$K_{ij}(\tau) = \langle v_i(0)v_j(\tau) \rangle = \langle v_i(-\tau)v_j(0) \rangle = K_{ji}(-\tau). \quad (2.104)$$

²¹The derivation is a generalization of that in [74, p. 52].

²²Sometimes therefore the same symbol $D_{ij}(\omega)$ is used for the diffusion tensor and the Fourier transform of the non-normalized correlation function such that D_{ij} depends on the frequency ω [36]. See also [81, 82, 83].

But this does not imply $K_{ij}(\tau) = K_{ij}(-\tau)$ unless $i = j$, and it does not imply that $K_{ij}(\tau) = K_{ji}(\tau)$. Both relations can, however, be derived using an additional physical argument. Under inversion of the time, $t \mapsto t' = -t$, all velocities change their sign:

$$v_i(t) = -v'_i(t') = -v'_i(-t) \quad (2.105)$$

where $v'_i(t')$ is the function that describes the same situation as $v_i(t)$ in the new time frame. Hence we can reform the velocity correlation function to

$$\langle v_i(0)v_j(\tau) \rangle = \langle v'_i(0)v'_j(-\tau) \rangle = \langle v'_i(\tau)v'_j(0) \rangle \quad (2.106)$$

where we have used the invariance under time shift for the last equal sign. We now can use the fact that the laws of classical mechanics are invariant under time inversion. This means that we cannot distinguish by a physical argument between v_i and v'_i . Both functions are equally well possible. Therefore

$$\langle v'_i(\tau)v'_j(0) \rangle = \langle v_i(\tau)v_j(0) \rangle \quad (2.107)$$

must hold. (The situation would be slightly different for functions like $x_i v_i$ that change sign under time inversion, or functions that depend on angular velocities or magnetic fields which also change sign due to the reversed velocities of the charged particles constituting the magnetic field.) Combining equation (2.107) with equation (2.106) we obtain

$$\langle v_i(0)v_j(\tau) \rangle = \langle v_i(\tau)v_j(0) \rangle, \quad (2.108)$$

or in other words, it is completely irrelevant which of the functions v_i and v_j is evaluated at the earlier time point. Hence we have $K_{ij}(\tau) = K_{ji}(\tau)$ which via equation (2.103) yields the symmetry of the diffusion tensor,

$$D_{ij} = D_{ji}. \quad (2.109)$$

This equation is a form of Onsager's reciprocity relations [73, 84]. It shall further be noted that equation (2.108) combined with the invariance of $K_{ij}(\tau)$ under time translations implies that $K_{ij}(\tau)$ is even, $K_{ij}(\tau) = K_{ij}(-\tau)$ which has been used in equation (2.102). Since $K_{ij}(t) \in \mathbb{R}$ it further ensures that its Fourier transform, and hence D_{ij} , is purely real. For completeness it shall be mentioned that the diffusion tensor of charged particles in a magnetic field is not necessarily symmetric, due to the Lorentzian forces acting on the particles [15].

2.2.7 The eigenvector basis

The symmetry of D implies [85] that the matrix D can be diagonalized: for any symmetric real 3×3 matrix D an orthogonal²³ matrix S exists such that

$$S^T D S = \begin{pmatrix} \lambda_1 & 0 & 0 \\ 0 & \lambda_2 & 0 \\ 0 & 0 & \lambda_3 \end{pmatrix} = \Lambda \quad (2.110)$$

²³ $S^T = S^{-1}$

with $\lambda_1, \lambda_2, \lambda_3 \in \mathbb{R}$. Application of \mathbf{S} to a basis vector produces an eigenvector of \mathbf{D} : if the basis is $\{\mathbf{e}_1, \mathbf{e}_2, \mathbf{e}_3\}$,

$$\mathbf{D}\mathbf{S}\mathbf{e}_i = \mathbf{S}\mathbf{A}\mathbf{S}^T\mathbf{S}\mathbf{e}_i = \mathbf{S}\lambda_i\mathbf{e}_i = \lambda_i\mathbf{S}\mathbf{e}_i. \quad (2.111)$$

This means that we can reduce the matrix of the diffusion tensor to the diagonal form Λ in (2.110) by a change from the basis $\{\mathbf{e}_1, \mathbf{e}_2, \mathbf{e}_3\}$ to $\{\mathbf{S}\mathbf{e}_1, \mathbf{S}\mathbf{e}_2, \mathbf{S}\mathbf{e}_3\}$ consisting of eigenvectors of \mathbf{D} . The eigenvalues λ_i of \mathbf{D} are independent of the chosen basis. Eigenvectors corresponding to different eigenvalues are orthogonal to each other. If two eigenvalues are equal, for example $\lambda_2 = \lambda_3$, then all vectors \mathbf{r} in the plane perpendicular to $\hat{\mathbf{e}}_1$ are eigenvectors, $\mathbf{D}\mathbf{r} = \lambda_2\mathbf{r} = \lambda_3\mathbf{r}$. The basis vectors $\hat{\mathbf{e}}_2$ and $\hat{\mathbf{e}}_3$ may be chosen at will in this plane. We will always assume that the eigenvector basis is orthonormal. This will automatically be the case if it is created by application of the orthogonal matrix \mathbf{S} to the old orthonormal basis. We will henceforth use the symbol $\hat{\mathbf{e}}_i$ to represent an element of the orthonormal eigenvector basis. The eigenvector directions have a useful physical meaning: from Fick's first law (2.93) we infer that a concentration gradient that is parallel to one of the eigenvectors, $\nabla c = a\hat{\mathbf{e}}_i$ ($a \in \mathbb{R}$), leads to a flux density \mathbf{j} that is (anti)parallel to the concentration gradient,

$$\mathbf{j} = -\mathbf{D}(a\hat{\mathbf{e}}_i) = -\lambda_i a\hat{\mathbf{e}}_i. \quad (2.112)$$

By comparison with equation (2.80) a diffusion *coefficient* λ_i can be assigned to these directions. Hence the eigenvector directions are often termed the principal directions.

We can now show the existence of the inverse of \mathbf{D} which was used in equation (2.94). To this end we first prove that the eigenvalues of \mathbf{D} are positive (*i.e.* \mathbf{D} is positive definite [85, section 6.7.2]). Let us assume that one of the eigenvalues would be negative, $\lambda_i < 0$. In this case equation (2.93) implies that for a concentration gradient $\nabla c = a\hat{\mathbf{e}}_i$ ($a \in \mathbb{R}^{>0}$) along the principal direction corresponding to this eigenvalue the flux density is $\mathbf{j} = -\mathbf{D}(a\hat{\mathbf{e}}_i) = -a\lambda_i\hat{\mathbf{e}}_i = +c\hat{\mathbf{e}}_i$ with $c > 0$. Thus \mathbf{j} and ∇c point to the same direction. Such a situation would enhance the concentration gradient which would contradict the second law of thermodynamics. Hence we conclude that $\lambda_i \geq 0$ for $i = 1, 2, 3$. We can further explicitly exclude the case that an eigenvalue happens to be zero. This would mean that for a concentration gradient along the corresponding direction the equilibrium would never be reached. Hence, $\lambda_i > 0$ for $i = 1, 2, 3$. From \mathbf{D} being symmetric and positive definite we can conclude [85, section 6.7.9] that $\det \mathbf{D} > 0$ which implies that the inverse of \mathbf{D} in equation (2.94) exists. To determine \mathbf{D}^{-1} we realize that the inverse of Λ is

$$\Lambda^{-1} = \begin{pmatrix} 1/\lambda_1 & 0 & 0 \\ 0 & 1/\lambda_2 & 0 \\ 0 & 0 & 1/\lambda_3 \end{pmatrix}. \quad (2.113)$$

It then follows from the relation

$$\mathbf{D}(\mathbf{S}\Lambda^{-1}\mathbf{S}^T) = (\mathbf{S}\mathbf{A}\mathbf{S}^T)(\mathbf{S}\Lambda^{-1}\mathbf{S}^T) = \mathbf{S}\Lambda\Lambda^{-1}\mathbf{S}^T = \mathbf{S}\mathbf{S}^T = \mathbf{I}$$

(where \mathbf{I} means the identity matrix) that the inverse of \mathbf{D} is

$$\mathbf{D}^{-1} = \mathbf{S}\Lambda^{-1}\mathbf{S}^T. \quad (2.114)$$

Its eigenvectors are identical with those of \mathbf{D} , its eigenvalues are $1/\lambda_i$. In addition to (2.95) we calculate the root mean squared distance travelled along the direction of a given arbitrary

unit vector $\check{\mathbf{p}}$, $\langle(\mathbf{s} \cdot \check{\mathbf{p}})^2\rangle^{1/2}$. This quantity is important in NMR measurements where spatially constant field gradients are used to make the measurement sensitive to particle displacements along this direction (see chapter 3). It is given by (*cf.* (2.89))

$$\langle(\mathbf{s} \cdot \check{\mathbf{p}})^2\rangle = \int (\mathbf{s} \cdot \check{\mathbf{p}})^2 P_s(\mathbf{s}, t|0) d^3s \quad (2.115)$$

where we have assumed that $P_s(\mathbf{r}, t|\mathbf{r}_0)$, which is given in (2.94), is independent of \mathbf{r}_0 . The root mean square displacement must be independent of the coordinate system, and for convenience we choose the eigenvector system of \mathbf{D} for our calculation (the corresponding coordinates of \mathbf{s} then being \hat{s}_i). As the diffusion tensor is diagonal in the chosen basis we can calculate $\det \mathbf{D}$ and $\mathbf{s}^T \mathbf{D}^{-1} \mathbf{s}$ from (2.110) and (2.113) in terms of the eigenvalues λ_1 , λ_2 , and λ_3 . Let us suppose that the vector $\check{\mathbf{p}}$ is the first vector in some other orthonormal basis $\{\check{\mathbf{p}}, \cdot, \cdot\}$, and that $\mathbf{S}\check{\mathbf{p}} = \hat{\mathbf{e}}_1$ with \mathbf{S} being the transformation matrix between the bases. This is always possible by appropriate choice of the remaining vectors in the basis $\{\check{\mathbf{p}}, \cdot, \cdot\}$. Then the components of $\check{\mathbf{p}}$ in the eigenvector basis are

$$\check{\mathbf{p}} = \mathbf{S}^T \hat{\mathbf{e}}_1 = \mathbf{S}^T \begin{pmatrix} 1 \\ 0 \\ 0 \end{pmatrix} = \begin{pmatrix} S_{11} \\ S_{12} \\ S_{13} \end{pmatrix} \quad (2.116)$$

(the elements of \mathbf{S} are the same in both bases due to $\mathbf{S}^T \mathbf{S} = \mathbf{I}$) such that

$$(\mathbf{s} \cdot \check{\mathbf{p}})^2 = (S_{11}\hat{s}_1 + S_{12}\hat{s}_2 + S_{13}\hat{s}_3)^2. \quad (2.117)$$

Replacing this into the equation obtained from (2.115) with (2.94), (2.110) and (2.113) we obtain a sum of products of integral terms. Using the identities [38, p. 66]

$$\int_{-\infty}^{+\infty} x \exp[-\alpha^2 x^2] dx = 0 \quad \text{and} \quad \int_{-\infty}^{+\infty} x^2 \exp[-\alpha^2 x^2] dx = \frac{\sqrt{\pi}}{2\alpha^3} \quad (\alpha > 0) \quad (2.118)$$

we finally obtain

$$\langle(\mathbf{s} \cdot \check{\mathbf{p}})^2\rangle = 2t(S_{11}^2\lambda_1 + S_{12}^2\lambda_2 + S_{13}^2\lambda_3). \quad (2.119)$$

From this equation we can calculate the mean square displacement along any given direction if we know the eigenvalues and the eigenvectors of \mathbf{D} . The term in the brackets on the right hand side is equal to the first diagonal element of \mathbf{D} in the basis $\{\check{\mathbf{p}}, \cdot, \cdot\}$,

$$\tilde{D}_{11} = \sum_i S_{1i}^2 \lambda_i, \quad (2.120)$$

which can be derived from $\mathbf{D} = \mathbf{S}\mathbf{\Lambda}\mathbf{S}^T$. Hence,

$$\langle(\mathbf{s} \cdot \check{\mathbf{p}})^2\rangle = 2t\tilde{D}_{11} = 2t\check{\mathbf{p}} \cdot \mathbf{D}\check{\mathbf{p}} \quad (2.121)$$

where \tilde{D}_{11} is the first diagonal element of the diffusion tensor expressed in the basis $\{\check{\mathbf{p}}, \cdot, \cdot\}$. Equation (2.121) can be taken as a definition of the “diffusion coefficient in the direction of the unit vector $\check{\mathbf{p}}$ ”,

$$d(\check{\mathbf{p}}) = \langle(\mathbf{s} \cdot \check{\mathbf{p}})^2\rangle/(2t), \quad (2.122)$$

which is no diffusion coefficient in the sense of Fick's first law (2.93) because flux density and concentration gradient are in general not parallel, and $d(\tilde{\mathbf{p}})$ is a scalar. But it determines the mean square displacement in the direction $\tilde{\mathbf{p}}$ which is usually measured in NMR experiments (see chapter 3). Equation (2.121) can be generalized to

$$\langle s_i s_j \rangle = \langle (\mathbf{s} \cdot \mathbf{e}_i)(\mathbf{s} \cdot \mathbf{e}_j) \rangle = 2t D_{ij} = 2t \mathbf{e}_i \cdot \mathbf{D} \mathbf{e}_j \quad (2.123)$$

which is equivalent to (2.96). For its derivation we express \mathbf{e}_i and \mathbf{e}_j as a linear combination of the eigenvectors and using the matrix \mathbf{S} that transforms the basis into the eigenvector basis for writing

$$D_{ij} = (\mathbf{S} \mathbf{\Lambda} \mathbf{S}^T)_{ij} = \sum_k S_{ik} \lambda_k S_{jk} \quad \text{and} \quad \mathbf{e}_i \cdot \hat{\mathbf{e}}_j = \mathbf{e}_i \cdot \mathbf{S} \mathbf{e}_j = S_{ji}. \quad (2.124)$$

With the first identity in (2.118) which removes the cross terms for different eigenvector components we can then derive equation (2.123).

2.2.8 The diffusion ellipsoid

As a means of visualizing the diffusion process originating from a concentration $c(\mathbf{r}, t = 0) = \delta(\mathbf{r})$ we could use the surface of constant concentration which is equivalent to the surface of constant $P_s(\mathbf{r}, t|0)$. The positions \mathbf{r} that satisfy $P_s(\mathbf{r}, t|0) = P_0$ with an arbitrary constant P_0 between 0 and 1 form a surface that changes with time. But for sufficiently large t there will be no \mathbf{r} that satisfies the equation since $\max_{\mathbf{r}} P_s(\mathbf{r}, t|0) < P_0$. The surface of constant *relative* concentration (or probability P_s), $c(\mathbf{r}, t)/c(0, t)$, provides a better visualization. It can be obtained by setting $P_s(\mathbf{r}, t|0)/P_s(0, t|0) = e^{-1/2}$ where the constant on the right hand side is arbitrary. By replacing the definition (2.94) into this equation and taking the logarithm we obtain

$$\mathbf{r}^T \mathbf{D}^{-1} \mathbf{r} = 2t. \quad (2.125)$$

In the eigenvector basis this can be written as

$$\mathbf{r}^T \mathbf{\Lambda}^{-1} \mathbf{r} = \frac{\hat{x}^2}{\lambda_1} + \frac{\hat{y}^2}{\lambda_2} + \frac{\hat{z}^2}{\lambda_3} = 2t. \quad (2.126)$$

The positions \mathbf{r} that satisfy this equation form an ellipsoid. By comparison with the standard form of the ellipsoid equation,

$$\frac{\hat{x}^2}{a^2} + \frac{\hat{y}^2}{b^2} + \frac{\hat{z}^2}{c^2} = 1, \quad (2.127)$$

we conclude that the principal (half) axes of the ellipsoid are aligned with the eigenvector directions and their length is given by

$$a = \sqrt{2t\lambda_1}, \quad b = \sqrt{2t\lambda_2}, \quad c = \sqrt{2t\lambda_3}. \quad (2.128)$$

Hence the length of the position vector \mathbf{r}_e to the intersection of the ellipsoid with the i th eigenvector axis is

$$|\mathbf{r}_e| = \sqrt{2t\lambda_i} = \sqrt{\langle (\mathbf{s} \cdot \hat{\mathbf{e}}_i)^2 \rangle} \quad (2.129)$$

where the last equal sign follows from equation (2.121). Thus for all t the length of a principal (half) axis is equal to the mean distance travelled along that principal direction. This physical interpretation is possible due to the arbitrary constant $\exp(-1/2)$ above. However, if the three eigenvalues are different, the eigenvector directions are the only directions for which the intersection with the ellipsoid has this meaning, *i.e.* in general

$$|\mathbf{r}_e| = \sqrt{\langle (\mathbf{s} \cdot \tilde{\mathbf{p}})^2 \rangle} \quad \text{only if } \tilde{\mathbf{p}} \in \{\hat{\mathbf{e}}_1, \hat{\mathbf{e}}_2, \hat{\mathbf{e}}_3\}. \quad (2.130)$$

If (2.130) were valid for all directions $\tilde{\mathbf{p}}$ then the intersection $\nu\tilde{\mathbf{p}}$ of the ellipsoid with a straight line parallel to the arbitrary unit vector $\tilde{\mathbf{p}}$ would satisfy the ellipsoid equation

$$\frac{(\hat{\mathbf{e}}_1 \cdot \nu\tilde{\mathbf{p}})^2}{a^2} + \frac{(\hat{\mathbf{e}}_2 \cdot \nu\tilde{\mathbf{p}})^2}{b^2} + \frac{(\hat{\mathbf{e}}_3 \cdot \nu\tilde{\mathbf{p}})^2}{c^2} = 1 \quad (2.131)$$

and on the other hand $\nu = (2t\tilde{D}_{11})^{1/2}$ (2.121). If we substitute (2.116) into (2.131) we obtain

$$(S_{11}^2\lambda_1 + S_{12}^2\lambda_2 + S_{13}^2\lambda_3) \left(\frac{S_{11}^2}{\lambda_1} + \frac{S_{12}^2}{\lambda_2} + \frac{S_{13}^2}{\lambda_3} \right) = 1. \quad (2.132)$$

This equation is only true in the following special cases,

- $\lambda_1 = \lambda_2$ and $\tilde{\mathbf{p}} = u\hat{\mathbf{e}}_1 + v\hat{\mathbf{e}}_2$. In this case $S_{13} = 0$, and $S_{11}^2 + S_{12}^2 = \cos^2 \varphi + \sin^2 \varphi = 1$.
- $\lambda_1 = \lambda_2 = \lambda_3$
- $\tilde{\mathbf{p}} = \hat{\mathbf{e}}_1$.

Therefore equation (2.130) does not hold for arbitrary $\tilde{\mathbf{p}}$. Nevertheless, the ellipsoid given by (2.126) correctly describes at all times t the surface of constant relative concentration.²⁴

2.2.9 Implications for diffusion measurements in biological systems

In the current section 2.2 we have introduced two different views of the self-diffusion process: the Fickian view which considers the transport of (labelled) molecules, and the random walk approach which leads to the Einstein equation stating that the mean square particle displacement is proportional to the diffusion time. The former will be used in chapter 3 to derive the principle of NMR diffusion measurements. The random walk model allowed us to define an effective diffusion coefficient in the case of restricted diffusion. Restrictions to diffusion play a major role for diffusing water molecules in brain tissue (see the discussion in section 3.4.3). An anisotropic arrangement of diffusion barriers introduces anisotropy into the equations governing particle motion which is accounted for by the definition of the self-diffusion tensor.

As the symmetry of the diffusion tensor is not obvious from (the anisotropic form of) Fick's laws it was derived using an equivalent definition of the diffusion tensor that was based on particle velocity correlations. This symmetry property together with the propagator formalism arising from random walk theory allowed us to construct a geometrical representation of the diffusion characteristics of homogeneous anisotropic substances. The symmetry of the diffusion

²⁴The diffusion coefficient along a direction in the $\hat{\mathbf{e}}_1$ - $\hat{\mathbf{e}}_2$ plane as a function of the polar angle is given by $d(\varphi) = \lambda_1 \cos^2 \varphi + \lambda_2 \sin^2 \varphi$. Note that although $\sqrt{d(\varphi)}$ resembles the distance from the origin, r , in the parametric form of the ellipse equation, $r(\psi) = \sqrt{a^2 \cos^2 \psi + b^2 \sin^2 \psi}$, ψ is *not* the polar angle φ of the point $(x, y) = (r \cos \varphi, r \sin \varphi)$ on the ellipse.

tensor is essential for the possibility to derive the complete diffusion characteristics in all spatial directions from 6 independent tensor elements in any basis that can be measured in a finite number of experiments (see ch. 3). This possibility is particularly important if a spatially resolved measurement of the direction with the largest diffusion coefficient in a macroscopic sample is intended.

2.3 Tensors

Since the quantity describing diffusion in anisotropic media is a tensor we now define the term tensor, in order to provide a firmer mathematical basis than previously.

- If in an N -dimensional vector space \mathcal{V} , N^{k+l} numbers $a_{i_1 \dots i_k}^{j_1 \dots j_l}$ ($i_\nu, j_\mu = 1, \dots, N$) are given which transform under a change of the basis of \mathcal{V} according to [38]

$$a_{i_1 \dots i_k}^{j_1 \dots j_l} = \left(\frac{\partial x'^{j_1}}{\partial x^{s_1}} \dots \frac{\partial x'^{j_l}}{\partial x^{s_l}} \right) \left(\frac{\partial x^{r_1}}{\partial x'^{i_1}} \dots \frac{\partial x^{r_k}}{\partial x'^{i_k}} \right) a_{r_1 \dots r_k}^{s_1 \dots s_l} \quad (2.133)$$

(where we have used Einstein's summation convention that a summation is carried out over all indices that appear both as a superscript and as a subscript), then the numbers $a_{i_1 \dots i_k}^{j_1 \dots j_l}$ are called the coordinates of a *tensor* of rank $(k + l)$, and the tensor is called covariant of order k and contravariant of order l .

- An equivalent definition of a tensor is the following [86]: a multilinear function $\alpha : \mathcal{V}^{*l} \times \mathcal{V}^k \rightarrow \mathbb{R}$ is called a tensor that is covariant of order k and contravariant of order l .²⁵ The N^{k+l} values of the function α for the basis vectors, $A_{j_1 \dots j_k}^{i_1 \dots i_l} = \alpha(\boldsymbol{\varepsilon}^{i_1}, \dots, \boldsymbol{\varepsilon}^{i_l}, \mathbf{e}_{j_1}, \dots, \mathbf{e}_{j_k})$, are called the coordinates of the tensor. This definition implies that under a change of basis in \mathcal{V} and \mathcal{V}^* the $A_{j_1 \dots j_k}^{i_1 \dots i_l}$ transform according to (2.133).²⁶
- If a physical law is expressed in terms of tensors, the equations have the same form in any basis [86, p. 70]. This is the major benefit from expressing equations in terms of tensors.
- A covariant tensor of order two is called *symmetric* if $A_{ij} = A_{ji}$ in some coordinate system. This relation then holds for any basis in \mathcal{V} . Symmetric contravariant tensors are defined in an analogous manner. For higher-order tensors the definition relates to a pair of the indices. For a mixed tensor that is contravariant of order 1 and covariant of order 1, this definition would not make sense since $A_j^i = A_i^j$ does not necessarily hold for any basis. However, such a tensor may be called symmetric if for $a^{jk} = a_{\cdot i}^j g^{ik}$ the relation $a^{jk} = a^{kj}$ holds, where g^{ik} is the metric tensor [38, section 8.3.1.3].²⁷
- A Euclidean vector space²⁸ of finite dimension is “dual to itself”, *i.e.* one can define an isomorphism between the vector space and its dual space such that we can identify the two spaces with each other [86, section 1.7]. This means that the bases of \mathcal{V} and \mathcal{V}^* consist

²⁵ \mathcal{V}^* denotes the dual space of the vector space \mathcal{V} , *i.e.* the vector space of all linear functions $f : \mathcal{V} \rightarrow \mathbb{R}$, given that \mathcal{V} is a vector space over the field (*german* Körper) \mathbb{R} . Multilinear means linear in every argument.

²⁶The term covariant derives from the fact that covariant coordinates transform in the same way as the basis vectors in \mathcal{V} [87, p. 295].

²⁷By means of the metric tensor covariant coordinates can be converted into contravariant coordinates.

²⁸A vector space is called Euclidean if there is a scalar product defined on it.

of vectors in the same space. An orthonormal basis in a Euclidean vector space of finite dimension is identical with its dual basis. Therefore we need not distinguish between covariant and contravariant coordinates *as long as we restrict ourselves to orthonormal bases* [86, p. 38]. In this case $a^i = a_i$ holds, for example, for the coordinates of a vector.

- Strictly speaking, the gradient of a scalar field is a covariant tensor of rank 1 [86, p. 191]. It maps a contravariant displacement vector onto the change of the scalar. Forces are covariant vectors (tensors of rank 1) [86, section 4.1]. Conservative forces for example can be expressed as $\mathbf{f} = \text{grad } c$, or in coordinates $f_i = \partial_i c = \partial c / \partial x^i$.²⁹ Position and velocity are contravariant tensors of rank 1. Since the current density \mathbf{j} is proportional to a velocity, it is also a contravariant vector. Hence Fick's first law (2.93) must be written in the form

$$j^i = -D^{ij}(\nabla c)_j = -D^{ij} \frac{\partial}{\partial x^j} c = -D^{ij} \partial_j c. \quad (2.134)$$

This can be taken as a definition of \mathbf{D} as a contravariant tensor of rank two. Because the definition (2.103) of the diffusion tensor is based on the contravariant vectors of particle velocities it is also consistent with D^{ij} being contravariant of rank two.

- Sometimes it is convenient to have a symbol that represents all coordinates of a tensor. This notation is used for some tensors occurring in physics and is called dyadic notation [88, 38]. A dyadic can be thought of as a linear vector function $\Phi : \mathcal{V} \rightarrow \mathcal{V}$ with [38]

$$\mathbf{w} = \Phi \mathbf{v} = v^i a_i^j \mathbf{e}_j \quad (2.135)$$

where a_i^j are the coordinates of a rank two tensor, covariant of order 1 and contravariant of order 1. By equation (2.135) the mapping Φ is related to the function α in the second tensor definition given above. Comparing this equation with (2.134) we note that the diffusion tensor deviates from a dyadic in that $\Phi \equiv \mathbf{D}$ maps a *covariant* vector with coordinates $\partial_j c$ to a contravariant vector j^i . Nevertheless we can adopt the notation $\mathbf{j} = -\mathbf{D}(\nabla c)$ which is nothing else than the matrix notation of equation (2.93).

We will in the following chapters exclusively use orthonormal bases and will therefore not distinguish between co- and contravariant indices, and will treat \mathbf{D} simply as a matrix.

²⁹See [86, section 4.1] for further explanation.

Chapter 3

NMR measurement of anisotropic self-diffusion

There are two possible strategies to measure self-diffusivities. One strategy is based on a measurement of the concentration of labelled particles. The second possibility is to measure the mean displacement of the particles within a given time. These two approaches correspond to the two possible definitions of self-diffusivity, Fick’s first law (2.93) and the Einstein relation (2.90).

The concentration, or “tracer” techniques often use radioactive isotopes to produce a variant of the molecule under investigation. The isotope must be detectable by means of the emitted radiation but still similar enough to the original molecule to diffuse in the same way. Especially for isotopes with a similar atomic weight this assumption is quite well met.

Among the non-tracer techniques, neutron and light scattering techniques exploit the effect of molecular motion on the scattering pattern. Hence they are well-suited to investigate the elementary steps of diffusion [74]. Nuclear magnetic resonance is the only non-tracer technique that allows the observation of path lengths that are much larger than the mean length of the elementary jump of a particle in the random walk model [77]. This is necessary since the Einstein relation is only valid for observation times that are much longer than the velocity correlation time [36, p. 336].

The investigation of living tissue imposes further requirements on the method of measurement. The experiment should be non-invasive, and it should supply a three-dimensional spatial resolution in the millimeter range. Moreover, for our purpose it must provide directional information, *i.e.* all elements of the self-diffusion tensor. Finally, the mean displacement of a molecule within the observation time must be larger than or comparable to the cell size. Only under this condition a measurement can reveal restrictions to molecular motion due to tissue structure. Nuclear magnetic resonance fulfils these requirements to a high degree and is currently the only method capable of such measurements.

3.1 The Bloch equations including diffusion and flow

In 1956, Torrey [40] modified Bloch’s phenomenological equations (2.36) to account for diffusional motion of spins in a fluid. In order to treat also flow and anisotropic and restricted diffusion, Stejskal [89] modified Torrey’s approach. To prepare ourselves for diffusion tensor imaging, we sketch Stejskal’s derivation of the additional terms that have to be introduced in

the Bloch equations.

In an NMR experiment, both diffusion and flow of spins may be seen as a “transport of magnetization”. The magnetization (*i.e.* the magnetic moment per unit volume) in an infinitesimally small volume element depends on the population of the spin eigenstates and the spin density in the volume element. If the spins move, both populations and spin density may change at the location of the volume element. To analyze the effect of diffusion and flow it is thus reasonable to consider the magnetization to be a function of position and time. The three axes of a Cartesian coordinate system may be chosen arbitrarily with respect to the direction of the magnetic field. Recalling that the quantization of angular momentum does not require a magnetic field, we state that a measurement of the x component of the magnetic moment of a spin can only yield the results $\pm\hbar\gamma/2$. For simplicity we restrict ourselves to the spin $I = 1/2$ case but the result shall be independent of I . The spins may be grouped according to the orientation of their magnetic moment relative to the x axis, such that we can define two separate spin density functions, n_+ and n_- , and corresponding current densities, \mathbf{j}_+ and \mathbf{j}_- . For the fluxes it follows from equation (2.93) that

$$\mathbf{j}_{\pm} = \mathbf{v}n_{\pm} - \mathbf{D}\nabla n_{\pm} \quad (3.1)$$

in a medium flowing with the velocity \mathbf{v} . The diffusion tensor \mathbf{D} , \mathbf{v} , and n_{\pm} may be functions of both position and time. The net flux of magnetization can be written as

$$\mu(\mathbf{j}_+ - \mathbf{j}_-) = \mathbf{v}M_x - \mathbf{D}(\nabla M_x) \quad (3.2)$$

where $\mu = \hbar\gamma/2$. For simplicity the notation does not explicitly show that \mathbf{M} (and possibly \mathbf{v} and \mathbf{D}) are functions of position and time. The continuity equation equates the rate of change of the x component of the total magnetic moment, $M_x V$, of a small volume element V to the flux through its surface ∂V , such that

$$\left(\frac{\partial}{\partial t} M_x V\right)_{\mathbf{D}, \mathbf{v}} = - \oint_{\partial V} \mu(\mathbf{j}_+ - \mathbf{j}_-) \cdot d\mathbf{s} = \oint_{\partial V} (-\mathbf{v}M_x + \mathbf{D}\nabla M_x) \cdot d\mathbf{s} \quad (3.3)$$

where the subscripted \mathbf{D}, \mathbf{v} on the left hand side mean that diffusion tensor and velocity are assumed to be constant. Using the divergence theorem of Gauß we can rewrite this to

$$V \left(\frac{\partial M_x}{\partial t}\right)_{\mathbf{D}, \mathbf{v}} = \int_V \text{div}(-\mathbf{v}M_x + \mathbf{D}\nabla M_x) dV. \quad (3.4)$$

By partial differentiation with respect to V we obtain

$$\left(\frac{\partial M_x}{\partial t}\right)_{\mathbf{D}, \mathbf{v}} = -\text{div}(\mathbf{v}M_x) + \text{div}(\mathbf{D}(\text{grad } M_x)). \quad (3.5)$$

This term has to be added to the dM_x/dt expression in the Bloch equations (2.36). After analogous calculation for M_y and M_z one obtains the modified Bloch equations

$$\begin{aligned} \frac{\partial M_x}{\partial t} &= \gamma(\mathbf{M} \times \mathbf{B})_x - \frac{M_x}{T_2} - \text{div}(\mathbf{v}M_x) + \text{div}(\mathbf{D}(\text{grad } M_x)) \\ \frac{\partial M_y}{\partial t} &= \gamma(\mathbf{M} \times \mathbf{B})_y - \frac{M_y}{T_2} - \text{div}(\mathbf{v}M_y) + \text{div}(\mathbf{D}(\text{grad } M_y)) \\ \frac{\partial M_z}{\partial t} &= \gamma(\mathbf{M} \times \mathbf{B})_z - \frac{M_z - M_0}{T_1} - \text{div}(\mathbf{v}M_z) + \text{div}(\mathbf{D}(\text{grad } M_z)) \end{aligned} \quad (3.6)$$

where now a strong magnetic field in z direction has been assumed. The total time derivative in the equations (2.36) has been replaced by a partial derivative since now the components of \mathbf{M} depend on both position and time.

Strictly speaking, a further term should have been included in equation (3.1). An inhomogeneous magnetic field exerts both a torque $\boldsymbol{\mu} \times \mathbf{B}$ and a force $-\nabla(\boldsymbol{\mu} \cdot \mathbf{B})$ on a magnetic moment. Torrey added a term to equation (3.1) accounting for the drift velocity that is in liquids proportional to this force. It leads¹ to a further term $-\text{div}(\mathbf{D} \text{grad } M_{i,0})$ in the expression for $\partial M_i / \partial t$ [40]. Since the gradients of the equilibrium magnetization are much smaller than gradients of M_i this term is very small [40, 43, 89, 91] and therefore neglected.

3.2 The Stejskal-Tanner experiment

Based on the Bloch equations including diffusion and flow, Stejskal [89] calculated the effect of diffusion in the presence of a time dependent magnetic field gradient in a spin echo experiment. He separated the effects of diffusion, flow, reversible dephasing due to external gradients, relaxation, and precession in the main magnetic field,

$$m = M_x + iM_y = A(t)e^{i\Phi(\mathbf{v},t)}e^{-ig(t)}e^{-t/T_2}e^{-i\omega_0 t}. \quad (3.7)$$

with some real-valued functions $A(t)$, $\Phi(t)$ and $g(t)$. The effect of flow is a phase shift of the transverse magnetization. Diffusion in the presence of a magnetic field gradient (that may be time dependent), however, reduces the magnetization amplitude according to

$$\ln \frac{A(t)}{A(0)} = -\gamma^2 \int_0^t (\mathbf{F}(t') - 2\Theta(t' - \tau)\mathbf{f}) \cdot \mathbf{D} (\mathbf{F}(t') - 2\Theta(t' - \tau)\mathbf{f}) dt' \quad (3.8)$$

$$\text{where } \mathbf{F}(t) = \int_0^t \mathbf{G}(t')dt', \quad \mathbf{f} = \mathbf{F}(\tau), \quad \text{and} \quad \Theta(t) = \begin{cases} 1 & \text{if } t \geq 0 \\ 0 & \text{otherwise} \end{cases} \quad (3.9)$$

if the refocusing RF pulse occurs at $t = \tau$. If the diffusion tensor \mathbf{D} is constant this can be reformed to [89]

$$\ln \frac{A(t)}{A(0)} = -\gamma^2 \left[\int_0^t \mathbf{F}(t') \cdot \mathbf{D} \mathbf{F}(t') dt' - 4\Theta(t - \tau)\mathbf{f} \cdot \mathbf{D} \int_\tau^t \mathbf{F}(t') dt' + 4\Theta(t - \tau)(t - \tau)\mathbf{f} \cdot \mathbf{D} \mathbf{f} \right] \quad (3.10)$$

where we have used $\mathbf{f} \cdot \mathbf{D} \mathbf{F} = \mathbf{F} \cdot \mathbf{D} \mathbf{f}$ which follows from the symmetry of the diffusion tensor. If the gradient is constant with space and time, and \mathbf{D} is time independent and isotropic, this equation (at $t = 2\tau$) reduces to Hahn's result for the spin echo attenuation by diffusion in equation (2.44),

$$\ln \frac{S(2\tau)}{S_0} = -\gamma^2 D G^2 \frac{1}{3} (2\tau)^2. \quad (3.11)$$

For the further discussion of the principle of NMR diffusion measurements let us temporarily focus on the situation where diffusion is isotropic. The reason for the signal attenuation can be

¹By means of the Nernst-Einstein equation [90] the diffusion tensor and a term kT are introduced, the latter is the reason for the appearance of equilibrium magnetization $M_{i,0}$.

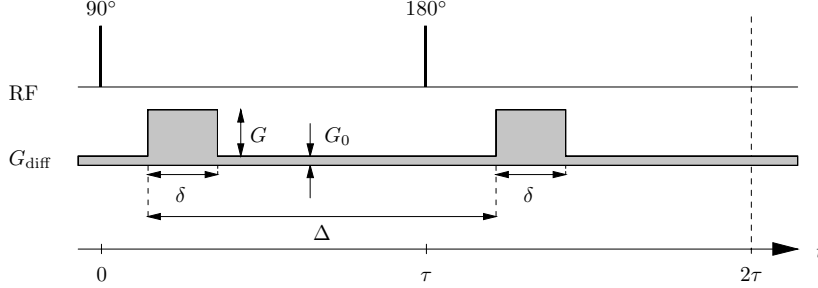


Figure 3.1: Stejskal-Tanner type spin echo preparation experiment for diffusion weighting.

understood in a qualitative manner by considering the phase shift of a spin due to a constant gradient during the spin echo experiment: a stationary nucleus accumulates a phase shift $\phi = \int_0^\tau \gamma \omega(t) dt$ during the first τ period until the refocusing pulse. The refocusing RF pulse inverts the phase of all spins, *i.e.* it maps $\phi(\tau)$ to $-\phi(\tau)$. The time between the refocusing pulse and the echo is also τ , such that the phase accumulated in the second τ period is again $\phi(\tau)$. Hence the phase of the spin at $t = 2\tau$ is $-\phi(\tau) + \phi(\tau) = 0$. If, however, the spin position changes during the experiment, the net phase at $t = 2\tau$ is

$$\phi(2\tau) = - \int_0^\tau \omega(\mathbf{r}(t')) dt' + \int_\tau^{2\tau} \omega(\mathbf{r}(t')) dt' \neq 0 \quad (3.12)$$

provided that the trajectories $\mathbf{r}(t)$ before and after the refocusing pulse do not by accident satisfy $\int_0^\tau \mathbf{r}(t') \cdot \mathbf{G} dt' = \int_\tau^{2\tau} \mathbf{r}(t') \cdot \mathbf{G} dt'$. Since motion due to diffusion is of random nature, after a short time the phase shifts that the nuclei have accumulated will be distributed over a range about zero. Because the total magnetization is a vector average over the ensemble of spins, this results in an attenuation of the spin echo signal.

The influence of diffusion on the spin echo amplitude can be exploited to measure the diffusion tensor. The diffusion attenuation can be discriminated from relaxation effects by measuring the dependence of the signal on the gradient strength, G . If slice-selective RF pulses are used a diffusion-sensitizing gradient during the RF pulses interferes with the slice selection gradients. This problem is circumvented by the application of pulsed magnetic field gradients. If we apply two rectangular gradient pulses (*i.e.* with infinitesimally short switching time) of a duration δ whose onset is separated by a time Δ and which occur before and after the refocusing RF pulse as shown in Fig. 3.1, the signal attenuation for isotropic diffusion is given by [91, 77]

$$\ln \frac{A(2\tau)}{A(0)} = -\gamma^2 D \left\{ \frac{2}{3} \tau^3 G_0^2 + \delta^2 \left(\Delta - \frac{\delta}{3} \right) G^2 - \delta \left[(t_1^2 + t_2^2) + \delta(t_1 + t_2) + \frac{2\delta^2}{3} - 2\tau^2 \right] \mathbf{G} \cdot \mathbf{G}_0 \right\} \quad (3.13)$$

where \mathbf{G}_0 is a constant field gradient that may account for an inhomogeneity of the main magnetic field, and $G = |\mathbf{G}|$, $G_0 = |\mathbf{G}_0|$. The first term in the curly brackets is already known from equation (3.11). In the limiting case $\mathbf{G}_0 = 0$ equation (3.13) reduces to the well known

formula²

$$\ln \frac{A(2\tau)}{A(0)} = -D \{ \gamma^2 \delta^2 (\Delta - \delta/3) G^2 \} . \quad (3.14)$$

The fact that the right hand side of equation (3.14) is proportional to the mean square displacement during the time $t_d = \Delta - \delta/3$ is the reason for t_d sometimes being called the effective diffusion time [36, p. 342]. In the case of anisotropic diffusion, D in equation (3.14) has to be replaced by D_{11} which is the first diagonal element of the diffusion tensor expressed in a basis whose first basis vector is parallel to \mathbf{G} (cf. equation (2.121)). In equation (3.14) the expression in curly brackets, which describes the timing and amplitude of the gradient pulses, is commonly denoted by b such that the spin echo attenuation caused by the diffusion gradient pulses, neglecting field inhomogeneity, can be written as

$$\frac{S}{S_0} = e^{-bD} \quad (3.15)$$

where S and S_0 denote the echo amplitude with and without the diffusion gradient pulses, respectively. Equation (3.15) is fundamental to NMR diffusion measurements. It states that $\ln S$ depends linearly on b . Since b solely depends on experimental parameters, we can apply different b values and calculate D from a linear regression of $\ln S$ versus b . This measurement principle can be combined with NMR imaging methods to obtain a spatially resolved measurement of the diffusion coefficient [92]. An imaging experiment designed to make the signal intensity of an image pixel dependent on the diffusion coefficient is called diffusion weighted imaging (DWI). It can be realized by incorporating diffusion gradients in the imaging pulse sequence, or by replacing the RF excitation pulse of the imaging sequence by the scheme shown in Fig. 3.1 (preparation experiment). The preparation experiment need not be a spin echo sequence. It can also be based on the stimulated echo scheme [93, 77, 94].

3.2.1 Restricted diffusion

In the case of restricted diffusion, D varies with the diffusion time. Hence it is not possible to transform equation (3.8) where the integration has to be carried out over $D(t')$ to (3.10). However, in the case of isotropic diffusion we can define an effective diffusivity D_{eff} by the time average of $D(t)$ over the echo time to restore equation (3.14) with D replaced by D_{eff} [74, section 7.2]. The term “apparent diffusion coefficient” (see p. 50) is sometimes used as a synonym for D_{eff} [95].

The pulsed field gradient technique has a further advantage over constant field gradient measurements of diffusivity where systems with restricted diffusion are concerned. In the PFG experiment any diffusional motion before the first gradient pulse or after the second pulse does not contribute to $d \ln S / db$. Hence the time over which the diffusion process is observed is more clearly defined and more easily to be varied than in constant gradient measurements [91].

3.3 Diffusion tensor imaging (DTI)

We now turn to the measurement of anisotropic diffusion with NMR methods. In the case of anisotropic diffusion we have to define an effective diffusion tensor \mathbf{D}^{eff} to be able to carry

²Stejskal and Tanner [91] point out that, strictly speaking, no spin echo occurs if \mathbf{G}_0 vanishes everywhere. However, this does not affect the validity of equation (3.14).

out the integral in equation (3.8) without knowing $\mathbf{D}(t)$. With the shorthand notation $\mathbf{A} = \mathbf{F}(t') - 2\Theta(t' - \tau)\mathbf{f}$ where the symbols \mathbf{F} , \mathbf{f} , and Θ are defined in (3.9), and with $\tau = TE/2$, we obtain from equation (3.8)

$$\ln \frac{S}{S_0} = -\gamma^2 \int_0^{2\tau} \mathbf{A} \cdot \mathbf{D}(t') \mathbf{A} dt' = -\gamma^2 \int_0^{2\tau} \sum_{i,j=1}^3 A_i A_j D_{ij}(t') dt' = -\gamma^2 \sum_{i,j=1}^3 \int_0^{2\tau} A_i A_j dt' D_{ij}^{\text{eff}} \quad (3.16)$$

which can be taken as the definition of the effective diffusion tensor \mathbf{D}^{eff} [15]. In *in vivo* NMR applications, the term “apparent diffusion tensor” is commonly used. We further define a matrix \mathbf{b} that depends on the gradient time course $\mathbf{G}(t)$ by [15, 96]

$$b_{ij} = \gamma^2 \int_0^{2\tau} A_i A_j dt' = \gamma^2 \int_0^{2\tau} [\mathbf{F}(t') - 2\Theta(t' - \tau)\mathbf{f}]_i [\mathbf{F}(t') - 2\Theta(t' - \tau)\mathbf{f}]_j dt', \quad (3.17)$$

$$\text{where } \mathbf{F}(t) = \int_0^t \mathbf{G}(t') dt' \quad \text{and} \quad \mathbf{f} = \mathbf{F}(\tau) \quad (3.18)$$

are defined as in equation (3.8). If we now use a double dot product between matrices which may be defined by

$$\mathbf{b} : \mathbf{D}^{\text{eff}} \equiv \sum_{ij} b_{ij} D_{ij}^{\text{eff}} \in \mathbb{R} \quad (3.19)$$

we may write equation (3.16) in the simple form

$$\frac{S}{S_0} = e^{-\mathbf{b} : \mathbf{D}^{\text{eff}}} \quad (3.20)$$

in complete analogy with (3.15).³ \mathbf{b} is called a matrix rather than a tensor since it does not reflect properties of the sample as the diffusion tensor does. The \mathbf{b} matrix is symmetric by construction. In the case of the pulsed field gradient experiment the time courses $G_i(t)$ differ only by a multiplicative factor such that we can write $\mathbf{G}(t) = \mathbf{G}^0 c(t)$ with some scalar real function $c(t)$. By integration it can be shown that for the pulsed field gradient spin-echo experiment with symmetrical trapezoidal gradient pulses with rise time ε its elements are given by [96]

$$b_{ij} = \gamma^2 G_i^0 G_j^0 [\delta^2 (\Delta - \delta/3) + \frac{\varepsilon^3}{30} - \frac{\varepsilon^2}{6} \delta] \quad (3.21)$$

which reduces to (3.14) if \mathbf{G}^0 is parallel to one of the coordinate axes and $\varepsilon = 0$. In the context of anisotropic diffusion the degree of diffusion weighting may be estimated by the b value that would determine the signal attenuation in an isotropic sample which is equal to the trace of the \mathbf{b} matrix: The attenuation in an isotropic sample with diffusion coefficient D_0 is given by

$$\frac{S}{S_0} = \exp[-D_0(b_{11} + b_{22} + b_{33})] = \exp[-D_0 \text{Tr } \mathbf{b}]. \quad (3.22)$$

³The tensor notation of the integrand before the last equal sign in equation (3.16) is $A_i D^{ij} A_j = A_i A_j D^{ij}$. Equation (3.20) has the form $\ln S/S_0 = -\exp(b_{ij} D_{\text{eff}}^{ij})$.

We henceforth call $\text{Tr } \mathbf{b}$ the b value which is consistent with equation (3.15). Since the trace is invariant under rotation this definition is independent of the coordinate system.

For specifying the elements of \mathbf{b} it is useful to adopt the coordinate system of the imaging experiment in terms of read, phase, and slice gradient axis. The associated coordinates may be x, y , and z , respectively. If the gradient $\mathbf{G}(t)$ is at all times parallel to the x direction the only non-zero element of the \mathbf{b} matrix is b_{xx} . Equation (3.20) states that in this case the signal solely depends on the element D_{xx} of the diffusion tensor as expressed in the (x, y, z) coordinate system. Application of different b_{xx} values, for example via different gradient amplitudes, and linear regression of $\ln S$ versus b_{xx} yields the element D_{xx} . The elements D_{yy} and D_{zz} are accessible in an analogous manner. The diagonal elements of the diffusion tensor can thus directly be measured by x, y , and z gradients [97]. If however the diffusion weighting gradient has components in x and y direction, say, the signal intensity depends on D_{xx}, D_{yy} , and $D_{xy} = D_{yx}$. For this reason the remaining elements of \mathbf{D} are not directly accessible. It is also not possible to calculate them from the diagonal elements. An arbitrary tensor element can be calculated either from the eigenvalues and the relative orientation of the principal axes with respect to the basis, according to $\mathbf{D} = \mathbf{S}\mathbf{\Lambda}\mathbf{S}^T$ (2.110). Or it can be determined if we happen to know the diffusion tensor in any other basis whose orientation with respect to our basis is known. The information contained in the diagonal elements D_{xx}, D_{yy}, D_{zz} in *any* basis however does not allow the reconstruction of the complete tensor — unless we know that x, y , and z are the principal axes.

In order to determine all tensor elements we have to vary the elements of the \mathbf{b} matrix and perform a multivariate linear regression [15, 16] according to

$$\ln S = \ln S_0 - b_{xx}D_{xx} - b_{yy}D_{yy} - b_{zz}D_{zz} - 2b_{xy}D_{xy} - 2b_{yz}D_{yz} - 2b_{xz}D_{xz} \quad (3.23)$$

which is equivalent to equation (3.20). The logarithmic transformation of equation (3.20) into (3.23) has disadvantages at low SNR but allows the use of fast linear fit routines [98]. It can be avoided by applying a nonlinear fit routine by minimizing the difference between the measured signal and the signal value calculated from (3.20) [99].

Irrespective of the method chosen to determine the unknown parameters in (3.20), the gradients $\mathbf{G}(t)$ have to be varied in such a way that the resulting \mathbf{b} matrices span the 6-dimensional vector space of symmetrical 3×3 matrices. (This requirement on the \mathbf{b} matrices is not necessarily satisfied if the gradient amplitude vectors \mathbf{G}^0 are non-collinear in \mathbb{R}^3 .) If we do not determine S_0 by a separate measurement without diffusion gradients, equation (3.23) contains 7 unknown variables. Hence we have to use at least seven different \mathbf{b} matrices

Basser *et al.* [100, 15] have pointed out that the off-diagonal elements of the diffusion tensor can in general not be neglected. In *in vivo* experiments the orientation of the principal axes of the diffusion tensor is usually not known, and the orientation is not necessarily homogeneous within the sample. Therefore it is necessary to measure all six independent tensor elements.

3.3.1 Spatial localization

For *in vivo* applications it is in general desirable to combine a measurement of the diffusion tensor with some kind of spatial localization. A combination [92] of the pulsed-gradient spin-echo experiment with two-dimensional ^1H NMR imaging sequences for spatially localized tensor measurements was proposed by Basser *et al.* [15]. The imaging method without diffusion gradient pulses provides a signal intensity for each of the volume elements in a slice. The dominant factors that determine this intensity are proton density and relaxation times in the voxel. Due

to the presence of imaging gradients and magnetic field inhomogeneities the signal intensity is also influenced by diffusion. In the case of spin echo sequences the diffusion dependence is described by equation (3.10). But this contribution is in most situations negligible. If we however introduce strong additional gradient pulses into the sequence as described for the Stejskal-Tanner experiment, the signal intensity of an image pixel will strongly depend on the diffusion tensor in the corresponding voxel. The image is then said to be diffusion weighted.

We can incorporate diffusion weighting gradient pulses in an imaging sequence and perform the tensor experiment with different gradient directions and amplitudes. Application of the linear regression algorithm to each pixel intensity will then eliminate the influence of proton density and relaxation rates. This procedure yields a diffusion tensor for each image pixel.

A variety of NMR imaging methods can be combined with PFG-NMR to provide spatial localization. Many of them are based on the spin echo principle such that we can place the diffusion weighting gradients next to the refocusing pulse as in the Stejskal-Tanner experiment. It is also possible to use a preparation experiment where the equilibrium magnetization is manipulated in a Stejskal-Tanner pulse sequence before the actual imaging sequence starts [101, 102].

3.3.2 Measures of diffusion anisotropy

In order to specify the degree of anisotropy of self-diffusion, a number of different parameters have been proposed. As a general requirement the parameter has to be invariant under rotation of the coordinate system and under reordering of the basis vectors. In mathematical terms, the parameter must not change if we transform \mathbf{D} by application of an orthogonal⁴ matrix \mathbf{S} to $\mathbf{D}' = \mathbf{S}^T \mathbf{D} \mathbf{S}$.

- A simple measure of anisotropy is the ratio of the largest and the smallest eigenvalue,

$$a_e = \frac{\lambda_{\max}}{\lambda_{\min}}. \quad (3.24)$$

To calculate this parameter, the eigenvalues have to be ordered according to size. Thereby a bias towards anisotropy at low signal-to-noise ratios is introduced [103]: in the presence of noise, the eigenvalues will in general be different such that $a_e < 1$. The situation $a_e > 1$ however will never occur.

- The volume ratio [103] is based on a geometrical argument. It measures the volume of an ellipsoid with principal (half) axes $\lambda_1, \lambda_2, \lambda_3$, divided by the volume of a sphere with the radius $\text{Tr } \mathbf{D}/3$:

$$a_v = 27 \frac{\det \mathbf{D}}{(\text{Tr } \mathbf{D})^3}. \quad (3.25)$$

- If we separate the diffusion tensor into an isotropic and an anisotropic part,

$$\mathbf{A} = \mathbf{D} - \frac{\text{Tr } \mathbf{D}}{3} \mathbf{I}, \quad (3.26)$$

⁴Orthogonal matrices \mathbf{S} with $\det \mathbf{S} = -1$ represent a rotation combined with a reflection. Any orthonormal basis can be converted into another orthonormal basis by application of the appropriate orthogonal matrix.

we can define the fractional anisotropy index [17, 104] by

$$a_f = \sqrt{\frac{3}{2} \frac{\sqrt{\mathbf{A} : \mathbf{A}}}{\sqrt{\mathbf{D} : \mathbf{D}}}} \quad \text{with} \quad \mathbf{B} : \mathbf{C} \equiv \sum_{i,j} B_{ij} C_{ij}. \quad (3.27)$$

The invariance of a_f is due to the invariance of the “generalized tensor product” ($\mathbf{B} : \mathbf{C} = \mathbf{S}^T \mathbf{B} \mathbf{S} : \mathbf{S}^T \mathbf{C} \mathbf{S}$) which can be shown using $\mathbf{S}^T = \mathbf{S}^{-1}$. a_f ranges between 0 ($\lambda_1 = \lambda_2 = \lambda_3$) and 1 ($a_f \rightarrow 1$ as $\lambda_2 \rightarrow 0$ for $\lambda_1 > \lambda_2 = \lambda_3$).

- The lattice index [103] measures the similarity of the diffusion tensors in neighbouring volume elements. It is not a pure anisotropy measure in a strict sense. However, the anisotropy indices described above can measure the degree of order in white matter (see p. 52): randomly oriented fibres lead to an isotropic diffusion tensor, $\mathbf{D} = c\mathbf{I}$ with some $c \in \mathbb{R}$. In a grid of volume elements that are each characterized by a diffusion tensor we can also measure the degree of order on the macroscopic scale. If the fibres in a voxel have the same orientation as in the surrounding voxels, the “lattice index” shall be large, and it shall be small in a grid of randomly oriented diffusion ellipsoids. Using the anisotropic part \mathbf{A} from equation (3.26) and the abbreviation

$$L_{M,N} = \sqrt{\frac{3}{8} \frac{\sqrt{\mathbf{A}_M : \mathbf{A}_N}}{\sqrt{\mathbf{D}_M : \mathbf{D}_N}}} + \frac{3}{4} \frac{\mathbf{A}_M : \mathbf{A}_N}{\sqrt{\mathbf{D}_M : \mathbf{D}_M} \sqrt{\mathbf{D}_N : \mathbf{D}_N}} \quad (3.28)$$

in a two-dimensional grid, we can define the lattice index of voxel M by

$$a_l(M) = \left(\sum_{N=1}^8 c_N L_{M,N} \right) / \sum_{N=1}^8 c_N. \quad (3.29)$$

The weighting factor c_N is the ratio of the side length of the cubic voxels divided by the distance between the centre of voxel N and the centre of the reference voxel, M , such that $c_N = 1$ or $c_N = 1/\sqrt{2}$, depending on N . The lattice index depends on the degree of anisotropy in the individual voxels. It vanishes in isotropic media. Since the double dot product between different tensors may be negative equation (3.28) does not allow a stringent definition of a_l . A similar measure of tissue organization based on the double dot product between tensors has been proposed that does not suffer from this drawback [104].

3.4 In vivo application

3.4.1 Determinants of water self-diffusion *in vivo*

Biological tissues consist mainly of water but are inhomogeneous on the scale of a few microns due to the presence of cell membranes. Although cell membranes in animal tissues⁵ are highly permeable for water molecules [105, p. 348] they impede water diffusion and create separate compartments. Water is present inside the cells as well as in the intercellular space. Mammalian cell dimensions are typically about 100 μm which is considerably less than the spatial

⁵Cell membranes in plants are almost impermeable for water [105, p. 348].

resolution achievable with medical MRI systems.⁶ Therefore results from NMR diffusion measurements represent an average over many cells and the space between them. Due to different concentrations of macromolecules the intra- and extracellular diffusion coefficients, D_{in} and D_{ex} , respectively, are in general different [106]. As the NMR measurement yields an average of the diffusion coefficients in all compartments, the result of the measurement depends on the ratio of compartment volumes. There is still controversial discussion about the values of D_{in} and D_{ex} [107]. For long diffusion times (about 50 ms) water self-diffusion in tissue is restricted due to the presence of cell membranes (see section 3.4.3). A measurement of the effective diffusion tensor in this case can yield an anisotropic diffusion tensor. This can be used to obtain geometric information about structures that are much smaller than the typical spatial resolution of an MRI experiment. The following tissue properties determine the measured diffusion tensor of water:

- concentration of macromolecules in intra- and extracellular space, concentration and structure of intracellular organelles
- relative water content of intra- and extracellular space
- permeability of cell membranes
- geometric arrangement of membranes, *i.e.* cell shape and orientation. These influence the tortuosity of the extracellular space, and eigenvalues and principal axes of the diffusion tensor. The apparent diffusion tensor is anisotropic if in a given volume of tissue (that can be considered as having a homogeneous structure) some of the membrane orientations are privileged (the surface integral over all membranes⁷ $\int |\vec{p} \cdot d\vec{s}|$ depends on the direction of \vec{p}) and the membrane distance is of the order of the diffusion length for free diffusion during the time of the measurement (50 ms).
- pseudo diffusion (see below).

Pseudodiffusion

The presence of moving blood in living animal tissue can influence diffusion measurements [108]. A network of fine blood vessels within the tissue provides supply of nutrients and removal of toxic metabolic end-products. Since the capillary network can be modelled to a good approximation as a mesh of randomly oriented short vessel segments, a particle flowing in the network performs a random walk. Although the same path is shared by many molecules, the water molecules that are contained in a volume element of 1 mm³ (which is the size of a voxel that can be resolved by MRI) follow very different paths within an observation time of about 50 ms. The consequent dephasing of spins in the volume element in the presence of a field gradient causes the detectable NMR signal to decrease. Le Bihan *et al.* [109, 110] coined the term intravoxel incoherent motion (IVIM) to refer to this phenomenon. It causes an additional signal loss in NMR measurements of diffusivity in perfused tissue which can be described using a “pseudo diffusion coefficient” D^* defined by [108]

$$D^* = lv/6 \quad (3.30)$$

⁶The spatial resolution of MRI is about 1 mm employing a gradient system that is designed to image objects of the size of a human head. For fundamental reasons it is limited by the low sensitivity to a few micrometers [36, p. 173].

⁷This integral does not discriminate between surface normal vectors pointing in opposite directions.

with l being the average length of straight capillary segments, and v the mean velocity of spins. The signal attenuation by diffusion weighting is then governed by [105]

$$S(b) = (1 - f)S_{0,\text{stat}}e^{-bD} + fS_{0,\text{circ}}e^{-b(D+D^*)} \quad (3.31)$$

where the volume fraction of circulating spins is denoted by f . Anisotropy of diffusion, and differences in diffusivity or relaxation times between tissue and blood have been neglected here. The “pseudodiffusion” coefficient D^* in perfused brain tissue is of the order $20 \cdot 10^{-9} \text{m}^2 \text{s}^{-1}$ which is by a factor of 10 larger than D . Equation (3.31) leads to a deviation from the linear relation between b and $\ln S$ for small b values ($b \leq 100 \text{ mm}^2 \text{s}^{-1}$). Diffusion weighting with low b values can be used to selectively suppress the signal arising from water within the capillary network [111]. Although diffusion measurements in brain grey matter have been reported to be affected by IVIM, the perfusion contribution is completely negligible in the much less perfused white matter.

The term “apparent” diffusion coefficient was originally used to express the influence of pseudodiffusion on the measured diffusivity [105, p. 361]. However, it is nowadays mostly used to refer to the measured diffusion coefficient as opposed to the definition of the microscopic diffusion coefficient in the Fickian sense, *e.g.* taking into account restrictions to diffusion [95, p. 32]. We will use the term in this latter, broader sense.

3.4.2 Applications of diffusion weighted imaging

The term diffusion weighted imaging (DWI) is applied to NMR imaging experiments that are performed to produce an image contrast between tissues of different water self-diffusivity. DWI is used if one is interested in the mobility of diffusing water molecules irrespective of the direction. Diffusion weighting can for example be achieved in a PFG experiment combined with an imaging sequence, using one single gradient direction. The signal intensity then depends on the first diagonal diffusion element D_{11} of the tensor expressed in a basis whose first basis vector is parallel to the gradient direction \mathbf{G} (see equations (2.121) and (3.14)). D_{11} is the apparent diffusion coefficient (ADC) along the chosen direction. From a number of DWI images with different b values, D_{11} can be calculated. However, the diffusion weighted images themselves are often used instead of maps of D_{11} . DWI has been successfully applied in clinical imaging of stroke, tumours [112], and multiple sclerosis [113].

Stroke

In 1990 Moseley *et al.* [9] observed in cats that within minutes after the occlusion of a supplying artery the affected brain region appeared hyperintense in diffusion weighted MR images. This was due to a decrease of the effective diffusion coefficient in the ischemic⁸ brain area. Conventionally used T_2 weighted images did not show the lesion until many hours after the insult. The same observation has been made in human patients [114]. The reason for the reduction of the ADC in ischemic tissue by about 40% is still being controversially discussed.⁹ The most widely accepted hypothesis is based upon cell swelling due to the lack of energy supply [116, 117, 118]. The cell membrane of neurons is equipped with molecular ion pumps that maintain a constant voltage of -60 mV between the cell plasma (more negative potential) and the extracellular

⁸derived from greek $\iota\sigma\chi\epsilon\nu$ — hinder, detain; and $\alpha\iota\mu\alpha$ — blood.

⁹See, for example, [107, 115].

space. Within minutes after the interruption of blood supply the energy reserves of the cells are exhausted, and consequently the function of the transmembrane pumps ceases. Due to the high transmembrane concentration gradient, Na^+ ions will then diffuse into the cell. The resulting osmotic pressure¹⁰ causes a massive influx of water into the cell, and consequently leads to cell swelling. This state is called a cytotoxic edema. It is characterized by a reduced extracellular space with increased tortuosity, in particular if adjacent cells touch each other. Water molecules trapped between cells can only diffuse over large distances if they enter the more viscous intracellular medium. For a certain range of observation times their displacement will thus be determined by the low intracellular diffusion coefficient.¹¹ The pure shift of water molecules into the intracellular space which is characterized by a higher viscosity is unlikely to produce the observed ADC change [116].¹⁶ More recent experiments have shown that the ADC decreases both in the intracellular and in the interstitial space [107, 119].

The predictive value of diffusion weighted images for the clinical perspective of stroke patients is currently under investigation [120, 121, 122]. It is intended to optimize the medication at an early stage according to lesion extent, position, and severeness obtained from combined diffusion and blood perfusion measurements [120].

Isotropic diffusion weighting

A major difficulty for the clinical application of DWI on stroke patients is the fact that the intensity of an image pixel depends on the relative orientation of the tissue and the diffusion gradient if the ischemic lesion is situated in white matter (see below: Anisotropic diffusion in brain white matter). This makes the delineation of the lesion difficult [123, 23] because an ADC reduction due to an ischemic event is indistinguishable from a low ADC due to fibres running perpendicularly to the gradient direction. There are several approaches to address this problem. The simplest way is to record three diffusion weighted images with orthogonal gradient directions. The sum of the three signal intensities for a pixel will then depend on Tr D rather than on a single tensor element. The trace of the diffusion tensor is invariant under rotation of the coordinate axes. In order to circumvent the increased measurement time, gradient time courses $\mathbf{G}(t)$ have been developed which produce a signal attenuation according to $\ln(S/S_0) \sim \text{Tr D}$ [124, 125, 126, 127]. For this isotropic diffusion weighting the \mathbf{b} matrix is optimized numerically to be as close as possible to a matrix that differs from the identity matrix only by a factor, $b_{ij} = b_0 \delta_{ij}$ with some $b_0 \in \mathbb{R}$. In the ideal case this leads to

$$\frac{S}{S_0} = e^{-\sum_{i,j} b_{ij} D_{ij}} = e^{-b_0 \text{Tr D}}. \quad (3.32)$$

3.4.3 Applications of diffusion tensor imaging

Anisotropic diffusion in brain white matter

In this thesis we will mainly be concerned with anisotropic diffusion in human brain tissue. Anisotropic diffusion has been reported in muscle tissue, *e.g.* in cardiac tissue, as well as in the white matter (WM) of the central nervous system of vertebrates. The anisotropy is due to the

¹⁰due to the difference between intra- and extracellular space in the overall concentration of molecules and ions for which the membrane is impermeable as compared to the membrane permeability for water

¹¹The argument assumes free exchange of intra- and extracellular water on the scale of the observation time, *i.e.* infinitely high membrane permeability for water.

tissue structure on a microscopic scale. The main constituents of human brain white matter are the axons of neurons, and glial cells. The somata of neurons are concentrated on the surface of the human brain (cortex, or external grey matter) and in regions inside (nuclei, internal grey matter) surrounded by white matter. Most of the neuronal axons in white matter are covered by specialized glial cells. During ontogeny, oligodendrocytes wind specialized processes around the axons thereby forming a dense sheath consisting of many layers of the oligodendrocyte cell membrane and a small amount of cell plasma. This envelope is called the myelin¹² sheath. It provides the axon with electrical insulation from its environment. The thickness of the myelin sheath varies within the central nervous system. It is positively correlated with the axon diameter [128] and typically in the range of several microns. However, the axons are not completely covered by oligodendrocytes. An oligodendrocyte covers a segment of ca. 1 mm of an axon. Between the segments covered by different oligodendrocytes a small part (about 1 to 2 μm [129, p. 40]) of the axonal membrane is left blank. In these zones which are known as the nodes of Ranvier the density of ion channels in the axonal membrane is very high. They make a fast signal transduction along the axon possible: the depolarization of the membrane¹³ involved in signal transmission can skip from node to node. This type of signal transduction is termed saltatory conduction. It is a factor of up to 100 faster than the spreading of action potentials along unmyelinated membranes [128]. Saltatory conduction is most efficient if the axon's myelin sheath is thick. It is in fact the main function of the sheath to enable saltatory conduction, rather than simply to prevent electrical leakage [130]. The oligodendrocyte membranes that form the myelin sheath differ from other cell membranes in their chemical composition. While usual cell membranes consist of 60% proteins and 40% lipids in the dry fraction, myelin contains 30% proteins and 70% lipids [131, p. 62].¹⁴ This property ensures a good electrical insulation.

Axons can be up to about 1 m long and between 0.2 and 20 μm in diameter [2, p. 23]. Distant parts of the human central nervous system (CNS) are interconnected via “fibre bundles” of many parallel axons, each covered by a myelin sheath. These bundles constitute the majority of brain white matter. For example in the corpus callosum a cubic 1 mm³ volume element contains about $3.7 \cdot 10^5$ parallel axons.¹⁵ The volume element is traversed by parallel extra- and intracellular “channels” that extend over the full length of the volume element. The axon diameter is typically about 1 μm [132], the extracellular “channels” in a densely packed fibre bundle possibly have even smaller diameters. This may be compared to the mean displacement of a water molecule that freely diffuses in bulk water, which is about 24 μm within 50 ms (at room temperature). Hence, provided that the cell membranes are sufficiently impermeable to water molecules, the diffusion process in a white matter fibre will on the time scale of 50 ms appear restricted perpendicular to the fibre axis, while motion parallel to this axis will not be affected. This is the basis for an explanation of the findings of anisotropic water self-diffusion in brain white matter.

However, the precise mechanism that causes the observed diffusion anisotropy in brain tissue is still under discussion. An alternative explanation is the presence of axonal transport

¹²The name is derived from greek $\mu\upsilon\epsilon\lambda\omicron\varsigma$ — marrow.

¹³Electrical signals spread in the CNS along the cell membranes of neurons. Ion channels in the membrane switch to the “open” position if a signal is to be transmitted. This results in a Ca^+ and Na^+ influx into the cell and consequently a dramatic change of the voltage between internal and external side of the axonal membrane. The process is called depolarization of the membrane: the voltage over the membrane which is taken to be negative during rest changes upon excitation suddenly to a more positive value. The depolarization lasts for approx. 1 ms. The resulting voltage peak migrates along the membrane. It is called an action potential.

¹⁴The water content of tightly wound myelin is about 40% [130].

¹⁵For this value axons with diameters below 0.4 μm are neglected [132].

mechanisms in the cell plasma [105, p. 350]: Most of the neurotransmitters and nutrients that are used at the end of an axon (at the synapse to another neuron) are synthesized in the cell soma and then transported through the cell plasma [130, ch. 4]. However, axonal transport is unlikely to play a role for the anisotropy of diffusion in WM since the transport velocities are low, and there is no evidence for a sudden reduction in anisotropy upon cell death. (However, observations of a slight reduction of anisotropy in ischemic brain tissue do exist [24].) Moreover, transport cannot explain that the diffusion coefficient perpendicular to the fibre direction depends on the observation time [133]. Experiments on excised nerves [134] and measurements on single axons [135, 136] also appear to exclude a significant role of microtubules and fast axonal transport for anisotropy.

Although measurements on excised garfish nerves [134, 137] showed that nonmyelinated nerves also exhibit diffusion anisotropy, the observation that in human white matter the diffusional anisotropy decreases with progressing pathological demyelination indicates that the myelin sheath contributes to diffusion anisotropy in WM. However, the relatively low permeability of the myelin sheath is possibly not decisive: Szafer *et al.* [118] concluded from a theoretical model of brain tissue that the ADC is largely insensitive to reductions in cellular membrane permeability. However, even if the permeability of axonal walls for water molecules is not substantially lowered by the myelin sheath, the presence of myelin sheaths has an influence on the tortuosity of the extracellular space. The situation encountered in normal white matter may be similar to the model that was presented above (p. 51) to explain the ADC reduction in ischemic tissue. The extracellular space of white matter is comparable to the traps between swollen cells in that model. Many authors therefore consider the tortuosity of the extracellular space to be the most important reason for diffusion anisotropy in white matter [138, 116].

The geometry of white matter fibre tracts varies between different brain regions, and intra- and extracellular diffusion coefficients as well as membrane permeabilities are only known to an order of magnitude.¹⁶ In consequence the eigenvalues of the water self-diffusion tensor can only very roughly be estimated from *a priori* knowledge. Numerical and analytical models have been applied to the problem [139, 140]. In a homogeneous bundle of parallel fibres however the diffusion ellipsoid will have cylindrical symmetry, and one of the principal axes will always be aligned with the fibre axis.

Clinical application and application for functional neuroanatomy

The applications of DTI can be divided into three broad categories. DTI can yield information on

- fibre anatomy,
- diffusion anisotropy which reflects the degree of axon myelination or tissue organization, and
- the tensor of electrical conductivity in brain tissue.

The latter will be discussed in a separate section below. Diffusion tensor imaging has been used to obtain anatomical information in white matter [141] which is of use for both functional brain research and neurosurgical problems where the position of fibre tracts is of interest. The

¹⁶ In fact, the question of whether the intracellular and extracellular diffusivities differ at all is still open, see for example [107].

relevance of fibre imaging arises from the fact that it is not possible to derive such information from necropsy since extent and morphology of most brain WM fibre tracts vary considerably between subjects.¹⁷

DTI has also been applied to investigate and diagnose white matter disorders in human patients. In this context DTI is used as a means to detect the degree of diffusion anisotropy. Although T_2 weighted MRI is widely used as a diagnostic tool, information on pathological processes can more easily be deduced from the parameters measured by DTI than from the T_2 value. A number of white matter diseases involve a degeneration of axonal myelin shields (demyelination) which can be detected as a reduction of anisotropy. DTI can therefore be used for an investigation of multiple sclerosis [22, 142]. It can also be applied to detect processes secondary to neuronal death: Upon injury of an axon the cell soma may survive while the distal part of the axon disintegrates (Wallerian degeneration). A neuron upon which the axon projects can then also disintegrate if it does not have a large number of other afferent neurons (transneuronal degeneration) [131, p. 51]. Both processes can be detected with DTI through the subsequent decay [128, p. 5] of the myelin shield [143, 144, 145]. Measurements of diffusion anisotropy or full diffusion tensor imaging have also been applied to schizophrenia [27, 28], stroke [23, 24], tumours [25, 26], traumatic brain injury [146], hemiparesis [147], and physiology and pathology of heart muscle tissue [21, 148, 149].

One of the most important aims of functional neuroanatomy is to derive anatomical definitions of what can be regarded as a “functional unit” in the cerebral cortex. By means of “functional” MRI experiments (see section 6.1.2) the cortical regions can be identified that are involved in a specific task, yielding regions whose extension is of the order of centimeters. To date the anatomical characteristics that determine these regions are unknown. Subdividing the cerebral cortex on the basis of histological criteria leads to areas (Brodmann’s areas [2]) that are considerably larger than those activated in a functional experiment. Since diffusion tensor imaging can achieve a resolution of 1 to 3 mm it can possibly be used to define those cortical regions that represent a functional unit on the basis of the afferent white matter fibre bundles. Even if this should prove impossible the information regarding fibre tracts can be incorporated in models of the brain function as additional knowledge regarding the main communication pathways between parts of the brain.

Application in MEG source localization

Tissue structure not only determines the diffusion tensor of brain tissue but also its electrical properties. Therefore the knowledge of tissue structure that is obtained from a DTI experiment contains information on the tensor of electrical conductivity, σ . Conductivity data are required in the localization of activated brain regions from a magnetoencephalogram. Magnetoencephalography (MEG) measures the magnetic field at the head surface that is caused by the electrical activity of neurons. A comprehensive overview of this method can be found in [1]. Numerical source localization algorithms attempt to reconstruct the current sources of the magnetic field under the assumption that the field arises mainly from the electrical current in the apical dendritic tree of a certain type of activated cortical neurons (pyramidal cells), which is predominantly oriented perpendicular to the cortical surface.¹⁸ It is clear that the electrical field driving the current in a dendrite is not confined to the dendrite and, since the dendrite

¹⁷Interindividual differences are common in many regions of the human brain [18, p. 173].

¹⁸The measured magnetic fields are of the order of 10^{-13} T, comprising the contributions of about 50 000 synchronously activated neurons [1, p. 198].

is embedded in conducting material, can give rise to “secondary currents” at distant locations. A source reconstruction algorithm must also take the secondary currents into account. Spatial distribution, orientation, and amplitude of the secondary currents depend on the conductivity tensor in the tissue around the source. To date only very coarse assumptions on the conductivity in the human head are used, partly because no reliable method is available to measure σ *in situ*. Since in white matter the presence of myelin sheaths reduces the conductivity perpendicular to the fibre direction [131, p. 62] it is generally accepted that the self-diffusion tensor of water and the conductivity tensor share the eigenvector directions [16]. The fibre direction obtained from DTI measurements can therefore be used to derive an estimate of the conductivity tensor to be used in MEG source localization. From such an approach a considerable improvement of current source reconstruction is expected. The required spatial resolution of the DTI data is expected to be in the range of a few millimeters.

Moreover, it may even be possible to derive not only the eigenvector directions but also the eigenvalues of the conductivity tensor from the diffusion tensor of water. Although at first sight such an attempt seems unlikely to be successful since the transport of electrical charge is not mediated by water molecules, it may be based on the knowledge of intra- and extracellular self-diffusivities of water, D_i and D_e , respectively. The apparent diffusion tensor can be thought of as being derived from the diffusivities in the intra- and extracellular space, the membrane permeability, and the geometric arrangement of membranes. The tensor of electrical conductivity is in principle constructed by similar rules from intra- and extracellular conductivity (σ_i and σ_e), membrane resistivity, and the same geometrical arrangement. The construction rules that determine the macroscopic properties of inhomogeneous media are dealt with in effective medium theory [150]. Hence it may be possible to derive the eigenvalues of the conductivity tensor from d_i , d_e , and the diffusion tensor eigenvalues if σ_e is known and the cell membrane resistivity is approximated as infinitely large ($\sigma_i = 0$) [151].

Chapter 4

Implementation of diffusion tensor imaging

In this chapter the experimental methods used for the diffusion tensor measurements are described, and the procedure for tensor calculation and display is outlined.

4.1 Instrumentation and subjects

The experiments were performed using an NMR whole body tomograph (Medspec 30/100, Bruker Medizintechnik, Ettlingen, Germany) equipped with a liquid helium cooled superconducting magnet operating at 3 Tesla. The horizontal bore of the cryostat had an internal diameter of 92 cm. The system was equipped with a whole-body gradient set of 29.2 mT m^{-1} maximum gradient strength. Minimum switching time from zero to maximum amplitude was $450 \mu\text{s}$. A removable head gradient insert was also available (Magnex Scientific, Oxon, U.K.) which could switch gradients of 35 mT m^{-1} max. amplitude within $150 \mu\text{s}$. Both gradient sets incorporated three self-shielded coils that produce gradients in three orthogonal directions, one of which is aligned with the subject's body axis which was parallel with the direction of the main magnetic field (z). The whole-body gradient set was used unless stated otherwise. Both gradient sets were connected to power supplies capable of 600 A and 350 V output. Eddy currents induced by gradient switching were reduced by a digital preemphasis unit that modifies the wave form of the current applied to the switched gradient coil in order to minimize deviations from the desired magnetic field pulse shape. The preemphasis unit was unable to correct for the components of eddy current induced field gradients in the directions orthogonal to the applied gradient ("cross terms"). Main field homogeneity was adjusted for each subject by an automatic shimming routine controlling the linear field components by applying appropriate currents to the gradient coils. The currents in the 11 additional shim coils were only adjusted during system setup. For RF transmission and signal reception a quadrature birdcage head resonator (28 cm internal diameter) was employed. Images were reconstructed off-line, including baseline correction before the Fourier transform. For data evaluation the IDL (Interactive Data Language, Research Systems Inc., Colorado, USA) software package was used on a computer workstation (Silicon Graphics Inc., Mountain View, California, USA).

Healthy human subjects volunteered for the *in vivo* experiments. Written informed consent was obtained in each case prior to examination. The total scan time did not exceed 2 hours. The subjects were protected from acoustic noise by earplugs and by the earphones that were

also used for communication with the personnel performing the experiment. The experiments were generally approved by the ethics committee of the Universität Leipzig.

4.2 Imaging sequences

Although diffusion tensor imaging studies are almost exclusively based on echo planar imaging, it is in principle possible to perform diffusion tensor imaging with any diffusion weighted imaging sequence. But not all sequences that are common in conventional T_1 , T_2 or even diffusion weighted imaging are suited for *in vivo* DTI.

First of all, a DTI imaging sequence has to be sensitive, and fast since a large number of images with different diffusion weighting must be acquired. Since in addition it is often necessary to increase SNR by averaging, the application of conventional sequences would increase the scan time beyond what is tolerable for a patient or even for a volunteer. A volunteer cannot stay in the scanner for much more than about 1.5 hours without moving, for patients this time limit is generally considerably lower.

A second condition for an imaging sequence to be used for DTI is that it must be compatible with *in vivo* diffusion weighting. Diffusion weighted sequences are sensitive to motion on a micrometer scale. As physiological motion induced by cardiac and respiratory cycle as well as small subject movements are inevitable, the sequence must be insensitive to bulk motion. If we assume that diffusion weighting is generated by two strong gradient pulses (see section 3.2) then a coherent object displacement between the gradient pulses will for example induce a global phase shift of all excited spins in the sample. In spin-warp imaging, diffusion weighting must be applied to the newly created transverse magnetization after each excitation pulse. As the displacement is unforeseeable the data of every phase-encoding step in a spin-warp sequence can be subjected to a different phase shift such that the spatial information contained in the signal phase is disturbed and severe image artefacts are generated. Although in single-shot sequences diffusion weighting has to be applied only once they can also suffer from the motion-induced phase shift since the fulfillment of the CPMG condition is no longer ensured (*cf.* section 2.1.1). This precludes the application of standard RARE to *in vivo* diffusion imaging. The effects of motion are discussed in greater detail in section 5.8.

Diffusion weighted FLASH [101, 102] can be used for DWI but suffers from low SNR and from errors in the determination of diffusion coefficients introduced by longitudinal relaxation during the imaging period [102]. There have been attempts to employ line scan techniques in NMR diffusion imaging [152, 153]. Hybrid sequences (GRASE) that combine the principles of gradient and RF refocusing have also been applied to DWI [154].

In the context of this work two types of DTI sequences were implemented, EPI as a gradient echo based sequence, and the RARE variant U-FLARE as an RF refocusing sequence.

4.2.1 Diffusion weighting

In the DTI experiments diffusion weighting was provided by a Stejskal-Tanner spin-echo preparation with two unipolar trapezoidal gradient pulses flanking a 180° refocusing pulse. The minimum b value was always larger than 20 s mm^{-2} such that the diffusion gradients were large enough to dephase any transverse magnetization created by the refocusing RF pulse, and no additional spoiler gradients were necessary. The diffusion gradient pulses were placed as early in the sequence as possible to minimize the effect of eddy currents (see section 5.6). In spin

echo experiments the slice selection gradient for the excitation pulse is commonly refocused after the refocusing RF pulse (with a gradient pulse of the same polarity) to dephase any transverse magnetization created by the refocusing pulse [33, section 3.2.3]. Unlike this scheme, in the imaging sequences used for the DTI experiments the excitation slice gradient is refocused immediately after excitation in order to minimize the contributions to diffusion weighting [103]. The excitation pulse and the refocusing pulse in the diffusion preparation were Gaussian shaped and of 1.5 to 3 ms duration. For the EPI sequence, a modified diffusion weighting [155] was also implemented to reduce residual eddy currents caused by the diffusion gradient pulses. This scheme (Fig. 5.5) will be discussed in section 5.6.

The loop structure in the acquisition program started with the acquisition of all slices for the first (lowest) diffusion weighting (b matrix), then the diffusion gradient direction was changed. This was repeated NR times for averaging before the b value was incremented. The number of averages depended on the b value since the signal level is lower at high b values. The b value was adjusted by variation of the gradient amplitude rather than the gradient duration. The directions of the diffusion gradients were chosen to generate 7 b matrices that span the 6-dimensional vector space of symmetrical 3×3 matrices. The gradient vector directions in read, phase, and slice direction coordinates were given by

$$\begin{pmatrix} 1 \\ 1 \\ 0 \end{pmatrix}, \begin{pmatrix} 1 \\ 0 \\ 1 \end{pmatrix}, \begin{pmatrix} 0 \\ 1 \\ 1 \end{pmatrix}, \begin{pmatrix} 1 \\ -1 \\ 0 \end{pmatrix}, \begin{pmatrix} -1 \\ 0 \\ 1 \end{pmatrix}, \begin{pmatrix} 0 \\ -1 \\ 1 \end{pmatrix}, \sqrt{\frac{2}{3}} \begin{pmatrix} 1 \\ 1 \\ 1 \end{pmatrix}. \quad (4.1)$$

Directions parallel to one of the axes of the gradient system were avoided so that the necessary current was divided between at least two gradient coils. The selection of the diffusion gradient directions has an influence on the susceptibility to noise: It has been shown [156, 157] that for a measurement including N gradient vectors it is optimal to align the vectors along N straight lines through the origin that are spread out in three-dimensional space such that the $2N$ intersections of the lines with a sphere centred at the origin have maximum distance from each other. The gradient vector arrangement used is a coarse approximation to this requirement obeying the boundary condition that none of the vectors is parallel to a coordinate axis.

The axial slices deviated from the yx plane of the gradient system in that they were tilted about the x axis. This was necessary to align the slices with the common Talairach coordinate system that defines axial slices as parallel to a plane that contains the anterior and posterior commissure¹.

4.2.2 EPI

Echo planar imaging [63] supplies images with a high signal-to-noise ratio within only about hundred milliseconds. It is largely insensitive to phase shifts that are induced by motion during and between the diffusion weighting gradient pulses. However, the low T_2^* values in regions with a high variability of magnetic susceptibility limit the resolution that is achievable in single-shot imaging. Segmented acquisition of k space after several excitations can provide higher resolution but is, like spin-warp imaging, vulnerable to motion. The resulting image artefacts can only be avoided by some kind of motion correction, *e.g.* navigator echo methods (see section 5.8). A detailed discussion of echo planar imaging can be found elsewhere [158].

¹Anterior and posterior commissure are fibre tracts that connect the left and right hemisphere of the brain (cerebrum).

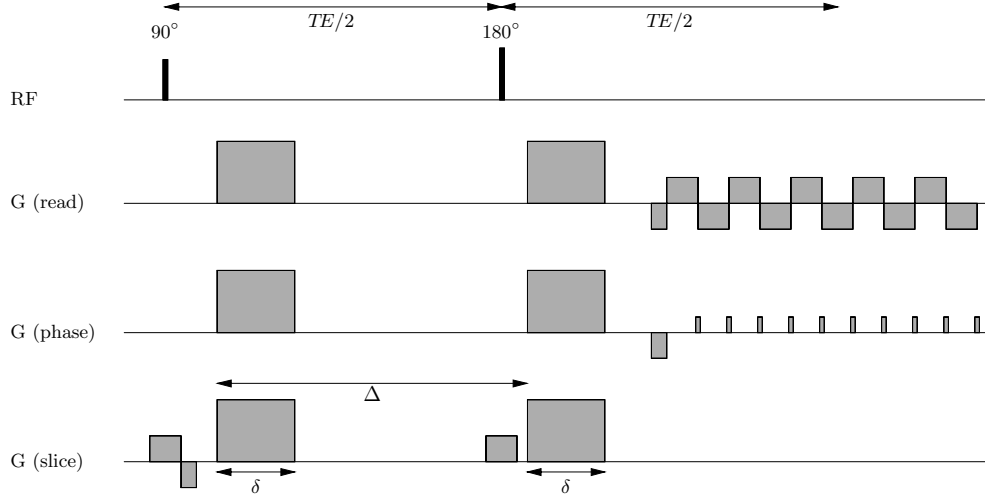


Figure 4.1: Diffusion weighted EPI sequence.

The DTI sequence implemented was based on a single-shot SE-EPI sequence with blipped phase encoding. With a 19.2 cm field-of-view and a 64×64 data matrix an in-plane resolution of 3 mm was achieved. The receiver bandwidth was set to 100 kHz. Nyquist ghosts in the images were removed by off-line phase correction [158, p. 96] based on a reference scan without phase encoding acquired immediately before the DTI experiment. A 10 ms 90° Gaussian RF pulse tuned to a frequency 420 Hz below the water proton frequency was applied before water excitation to saturate the fat signal.

The x (subject's left-right) axis was chosen as the readout direction. For the tilted axial slices this avoided the necessity of using two gradient coils to produce the readout gradient which can lead to artefacts due to slight differences in gradient timing.

4.2.3 U-FLARE

As single-shot EPI suffers from low resolution, and image distortions and signal extinctions in low homogeneity regions (see p. 26) an alternative method based on RF refocusing was implemented for comparison. Since standard RARE cannot be used for DTI (see p. 58) the fast RARE variant U-FLARE [159] was employed instead which is based on refocusing pulses with flip angles below 180° . In the experiments presented here 70° to 80° pulses were typically used. The small refocusing angle keeps power deposition low and thereby allows short repetition times. This advantage is bought at the price of signal-to-noise ratio. In addition, a multipulse sequence with flip angles other than 180° gives rise to many coherence pathways in addition to the pure spin echo pathway (see section 2.1.1). This is due to the fact that every refocusing pulse can also create longitudinal and dephasing transversal magnetization such that, for example, M_{11} and M_{10} in equation (2.50) are no longer zero. The existence of these pathways is not disadvantageous as long as the CPMG condition is fulfilled. In the case of motion in the presence of diffusion weighting, however, this condition no longer holds in general. From a geometrical argument it can be seen that a 180° pulse with a \mathbf{B}_1 vector that subtends an angle

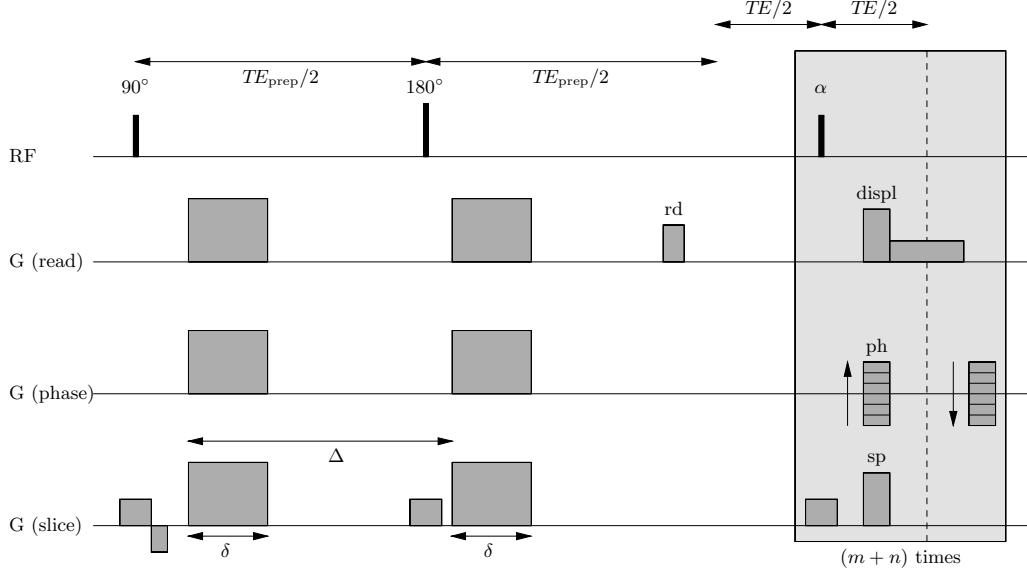


Figure 4.2: Displaced U-FLARE sequence for diffusion tensor imaging with a spin-echo preparation experiment (echo time TE_{prep}). The shaded part of the sequence is first repeated m times without acquiring data to equalize the contributions of odd and even echo pathways, followed by n repetitions to acquire the data for n lines in k space. The dashed vertical line indicates the time of echo formation. The displacing gradient ('displ') shifts the odd echoes out of the acquisition window. An additional spoil gradient ('sp') on the slice axis suppresses eventually remaining odd pathway magnetization. The effect of the phase encoding gradient ('ph') which is varied during the acquisition cycles is rewound after each acquisition. The read dephase gradient lobe is indicated by 'rd'.

ϕ with the initial vector of transverse magnetization, \mathbf{M} , refocuses the magnetization along a direction that is rotated by 2ϕ relative to \mathbf{M} . In contrast, the echo elicited by a second 180°_ϕ pulse will form with zero phase. This is why the sign of the echoes in a Carr-Purcell pulse train alternates. Likewise, the phase of refocused magnetization in a U-FLARE experiment depends on the coherence pathway. The pathways (q_0, \dots, q_n) can be subdivided into those with an even number of sign changes in q_i (even parity) and those with an odd number of sign changes (odd parity), neglecting the zero entries [160]. The magnetization from odd and even pathways will refocus along directions that are rotated against each other by 2ϕ . This means that the two contributions can destructively interfere if the CPMG condition is contravened. Due to equation (2.65) it is possible to separate the time of echo formation for odd and even pathways. This is used in displaced U-FLARE [160, 161] where an additional gradient pulse preceding each readout gradient shifts the odd echoes out of the acquisition window while the position of the even echoes remains unaltered. Since half the magnetization does not contribute to the acquired signal the SNR is reduced by a factor of 2. The image artefacts due to interference between coherence pathways are, however, removed. Displaced U-FLARE has been successfully applied for diffusion weighted *in vivo* imaging [162].

The relative contribution of odd and even coherence pathways to an individual echo depends

on the number of refocusing pulses previously applied [161, 163]. Because odd and even pathway contributions have approximated each other after about 6 refocusing pulses data acquisition does not usually start until 7 refocusing pulses (“dummy cycles”) have been applied. Alternatively, amplitude variations in the echo train can be avoided by applying different optimized flip angles for the refocusing pulses [163, 164].

For the DTI experiments, two different U-FLARE protocols were employed. In the normal version, which will be termed “standard U-FLARE”, we used centre-out phase encoding [165], *i.e.* the centre line of k space was acquired first, followed by the lines from the centre outwards, alternating between positive and negative k_{ph} . This phase-encoding scheme has a great SNR advantage over linear phase encoding since the zeroth phase-encoding step is less affected by relaxation. However, the point spread function (see below) in the phase encode direction is broader compared to the linear phase encode scheme because the doubled time delay between the acquisition of neighbouring k -space lines leads to a larger amplitude difference. As for EPI, U-FLARE was used only in the single-shot mode since k -space segmentation would have required navigation techniques to suppress motion artefacts. The second version of U-FLARE is described in the next section.

U-FLARE with improved SNR and resolution

In particular for the investigation of white matter fibres in the human brain that exhibit only slightly anisotropic diffusion a sequence with better resolution was required than was attainable with EPI (with the given equipment and main field strength). Although U-FLARE offers higher achievable spatial resolution it has also disadvantages in comparison with EPI, the most striking of which are lower SNR and higher power deposition. We therefore developed a second U-FLARE protocol with reduced power deposition and increased SNR. A high in-plane resolution can be achieved with a large number of RF pulses (phase encode direction) and sampling points during the readout periods (read direction). Increasing the data matrix (and, consequently, the echo train length) has two consequences:

First, the true resolution (as opposed to the nominal resolution which is given by field-of-view and data matrix) is only increased if the width of the point spread function (PSF) does not exceed the voxel size. The point spread function of an imaging process represents the image of an ideal point which can be described by a $\delta(\mathbf{r})$ “function”. The PSF width is a measure of the maximum attainable spatial resolution. The image of an object is obtained by the convolution of the object function with the PSF. Just as the T_2^* decay determines the line width in NMR spectroscopy (*cf.* p. 15) the signal decay in a train of echoes determines the maximum achievable spatial resolution. Due to the convolution theorem [67] the 1-dimensional PSF for the phase-encode direction is the Fourier transform of the amplitude variation in k space, $S(k_{\text{ph}})$. If the signal $S(k_{\text{ph}}(t))$ decays exponentially with a time constant T_2 we can deduce from the equations (2.76) that the decay constant in k space is $c_k = T_2/(\tau\text{FOV}) = T_2M/(t_a\text{FOV})$ if M echoes are acquired in total within the time t_a (τ is the sampling rate). The PSF is a Lorentzian with $\Gamma_r = (\pi c_k)^{-1}$ FWHM (for the real part). The resolution can only be increased as long as Γ_r is less than the size of a voxel, FOV/M . In other words, the maximum resolution is reached at $M = \pi T_2/\tau$ or, equivalently,

$$t_a = \pi T_2. \quad (4.2)$$

The second effect of an increased echo train length is that the signal-to-noise ratio will be changed. In an experiment where the MR signal is subject to a decay during the acquisition

the relative noise content in the detected signal increases with time. Hence, at very large times t after the start of the echo train acquisition, the acquisition of further echoes *decreases* the SNR. The signal-to-noise ratio is usually defined as the peak signal amplitude in the image divided by the standard deviation of the background noise [166, section 4.3.1],

$$\text{SNR} = S/\sigma_N. \quad (4.3)$$

If we assume that the signal decays exponentially with an envelope $s(t) = s(0) \exp[-t/T_2]$ (in fact the time constant will be slightly longer for U-FLARE since the echoes contain different coherence pathways and hence different contributions of T_1 relaxation) the peak signal in the image will be determined by [166, section 4.3.1]

$$S = n \frac{M}{t_a} \int_0^{t_a} s(t) dt = n \frac{M}{t_a} T_2 (1 - \exp[-t_a/T_2]) s(0) \quad (4.4)$$

where t_a is the time required for the acquisition of the M echoes, and n is the number of averaged experiments. The standard deviation of the noise in the image domain is given by [166, section 4.3.1]

$$\sigma_N = M \sqrt{n/t_a} \rho_N \quad (4.5)$$

where ρ_N is the square root of the (frequency-independent) power spectrum (density)² of the noise in the time domain. Hence the signal-to-noise ratio is

$$\text{SNR} = S/\sigma_N = \sqrt{n} T_2 (1 - \exp[-t_a/T_2]) s(0) / (\rho_N \sqrt{t_a}). \quad (4.6)$$

This function attains a broad maximum at³

$$t_a = 1.26 T_2. \quad (4.7)$$

With $T_2 \approx 80$ ms in brain tissue at 3 T field strength the optimum echo train length is approximately 100 ms. The echo time between successive refocusing pulses in U-FLARE is about 5 ms such that the echo train length for a 64×64 matrix (smaller matrices are seldom used) is far beyond the SNR optimum. Incrementing the number of sampled k-space lines would reduce the SNR. The loss in SNR is not very drastic though, since the SNR varies only slowly with the echo train length.⁴

The maximum spatial resolution in phase encode direction is reached at $M = 51$ points, according to equation (4.2) and for the given values of echo time and T_2 . Hence increasing the number of phase encoding steps beyond 51 does not increase the resolution. On the contrary, it increases power deposition such that the repetition time would have to be extended. Because of the relatively low SNR, displaced U-FLARE is normally operated at the highest refocusing pulse angle that does not contravene the SAR limit. A high number of refocusing pulses is thus undesirable.

Hence, for an improvement of spatial resolution a different approach must be employed. To this end the U-FLARE protocol was modified in the following four points.

²which can be calculated from the Fourier transform of the (normalized) autocorrelation function of the noise [67, p. 115].

³The maximum can be found by differentiating with respect to t_a , assuming that t_a^{\max} is proportional to T_2 , and expanding the exponential function to second order.

⁴For the purpose of this consideration it was assumed that the voxel size, FOV/M , remains constant. Since the SNR is proportional to the voxel volume it rapidly decreases with an increasing number of phase encoding steps unless the FOV is increased accordingly. In practice, however, the field of view is in general chosen as small as possible in order to achieve maximum resolution.

- The phase encode direction was chosen to allow a minimum FOV. Since the head dimension is smaller along the subject's left-right axis than along the anterior-posterior direction, the left-right axis was chosen as the phase direction. With 19.2 cm×14.4 cm FOV and a 128 × 96 data matrix a nominal in-plane resolution of 1.5 mm×1.5 mm was achieved.
- Centric phase encoding was replaced by a linear scheme. The standard U-FLARE protocol employs a centre-out phase encoding scheme since the effective echo time must be minimized to achieve a large SNR. The SNR advantage of centric phase encoding is, however, counterbalanced by a lower resolution due to the broad PSF. If, however, the data are acquired starting at one end of k space and proceeding line by line to the other end (linear phase encoding), the PSF is considerably sharper since the amplitude variation as a function of k_{ph} in k space is transformed to a less rapid decrease. One could think of raising the low SNR associated with linear phase encoding simply by starting in the centre of k space and acquiring the first lines at the end. This scheme would induce image artefacts due to the fact that the amplitude variation in k space then has a sharp discontinuity between the first acquired line and the last one. In spite of this fact we were able to use linear phase encoding since the symmetry of the data in k space offers a solution to the problem:
- Data were acquired for only one half of the k-space lines and the rest was calculated based on the symmetry of the echo raw data. As a side effect the reduced number of RF pulses lowered the power deposition in the tissue. Since the proton density $\rho(\mathbf{r})$ is a real function the Fourier relationship (2.74) implies that the signal $\tilde{S}(\mathbf{k})$ is subject to the symmetry

$$\tilde{S}(\mathbf{k}) = \tilde{S}^*(-\mathbf{k}) \quad (4.8)$$

where the asterisk means complex conjugation (see also equation (2.43)). This redundancy in the data can be utilized to reduce the scan time by sampling only one half of k space [167]. Depending on whether the resulting echo train length is then closer to the optimum echo train length t_a in equation (4.7) the echo train length reduction can lead to a gain or loss in SNR. Due to the long echo train in U-FLARE with a 128 × 128 data matrix an improvement of the SNR is expected. The calculation of the missing data in k space requires some data manipulation: Although the proton density is purely real, due to the phase factor $e^{i\phi}$ in equation (2.41) this need not be the case for the Fourier transform (FT) of the acquired data. Before equation (4.8) can be applied to calculate the missing lines in k space, the raw data $\tilde{S}(\mathbf{k})$ must therefore be modified so that its FT is rendered purely real. To calculate the required correction matrix the acquisition started 6 k-space lines before the zero line such that 96/2 + 6 = 54 lines were acquired in total. From the raw data a stripe of 12 lines symmetrical about the zero line was extracted. A full data matrix containing only these 12 data lines was Fourier transformed to real space, and for each $z(\mathbf{r})$ in the resulting matrix a complex number $\zeta(\mathbf{r}) = z^*(\mathbf{r})/|z(\mathbf{r})|$ was computed, which obeys $z\zeta = |z|$. The matrix of acquired data was then zero filled and converted to real space data by Fourier transformation. The resulting image data were multiplied with $\zeta(\mathbf{r})$ and transformed back into k space. Since $|\zeta(\mathbf{r})| = 1$ the multiplication did not change the magnitude of $S(\mathbf{r})$ which is generally displayed. The phase of $S(\mathbf{r})$ does not contain any information about the real object. The k-space data obtained by this procedure were such that the imaginary part of their Fourier transform is approximately

zero. This allows the missing matrix elements to be calculated according to equation (4.8). The Fourier transform of the completed matrix finally provides an image with the same spatial resolution as the Fourier transform of conventionally acquired full k-space data. For details of the k-space completion algorithm see [167].

- In order to further reduce the effective echo time the delayed start of echo acquisition due to dummy cycles was given up and replaced by a method to determine the phase encoding order that leads to a monotonous amplitude variation for successive lines in k space. This approach has been suggested under the name TIPE (template interactive phase encoding) for GRASE (gradient and spin echo) imaging [168]. Since the variation of echo amplitudes depends on the object it requires the acquisition of a reference scan without phase encoding gradients. On the basis of the reference data the echo amplitudes are determined, and the phase encoding gradients are ordered accordingly. Since no even echo is present before the second refocusing pulse one dummy cycle is still necessary. It would have been possible to use the odd echo instead of the even echo by placing the displacing gradient after the readout gradient rather than before it. Although this would abolish the need for one dummy cycle, the amplitude difference between the first and second odd echo is very large (unless very low flip angles are used) such that it would not be possible to achieve a smooth amplitude variation in k space.

With this modified U-FLARE protocol it was possible to acquire a tensor map of a 5 mm slice with 1.5 mm in-plane resolution within about 35 min. The quality of the resulting fibre orientation map was comparable to a DTI map based on EPI (acquired in about the same scan time) with 3 mm in-plane resolution. An example is shown in Fig. A.6. The U-FLARE tensor maps did not change significantly if k-space completion was replaced by zero filling. Hence for the application described in chapter 6 the images were reconstructed with zero filling although the real spatial resolution is in this case again somewhat reduced compared to proper k-space completion.

4.3 Data processing for diffusion tensor imaging

4.3.1 Tensor calculation

Based on the diffusion weighted images for each image pixel a diffusion tensor was calculated. The calculation program was written in IDL (Interactive Data Language, Research Systems Inc., Bolder, Colorado, USA). All calculations were performed in the coordinate system given by the orthogonal directions of readout, phase encode, and slice selection gradients. The \mathbf{b} matrix for each experiment was calculated neglecting the contribution of imaging gradients according to equation (3.21) where ε was set to the maximum ramp time for switching a gradient to 100% amplitude. Since for U-FLARE all gradients were switched in the minimum possible time ("constant slope mode") the gradient ramp time actually depended on the specified gradient amplitude. However, the error introduced in the \mathbf{b} matrix calculation by the incorrect ramp times of the diffusion gradient pulses of low amplitude is small (relative error below $5 \cdot 10^{-5}$). For all pixels above a noise threshold the diffusion tensor was calculated by multivariate linear regression [15] to the equation (3.23) which uses the symmetry of the diffusion tensor to restrict the number of fit parameters to seven, including the logarithm of the amplitude in the absence of diffusion weighting, $\ln S_0$. Although S_0 could also be measured,

such a measurement would be inaccurate unless the diffusion weighting effect caused by imaging gradients is taken into account for the calculation of the \mathbf{b} matrix (see section 5.2. Before starting the regression algorithm (and before taking the logarithm), the images obtained with identical diffusion weighting were averaged in order to limit computing time. Averaging was performed with the reconstructed magnitude images since otherwise phase differences between the complex images due to different movements during diffusion weighting could cause signal interference. Strictly speaking, the measured amplitude values must be weighted differently in the fit since the transformation of equation (3.20) into (3.23) overemphasizes the uncertainties for large values of S such that the fit will be better optimized for small S [169, section 9-3]. A multilinear fit to equation (3.23) without weighting assumes that the uncertainties are equal on the logarithmic scale. The weights can be determined by a log-transformation of assumed equal uncertainties or of the measured amplitude variations over the repeated experiments. None of the two possibilities had a noticeable effect on the tensor maps and hence the fit was performed without weighting correction. The goodness of the fit can be assessed using the multiple correlation coefficient. If we denote the elements of the \mathbf{b} matrix that occur in equation (3.23) by b_1, \dots, b_6 , the corresponding diffusion tensor elements (including the factor 2 in the case of the diagonal elements) by $d_1 \dots d_6$, and the measured quantity $\ln S$ by y , then the multiple correlation coefficient is given by [169, p. 131]

$$r = \sqrt{\sum_{j=1}^6 d_j \frac{s^2(b_j, y)}{s^2(y, y)}} \quad (4.9)$$

where the empirical covariance, $s^2(b_j, y)$, of the two variables b_j and y and the empirical variance of y , $s^2(y, y)$, can be calculated from

$$s^2(b_j, y) = \frac{1}{N-1} \sum_{i=1}^N (b_j^{(i)} - \bar{b}_j) (y^{(i)} - \bar{y}), \quad s^2(y, y) = \frac{1}{N-1} \sum_{i=1}^N (y^{(i)} - \bar{y}) (y^{(i)} - \bar{y}). \quad (4.10)$$

The superscript, $i = 1 \dots N$, specifies the number of the experiment. If the multiple correlation coefficient was below 0.8, no tensor was stored for this particular pixel. This threshold was approximately the highest possible value that was still low enough to include all voxels containing white matter.

4.3.2 Eigenvector calculation and display

The main objective of measuring the diffusion tensor in the human brain was to image fibre directions in white matter. From the calculated diffusion tensors in each image pixel the fibre direction was determined in the following way. The symmetric tensor is converted to tridiagonal form⁵, and its eigenvectors and eigenvalues are calculated⁶ using built-in routines of IDL. Nonpositive eigenvalues that can occur due to numerical or measurement errors are set to zero. For each image pixel the eigenvector corresponding to the largest eigenvalue is displayed unless all three calculated eigenvalues are negative. The projection of these vectors onto the image plane is displayed. To allow an assignment of the tensor data to anatomical

⁵by Householder's method [170, section 11.2]

⁶employing the "QL algorithm with implicit shifts" [170, section 11.3]

structures each DTI measurement was preceded by anatomical T_1 weighted imaging of the same slice employing an MDEFT sequence [171, 172], and the eigenvector projections are overlaid onto the anatomical image. An example of a resulting fibre orientation map based on the EPI sequence for a slice in a volunteer's brain is shown in Fig. A.1. The fibre orientations agree well with anatomical expectations. Fig. 4.3 shows the distribution of the trace of the diffusion tensor and the anisotropy index a_f (*cf.* 3.3.2) calculated from a DTI experiment based on TIPE U-FLARE.

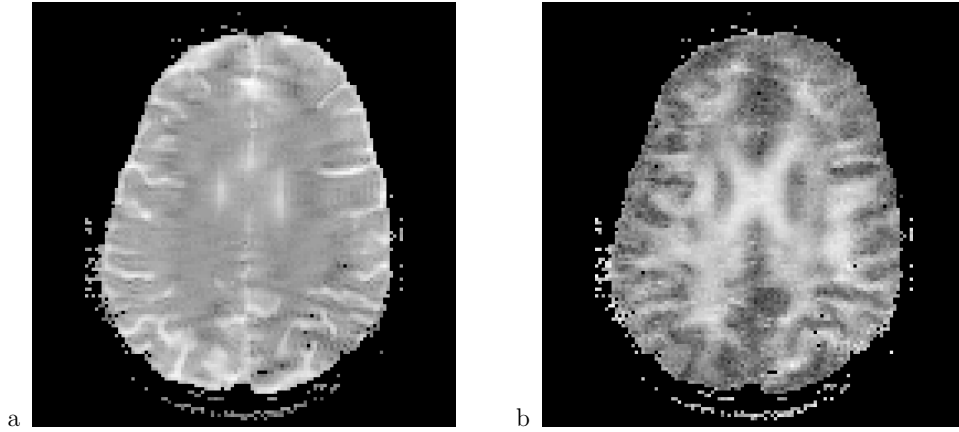


Figure 4.3: Trace map (a) and a_f map (b) based on TIPE U-FLARE sequence.

Chapter 5

Sources of systematic error and possible solutions

Possible sources of errors in the measurement are discussed in this chapter, and for some of them a solution to the problem is presented. The results of a (standard) U-FLARE tensor measurement are summarized in Fig. 5.1 in terms of Tr \mathbf{D} and fractional anisotropy index (*cf.* 3.3.2) in different regions of interest. The regions were positioned manually as follows: in a water container attached to the subject's head,¹ in the background where only artefactual signal occurs ("ghost", see section 5.6.3), and in different anatomical regions of the brain. The trace values for water given in Fig. 5.1 are consistent with the literature ADC values listed in Table 5.1, provided the water has assumed body temperature by the direct contact with the subject's head.

Temperature	25 °C	37 °C	45 °C
$D/10^{-9}\text{m}^2\text{s}^{-1}$	2.30	(3.06)	3.56

Table 5.1: Literature values for the diffusion coefficient of liquid water at saturated vapour pressure [173]. The value for 37 °C was determined by linear interpolation.

The highest anisotropy values are found in the splenium of the corpus callosum (WM₂ in Fig. 5.1) which is consistent with published results [141]. The regression routine delivers for example for a pixel in WM₂ the diffusion tensor

$$\begin{pmatrix} 0.473 & 0.165 & -0.038 \\ 0.165 & 1.651 & -0.046 \\ -0.038 & -0.046 & 0.357 \end{pmatrix} \pm \begin{pmatrix} 0.060 & 0.029 & 0.029 \\ 0.029 & 0.060 & 0.029 \\ 0.029 & 0.029 & 0.060 \end{pmatrix} \quad (5.1)$$

in units of $10^{-9}\text{m}^2\text{s}^{-1}$, in read, phase encode, and slice select coordinates with the phase encode axis being parallel to the subject's left-right direction. The eigenvalues of this tensor are calculated to be 0.459, 0.346, and $1.675 \cdot 10^{-9}\text{m}^2\text{s}^{-1}$, the fractional anisotropy is $a_f = 0.72$. Grey matter exhibits in general much lower anisotropy. However, nucleic grey matter can be as anisotropic as some white matter regions. The relatively high anisotropy found in the thalamus is consistent with the high degree of myelination in some grey matter regions that are

¹An inanimate sample that is used for testing purposes is called a "phantom" in the context of biomedical imaging.

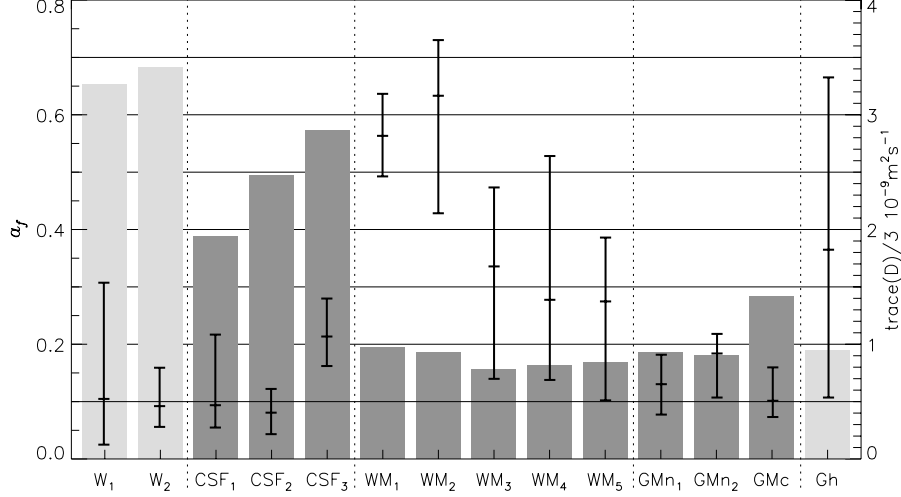


Figure 5.1: Fractional anisotropy a_f and trace values for different tissue types. $\text{Tr } D/3$ (mean over region of interest) is indicated by grey bars, a_f is indicated by lines that show minimum, average, and maximum over the region of interest. The tissue types of the regions of interest listed in the bottom line are as follows: cerebrospinal fluid (CSF₁ to CSF₃, CSF₃ is in the lateral ventricles), white matter (WM₁ to WM₅, WM₁ genu and WM₂ splenium of corpus callosum), grey matter in the caudate nucleus (GMn₂), grey matter in the thalamus (GMn₂), cortical grey matter (GMc). Values for a water phantom (W₁, W₂) that was fixed to the subject's head and for a region in the "ghost" (Gh) are given for comparison. A horizontal line at $a_f = 0.1$ indicates the minimum a_f threshold that is applied to fibre orientation maps to suppress CSF and grey matter. Values are taken from a (standard) U-FLARE measurement. The regions of interest contained about 10 to 20 voxels each.

surrounded by white matter (nuclei). The anisotropy indices for grey and white matter show that it is not possible to suppress cortical grey matter completely without also suppressing parts of white matter. An $a_f > 0.1$ threshold (as indicated by the horizontal line in Fig. 5.1) was well-suited to suppress most artefactual anisotropy in the fibre orientation maps shown in this thesis. Cerebrospinal fluid was expected to have low anisotropy and high trace values. For CSF in the lateral ventricles (CSF₃) this is not the case. Here water diffusion is characterized by relatively high anisotropy and high trace values. This behaviour is probably due to flow (see section 5.9). For a discussion of the anisotropy in the water phantom (regions W₁ and W₂) refer to section 5.7.

Although the values given in Fig. 5.1 agree well with previously published data [142, 24] the apparent anisotropy of diffusion in CSF and in water and the presence of anisotropic ghost signal that might interfere with the object image clearly indicate errors in the diffusion tensor measurement. Possible reasons for inaccuracies are noise, flow in the CSF compartments, background gradients at tissue borders, eddy currents, and subject motion. A further source of inaccuracy may be given by contributions of the imaging gradients to the diffusion weighting that have not been accounted for in the \mathbf{b} matrix calculation. Systematic and non-systematic errors shall be discussed in the following sections.

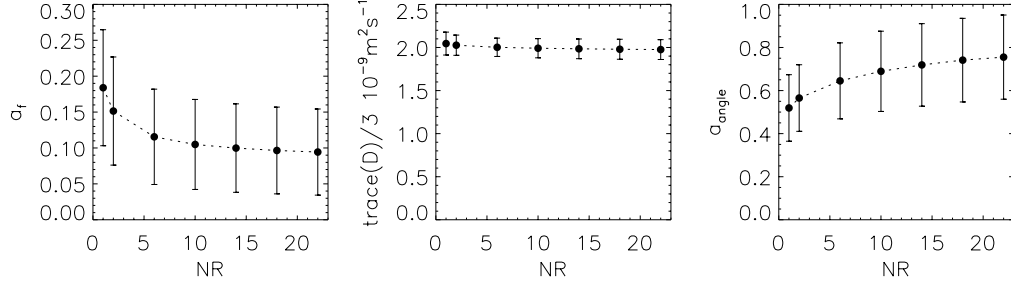


Figure 5.2: Noise dependence of fractional anisotropy, trace, and the organization index a_{angle} defined in equation (5.2), for the agarose phantom in Fig. A.2. NR denotes the number of averages. The mean value over the phantom is given in all plots along with the standard deviation indicated by vertical lines. (derived from the same data as Fig. A.2)

5.1 Influence of noise

DTI experiments on an agarose gel phantom were performed to assess the measurement accuracy and the influence of image noise. Although the diffusion coefficient of this gel was not known it was preferred to water to exclude any errors due to convective motion. The experiments revealed that water diffusion does not appear isotropic in the isotropic gel phantom. Fig. A.2b indicates systematic errors that render the measured diffusion tensor anisotropic even for isotropic substances. The map in Fig. A.2a was calculated from the same data but included only one image for each diffusion weighting instead of averaging over 22 images as in Fig. A.2b. Fig. 5.2a shows that the fractional anisotropy index decreases with increasing image SNR. As the linear regression algorithm described in section 4.3.1 is performed on averaged raw images the signal-to-noise ratio could be modified by reducing the number of averaged repetitions. At high noise levels the fractional anisotropy index, a_f , will overestimate the diffusion anisotropy [174, 175, 141, 103]. However, for 22 averaged repetitions most voxels are below the $a_f > 0.1$ threshold.

The existence of a position-dependent preferential “fibre” direction in the isotropic phantom can be measured with the lattice anisotropy index, a_l , defined in equation (3.29). This index measures the similarity of diffusion tensors in neighbouring voxels but also depends on the degree of anisotropy ($a_l = 0$ for $\mathbf{A} = 0$ in equation (3.29)). Because the anisotropy (a_f) depends on the signal-to-noise ratio, a_l is not an appropriate measure of the similarity of the eigenvector directions. To assess the degree of similarity between eigenvectors in neighbouring voxels an index was therefore defined in the same manner as the lattice index but based on the scalar product between the “fibre direction” vectors of neighbouring voxels, *i.e.* the eigenvectors corresponding to the largest eigenvalue. In analogy with (3.29) we defined this “angle index” by

$$a_{\text{angle}}(M) = \left(\sum_{N=1}^8 c_N L_{M,N} \right) / \sum_{N=1}^8 c_N \quad \text{with} \quad L_{M,N} = |\mathbf{e}_M \cdot \mathbf{e}_N| \quad (5.2)$$

where \mathbf{e}_N is the eigenvector corresponding to the largest eigenvalue in voxel N . This index increases with SNR, as Fig. 5.2 shows. This is a manifestation of the increasing separation of the red, green, and blue colours into different regions with increasing SNR in Fig. A.2.

In *in vivo* experiments, extensive averaging was required to achieve fibre orientation maps with an acceptable noise level. In a typical DTI experiment, 30 to 40 images with identical diffusion weighting were acquired for b values of the order of 600 s mm^{-2} . Because of the lower SNR of U-FLARE, with U-FLARE as the imaging sequence more averages are required than with EPI. The number of required averages was adjusted by assessing the noise level in the calculated fibre orientation maps.

Anisotropy of the measured diffusion tensor in isotropic substances is not uncommon [156, 15]. The deviation of the diffusion tensor from an isotropic tensor is usually even significant [15] which means that the anisotropy is due to systematic errors. This also seems to be the case in our experiments. Often the systematic error largely exceeds the standard deviation in the tensor elements which is calculated in the multiple linear regression analysis. In the remaining sections of this chapter we discuss the possible sources of these systematic errors.

5.2 Contribution of imaging gradients

It is clear from equations (3.20) and (3.17) that the signal amplitude in a diffusion weighted imaging experiment also depends on the gradient pulses which are used in the imaging sequence. A correct calculation of the \mathbf{b} matrix must therefore account for the imaging gradients [15, 96, 176]. In EPI based DTI, the error in the \mathbf{b} matrix elements (and hence in the tensor elements) due to neglected imaging gradients can attain values of 2% [176]. Unfortunately, for the U-FLARE experiment there is no straightforward way to include the imaging gradients in the \mathbf{b} matrix calculation. A correct calculation would have to treat the coherence pathways separately since a gradient does not have a dephasing effect on longitudinal magnetization. Because the relative amplitudes of the pathways depend on the relaxation times the exact diffusion weighting \mathbf{b} matrix can, strictly speaking, not exactly be determined from the experimental parameters. Moreover, an exact calculation would require the knowledge of the slice profile for the refocusing pulses: the pathway amplitudes depend on the refocusing pulse angle which varies along the slice-selection axis. To obtain an estimate of the error in the \mathbf{b} matrix that is introduced by neglecting the imaging gradients in the (standard) U-FLARE sequence, the gradient sequence was numerically integrated according to equation (3.17), treating the refocusing pulses in the imaging sequence as perfect 180° pulses.² This was achieved by inverting the sign of all gradient pulses that are preceded by an odd number of refocusing pulses (excluding the 180° pulse during the diffusion preparation). All gradient pulses were approximated by rectangular functions. The error introduced by this simplifying approximation is only about 0.005% at $b = 600 \text{ s mm}^{-2}$ (comparison of b value for diffusion gradients evaluated by means of (3.21) with $\varepsilon = 450 \text{ } \mu\text{s}$ and $\varepsilon = 0$). The gradient sequence was evaluated until the centre of the first acquired echo. In centre-out phase encoding this echo corresponds to $k_{\text{pe}} = 0$ such that it was not necessary to include the phase encoding gradient pulse. For numerical integration the gradient sequence was specified by 2000 points which corresponds to a temporal resolution of $62 \text{ } \mu\text{s}$. The \mathbf{b} matrix calculated exclusively from the diffusion gradients according to (3.17) with $450 \text{ } \mu\text{s}$ ramp time, $\delta = 22 \text{ ms}$, $\Delta = 40 \text{ ms}$, and $G = 23.4 \text{ mTm}^{-1}$ (which is 80% of the maximum gradient strength

²Analytical integration is tedious but also possible.

for the whole-body gradient set) is given in units of s mm^{-2} by

$$\begin{pmatrix} 617.4 & 0 & 0 \\ 0 & 0 & 0 \\ 0 & 0 & 0 \end{pmatrix}, \quad \begin{pmatrix} 0 & 0 & 0 \\ 0 & 617.4 & 0 \\ 0 & 0 & 0 \end{pmatrix}, \quad \begin{pmatrix} 0 & 0 & 0 \\ 0 & 0 & 0 \\ 0 & 0 & 617.4 \end{pmatrix}$$

for the diffusion gradient along the readout, phase encode, and slice selection directions, respectively, whereas the numerical calculation including the imaging gradients ($TE_{\text{prep}} = 80$ ms, FOV = 25 cm, 5 mm slice thickness, matrix 128×128) yields

$$\begin{pmatrix} 616.19 & 0.00 & -0.51 \\ 0.00 & 0.00 & 0.00 \\ -0.51 & 0.00 & 0.12 \end{pmatrix}, \begin{pmatrix} 0.63 & 0.00 & -0.19 \\ 0.00 & 615.56 & -0.32 \\ -0.19 & -0.32 & 0.41 \end{pmatrix}, \begin{pmatrix} 0.63 & 0.00 & -0.19 \\ 0.00 & 0.00 & 0.00 \\ -0.19 & 0.00 & 615.04 \end{pmatrix}.$$

In view of the low influence of imaging gradients and the inevitable errors in the \mathbf{b} matrix for U-FLARE it was decided to neglect the influence of imaging gradients. The error introduced in the tensor maps is expected to be spatially constant in the imaging slice(s), in contrast to the errors apparent in Fig. A.2.

5.3 Concomitant gradients

It is impossible to produce a magnetic field with spatially uniform direction and an amplitude that is strictly proportional to only one cartesian coordinate [177]. This is due to Maxwell's equations which require that [66, p. 255]

$$\text{div } \mathbf{B} = 0 \quad \text{and} \quad \text{rot } \mathbf{H} = \mathbf{j} + \frac{\partial \mathbf{D}}{\partial t}. \quad (5.3)$$

In a vacuum the electric displacement \mathbf{D} has to be replaced by the electric field \mathbf{E} . The magnetic field quantities \mathbf{B} and \mathbf{H} only differ by a scalar factor in diamagnetic substances.³ If we assume the absence of electric currents within the imaging volume ($\mathbf{j} = 0$), and constant electric fields ($\partial \mathbf{D} / \partial t = 0$) the equations (5.3) reduce to

$$\text{div } \mathbf{B} = 0 \quad \text{and} \quad \text{rot } \mathbf{B} = 0. \quad (5.4)$$

While for a pure x gradient with

$$\mathbf{B}(\mathbf{r}) = xG\mathbf{e}_z \quad (5.5)$$

the condition $\text{div } \mathbf{B} = 0$ is satisfied, the second condition in (5.4) is violated since in this case

$$(\text{rot } \mathbf{B})_k \equiv \partial_i B_j \varepsilon_{ijk} \quad (5.6)$$

does in general not vanish for $k = y$.⁴ Hence, if it is attempted to generate a magnetic field whose z component follows (5.5) the actually produced field is of the form

$$\mathbf{B}(\mathbf{r}) = zG\mathbf{e}_x + xG\mathbf{e}_z. \quad (5.7)$$

³See equation (2.78).

⁴ ∂_i is an abbreviation for $\partial / \partial r_i$. $\varepsilon_{ijk} = 1$ if (i, j, k) is a cyclic permutation of $(1, 2, 3)$, $\varepsilon_{ijk} = -1$ for cyclic permutations of $(i, j, k) = (3, 2, 1)$, and $\varepsilon_{ijk} = 0$ if any two of the three indices are equal.

For a y gradient we obtain the same equation with x replaced by y . For a pure z gradient, $\text{rot } \mathbf{B} = 0$ holds but $\text{div } \mathbf{B} = 0$ can only be achieved if

$$\mathbf{B}(\mathbf{r}) = axG\mathbf{e}_x + byG\mathbf{e}_y + zG\mathbf{e}_z \quad (5.8)$$

with $a + b = -1$. The arising components of the magnetic field in x and y direction are proportional to x and y . These gradients are called concomitant gradients [177] or Maxwell terms. Their existence can cause image artefacts [177, 178]. To decide whether or not they contribute significantly to diffusion weighting we assess the amplitude of an x gradient field as in (5.5) superimposed on the main magnetic field $B_0\mathbf{e}_z$,

$$|\mathbf{B}(\mathbf{r})| = \sqrt{z^2G^2 + (B_0 + xG)^2}. \quad (5.9)$$

By expansion to second order for $|B_0| \gg |xG| \approx |zG|$ we obtain

$$|\mathbf{B}(\mathbf{r})| \approx B_0 + xG + \frac{z^2G^2}{2B_0} \quad \text{and} \quad |\nabla|\mathbf{B}(\mathbf{r})|| \approx \sqrt{G^2 + \frac{z^2G^4}{B_0^2}} \quad (5.10)$$

which gives a ratio between real and intended (G) gradient amplitude of $1 + 5 \cdot 10^{-7}$ for $B_0 = 3 \text{ T}$, $z = 0.1 \text{ m}$, and $G = 30 \text{ mT m}^{-1}$. Thus the influence of the concomitant fields will only be noticeable at low main field strength and in applications with strong magnetic field gradients. According to equation (5.10) the concomitant field is to a good approximation invariant under inversion of the applied field gradient. This means that the dephasing effects due to concomitant gradients of two gradient pulses of opposite polarity do not cancel. In the Stejskal-Tanner gradient sequence, however, no dephasing is induced for static spins. The effects on the signal attenuation in Stejskal-Tanner diffusion experiments are expected to be negligible at 3 T.

5.4 Miscalibration and non-orthogonality of gradients

Since diffusion tensor imaging is sensitive to any deviation of the gradient fields from the ideal behaviour it was proposed [15, 79, 179] that DTI may be used to probe the orthogonality of the field gradients produced by the (usually three) gradient coils of an MR imaging system. In particular, it was suggested that the apparent anisotropy found in isotropic substances might be used as the basis for calibrating and aligning magnetic-field gradients [15]. The effect of gradient misalignment on the diffusion tensor measured in an isotropic substance is based on the fact that the amplitude of an arbitrary gradient is created by a linear superposition of the field gradients produced by the three coils,

$$G = |a\mathbf{G}_x + b\mathbf{G}_y + c\mathbf{G}_z|, \quad (5.11)$$

and depends on the angle between the vectors \mathbf{G}_i , $i = x, y, z$. The influence of gradient misalignment on the tensor measurement depends in a complicated way on the directions of the diffusion gradients used. It is however possible to extract the misalignment between two gradients from diffusion measurements on an isotropic phantom where the diffusion gradient is rotated within a plane. Let us assume we are interested in determining the angle between the x and the y gradient, and let us denote the deviation of this angle from $\pi/2$ by α . If a gradient vector is generated by choosing the x and y gradient strengths to be A and B , respectively, as depicted in Fig. 5.3, then the amplitude of the resulting gradient will be

$$G = \sqrt{A^2 + B^2 + 2AB \sin \alpha}. \quad (5.12)$$

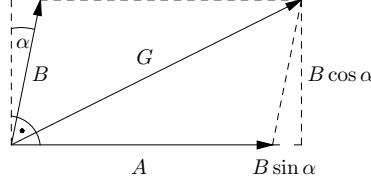


Figure 5.3: Generation of a gradient vector by superposition of two misaligned gradients.

We further assume the gradient direction is selected in terms of an angle Θ such that the amplitudes are calculated by

$$A = L_A \cos \Theta \quad (5.13)$$

$$B = L_B \sin \Theta \quad (5.14)$$

where the gradient strength values L_A and L_B may be unknown and not necessarily equal. Substituting (5.13) and (5.14) into (5.12) and using the identities $2 \cos x \sin x = \sin(2x)$ and $2 \sin^2 x = 1 - \cos(2x)$ we can express the gradient amplitude by

$$G^2(\Theta) = \frac{L_A^2 + L_B^2}{2} + \frac{L_A^2 - L_B^2}{2} \cos(2\Theta) + L_A L_B \sin(2\Theta) \sin \alpha. \quad (5.15)$$

We now would like to extract the values of L_A , L_B , and α from diffusion measurements on an isotropic phantom. We first realize that $G^2(\Theta)$ has the form of a sine function of Θ . Actually this is true for any weighted sum of sine functions of the same variable but with an arbitrary constant phase shift which can be proven in complex notation: If we seek to determine real numbers $r > 0$ and ϕ such that

$$r_1 e^{i\phi_1} + r_2 e^{i(\phi_1 + \phi_d)} = r e^{i\phi} \quad (5.16)$$

we can deduce arithmetically or from a geometric argument that $\phi = \phi_1 + \text{const}$ and that r is independent of ϕ . The real part of equation (5.16) implies that $G^2(\Theta)$ can be expressed in the form $G^2(\Theta) = c + r \sin(2\Theta + d)$ with $c, r, d \in \mathbb{R}$ being independent of Θ . According to equation (3.15) the signal attenuation S/S_0 in the Stejskal-Tanner experiment follows

$$\ln S = \ln S_0 - bD = \ln S_0 + G^2(\Theta)c_1 \quad (5.17)$$

where c_1 is independent of the gradient amplitude and can be calculated from the diffusion coefficient and the gradient timing. We can determine S_0 from a fit to measurements with different b values. It does not depend on the true value of the gradient amplitude although the slope of $\ln S$ as a function of b does depend on it. Combining equation (5.17) with (5.15) and evaluation for selected values for Θ yields

$$\frac{1}{c_1} \left(\ln S(0) - \ln S\left(\frac{\pi}{2}\right) \right) = L_A^2 - L_B^2 \quad (5.18)$$

$$\langle \ln S(\Theta) \rangle_{\Theta \in [0, 2\pi]} = \ln S_0 + \frac{c_1}{2} (L_A^2 + L_B^2) \quad (5.19)$$

$$\frac{1}{2c_1} \left(\ln S\left(\frac{\pi}{4}\right) - \ln S\left(\frac{3\pi}{4}\right) \right) = L_A L_B \sin \alpha \quad (5.20)$$

where $S(\Theta)$ is the signal amplitude measured for a gradient specified by (5.12) to (5.14). From these equations the three unknown variables L_A , L_B , and α can be calculated. It turns out that α is independent of c_1 which makes the measurement of α insensitive to errors in the determination of the diffusion coefficient.

Stejskal-Tanner experiments on a glass container filled with water at about 20°C were performed without spatial resolution. The spherical container was approx. 5 cm in diameter and was centred at the system's isocentre⁵. The amplitude of the spin echo profile as a function of the diffusion gradient was evaluated. For each of the planes specified by $x = 0$, $y = 0$, and $z = 0$ four diffusion gradients were applied in such a way that the angle between the applied gradient direction and the direction of a "pure" gradient was $\Theta = n\pi/4$ with $n = 0, 1, 2, 3$. At the beginning of the experiment automated shimming was performed to achieve main field homogeneity. The gradient strength was varied from 3 to 23 mTm⁻¹ corresponding to b values of 12 to 777 s mm⁻² ($\Delta = 184$ ms, $\delta = 10.5$ ms, whole-body gradient set). The measurements yielded α values below 1° for all possible combinations of gradient coils. However, due to the high variance of results for different b values the accuracy is not better than approximately $\pm 0.5^\circ$. In addition, the angle between the x , y , and z gradients is most certainly a function of position. The spatial variation could be measured by performing an ADC calculation for every image pixel in a DWI image.

From equation (5.15) we can conclude that the effect of gradient misalignment assumes a maximum at $\Theta = \pi/4$. In this case A and B are equal provided that $L_A = L_B$. According to equation (5.12) a misalignment of 1° then leads to a 2% change in G^2 and thus also in the calculated diffusion coefficient for that direction. This will lead only to a minor change in diffusion anisotropy.⁶ Experiments on canine heart muscle in an MR microimaging system [12] have shown that the fibre orientation derived from DTI measurements can achieve $\pm 1\%$ accuracy in the agreement with the histologically measured fibre orientation.

In a medical whole-body imaging system the error will certainly not be smaller. Although the effect of gradient non-orthogonality on the measured fibre direction is not simply a rotation, the error in the fibre direction is unlikely to be larger than the gradient misalignment, α . In view of the large artefactual anisotropy measured in isotropic substances the influence of gradient misalignment is probably negligible compared to other sources of error. Angular accuracy could be assessed using a phantom of known, anisotropic diffusion tensor. However, anisotropically diffusing substances are rare (*e.g.* liquid crystals) and phantoms with an appropriate microstructure are either not sufficiently well-ordered (plant fibres) or hard to construct. Dialysis filters have an appropriate axisymmetrical microstructure but very large diffusion times are required because of the large diameter (200 μ m) of their hollow fibres [180, 181].

Misadjustment of the gradient amplitudes causes L_A and L_B to be unequal which can introduce considerable anisotropy in the measured tensor. Gradient calibrations in clinical MR imaging systems usually have an error of approx. 1% [98]. Conturo *et al.* estimate that the errors in gradient amplitude, direction and linearity could altogether lead to a 10% inaccuracy in the measurement of diffusion coefficients [98]. In fact the signal amplitudes for the diffusion gradient directions parallel to x , y , and z deviated from each other by factors of up to 1.5 (water phantom, $b = 500$ s mm⁻²). The differences cannot be attributed to gradient nonorthogonality since for the employed gradient directions the AB term in equation (5.12) vanishes. The ratio of the diffusion weighted signal amplitudes for two diffusion gradient directions depends on

⁵The position where the magnetic fields produced by the gradient coils pass through zero is called the isocentre.

⁶For an estimation of the effect on diffusion anisotropy *cf.* section 5.7.

the diffusion coefficient and thus on the temperature such that readjustment of the gradient amplitudes by means of the signal ratio requires a device that keeps the phantom temperature constant over the duration of the experiment. Changes on the time scale of minutes were observed in the ratio of signal amplitudes that must be attributed to temperature changes in the phantom.

The difficulty to separate the effects of gradient nonorthogonality and inaccurate gradient scaling in a diffusion tensor measurement rules out the possibility to test gradient orthogonality in a simple way by means of DTI.⁷

5.5 Nonlinearity of gradient fields

The gradient coils of MR imaging systems are designed to produce constant field gradients within the volume containing the sample. The fields generated may however deviate from the desired linear spatial dependence, in particular at a large distance from the isocentre. This would introduce a position dependent error in the calculated \mathbf{b} matrix. The generated magnetic field can be expressed in terms of associated Legendre functions: For a stationary magnetic field in the absence of electric current it follows from Maxwell's equations that

$$\text{rot rot } \mathbf{B} = 0. \quad (5.21)$$

Using $\mathbf{e}_i \cdot \text{rot rot } \mathbf{B} = \text{grad div } \mathbf{B} - \text{div grad } B_i$ [182, p. 124] and $\text{div } \mathbf{B} = 0$ (5.3) this equation leads to the Laplace equation for B_z ,

$$\nabla^2 B_z = 0, \quad (5.22)$$

and the analogous equations for the B_x and B_y components [46, section 3.3]. In the volume of interest the magnetic field must obey equation (5.22). The general solution of the Laplace equation (5.22) is, written in spherical coordinates,

$$B_z(r, \vartheta, \varphi) = \sum_{n=1}^{\infty} \left(c_n r^n + \frac{d_n}{r^{n+1}} \right) \sum_{m=0}^n P_{nm}(\cos \vartheta) (a_{nm} \cos m\varphi + b_{nm} \sin m\varphi) \quad (5.23)$$

where a_{nm}, b_{nm}, c_n , and d_n are arbitrary real numbers and $P_{nm}(s)$ are the associated Legendre functions [38]. We can set $d_n = 0$ since solutions with $B_z \sim r^{n+1}$, $n > 1$, are infinite at the origin which is certainly not the case in our volume of interest [46]. Further we assume that the x and y components of the magnetic field are negligible compared to B_z . Then the specification of a_m, b_m , and c_n via equation (5.23) provides a complete description of the magnetic field in the volume of interest. In practice, terms with $n > 6$ may usually be neglected [46, p. 91]. If we set $c_n = (r_0)^{-n}$ and measure B_z at $r = r_0$ we can specify the function $B_z(r, \vartheta, \varphi)$ in terms of the coefficients a_{nm} and b_{nm} .

For the head gradient set, the manufacturer supplied the values of a_{nm} and b_{nm} at $r = 20$ cm distance from the origin which are listed in Table 5.2. In order to test the influence of gradient nonlinearity on the DTI measurements, the field gradient was calculated by applying the ∇

⁷In fact in the presence of gradient misalignment the diffusion tensor is measured in a nonorthogonal coordinate system. If the misalignment were known it should in principle be possible to transform the tensor to an orthogonal basis according to equation (2.133). In this context we would have to distinguish between co- and contravariant indices due to the nonorthogonality of the measurement basis.

Coefficient	Name	Value	Coefficient	Name	Value	Coefficient	Name	Value
a_{11}	x	100.00	b_{11}	y	100.00	a_{10}	z	100.00
a_{21}	zx	-2.53	b_{21}	zy	-2.53	a_{20}	z^2	0.00
a_{31}	z^2x	0.11	b_{31}	z^2y	0.11	a_{30}	z^3	-2.13
a_{41}	z^3x	-0.14	b_{41}	z^3y	-0.14	a_{40}	z^4	0.00
a_{51}	z^4x	-1.36	b_{51}	z^4y	-1.36	a_{50}	z^5	-4.30
a_{61}	z^5x	0.23	b_{61}	z^5y	0.23	a_{60}	z^6	0.00
a_{71}	z^6x	0.20	b_{71}	z^6y	0.20	a_{70}	z^7	0.52

Table 5.2: Values of a_{nm} and b_{nm} at $r = 10$ cm as supplied by the manufacturer (Magnex Scientific, Ltd., Oxon, U.K.) of the head gradient set, to be used in equation (5.23) to specify the field produced by the gradient coils. The coefficient values were normalized to $a_{11} = 100$. The middle columns contain the coefficient's conventional name in terms of Cartesian coordinates [46].

operator to equation (5.23). From the geometrical parameters used in a DTI experiment, the positions of all voxels in the imaged slice were calculated in terms of x, y , and z coordinates, and the gradient amplitudes that are used to calculate the \mathbf{b} matrix were corrected accordingly. Field plots for the x and z gradients are shown in Fig. 5.4. The voxel position is calculated in Cartesian coordinates and converted to spherical coordinates. Then the gradient at this position is calculated in spherical coordinates and converted to the Cartesian system. This value is scaled with the applied nominal gradient strength and is finally used to correct the \mathbf{b} matrix that was calculated from the nominal gradient values.

The DTI fibre orientation maps generated with this procedure did not differ noticeably from the fibre maps without correction. Even with artificially increased correction values it was hardly possible to force modifications within about 10 cm from the isocentre. The shape of the modifications introduced in this case suggested that it would not be possible to correct for the pattern of anisotropy found in the isotropic gel phantom as shown in Fig. A.2. The artefactual anisotropy within a distance of about 10 cm from the isocentre cannot be sufficiently explained by gradient field nonlinearity. Unfortunately, field values for the whole-body gradient set (Bruker Medizintechnik, Ettlingen, Germany), which was used for the fibre orientation map in Fig. A.2, were not available. Due to the larger dimensions of the whole-body gradient set compared to the head-gradient set it is expected to have a larger volume of gradient field linearity.

5.6 Eddy currents

A change in the magnetic field strength induces an electrical field (law of induction). The switching periods of the gradients in an MR imaging experiment therefore induce eddy currents in conducting material. These eddy currents in turn produce a magnetic field that opposes the field change and thereby modify the time dependence of the field gradients. Such problems are particularly acute in whole-body imaging systems in which space is restricted and the outer windings of the gradient set are in close proximity to the cryostat. In particular eddy currents in the cryostat can persist for a relatively long time (of the order of 100 ms) due the low resistance of the cold metal. While the widespread availability of self-shielded gradients and digital preemphasis units (see below) have largely eliminated the problem of eddy currents in many imaging experiments, for those requiring strong diffusion weighting gradients they can

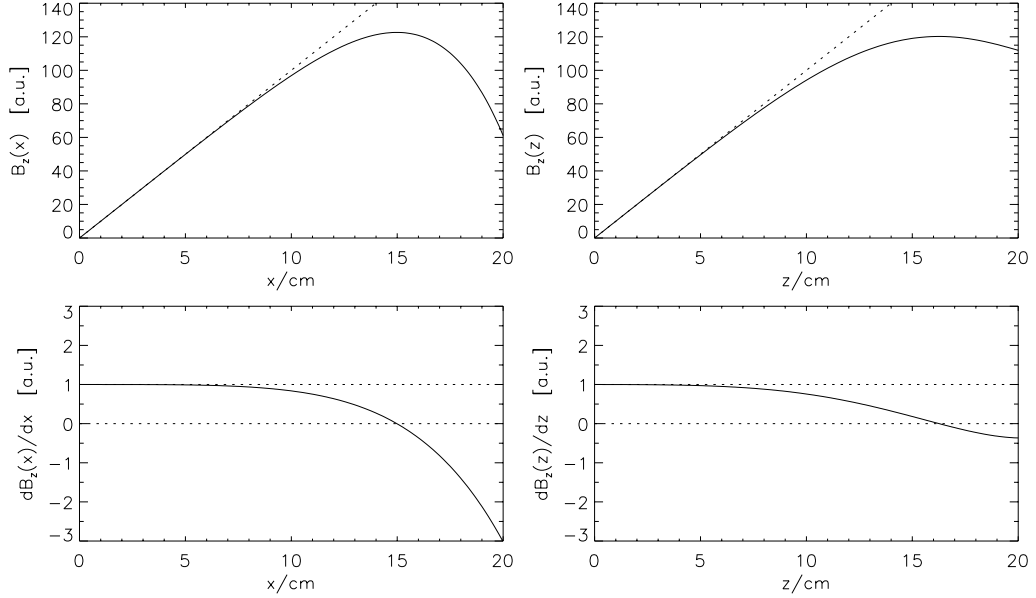


Figure 5.4: Spatial dependence of magnetic field (top) and gradient (bottom) calculated according to equation (5.23) with the coefficients given in Table 5.2. Field and gradient are given for the x gradient coil (left) and the z gradient coil (right), along the respective gradient axis. The y gradient has the same spatial dependence as the x gradient, apart from a $\pi/2$ rotation. The dotted line in the field plots indicates the ideal linear behaviour. The field is given in terms of % of the strength expected at $r_0 = 10$ cm for ideal behaviour, the gradient is given in this percentage per mm.

still be significant. The calculation of the diffusion tensor and some methods of measuring its trace rely on measurements in which the direction of the diffusion weighting gradient varies between experiments. These are then vulnerable to the effects of eddy currents which may be unremarkable in a simple DWI experiment, because the degree and nature of the artefacts will typically vary both with the strength and orientation of the diffusion weighting gradients. Systematic errors in the calculated diffusion tensor can arise from the following reasons.

- The gradient pulse shape $\mathbf{G}(t)$ differs from the intended (mostly trapezoidal) form. The associated error in $\int_0^\tau \mathbf{G}(t) dt$ affects the degree and possibly direction of diffusion weighting.
- The eddy currents generated by the first diffusion gradient pulse in a Stejskal-Tanner experiment have not decayed to zero at the time $t = \tau$ of the refocusing RF pulse such that $\int_0^\tau \mathbf{G}(t) dt \neq \int_\tau^{2\tau} \mathbf{G}(t) dt$. The inequality of the integrals causes the signal to dephase [183]. The eddy currents can also disturb the direction and time dependence of the slice selection gradient for the refocusing pulse [184].
- The eddy current related fields at the time of the actual imaging experiment disturb the imaging process. For example, eddy current induced magnetic fields can shift, shear, or scale echo planar images [185]: A global change in the main magnetic field and hence in

the resonance frequency leads to a phase ramp over a train of successively acquired data points. Since the time between phase encoding steps is much larger than that between successive sampling points in one echo the effect in phase encode direction is much more pronounced. The linear phase ramp in k_{ph} direction produces a shift of the image in the corresponding direction, which can be deduced from the shift theorem of the Fourier transform (*cf.* section 93), analogous to the effect of susceptibility gradients described by equation (2.79). A linear field variation along the readout axis leads to an x -dependent shift in y direction, *i.e.* the image is sheared. A constant eddy current induced field gradient in phase encode direction adds a constant value to the phase encoding gradient integrals between two echo acquisitions such that the increment of k_{ph} is effectively larger than $1/\text{FOV}$ (*cf.* equation (2.76)). Consequently the object image dimensions in phase encode direction are changed (scaling).

Fibre orientation maps based on diffusion tensor imaging suffer in particular from the dependence of the eddy currents on the direction of the diffusion gradient. Differences in the eddy current properties of the three gradient coils generate a high artefactual anisotropy in the calculated diffusion tensor.⁸

Gradient coils in medical imaging systems are usually surrounded by coil windings whose magnetic field counteracts the primary gradient field (active shielding), thereby minimizing the magnetic field in the nearby parts of the cryostat [46, p. 110]. A further improvement is achieved by changing the time dependence of the electrical current in the gradient coils in such a way that the generated field time dependence approximates the intended pulse shape (preemphasis). The preemphasis approach cannot completely suppress eddy currents. One reason for this is that the spatial distribution of the eddy current induced field differs from the distribution of the primary field generated by the gradient coil [183]. The gradient of the eddy current induced field need thus not be parallel to the pulsed gradient that was switched before (cross terms).⁹ The preemphasis unit that calculates the required current modifications has to be adjusted carefully. Adjustment involves specification of the time constant and amplitude of exponential functions that are added to the desired pulse shape. For common imaging sequences, such as EPI in particular, the adjustment of the short time constant exponentials is crucial. In diffusion imaging however it is rather the slowly decaying eddy currents induced by the strong diffusion gradients that induce errors in the tensor measurement. The preemphasis unit that had been sufficiently well adjusted to enable echo planar imaging had to be carefully readjusted to also suppress the slowly decaying eddy current components. Without readjustment high global anisotropy was apparent in the measured tensor maps.

In pulse sequence design it is advisable to increase the temporal separation of the diffusion gradient pulses such that a lower gradient amplitude for the same b value is required. A long delay after the diffusion weighting gradients ensures that the eddy currents have sufficiently decayed before the start of the imaging sequence but leads to an increased echo time.

The following sections are concerned with: an assessment of the eddy current sensitivity of EPI and U-FLARE, the eddy current properties of a modified preparation experiment, and an algorithm to measure and correct the influences of slowly decaying eddy currents on echo planar images.

⁸Differences between the three gradient coils in the deviation from the ideal gradient pulse shape can also lead to artifacts in the images themselves [186].

⁹See, for example, [184].

5.6.1 Strategies for avoiding eddy current effects

A number of methods for reducing the effects of eddy currents in diffusion weighted imaging have been proposed, and these may be divided into three broad categories.

- In the first the diffusion-weighting part of the experiment, generally the Stejskal-Tanner pulsed gradient spin echo experiment [91], is left unmodified and some form of correction is applied, which often involves the acquisition of additional data to obtain the correction parameters [185, 187, 188]. The nature of this correction depends upon the specific imaging sequence employed.
- In the second the diffusion weighting is modified in such a way that less eddy currents are produced [155, 189, 184, 190].
- In the third the effect of eddy currents on the image is diminished by modification of the imaging part of the sequence.

The most comprehensive method proposed to date in the first category is that of Jezzard *et al.* [185] who proposed post-acquisition correction methods for use in combination with the echo-planar imaging sequence [63]. This corrects for both shifting and scaling in the phase-encoding direction and shearing, the latter being a shift that depends on the position in frequency encoding direction. The correction factors required are generated from a pair of scans acquired without phase-encoding, one with the frequency encode axis and the phase encode axis as in the imaging scan, and one with these axes exchanged. Details concerning the implementation of this method are given below. As an alternative approach it has been suggested by Haselgrove and Moore [187] to geometrically correct the images by shift, shear, and scale operations until they coincide with an image acquired without diffusion weighting.

Only the methods in the second category are able to reduce all eddy current effects listed in the preceding paragraph. In this category the use of bipolar gradient pulses as proposed by Wider *et al.* [155, 183] is the most promising, and has been shown to give a reduction in artefact level when combined with EPI [191]. This is because the reduction in the generation of eddy currents is achieved without a significant change in the diffusion weighting for the same (effective) echo time (TE). The gradient scheme is shown in Fig. 5.5. Although a simple replacement of each gradient lobe in the Stejskal-Tanner experiment by a bipolar gradient pulse (a pair of gradient pulses with opposite polarity) also reduces the generated eddy currents, in such a scheme the achievable b value is considerably lower for the same echo time [184]. This is due to the fact that the temporal separation between dephasing and rephasing gradient lobe is shorter than in the Stejskal-Tanner scheme. The reason why the scheme proposed by Wider *et al.* [155] is appropriate for suppressing eddy currents can be explained as follows: Eddy currents that persist after a gradient pulse are mainly determined by the time delay between the two switching events at the start and end of the pulse. The two switching events induce electric fields of opposite sign, which will cancel if the time constant of the eddy current decay is much larger than the delay between the events. Eddy currents that have significantly decayed by the time of the second event will not cancel. Hence as the delay between switching events increases, so does the value for the eddy current time constant above which the eddy current effects cancel. These residual eddy currents can be reduced through the introduction of a second gradient pulse of opposite polarity. Assuming that eddy currents decay exponentially, and by using the timing definitions defined in Fig. 5.5 then the decay of a single eddy current gradient

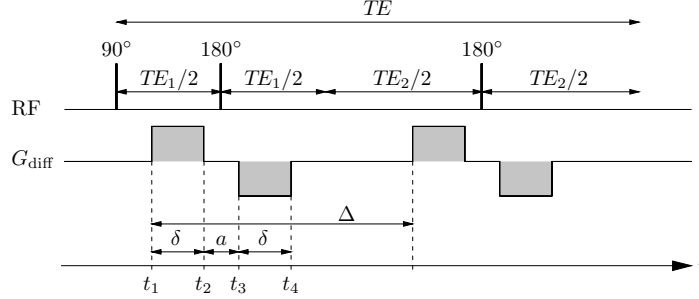


Figure 5.5: Diffusion weighting gradient scheme for the double-SE EPI sequence.

with time-constant τ is given by:

$$E_i(t) = \begin{cases} c \exp[-(t - t_i)/\tau] & \text{if } t \geq t_i \\ 0 & \text{otherwise} \end{cases} \quad (5.24)$$

where $c > 0$ is a real constant. If we consider the duration of the 180° pulse between the two gradient pulses to be vanishingly small and the gradient rise times to be short then the pair of opposing gradient pulses will be equivalent to a single pulse applied for the same total duration. The net eddy current after the single pulse, at $t > t_4$, is given by

$$A_I = E_1 - E_4 \leq 0 \quad (5.25)$$

whereas after the pair of pulses it is

$$A_{II} = E_1 - E_2 - E_3 + E_4 \geq 0. \quad (5.26)$$

The polarity of the eddy currents induced by the two schemes is opposite. The magnitude of the induced eddy currents will be reduced provided that

$$|A_{II}| < |A_I| \quad (5.27)$$

which is equivalent to

$$2E_1 - E_2 - E_3 < 0. \quad (5.28)$$

Inspection of equation (5.24) shows that the inequality (5.28) will always be satisfied, except for when all terms on the left hand side are zero, which corresponds to the irrelevant condition that the eddy currents are measured at an infinite length of time after cessation of the gradient pulse.

5.6.2 Assessment of strategies for avoiding eddy current effects

The effects of eddy currents on the final image depend naturally on the specific imaging sequence employed. Single-shot EPI is widely used because of its speed and insensitivity to motion, however the very low bandwidth in the phase-encoding direction make it particularly sensitive

to unwanted residual gradients. In this section the eddy current sensitivity of the double spin-echo approach in conjunction with the echo planar imaging technique shall be compared with the Stejskal-Tanner scheme. In addition, the performance of the correction method shall be examined and compared to the double spin-echo results.

Single-shot imaging experiments that are based on the RARE experiment should be insensitive to constant eddy currents during the echo train, because the spin phase evolution is rewound by each refocusing pulse, thereby abolishing the influence of eddy current induced fields on the signal phase. This hypothesis is experimentally tested and the potential use of RARE-based sequences discussed. It should be noted that RARE-based sequences can only be expected to be insensitive to eddy current effects on the imaging process itself, not to dephasing by unbalanced diffusion gradients or to additional damping due to eddy currents. Both of these effects are independent of the imaging sequence employed.

Experimental

All experiments were performed with the agarose gel phantom used for the experiment in Fig. A.2 placed close to the magnet isocentre. Six different diffusion preparation experiments were applied by varying both the b value (50 and 800 s mm⁻²), and orientation of the diffusion-weighting gradient pulses (parallel to the read, phase, and slice directions). In all experiments single-shot images were acquired on a 64 × 64 matrix with a 19.2 cm FOV and 5 mm slice thickness. In order to assess how the images are affected by the presence of strong diffusion gradients, the images for $b = 50$ and $b = 800$ s mm⁻² were subtracted from each other. Before subtraction, differences in signal intensity caused by different diffusion weighting were compensated by averaging the $b = 800$ s mm⁻² images until approximately the same SNR was achieved as for a $b = 50$ s mm⁻² image.

In the EPI experiments a repetition time of 3 s was applied and the acquisition bandwidth was set to 100 kHz which implies a total echo-train length of 41 ms. Blipped phase-encoding was used with the phase-encoding zero at the middle of the echo train which was timed to coincide with the centre of the spin echo. Images were obtained in transaxial section with the readout gradient applied along the x axis. To remove Nyquist ghosts the images were reconstructed using a phase correction based on a separate reference scan obtained without phase encoding. All the diffusion weighted images were reconstructed using the same reference scan (with $b = 50$ s mm⁻² diffusion weighting parallel to read). Readout gradient switching during data acquisition was also corrected for during reconstruction. Diffusion weighting for conventional SE EPI consisted of two gradient pulses flanking the 180° refocusing pulse. Employing the standard notation the gradient timings were $\delta = 22$ ms and $\Delta = 40$ ms. The echo time was 120 ms which was the minimum echo time for the double-SE EPI sequence for a b value of $b = 800$ s mm⁻². The presence of the diffusion gradient pulses made additional spoiler gradients unnecessary. In the double spin-echo EPI sequence the scheme from excitation to the 0th phase-encoding step was 90°- $TE_1/2$ -180°-($TE_1 + TE_2$)/2-180°- $TE_2/2$. The echo time was $TE = TE_1 + TE_2 = 120$ ms. Each of the Stejskal diffusion gradients was split into two parts of opposite polarity, separated by a 180° pulse as shown in Fig. 5.5. The b value for the gradient scheme (assuming rectangular gradient pulse shape) in Fig. 5.5 is given by¹⁰

$$b = \gamma^2 G^2 (2\delta)^2 \left(\Delta - \frac{a}{2} - \frac{2\delta}{3} \right) \quad (5.29)$$

¹⁰Reference [155] contains an error in the formula for b .

where δ and G are duration and amplitude of the gradient pulses, Δ is in this context the time delay between the onset of two gradient pulses of the same polarity, and a is the duration of the interval between the end of the first and the start of the second gradient. In the double-SE EPI experiments, $\delta = 9$ ms and $\Delta = 60$ ms were used. Spoiler gradients before the positive and after the negative gradient lobes were incorporated to dephase any transverse magnetization created by the 180° pulses.

The U-FLARE imaging sequence was used in the displaced version [159, 160, 161], starting with a spin echo diffusion preparation experiment. Diffusion weighting was achieved with the Stejskal-Tanner gradient scheme, just as in the conventional SE EPI sequence. The field of view, slice orientation, slice thickness and timing of the diffusion weighting gradients were the same as in the EPI experiments. The echo time in the preparation experiment was in this instance 70 ms. The repetition time was 3 s. The 70° refocusing pulses (sinc shape, 2 ms duration) in the imaging sequence had a spacing of $TE = 4.4$ ms, 7 refocusing cycles (dummy cycles) were applied prior to data acquisition to ensure that the signal had reached a steady state. Centre-out phase encoding was applied as this offers high sensitivity, resulting in an effective echo time of 121 ms. The total echo train length including dummy cycles (excluding the preparation period) was 317 ms. All RF pulses in the sequence were slice-selective. Excitation and refocusing pulses in the preparation experiment were 3 ms long and Gaussian shaped.

Eddy current correction for EPI

For all EPI images the eddy current correction of Jezzard *et al.* [185] was applied, and the results with and without correction compared. The reader may refer to [185] for details of the algorithm employed. The only significant deviations from this algorithm concerned the correction for eddy current gradients in the phase encode direction and the way the values for eddy gradients in read direction are used for the calculation of the corresponding correction. It should also be noted that eddy gradients in the slice selection direction are not corrected for in this approach. In order to measure the eddy current related gradients and the B_0 shift during the EPI readout period, a separate diffusion weighted reference scan without phase encoding was acquired for each diffusion gradient strength and direction. Each of these reference scans was repeated with read and phase encode direction exchanged while leaving the diffusion gradient direction unaltered. For simplicity, in the following discussion the directions of readout and phase encode gradient will be considered to be aligned with the x and y axes, respectively. From the read direction reference scans the eddy current related field gradients in read direction, ε_x , can be calculated. After time reversal of odd echoes and 1D-Fourier transformation along read, for each acquired sampling point the phase difference to the corresponding data point in the following echo transform was calculated. (To avoid errors arising from differences between odd and even echoes the phase difference to the next echo of same readout gradient polarity was used.) The phase difference plot was phase unwrapped, and the additional B field caused by eddy currents was calculated from

$$B(x, t) = \frac{1}{\gamma\tau_{pe}}(\phi(x, t + 2\tau_{pe}) - \phi(x, t)), \quad (5.30)$$

with τ_{pe} being the time delay between two successive phase encoding blips. A linear fit of B as a function of the readout coordinate, x , was performed. The slope yields the x gradient, ε_x , for each echo, and the value of B at $x = 0$ is the B_0 field shift, ε_0 . In common with the original paper [185] we assume that all eddy current effects are constant during the EPI readout train.

It is expected that time varying effects during the echo train would only introduce a further blurring in the images [185]. This algorithm can in principle yield an ε_x value for each phase encoding step. If $\varepsilon_x(k_y)$ is not constant then this indicates a time-dependence of the x -gradient. In the correction the average of the ε_x values for 7 echoes about $k_y = 0$ was used. The eddy current related y gradient, ε_y , was calculated in the same way as the y gradient but using the reference scan which had the readout gradient parallel to the image phase encode direction.

The correction started with the B_0 shift correction which was performed by applying a 1-dimensional phase ramp in phase encode direction to the image raw data:

$$S(k_x, k_y) \mapsto S(k_x, k_y) \exp[-i\gamma\tau_{pe}\varepsilon_0 k_y] \quad (5.31)$$

where the median value of ε_0 over all phase encoding steps was used. The ε_0 values were calculated from the read direction templates but could equally well have been calculated from those for the phase direction. After time reversal of the odd echoes and 1D-Fourier transformation in the read direction, the x -gradient was corrected for by application of a phase ramp in k_y proportional to $\varepsilon_x x$, *i.e.* the complex raw data were multiplied by a phase factor according to

$$S(x, k_y) \mapsto S(x, k_y) \exp[-i\gamma\tau_{pe}\varepsilon_x x k_y]. \quad (5.32)$$

For correction of eddy current induced y -gradients Jezzard [185] suggested a k-space regrid-ding algorithm. We chose an approach instead that simply rescaled the reconstructed images according to the calculated eddy y -gradient amplitude. The images reconstructed from the ε_0 and ε_x corrected raw data were expanded to a $64 \times f_y 2048$ matrix with a linear interpolation routine, using a factor

$$f_y = 1 + \frac{\varepsilon_y \tau_{pe}}{G_y \tau_{ramp}} \quad (5.33)$$

where G_y is the maximum amplitude, and τ_{ramp} is half the total duration of the triangular phase-encoding gradient blips. An appropriate number of lines were then removed (for $f_y > 1$) or added symmetrically (for $f_y < 1$) to bring the matrix to exactly 64×2048 size. In the latter instance this was achieved simply by zero-filling. The resulting matrix was then reshunk to the original matrix size. This procedure rescales the image in the phase encode direction by the factor f_y .

Results

Figs. 5.6 to 5.8 show the resulting difference images for 3 different directions of the applied diffusion gradient (read, phase, and slice direction). The phase encode direction is the vertical direction in Figs. 5.6 to 5.8. Figs. 5.6 and 5.7 show the results for the conventional SE EPI sequence, and for the double-SE EPI method, respectively. Uncorrected data are shown in the upper row, and data after the eddy current correction are shown in the bottom row. Medium greyscale values indicate zero difference.

Conventional SE EPI In the difference images for conventional SE EPI shown in Fig. 5.6 the typical EPI image artefacts as described previously [187] lead to visible signal differences at the edges of the phantom. In the images with diffusion weighting in the phase-encoding or slice directions, an image shift is the most striking artefact. The difference images show a clearly visible one pixel wide dark and light edge at the border between phantom and background.

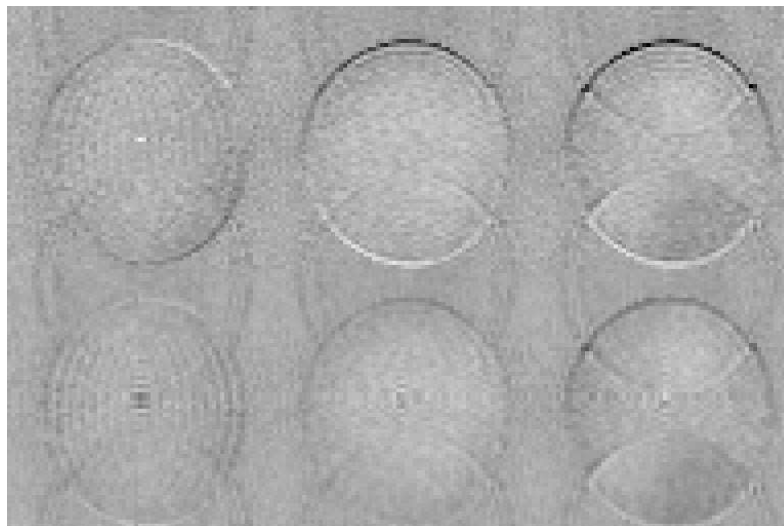


Figure 5.6: Difference between the single-SE EPI images for different degrees of diffusion weighting (at high b value minus at low b value). Images with strong diffusion weighting were averaged to achieve the same SNR as with weak diffusion weighting. Medium greyscale values indicate zero difference. Images are shown from left to right obtained with the diffusion gradient oriented parallel to the read (horizontal), phase encode (vertical), and slice axis (through-plane). Uncorrected data are shown in the upper row, and the corresponding corrected difference images are shown below.

Although somewhat diminished by eddy current correction it is still apparent in the corrected images. With the diffusion gradient in the read direction a shear occurs as predicted for eddy currents that cause a magnetic field gradient in the read direction. This is successfully removed by the correction algorithm. However, a new artefact is introduced, *i.e.* a ringing similar to the artefacts found if read gradient switching during acquisition is not corrected for. An image scaling due to eddy gradients in phase encode direction is not visible to the naked eye. Table 5.3 however shows that the correction algorithm nevertheless detects a gradient in phase encode direction and corrects for it.

With the diffusion gradient in slice direction, and to a lesser extent in the phase direction, high spatial-frequency ghosting is clearly visible in the difference images. This indicates that the ghost artefacts in EPI images are affected by eddy currents. An alternative explanation would be that the performance of the automatic phase correction depends on the presence of eddy currents. In order to investigate the latter possibility we performed a further experiment (results not shown) where in image reconstruction 6 separate, diffusion weighted reference scans were used for (Nyquist) phase correction. Each image was corrected by means of the corresponding reference scan, *i.e.* the reference scan with the same diffusion weighting. No improvement was observed in the images reconstructed in this manner compared to the images reconstructed by means of just one single reference scan (weighted with $b = 50 \text{ s mm}^{-2}$). These artefacts are believed to arise from short time-constant eddy currents induced in the birdcage resonator, and are as such system specific.

Close examination of Fig. 5.6 reveals that the noise in the corrected images is smoother

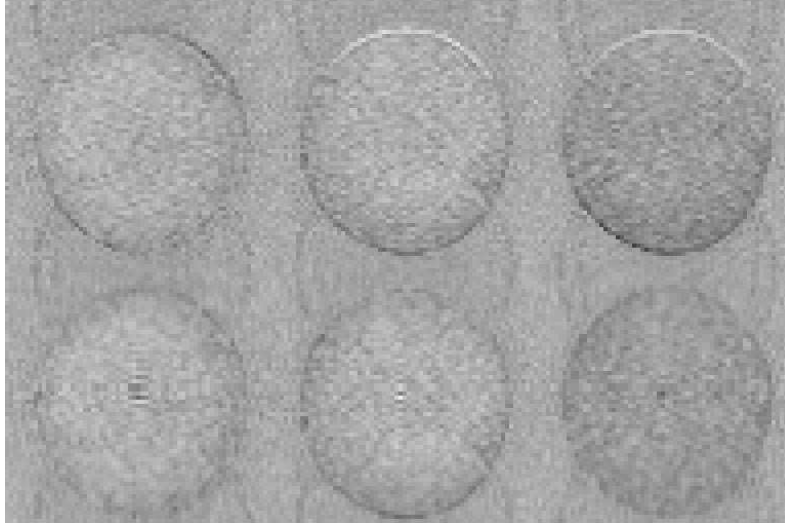


Figure 5.7: Difference images as in Fig. 5.6, obtained for the double-SE EPI sequence.

than before correction. This is because the interpolation used in the correction procedure has a smoothing effect on image noise.

The algorithm yields an ε_x value for each phase encoding step. The fact that $\varepsilon_x(k_y)$ is indeed not constant indicates a time-dependence of the x gradient. Although in the experiments reported here the mean of the ε_x values for the 7 echoes about $k_y = 0$ was used for phase correction, it would also be possible to either apply a different correction to each individual phase encode step (which can lead to artefacts since the variance of ε_x is large), or to fit a function $\varepsilon_x(k_y)$ to the data. In *in vivo* experiments (results not shown) none of these methods worked in all cases, in terms of reliably reducing the shear artefact without introducing new artefacts.

The algorithm clearly does not entirely eliminate all artefacts. There are at least two possible reasons for this: First, although eddy currents which vary during the echo train should only cause a blurring effect [185], the variation in signal through the echo train can introduce errors in the correction parameters. A second possibility is that the algorithm assumes that the eddy current induced magnetic fields are linear over the whole object, which may not be the case.

Double-SE EPI The form of the artefacts found in double-SE EPI images (*cf.* Fig. 5.7) did not differ qualitatively from that for the single-SE EPI sequence. Again shearing is observed for diffusion weighting in the read direction, and an image shift occurs with diffusion gradients along the phase-encoding or slice directions. However, compared to the conventional SE EPI method the differences between high and low diffusion weighting are small. Even in the double-SE EPI sequence eddy currents are strong enough to affect the imaging part of the sequence. The eddy currents however are greatly reduced. Application of the eddy current correction method to the double-SE EPI data brings the difference values down to the order of the noise level. The largest improvement compared to the conventional SE EPI sequence is the reduction



Figure 5.8: Difference images as in Fig. 5.6, obtained for the U-FLARE sequence.

in the B_0 field shifts. The amount of shearing does not seem to be significantly reduced for our system. The values for ε_0 in Table 5.3 are reduced considerably in the phase and slice direction case, compared to conventional SE EPI. The amplitude of the measured read direction eddy gradients is the same for both sequences.

The correction parameters obtained for both EPI experiments are summarized in Table 5.3 and 5.4. The relatively large value of ε_y even in the absence of diffusion gradients is almost certainly caused by the presense of inhomogeneity gradients in this direction. In comparing the correction factors for the two experiments it should be borne in mind that the double spin-echo experiment will generate eddy currents of the opposite polarity to the single spin-echo.

U-FLARE Fig. 5.8 shows the differences between high and low diffusion weighting for the U-FLARE sequence. The artefacts manifest themselves as a signal loss near the phantom boundaries in the phase encode direction. The artefacts are less localized than in the uncorrected SE EPI images. Shear, scale, or shift artefacts do not occur although eddy current induced shifts of the echoes in the acquisition window were present. Possible causes of the present artefacts will be described below.

Discussion

The correction scheme proposed by Jezzard *et al.* [185] considers eddy current effects to be constant during the EPI acquisition period. As this period is generally of about 50 ms duration the assumption is not unreasonable. In this situation the effects of eddy currents are identical with those of constant gradients produced for example by static field inhomogeneity combined with off-resonance effects (*cf.* p. 27), both of which have been reported in the EPI literature [65]. Naturally the strength of these effects is dependent on the diffusion-weighting gradients employed, and experiments such as DTI which often require a variation both in the orientation and strength of the diffusion-weighting gradient, will require a correspondingly large number of correction experiments. If eddy currents are produced in the slice-selection direction then these may lead to signal losses which are not corrected for in this scheme. The double spin-echo scheme significantly reduces the artefact level at very little cost in experimental duration although it is not clear why the magnitude of the shear gradient remains largely unaltered. If sufficient time is available then combination of the two experiments will lead to a further improvement. It is however questionable whether the small expected improvement is worth the effort of postprocessing all images. The difficulty in determining the appropriate correction

		$b = 50 \text{ s mm}^{-2}$			$b = 800 \text{ s mm}^{-2}$		
		Re	Ph	Sl	Re	Ph	Sl
SE-EPI	$\varepsilon_0/10^{-7} \text{ T}$	-2.338	-2.990	-3.229	-1.873	-4.292	-4.155
	$\varepsilon_x/10^{-7} \text{ T}$	5.938	2.115	-0.150	22.680	7.699	0.389
	$\varepsilon_y/10^{-7} \text{ T}$	45.826	45.773	46.619	55.035	45.289	47.287
	f_y	1.02325	1.02322	1.02365	1.02792	1.02297	1.02399
DSE-EPI	$\varepsilon_0/10^{-7} \text{ T}$	-1.967	-1.670	-1.610	-1.892	-0.766	0.087
	$\varepsilon_x/10^{-7} \text{ T}$	-7.170	-0.063	-0.461	-21.748	-0.959	-3.796
	$\varepsilon_y/10^{-7} \text{ T}$	44.065	39.665	42.979	45.615	28.223	41.893
	f_y	1.02235	1.02012	1.02180	1.02314	1.01432	1.02125

Table 5.3: Eddy current related gradients and field offsets for low and high b value, and for three directions of the diffusion gradient (read, phase, and slice direction). For the correction of eddy gradients in phase encode direction also the correction factor f_y from equation (5.33) is listed.

		Re	Ph	Sl
SE-EPI	$\Delta\varepsilon_0/10^{-7} \text{ T}$	0.465	-1.302	-0.926
	$\Delta\varepsilon_x/10^{-7} \text{ T}$	16.742	5.584	0.539
	$\Delta\varepsilon_y/10^{-7} \text{ T}$	9.209	-0.484	0.668
DSE-EPI	$\Delta\varepsilon_0/10^{-7} \text{ T}$	0.075	0.904	1.697
	$\Delta\varepsilon_x/10^{-7} \text{ T}$	-14.578	-0.896	-3.335
	$\Delta\varepsilon_y/10^{-7} \text{ T}$	1.550	-11.442	-1.086

Table 5.4: Differences of eddy current related gradients and field offsets between low and high b value, for three diffusion gradient directions. $\Delta\varepsilon_i = \varepsilon_i(800 \text{ s mm}^{-2}) - \varepsilon_i(50 \text{ s mm}^{-2})$ for $i = 0, x, y$.

parameter from the set of ε_x values obtained for the individual echoes is considered to be an important limitation of the correction technique for practical applications. If series of images are to be obtained in which only the b value is varied by means of varying the strength of the diffusion weighting gradients, and if one set of images is obtained with a b value close to zero, then the correction scheme of Haselgrove and Moore [187] may be applied without an experimental time penalty. If the double spin-echo experiment is to be used without a significant increase in TE then only a short delay can be permitted between switching off the first gradient pulse in the pair and the 180° pulse. It is hence necessary to have good correction of short time-constant eddy currents to utilise this scheme.

The U-FLARE experiment offers images with less geometrical distortion than EPI but the lower sensitivity and higher power deposition of this experiment make EPI preferable in most situations. As argued above, if the eddy currents are constant during the echo train then their effect is identical to that of linear inhomogeneity gradients and as such will be corrected by a RARE-type sequence. The echo train length in U-FLARE can however be an order of magnitude longer than for EPI, and the assumption of constant eddy current effects is then unlikely to be valid. In the centre-out phase-encoding scheme employed here the highest k-space coordinates are collected at the end of the echo train. Any temporal variation in the eddy current gradient will mean that each coherence pathway that contributes to the signal will have experienced a different total gradient, and the net signal will hence be reduced. The

resulting diminution of the intensity will affect the higher spatial frequencies and will hence be primarily visible at the edges perpendicular to the phase-encoding direction of the phantom used. Despite this secondary effect the sensitivity of displaced U-FLARE to eddy current effects is less than that of EPI and its use may well be considered in situations where strong eddy currents or poor main field homogeneity are present.

5.6.3 Consequences of eddy currents for DTI

The effects of eddy current induced image artefacts on diffusion tensor images can be catastrophic. The described shift, shear, and scale artefacts in EPI can severely degrade the tensor measurement at tissue borders, in particular the borders between brain tissue and CSF-filled compartments which have considerably different relaxation properties and hence signal levels. In our DTI experiments, the modification introduced by the eddy current correction algorithm in the fibre orientation maps based on EPI-DTI was only noticeable along this border. While the effect of shift, shear, and scale artefacts is largely restricted to relatively few image pixels the artefacts occurring in U-FLARE affect broader regions of the image. An example of a U-FLARE fibre orientation map that illustrates the consequences of blurring and broad image signal variation is shown in Fig. A.3a.¹¹

It is possible to reduce the erroneous anisotropy to some extent by modifying the \mathbf{b} matrices such that the tensor in a selected pixel in CSF is isotropic. To evaluate the use of such a normalization the \mathbf{b} matrix was modified by applying a constant factor to each gradient vector component. The gradient amplitudes used to calculate the \mathbf{b} matrix in (3.21) were modified according to

$$G_i \mapsto G_i \sqrt{\frac{\text{Tr } \mathbf{D}}{3D_{ii}}} \quad (5.34)$$

such that in the ideal case (multiple correlation coefficient $r = 1$) the diffusion tensor in the reference voxel would be rendered isotropic without changing the tensor trace. The approach can improve the coincidence between measured and actual fibre direction in the proximity of the selected reference pixel as can be seen in Fig. A.3b. For more distant pixels, however, it introduces an erroneous anisotropy in the diffusion tensor. Hence it can only be a last remedy to extract fibre orientations in restricted regions from acquired data that are heavily corrupted by eddy currents, and it is only applicable if the area of interest contains a voxel where the diffusion is known to be isotropic.

The anisotropy map in Fig. 5.9 was calculated from the same data as in Fig. A.2b but the threshold for the multiple correlation coefficient was set to 0.8, as usual for the *in vivo* experiments, and no image signal intensity threshold was applied. The high anisotropy values in the background of Fig. 5.9 are due to the presence of a “ghost” in the diffusion weighted images. Many fast imaging sequences are characterized by a relatively poor point spread function (see p. 62). Side peaks in the PSF can give rise to a displaced faint copy of the object (“ghost”). The signal in the background (as in region Gh in Fig. 5.1) can be high enough to pass the signal threshold for tensor calculation. Since the ghost is derived from the main object image it is also subjected to the same diffusion attenuation as the image itself. Hence it may also pass the threshold set for the multiple correlation coefficient, as can be seen in

¹¹In this example, image reconstruction involved $\sin^2 x$ filtering of the raw data to remove ripple artefacts [166, section 4.1.3.1].

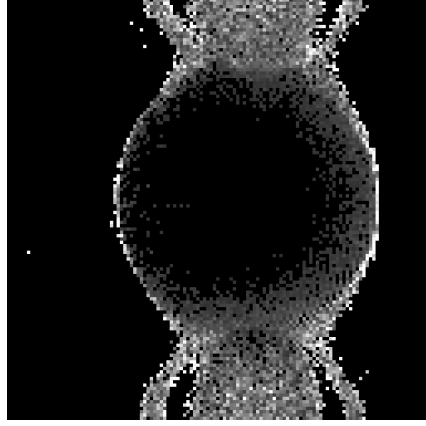


Figure 5.9: Map of a_f for an isotropic agarose gel phantom, with 22 repetitions. A linear greyscale between $a_f = 0.1$ and $a_f = 0.5$ was used, pixels with $a_f < 0.1$ appear in black. No image signal threshold was applied. The readout direction is horizontal. (For experimental details see Fig. A.2).

Fig. 5.9. A ghost image may be visible in the fibre orientation map even if the raw images are free of ghost artefacts. Because ghosts in the phase encode direction can arise from phase errors, eddy currents can modify the signal intensity of the ghost. The presence of b value dependent ghosting has been reported to affect ADC measurements [192]. The sensitivity of an imaging sequence to eddy currents is most likely dependent on the direction of the eddy current induced gradients such that the ghost intensity varies with the diffusion gradient direction. In the presence of highly anisotropic ghost signal the tensor measurement can be disturbed in brain regions where image and ghost overlap. While the Nyquist ghost in EPI always overlaps with the object unless it occupies less than half the field of view in phase encode direction, the position of the ghost in U-FLARE images depends on the refocusing pulse angle: pulse-angle dependent amplitude variations among the first echoes cause signal variations in k space that degrade the point spread function, in particular with centric phase encoding. However, in *in vivo* applications of U-FLARE the ghost is much less significant than in phantom images.

In summary, DTI can yield fibre anatomy information in white matter if eddy current effects are sufficiently reduced by preemphasis adjustment, sequence modification, or/and image postprocessing. The sensitivity of both EPI and U-FLARE to eddy current effects will however make reliable measurements of the diffusion tensor in cortical grey matter difficult. Whether EPI or U-FLARE should be preferred as imaging sequence for DTI depends on the magnetic field strength, the available gradient hardware, and the requested spatial resolution.

5.7 Background gradients

We have mentioned that the diffusion tensor measured in isotropic substances is often anisotropic. Fig. A.4 shows that in a macroscopic phantom containing isotropic water the anisotropy is higher close to the vessel wall. Region W_2 in Fig. 5.1 contains only the centre area of the water phantom while W_1 represents the whole phantom, including the more anisotropic boundary area. Moreover, the principal directions of the diffusion tensor in a voxel seem to depend on

the orientation of the nearest vessel wall. The restriction to diffusion by the mere existence of an impermeable boundary cannot be the reason for the observed anisotropy as the following argument shows. Since the mean displacement of water molecules within a diffusion time of 40 ms is about $20 \mu\text{m}$ ($D = 2 \cdot 10^{-9} \text{ m}^2 \text{ s}^{-1}$) only the molecules within $40 \mu\text{m}$ distance from the wall, say, can experience the restriction of the random walk by the vessel wall. Assuming cubic voxels of $(1.5 \text{ mm})^3$ volume, this corresponds to a fraction of about 3% of the total number of molecules in the voxel. For the remaining molecules diffusion will be unrestricted. The signal attenuation could then be described by the equation

$$S/S_0 = f_1 \exp(bD_1) + f_2 \exp(bD_2) \quad (5.35)$$

where $f_1 = 0.97$ and $f_2 = 0.03$, and D_1 and D_2 are the diffusion coefficients for the restricted and the unrestricted proton pool, respectively. To estimate the influence on the measurement of the diffusion coefficient, we assume a two-point measurement with $b = 20 \text{ s mm}^{-2}$ and $b = 500 \text{ s mm}^{-2}$, and $D_1 = 2 \cdot 10^{-9} \text{ m}^2 \text{ s}^{-1}$, and we set $D_2 = 0$ to obtain an upper limit for the influence on the diffusivity measurement. From a linear fit to the two data points we would obtain $D = 1.90 \cdot 10^{-9} \text{ m}^2 \text{ s}^{-1}$ which deviates from the real diffusion coefficient, D_1 , by 5 %. The fractional anisotropy index that would be induced by a 5 % deviation of one principal diffusivity from the isotropic case can be calculated from equation (3.27),

$$a_f = \frac{|c-1|}{\sqrt{2+c^2}} \quad \text{for } \mathbf{D} = \begin{pmatrix} cd & 0 & 0 \\ 0 & d & 0 \\ 0 & 0 & d \end{pmatrix}. \quad (5.36)$$

With $c = 0.95$ we obtain $a_f = 0.03$. As this is the result of a worst case approximation the actual anisotropy induced by partial restriction at the phantom wall will in general be much smaller. The anisotropy, however, that is found in the DTI experiment is of the order of $a_f = 0.1$ to 0.3 (see Fig. 5.1) which rules out the restriction explanation.

A more likely explanation is that the tensor measurement is influenced by background gradients that are induced by the large susceptibility change at the vessel wall (*cf.* p. 26). Equation (3.13) describes the influence of background gradients on the signal attenuation in a Stejskal-Tanner experiment. Given that $G_0 \ll G$ the G_0^2 term can be neglected. This implies that the geometric mean over the signal from two acquisitions with inverted gradient directions is largely independent of the background gradient, G_0 , since:

$$\frac{\sqrt{S(G)S(-G)}}{S_0} \approx \exp(-cG^2) \quad (5.37)$$

with some real positive constant c .¹² It has to be pointed out that susceptibility gradients can lead to image distortions without having a noticeable effect on the diffusion measurement. Distortions and extinctions are not corrected for by geometric averaging. The direction scheme (4.1) was modified by inclusion of the inverted gradient direction. In experiments with a glass container filled with ethanol which has about half the diffusion coefficient of water¹³ an anisotropy at the transition between ethanol and glass was also found. However, geometric averaging over opposite gradient directions did not at all affect this anisotropy at the border.

¹²The background gradients arising from susceptibility differences in the sample may to a small extent depend on strength and direction of an applied magnetic field gradient. This has not been accounted for in equation (3.13).

¹³for ethanol $D \approx 1.08 \cdot 10^{-9} \text{ m}^2 \text{ s}^{-1}$ at 25°C .

This was also the case for the water phantom in Fig. A.4. In tensor maps of a perspex container filled with vegetable oil which has an extremely low diffusion coefficient¹⁴ high artefactual anisotropy also occurs. However, this does not seem to be related to the phantom wall. The preferred diffusion direction in the rather broad regions of anisotropy in the oil phantom changes upon application of geometric averaging, in contrast to the ethanol and water cases. Anisotropic regions localized at the phantom borders were observed only at the surfaces of ethanol and water, and only to a low degree at the surface of agarose gel or vegetable oil. All experiments in this context were performed employing U-FLARE in the imaging part of the sequence. The remaining possible mechanisms that could lead to the observed anisotropy at the phantom wall are convective flow (see section 5.9) and eddy current effects that affect high spatial frequencies. In the experiment in Fig. A.4 convection is likely to play a role since the direct contact with the subject's skin almost certainly produces a temperature gradient in the phantom.

If in *in vivo* experiments positive and negative gradients are included, the situation can occur that a relatively large number of pixels does not pass the multiple correlation coefficient threshold. This must be attributed to the differences between the images for opposite diffusion gradient direction which can arise from residual eddy currents that influence the imaging sequence. Ghosting in particular can differ between the gradient directions such that the regression has to cope with different signals for the same \mathbf{b} matrix. This leads to a reduction in the multiple correlation coefficient.

On the grounds of these results it is anticipated that the artefactual anisotropy due to tissue borders is probably lower than at the border of a water phantom. For this reason and since geometric averaging does not reduce the erroneous anisotropy, the geometric mean approach was usually not applied to *in vivo* experiments.

5.8 Subject motion

Diffusion weighted sequences are designed to be sensitive to displacements on a micrometer scale and are hence also susceptible to motion other than diffusion. If incoherent motion occurs, as for example in a flowing fluid with a broad velocity profile (see section 5.9), the signal is attenuated by intravoxel dephasing which disturbs the measurement of the diffusion coefficient. For coherent motion such as head movement the motion induced phase errors are of a rather systematic nature and can in some circumstances be corrected for. The sensitivity of diffusion weighted imaging sequences to bulk motion has been mentioned in section 4.2. In 1992 Ordidge *et al.* [193, 194] proposed a “navigator echo” method to correct for the phase errors induced by subject motion in DWI. Because in single-shot imaging motion-induced phase errors are much less harmful than in sequences with multiple excitation, the algorithm shall only briefly discussed here. For a more detailed explanation the reader may refer to [195]. In the context of isotropic diffusion weighting attempts have been made to ensure that the first temporal moment of $\mathbf{G}(t)$ vanishes,

$$\int_0^t t' \mathbf{G}(t') dt' = 0 \quad (5.38)$$

where $\mathbf{G}(t)$ is identical with $\nabla B_z(t)$ apart from a sign change at every refocusing pulse. If this condition is satisfied, the susceptibility to uniform bulk motion is minimized [50]. Equation

¹⁴below $0.1 \cdot 10^{-9} \text{m}^2 \text{s}^{-1}$

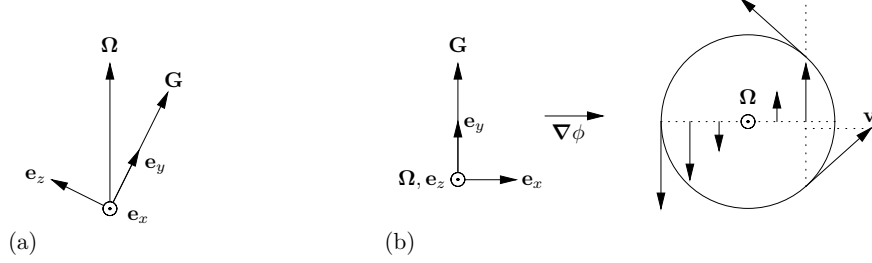


Figure 5.10: Rigid-body object rotation during a diffusion experiment: (a) Choice of basis for equation (5.41); (b) illustration of $\mathbf{v} \cdot \mathbf{G} \sim x$ (axis of rotation perpendicular to the diffusion gradient, for simplicity).

(5.38) does not hold for the Stejskal-Tanner gradient sequence.¹⁵ A translational displacement of the whole object between the diffusion gradient pulses in a Stejskal-Tanner experiment causes a global phase shift for all excited spins in the object. In the case of rotational motion, however, the phase error depends on the spin position: Suppose that the object's position in space differs between the two gradient pulses by a rotation. We approximate the pulses as rectangular. To a good approximation we can assume that the angular velocity is small enough that the velocity change of an individual spin during the short time Δ is negligible,

$$\mathbf{v}(\mathbf{r}(t)) \approx \mathbf{v}(\mathbf{r}_0) \quad (5.39)$$

with $\mathbf{r}_0 = \mathbf{r}(0)$. If we describe the rotation by the vector of angular velocity, $\mathbf{\Omega}$, the velocity is given by $\mathbf{v}(\mathbf{r}) = \mathbf{\Omega} \times \mathbf{r}$ such that the phase error accumulated by a spin initially at \mathbf{r}_0 is

$$\phi(\mathbf{r}_0) = \gamma \int_0^{\Delta+\delta} \int_0^t \mathbf{v}(\mathbf{r}(t')) dt' \cdot \mathbf{G}(t) dt \approx \gamma \int_0^{\Delta+\delta} t \mathbf{v}(\mathbf{r}_0) \cdot \mathbf{G}(t) dt = \gamma \mathbf{v}(\mathbf{r}_0) \cdot \mathbf{G} \Delta\delta = \gamma \delta \Delta [\mathbf{\Omega} \times \mathbf{r}_0] \cdot \mathbf{G} \quad (5.40)$$

where $\mathbf{G}(t) = \mathbf{G}(-1)^{\Theta(TE/2-t)}$ with $\Theta(t)$ defined as in (3.8) and $\mathbf{G} = \nabla B_z(t)$. By choosing an orthonormal basis whose y axis is aligned with the gradient direction and whose x axis is perpendicular to \mathbf{G} and $\mathbf{\Omega}$ (see Fig. 5.10a) we can write equation (5.40) as

$$\phi(\mathbf{r}) = \gamma \delta \Delta [(c\mathbf{e}_y + d\mathbf{e}_z) \times (x\mathbf{e}_x + y\mathbf{e}_y + z\mathbf{e}_z)] \cdot \mathbf{e}_y \mathbf{G} = x\gamma \delta \Delta G d \quad (5.41)$$

with $c, d \in \mathbb{R}$ and $\mathbf{r} = (x, y, z)$. This means that the phase of the signal contribution of a spin is proportional to its x coordinate and independent of y and z . In other words, $\nabla\phi$ is perpendicular to both \mathbf{G} and $\mathbf{\Omega}$. The situation is illustrated in Fig. 5.10b for the case that diffusion gradient and axis of rotation are orthogonal. Hence, if the image slice happens to be parallel to the xy plane, the reconstructed image is modified according to

$$S(x, y) \mapsto S(x, y) \exp(ix\gamma \delta \Delta G d). \quad (5.42)$$

¹⁵We will neglect the imaging gradients in the context of this section as they are of low amplitude compared to the diffusion-sensitizing gradient pulses. Note that (5.38) is also not valid for the double spin-echo scheme in Fig. 5.5.

		G		
		\rightarrow	\uparrow	\odot
Ω	\rightarrow	0	\otimes	\uparrow
	\uparrow	\odot	0	\leftarrow
	\odot	\downarrow	\rightarrow	0

Table 5.5: Components of $\nabla\phi$ arising from the components of \mathbf{G} and $\mathbf{\Omega}$ in readout (\rightarrow), phase encode (\uparrow), and slice select (\odot) direction. Slice-select components (\odot, \otimes) of $\nabla\phi$ cause only a constant phase shift.

To account for arbitrary slice orientations, we can express $\mathbf{\Omega}$ and \mathbf{G} in equation (5.40) in components parallel to the readout, phase encode, and slice selection gradient, and calculate the corresponding components of $\nabla\phi$ in this coordinate system. An overview of the resulting components of the phase error gradient is shown in Table 5.5. The component of $\nabla\phi$ which is parallel to the slice selection gradient produces only a uniform phase shift, and an echo attenuation due to intravoxel dephasing which is negligible if the slice thickness, as usual, is sufficiently small. We therefore only have to deal with the in-plane components of $\nabla\phi$. It is due to a property of the Fourier transform [67, p. 104] that a phase ramp in image space as in equation (5.42) effectively causes a shift in the raw data in the corresponding direction (and vice versa, *cf.* p. 27). The shift is proportional to the slope of the phase ramp.

Images from diffusion weighted sequences that sample k space with multiple excitations are prone to severe motion artefacts due to spatially constant (translation) or linear (rotation) phase errors since the subject motion usually is not identical for different excitations such that the phase errors interfere with the applied phase encoding.

In single-shot imaging rotation causes all data in k space to be shifted by the same amount such that after the Fourier transform of the raw data we obtain an image that is modified by a phase ramp as in (5.42). In the case of translation it is multiplied by a constant phase factor $\exp(i\phi)$. The commonly displayed magnitude images are insensitive to these phase variations. However, the phase encode component of the k-space shift caused by rotational motion can nevertheless affect the image quality. To understand the mechanism we realize that the Fourier transform of the proton density distribution typically is highly localized at $\mathbf{k} = 0$. This means that the echo with $\int G(t)_{\text{ph}} dt = 0$ will produce the largest signal. If the signal distribution in k space is shifted, the acquired echoes pertain to other k_{ph} values than intended. As the gradient sequence has not changed, this is, according to (2.73), equivalent to a temporal shift. In centre-out phase encoding for example the echo with $k = 0$ is therefore not necessarily the first echo any more, but it might be the second echo (or possibly for none of the echoes k_{ph} is exactly zero). However, the signal amplitude modulation due to relaxation is unchanged if expressed as a function of time. Hence the weighting of positions in k space is modified by rotational motion in the presence of diffusion weighting. The change depends on the selected phase encoding scheme, with centre-out phase encoding being more sensitive to this effect than the linear scheme where the slope of signal decay has largely decreased by the time of the 0th phase encoding step. It has two consequences. The first is a modification of the point spread function which can be considerable for linear phase encoding if the first acquired k-space line is near $k_{\text{ph}} = 0$ and the lines are cyclically reordered [165]: in this case a negative k_{ph} shift can move the echo with $k_{\text{ph}} = 0$ to the very end of the echo train. This would introduce a sharp edge in the signal distribution $S(k_{\text{ph}})$ and hence degrade the PSF.

The second consequence is a mere loss in signal intensity which will influence the ADC (or tensor) measurement. Provided that subject motion is more or less random¹⁶, both problems can be reduced by averaging, which is performed anyway for DTI. Averaging must be carried out on the reconstructed magnitude images to avoid destructive interference between images. The effectiveness, however, of such averaging will also depend on the phase encoding scheme: for linear phase encoding the phase errors induced by random rotations will be centred about zero whereas for centre-out phase encoding the signal is always decreased by rotation. However, the error is small: The rotation angles in an *in vivo* diffusion experiment have been reported [195] to be of the order of $\alpha = 0.5 \cdot 10^{-4}$ ($\Delta = 50$ ms, $\delta = 40$ ms). With $|\mathbf{\Omega}| = d = \alpha/\Delta$ and $G = 30 \text{ mT m}^{-1}$ we calculate from (5.41) that $\partial\phi/\partial y = 16 \text{ m}^{-1}$. We compare this value to the deliberately applied phase difference between successive phase encoding steps which we know from (2.76) to be

$$\phi_{\text{inc}}(y) = \gamma G_{y,\text{inc}} \tau y = \frac{2\pi}{\text{FOV}} y, \quad (5.43)$$

where τ is the phase encoding gradient duration, which implies $d\phi_{\text{inc}}/dy \approx 25.1 \text{ m}^{-1}$ for $\text{FOV} = 25 \text{ cm}$. Since the k-space shift will hence be of the order of one k-space line the consequences of rotational motion in single-shot sequences are very small. Compared to phase errors induced by eddy currents (see section 5.6) (which cannot be reduced by averaging) they are negligible.

As proposed by Ordidge *et al.* [194] motion artefacts in diffusion-weighted multiple-excitation imaging can be suppressed by a phase correction algorithm that uses the phase information contained in an additional “navigator echo” that is acquired without phase encoding. After a one-dimensional Fourier transformation with respect to the readout coordinate, k_{re} , of the navigator echo and the raw data acquired after the same excitation the navigator phases are subtracted¹⁷ from the raw data phase values [194, 195]. If the diffusion gradient is parallel to the phase encode direction each data point in the echo profiles contains the signal contributions of a single object column the spins in which share the phase error ϕ . In this case the phase error introduced by rotation is successfully removed. The phase correction cannot remove the artefacts induced by rotation (about an arbitrary axis) if the diffusion gradient has components in readout or slice-select direction since in this case the phase error gradient can have components in phase encode direction (see Table 5.5) [195]. This restriction to the direction of the diffusion gradient is bound to be violated in diffusion tensor imaging where diffusion gradients in different directions need to be applied. To address this complication, attempts have been made to measure both read and phase encode component of the k space shift by means of two navigator echoes with orthogonal readout direction [196, 185], or with a navigator echo with spiral [197, 126] or circular [198] k-space trajectory.

It shall finally be noted that there are other approaches to motion correction for diffusion weighted images than navigation [199]. An overview of motion correction techniques can be found in [200].

¹⁶This is certainly not the case for physiological brain motion induced by the cardiac cycle. However, the role of this type of motion can be neglected because cardiac triggering did not have a noticeable effect on the fibre orientation maps. Pulsatile motion in CSF represents an exception (see section 5.9).

¹⁷or added to (if navigator and image echo are separated by a refocusing RF pulse)

5.9 Flow

In fibre orientation maps of axial brain slices the diffusion in the lateral ventricles often appears anisotropic with the direction of the largest diffusion coefficient being the subject's anterior-posterior direction (see Figs. A.1 and A.6). In some pixels of the lateral ventricles the fractional anisotropy is comparable to that in the splenium of the corpus callosum. Such behaviour can be caused by CSF flow. A distribution of flow velocity components parallel to the diffusion gradient within a voxel leads to intravoxel dephasing and thereby to signal attenuation that depends on the strength of the diffusion gradient. A preferential flow direction would thus appear as anisotropic diffusion.

Anisotropic-appearing diffusion in CSF has been reported in the literature [184], and in fact CSF is known to be subjected to pulsatile motion. In addition, there is a slow net flow of CSF through the system of CSF-filled spaces since CSF is produced mainly in the plexus choroidei, a part of which covers the inner walls of the C-shaped lateral ventricles. The only outlet of the lateral ventricles is the foramen interventriculare Monroi¹⁸ which is situated inferior and anterior to the ventricles' top parts that are visible in Figs. A.1 and A.6. A preference of CSF flow in anterior-posterior direction therefore appears to be plausible. The presence of flow in the lateral ventricles is also noticeable from signal extinctions in the raw images. The extinctions are in part caused by the high flow sensitivity of the U-FLARE sequence [161]. If we assume 1 cm diameter of the lateral ventricle cross section, and given that 500 ml CSF per day are produced [128, p. 225] we calculate as an estimate of the net flow velocity $v = 37 \mu\text{m s}^{-1}$ which corresponds to a displacement of about $1.5 \mu\text{m}$ in 40 ms. Although this is much less than the typical diffusion displacement (at $D = 2 \cdot 10^{-9} \text{m}^2 \text{s}^{-1}$) in the same time which is about $20 \mu\text{m}$, an influence on the measurement of the diffusion tensor may indeed be possible: Since CSF motion is pulsatile and the velocity dispersion is unknown this is only a very rough estimate. Flow velocities between 4 and 6 cm s^{-1} are given in the literature for the narrowest point in the ventricular system¹⁹ [201].

Unfortunately the erroneous diffusion tensor measured in CSF can also influence the measurement in white matter voxels in close proximity to the lateral ventricles. Because the lateral ventricle walls are in general not perpendicular to the slice plane a number of the cubic voxels in the image slice contains both CSF and white matter (partial volume effect). The problem is more pronounced for large voxel sizes. It is aggravated by the large diffusivity (and flow rates) in CSF compared to WM. Due to the partial volume effect the anterior-posterior anisotropy of CSF can completely blot out the prominent left-right fibre direction in the corpus callosum. Partial volume contributions of CSF to the voxel volume are hardly visible in T_1 weighted images since CSF does almost not contribute to the signal in these images. At the brain surface, partial volume contributions to cortical GM voxels are also inevitable. This complication makes the investigation of diffusion anisotropy in cortical tissue difficult. Although the flow problem is less severe in the outer CSF spaces, contributions of WM or flowing CSF can introduce anisotropy that cannot be distinguished from genuine GM anisotropy. CSF suppression is possible [202] but leads to a reduced signal-to-noise ratio.

¹⁸connection between lateral ventricles and the third ventricle

¹⁹which is the aquaeduct of Sylvius, *i.e.* the connection between third and fourth ventricle

5.10 Different fibre directions in a volume element

The measured diffusion tensor describes the average behaviour of the water molecules in a voxel. Since a voxel does not necessarily have a homogeneous microstructure the diffusion anisotropy measured in DTI experiments can depend on the voxel size [103]: voxels that are crossed by many fibres of random direction exhibit isotropic diffusion on a macroscopic scale. The smaller the voxel size the less the diffusion anisotropy is reduced by averaging. Since in an imaging experiment the slice thickness is usually larger than the in-plane resolution averaging over fibres is more significant in the slice direction. This only has an effect if different fibre directions are present in the voxel. However, this mechanism does not favour any direction. Consider a volume of randomly oriented axon segments and assume high in-plane resolution and a very large slice thickness. A variation of the axon direction along the slice selection gradient will not be resolved and diffusion will appear isotropic although different directions are present in the voxel. If on the other hand the axonal direction varies along an in-plane direction, it will be resolved and anisotropic tensors with different principal directions will be measured at the different in-plane locations. However, in-plane and through-plane components will be treated exactly the same way such that no bias in the principal directions occurs. In a volume with randomly oriented axon directions the diffusion tensor will still be isotropic.

The averaging property of DTI can significantly reduce diffusion anisotropy in voxels at the crossing of two fibres. An example is shown in Fig. A.5. If the fibres are perpendicular to each other, if they contain an equal number of axons and intersperse each other homogeneously in the voxel at the crossing, then the measured diffusion tensor in this voxel should be represented by an oblate spheroid (see section 2.2.8). However, the situation may occur where the self-diffusion process in such a voxel cannot be described by the propagator in equation (2.94). This is for example the case if the water molecules in the voxel reside in two different compartments, each characterized by a propagator of the form in equation (2.94) but with different principal directions of \mathbf{D} . The diffusion coefficient along a direction $\check{\mathbf{p}}$, defined by $\langle (\mathbf{s}(t) \cdot \check{\mathbf{p}})^2 \rangle / (2t)$ as in equation (2.121), can then not be described by means of a symmetric tensor. The surface of constant relative concentration (of labelled molecules) that was introduced in section 2.2.8 is not an ellipsoid. This was shown by Tuch *et al.* [203, 204] measuring the dependence of the diffusion coefficient on the diffusion gradient direction with high angular resolution.

In the presence of fast exchange between the compartments in the voxel, diffusion can still be described with an average tensor. In this case a fibre crossing may be detected by assessment of the eigenvector direction corresponding to the minimum eigenvalue which is also shown in Fig. A.5b. The arrow indicates the region where the fibre originating from the precentral gyrus diverges. Here the anisotropy is reduced and the minimum-eigenvalue direction is almost perpendicular to the imaging plane. To decide whether or not the tensor description is appropriate in this voxel would require measurements with a high number of diffusion gradient directions, as performed by Tuch *et al.* [204].

Another interesting observation can be made in Fig. A.5b: In the precentral gyrus in the top left corner of Fig. A.5b both the eigenvector directions corresponding with the largest and those for the smallest eigenvalue lie in the imaging plane. The latter directions point to the sulcal walls. Assuming that the gyrus is perpendicular to the image plane this means that the fibres in the gyrus spread out less in the directions towards the sulcal walls than in the perpendicular direction.

5.11 Conclusion

In the current chapter possible sources of error in the NMR measurement of the diffusion tensor have been discussed. Experiments on an isotropic sample have been performed to assess the eddy current sensitivity of diffusion weighted U-FLARE and EPI. For EPI the performance of a modified diffusion weighting sequence and of an eddy current correction algorithm have been investigated. The results can be summarized as follows:

- With extensive averaging (or high image SNR) high-quality tensor maps can be achieved that reliably measure the fibre anatomy in human brain white matter.
- The influence of concomitant field gradients and the effects of nonorthogonal or not constant applied field gradients are negligible. Background gradients are also not significant for applications to head imaging. Gradient miscalibration is potentially harmful but the required degree of calibration accuracy is not significantly higher than for conventional imaging purposes.
- DTI is probably not an appropriate tool for measuring the orthogonality of the applied gradients.
- Subject motion is not a fundamental problem as long as single-shot imaging sequences are applied.
- Pulsatile flow of cerebrospinal fluid can introduce anisotropy in the measured apparent diffusion tensor. It occurs in particular in the lateral ventricles but was not observable in exterior CSF in vicinity to the cortex. Measurement distortions through partial volume contribution occur only at about one volume element distance to the lateral ventricles.
- The most important source of systematic error is the presence of eddy currents caused by switching strong pulsed field gradients to achieve diffusion weighting. As eddy current amplitude and distribution differ significantly between the applied gradient directions, this often leads to artefactual anisotropy in the measured diffusion tensor. Therefore, a well-adjusted preemphasis unit is a prerequisite for accurate diffusion tensor measurements. This can, however, not completely eliminate the eddy current related inaccuracies. The most important effects are disturbances of the phase-encoding mechanism, *i.e.* ghosting and spatial signal variations in the image. They often depend on the direction of the applied diffusion gradient. The shift, shear, and scale artefacts caused by eddy currents in diffusion weighted EPI images are predominantly relevant at tissue borders, and can be corrected for by image postprocessing.
- For an assessment of tissue structure in white matter on the basis of DTI it has to be borne in mind that the measured tensor is an average over a finite volume element. Tensors with low anisotropy can occur at crossings of white matter fibre tracts despite a high degree of tissue organization.

Since EPI is characterized by high SNR and short acquisition times as compared to U-FLARE it is usually preferred in DTI experiments. However, despite its lower SNR and the eddy current induced signal intensity variations in the imaging slice that occur with U-FLARE, it can in some circumstances be advantageous to use U-FLARE instead of EPI for diffusion tensor imaging. This is the case if EPI can (due to insufficient gradient performance or high main field

strength) only provide low spatial resolution. While diffusion anisotropy can often be assessed with sufficient accuracy using a coarse resolution this is not true for WM fibre imaging where the highest possible spatial resolution should always be applied. With the given equipment, the best assessment of fibre directions was obtained with the TIPE U-FLARE protocol described in chapter 4. It allows a reliable measurement not only of large commissural fibre trajectories but also of less coherent fibre tracts in subcortical white matter.

Chapter 6

Investigating the connectivity hypothesis

It has often been maintained that DTI can serve as a tool to investigate the functional connectivity of cortical areas [13, 205, 206]. DTI has been employed to identify the human sensory motor cortex through detection of the afferent fibres [207]. However, it has never been demonstrated that a strong fibre connection between cortical areas implies a close functional connection. This chapter describes experiments that are designed to image fibre orientation in human brain white matter with water diffusion tensor measurements, and to explore the use of such experiments for the investigation of functional connectivity in the human brain.

6.1 Introduction

6.1.1 Definition of functional connectivity

Functional connectivity has been defined as

“the observed temporal correlation between two electro/neurophysiological measurements from different parts of the brain” (*Friston et al.* [208]).

Functional connectivity is often considered as a measure of how closely two parts of the brain are functionally related.

6.1.2 Functional magnetic resonance imaging

Methods to observe the physiological function of organs by means of MRI are subsumed under the term functional magnetic resonance imaging (fMRI). Since MRI has become an important tool to investigate human brain function, fMRI is often used as a synonym for functional MRI of the brain. A more detailed discussion of the techniques can be found in the literature [5]. We confine ourselves to the description of the basic principle.

Although an activation-dependent shrinkage of the extracellular space has been observed by means of ADC measurements [209, 210], using diffusion measurements to detect neuronal activation appear difficult and have not been published yet. However, the signal intensity in T_2^* weighted *in vivo* MR images of human brain grey matter has been shown to increase upon activation of the brain region by an external stimulus. The phenomenon is based on haemodynamic effects. It has been known since 1936 that oxyhaemoglobin (oxyHb) and deoxyhaemoglobin

(deoxyHb) have different magnetic properties [211]. The iron atom in a deoxyhaemoglobin molecule represents a paramagnetic centre due to unpaired electrons. It is the binding site for oxygen molecules. By establishing the bond to an oxygen molecule the iron atom achieves noble gas configuration: since the iron in oxyHb has no unpaired electrons it is diamagnetic. The magnetic field around erythrocytes that contain a high concentration of paramagnetic deoxyHb is distorted such that T_2^* is shortened in the environment.

If in a localized population of neurons in the brain the frequency of generated action potentials is increased, local increases in blood flow¹ and fractional blood volume are induced in the brain tissue. The neuronal oxygen consumption in the activated state differs only little from the consumption at rest: the increase in blood flow overcompensates the increase in oxygen consumption (“luxury perfusion”). Consequently the deoxyHb concentration in venous blood is decreased. The decrease in deoxyHb concentration reduces the magnetic field inhomogeneity and thereby leads to an increase in the detectable MR signal. This influence on the intensity in T_2^* weighted images has been termed BOLD (blood oxygenation level dependent) contrast.² It provides a means to detect the activity of a localized population of neurons in the brain [3, 5]. In a standard fMRI experiment, T_2^* weighted images are acquired during alternating periods of stimulus and rest condition (blocked task paradigm). The brain regions that are activated by the stimulus can be identified as those regions whose signal time course correlates with a square wave describing the stimulus on and off periods. The reader may refer to [4, 5] for an introduction to BOLD based fMRI.

6.1.3 Biswal’s experiment

Biswal *et al.* [212] found in BOLD contrast images of “resting” human brain that the low-frequency signal fluctuations from the right and left human motor cortex were correlated. The experiment consisted of two parts. In the first part several time series of 512 T_2^* weighted echo planar images were acquired. The repetition time was varied between 250 and 1000 ms. The volunteers had been instructed to “refrain from any cognitive, language, or motor tasks as much as possible”. In the second part the subjects had to perform a bilateral motor task. They were instructed to sequentially tap each of their fingers to the thumb at an arbitrary rate. Finger tapping and rest condition alternated every 20 s. By means of echo planar images acquired during this period the motor cortex could be identified using correlation of the MR signal with a square wave of 20 s cycle duration. The signal time courses for all pixels in the images from the first, resting-state experiment were frequency filtered (low-pass with 0.08 Hz cut-off frequency) to remove the frequency components that are due to the respiratory and cardiac cycle. The filtered time courses for all possible pairs of pixels were correlated. If we divide the set of pixels into three sets R, L, and O that refer to the right motor cortex, the left motor cortex, and the rest of the brain, respectively, we can summarize Biswal’s results as

$$\frac{\bar{n}_{LL}}{n_L} > \frac{\bar{n}_{RR}}{n_R} > \frac{\bar{n}_{LR}}{n_L} \gg \frac{(\bar{n}_{OL} + \bar{n}_{OR})}{n_O} \quad (6.1)$$

¹Regional cerebral blood flow (rCBF) is defined as the volume of blood that passes through a given volume of tissue (specified in terms of mass) per unit time. It is commonly measured in the units $\text{ml g}^{-1} \text{min}^{-1}$. The mechanism that couples the haemodynamic changes and neuronal activity is unknown.

²Due to diffusion of water in the presence of magnetic field inhomogeneities there is also an effect on T_2 .

where \bar{n}_{LR} is the average number of pixels in L that correlate with a pixel in R,

$$\bar{n}_{LR} = \frac{1}{n_R} \sum_{y \in R} |\{x \in L \mid c(x, y) > 0.35\}|, \quad (6.2)$$

with n_R being the number of pixels in R, and $c(x, y)$ the correlation coefficient between the time courses in the pixels x and y . The remaining symbols are defined in analogous manner. In words, the normalized number of correlations between left (L) and right (R) motor cortex was higher than the normalized number of correlations between L (or R) and the rest of the brain. Thus the signal fluctuations in the left and right motor cortex are not independent. The differences between the first three terms in the relations (6.1) were not significant for a given subject. The overall result did not depend on the repetition time in the range between 250 and 1000 ms.

A more recent study [213] confirmed the interhemispheric correlation in the motor cortex and reported similar phenomena for the left and right primary visual cortices and the amygdalae.

6.1.4 Interpretation of Biswal's results

The trivial arguments aside (bulk motion, imperfect removal of cardiac and respiratory influences) there are two possible explanations for correlated signal fluctuations in left and right primary motor cortex:

1. The brain performs unknown tasks that change over time. Many tasks that require the left primary motor cortex also activate the right primary motor cortex.
2. Fluctuating action potentials spread along anatomical connections. They represent spontaneous activity that is not task-induced.

An example of the first possibility would be that a subject imagines finger tapping at some time during the scan. Biswal *et al.* interpreted the synchronous low-frequency fluctuations as a phenomenon that was not due to imagined motion ("motor imagery"). To rule out possible influences of motor task imagination the subjects had not been informed before the experiment that they would be asked to perform a motor task. Some volunteers were deliberately misled by the information that the experiment would measure the response to an auditory stimulus. In addition to these precautions the authors argue that, according to previous studies, imagined motor tasks elicit a haemodynamic response in the supplementary motor area (SMA) but not in the primary motor area.³

Biswal *et al.* consider the haemodynamic fluctuations that underly the correlation of the T_2^* weighted signals to be the same phenomenon as fluctuations of local cerebral blood flow observed by Golanov *et al.* in anaesthetized rats [215]. Golanov *et al.* observed spontaneous bursts of electrocortical activity that were followed by an increase in cerebral blood flow. Spontaneous electrical activity of neurons is common in the human vestibular and auditory systems and in the higher cognitive centres associated with them [129, p. 281]. However, to date it has not been shown that the correlated haemodynamic fluctuations observed by Biswal *et al.* are indeed due to this type of electrical activity.

³However, some imagery induced activation has also been found in primary motor cortex, see [214].

It is known that, apart from hand and foot area, all parts of the primary motor cortex send commissural fibres to the homotopic⁴ area in the contralateral hemisphere [18, p. 374]. The observed correlation is a manifestation of an increased conditional probability that a neuron in a region ‘A’ fires provided that a neuron in some other region ‘B’ has fired immediately before. This coincidence can be due to a direct influence mediated by an anatomical link between the regions. (The fact that the hand areas give rise to relatively few commissural fibres may be used as an objection against this interpretation of Biswal’s experiment.)

If we adopt the second of the two explanations above we can hypothesize that any random activity in the left motor area gives rise to activity in the right motor area since they are directly connected by axons in the corpus callosum. It might therefore be possible to infer from a correlation in BOLD signal fluctuations to a direct anatomical connection. If, however, the first explanation were true this inference would not be possible. It is well known that in a network of interconnected cortical areas the activation of one network element does not necessarily imply that the rest of the network is also activated.⁵ Whether a network element is activated strongly depends on the task. Cortical activation does not spread over all available physical connections but the physical connections are selectively used. This is the reason why a measurement of task-induced activation will not supply information about the fibre connections between two cortical regions. As diffusion tensor imaging reveals information on the fibre tracts that connect cortical areas it has been postulated that it is possible to use DTI as a tool to investigate functional connectivity. However, it remains to be shown whether predictions on the outcome of a functional connectivity experiment can be made on the basis of anatomical data obtained from a DTI experiment. If the correlations are a result of a strong neuronal connection then two regions that appear in DTI fibre maps to be strongly connected in an anatomical sense should also exhibit a high correlation of signal fluctuations.

6.1.5 The connectivity hypothesis

If the correlation in Biswal’s experiment is a consequence of the large number of axons that directly connect left and right motor cortex and if DTI is able to detect such fibre tracts then the following hypothesis should be true:

If a DTI fibre orientation map shows a thick and highly ordered fibre connecting two cortical areas ‘A’ and ‘B’ then the T_2^* weighted signal time courses for ‘A’ and ‘B’ under resting conditions will be highly correlated.

This hypothesis was investigated by simultaneous assessment of anatomical connections in diffusion tensor maps and the correlation of BOLD signal fluctuations between brain regions.

6.2 Measurement of functional connectivity

In order to investigate whether the connectivity hypothesis is true we measured for 7 normal healthy subjects the anatomical and functional connectivity of areas on adjacent cortical gyri. For fluctuation imaging we used a stimulus-free setup similar to that of Biswal’s experiment.

⁴Two cortical regions in different hemispheres are called homotopic if they service the same part (strict sense) or symmetric parts (broader sense) of the body [18]. This definition is not applicable to cortical regions that mediate higher functions.

⁵See, for example, [2, p. 17].

In contrast to Biswal *et al.* [212] we examined the correlation between cortical gyri rather than between symmetric areas in the hemispheres. We did not perform a stimulus-induced activation experiment to identify the function of cortical regions.

6.2.1 Experimental

A time series of 1024 gradient-recalled blipped EPI images was acquired for a single 5-mm axial slice (64×64 matrix, 3 mm in-plane resolution, $TR = 250$ ms, $TE = 30$ ms). To maximize SNR, the excitation pulse angle was set to the Ernst angle⁶ which was 36° . The read direction was the subject's left-right axis. The subjects were instructed to refrain from any voluntary movement during the 4 min scan time. Instructions like "think nothing" are not well defined, nor can they be controlled in any way, so we decided not to further specify the rest condition by any additional instruction. The lights were switched off so that apart from the noise produced by the scanner, acoustic and optical stimuli were absent.

6.2.2 Data Processing

A realignment algorithm was applied to the reconstructed images to remove bulk subject motion. Ripple artefacts in the images were reduced by Gaussian filtering with a standard deviation of 0.5 pixels [166, section 4.1.3.1]. The signal time courses of all image pixels above a noise threshold were digitally low-pass (< 0.08 Hz) frequency filtered to remove signal fluctuations due to the respiratory and cardiac cycle. The first 10 images were not in steady-state and therefore discarded. Linear Pearson correlation coefficients [216] between time courses were calculated for all possible pairs of pixels. In order to emphasize ubiquitous fluctuations that arise from spontaneous neuronal activity as opposed to those of limited duration due to brain function each time course was split in four equal parts of about 1 min duration. For each part the correlation coefficient between pixels was determined separately, and among the four coefficients the smallest one was selected for further processing. We expect to suppress any "real task activation" to a certain degree by this procedure. The Pearson (or product moment) correlation coefficient, c_f , of the time courses (x_i) and (y_i) , $i = 1, \dots, n$, of n data points is defined by [216]

$$c_f = \frac{\sum (x_i - \bar{x})(y_i - \bar{y})}{\sqrt{\sum (x_i - \bar{x})^2 \sum (y_i - \bar{y})^2}} = \frac{\sum x_i y_i - (\sum x_i y_i)/n}{\sqrt{(\sum x_i^2 - (\sum x_i)^2/n) (\sum y_i^2 - (\sum y_i)^2/n)}} \quad (6.3)$$

where the bar denotes the mean over the time course. All sums run over $i = 1, \dots, n$. To keep the calculation time low, pixels with a signal below approx. 10% of the maximum in the image were excluded from further processing.

6.3 Measurement of anatomical connectivity

Subsequent to the EPI scans, diffusion tensor imaging was performed for the same slice as in the functional experiment in order to determine the anatomical connections between cortical areas. The study focussed on the detection of fibres between regions of the cerebral cortex that

⁶The optimum excitation angle can be found by maximizing the transverse magnetization immediately after excitation which is obtained by multiplying equation (2.77) by $\sin \theta$ [36, p. 66]. T_1 was estimated to be 1.2 s.

were not more than a few centimeters apart from each other. This restriction was necessary since long fibre tracts are more difficult to follow and are usually not confined to a single plane. A long fibre will often merge with other fibres on its way and will split into diverging subfibres at other locations. Non-planar fibres can in principle be detected using a three-dimensional DTI protocol. However, due to the sensitivity of multiple-shot diffusion measurements to bulk motion (see section 5.8) the application of the available imaging methods to 3D imaging would have required the implementation of a complex navigation correction so that two-dimensional FT imaging was preferred. Fibre bundles that interconnect cortical areas are called association fibres. Short association fibres lie within the cortex, or in the superficial white matter whereas long association fibres lie in the deeper layers of white matter. Many adjacent cortical gyri are connected by short association fibres in the superficial white matter. Due to their shape these fibres are often called “U fibres” [217, 218]. Although in the DTI literature the term “U fibre” is often applied to fibre bundles visible on DTI fibre orientation maps, U fibres in a strict sense are far too thin to be visible at a typical DTI resolution. However, the U-shaped fibres that are encountered in DTI maps may nevertheless connect two adjacent gyri. But it has to be kept in mind that even if the mean fibre direction in subcortical white matter is tangential to the sulcal cortex between two gyral crowns the axons that enter grey matter in the two crowns may be not identical. The axons originating from a crown may leave the “fibre” on its way to the other crown, being replaced by other axons entering the bundle. If this axon exchange is distributed over the length of the bundle it is invisible in the DTI map and the pattern still appears as a continuous U-shaped fibre on the macroscopic scale.

Short association fibres connect the precentral with the postcentral gyrus, the precentral gyrus with the premotor area, and the postcentral gyrus with parts of the parietal lobe [18].

6.3.1 Experimental

A DTI sequence was required that is sensitive enough to image not only highly aligned commissural fibres but also less coherent association fibres with high spatial resolution. With the diffusion weighted EPI sequence it was not possible to improve the in-plane resolution beyond $3 \times 3 \text{ mm}^2$. In order to achieve a resolution that allows reliable detection of U-shaped fibres we used the displaced U-FLARE tensor imaging sequence with Stejskal-Tanner type spin-echo magnetization preparation and half k-space TIPE phase encoding (see p. 63. refocusing angle $\alpha \approx 120^\circ$, $TE \approx 7.5 \text{ ms}$, $TE_{\text{eff}} \approx 140 \text{ ms}$, echo train length $\approx 410 \text{ ms}$, $TR = 3 \text{ s}$). High resolution increases the anisotropy in a voxel (see section 5.10). In addition, it is essential for the distinction between a U-shaped fibre and a pattern of three fibres, two of which run from the crowns into deep white matter and are crossed by a third straight long-distance fibre that passes the sulcus between the gyri. Half k-space phase encoding was applied to increase the resolution without impairment of the SNR. To save the time required for dummy refocusing cycles, TIPE [168] phase encoding was employed. Diffusion weighting was varied using 4 different gradient amplitudes (b value between 20 and 800 s mm^{-2} , $\Delta = 40 \text{ ms}$, $\delta = 22 \text{ ms}$) and 7 directions of the diffusion gradient. The readout direction was the subject’s anterior-posterior axis. The acquisition of the tensor map involved 15 to 50 averages (depending on the b value) and took approx. 35 min, yielding an in-plane resolution of 1.5 mm (full data matrix 128×96 , FOV $19.2 \text{ cm} \times 14.4 \text{ cm}$, slice thickness 5 mm).⁷ Since proper k-space completion did not significantly change the resulting fibre orientation maps compared to simple zero filling the

⁷The 128×96 matrix for the FOV $19.2 \text{ cm} \times 14.4 \text{ cm}$ provides the same resolution as a 128×128 matrix for a FOV $19.2 \text{ cm} \times 19.2 \text{ cm}$ which was the FOV used in the functional experiment.

acquired data were zero filled to the 128×96 matrix before Fourier reconstruction. This somewhat reduced the true resolution in phase-encode direction. Due to the high power deposition in the U-FLARE sequence the acquisition of more than a single slice would have required a considerably longer scan time, or less repetitions per b value. A high quality tensor map of a single slice was preferred to multiple slice imaging with lower effect-to-noise ratio. The images were transformed to the 128×128 format covering $19.2 \text{ cm} \times 19.2 \text{ cm}$ FOV by symmetric addition of zero lines. An example of a fibre orientation map calculated from the acquired data is shown in Fig. A.6. If the image slice is not parallel to the plane in which a single U-shaped fibre is contained (this plane will in general be perpendicular to the sulcus axis) the crowns that appear in the image at both sides of the sulcus may in fact be not connected by a fibre although the fibre orientation map may indicate that. The only indication for such a situation would be that the through-plane component of the eigenvector direction corresponding to the largest tensor eigenvalue is not zero. In this case a U-shaped fibre originating from a neuron within the slice can end on the other side of the sulcus in a region that is not contained in the slice. The slice thickness of 5 mm however should ensure that this situation occurs only for a small number of neurons contained in the superficial layer of the imaging slice, and if the angle between the sulcus axis and the normal vector to the slice plane is large.

6.3.2 Quantification of fibre connections in DTI maps

A comparison of functional and anatomical connectivity requires a quantitative measure of anatomical connectivity. It is possible to extract the trajectories of individual fibre tracts from a DTI tensor map employing a fibre tracking algorithm [14, 219, 220]. However, these algorithms usually generate a trajectory by following the direction corresponding to the largest eigenvalue of the diffusion tensors. This approach does not use the full information contained in the tensor. It is independent of the ratio of eigenvalues that reflects the average over many axons with different directions in a voxel. For the assessment of anatomical connectivity between arbitrary regions an algorithm is needed that differentiates between trajectories in highly aligned bundles and paths through almost isotropic matter. In order to find a numerical measure meeting this requirement, a Monte-Carlo type algorithm was implemented. Imagine a particle in one of the voxels of a cortical region ‘A’ that jumps in a random manner from voxel to voxel. It will perform a random walk through the set of voxels. Let us further make the probability of a jump to a neighbouring voxel dependent on the diffusion tensor in the current (and in the neighbouring) voxel, such that the probability is higher the larger the diffusion coefficient in the jump direction. Then our particle will move with a higher probability along a fibre direction than perpendicular to it. If we perform this “experiment” many times and count how often our particle starting in a region ‘A’ has reached region ‘B’, we obtain a (relative) measure of the anatomical connectivity between regions ‘A’ and ‘B’. We repeated a 60-step “experiment” 4000 times. For each elementary jump the probabilities for the eight possible jump directions to a neighbouring voxel (the particle motion was confined to the imaging slice) were calculated from the diffusion tensors in the start voxel (m) and the target voxel (n) according to

$$p(m \rightarrow n) = \frac{[d(\mathbf{r}_{mn}, m) + d(\mathbf{r}_{mn}, n)]^a}{\sum_n [d(\mathbf{r}_{mn}, m) + d(\mathbf{r}_{mn}, n)]^a} \quad (6.4)$$

where $p(m \rightarrow n)$ is the probability for a jump from voxel m to voxel n , $d(\mathbf{r}_{mn}, m)$ is the “diffusion coefficient” defined in (2.122) in voxel m for the direction from the centre of voxel m to the centre of voxel n , and $a = 7$. The sum of the probabilities over the eight possible n is 1.

The exponent a was introduced to make the probability distribution sufficiently localized at the directions corresponding to the fibre orientation. With $a = 1$ the particle path was not confined to the fibre direction. The objective of the simulation was to obtain a numerical measure of the subjective impression of thickness and coherence of a fibre tract. Thus the exponent a was adjusted to keep the majority of the particle paths in the voxels that constituted a fibre on the DTI fibre orientation map. For the same purpose only jumps in the “fibre direction” in the previous voxel and the two directions that deviated from it by $\pm 45^\circ$ were allowed. The fibre direction in a voxel was defined as that among the 8 directions with the largest in-plane diffusion coefficient. Among these two opposite directions that direction was chosen that did not include an acute angle with the direction of the jump to the current voxel. If the angle was 90° then the choice was arbitrary.

The tensor map used in this procedure was thresholded by setting all tensor elements to zero if $a_f < 0.2$. To suppress the U-FLARE ghost artefact a signal intensity threshold was applied for tensor calculation. Only those image pixels were included in the tensor calculation for which the signal intensity in the first of the functional echo planar images was above a threshold. This removed the ghost signal since phase encode and readout directions were interchanged compared to the U-FLARE images.

A pseudo-random integer number between 0 and 7 with the calculated probability distribution was generated by the transformation method [170], and used to select the jump direction. The particle path was terminated if a voxel with a zero tensor was reached or 60 jumps had been performed. A tensor was considered to be a zero tensor if the sum of the in-plane diagonal elements was less than $1 \cdot 10^{-9} \text{ m}^2 \text{ s}^{-1}$. Although all tensors with $a_f < 0.2$ were set to zero this was necessary to treat also those voxels as isotropic where the fibre direction was perpendicular to the slice. The path was also terminated if zero tensors were encountered in all neighbouring voxels that could be reached by a permitted jump. The maximum number of elementary jumps was chosen to be sufficiently large to allow the particle to reach the neighbouring gyri when starting on a gyral crown. The frequency with which each voxel was hit (as a result of any particle jump during a path or at its terminating point) was recorded. This number was normalized to the maximum over all considered pixels in the slice. Increasing the number of experiments beyond 4000 did not alter the normalized simulation results significantly. The simulation was written in the programming language C. Figure A.7 shows that the particle paths in the simulation are consistent with the visual assessment of a fibre on the basis of the fibre orientation map.

6.4 Relations between anatomical and functional connectivity

A comparison of our measures of anatomical and functional connectivity has to account for several circumstances, some of which are inevitable:

- Anatomical connectivities are naturally only available for white matter voxels whereas correlated fluctuations are expected to occur only between grey matter voxels.
- Fibres in DTI maps can only be followed up to where the diffusion anisotropy in the diverging tract has fallen below the threshold that is set to exclude erroneous anisotropy. Treating only fibre direction measurements in voxels with $a_f > 0.2$ as reliable, this border

is typically at 1 to 2 voxels distance from the cortex. If the distance is larger than 1 voxel the fibre target cannot be specified with 1-voxel accuracy.

- The assignment of voxels in the 128×128 matrix of the U-FLARE (DTI) images to an element of the 64×64 matrix of the EPI (fMRI) images may be inaccurate due to EPI distortions [65].
- Due to the large voxel size in the functional experiment a high number of voxels will contain both cortex and CSF or white matter.

Owing to these circumstances, the white matter voxels at the end of a fibre tract have to be assigned to a set of grey matter voxels that define the target region of the fibre. It is not expected that a relationship between functional and anatomical connectivity on a voxel-to-voxel basis will exist. To make the requirements for a possible relationship less stringent, the functional and anatomical connectivity values need to be summarized for regions the size of which is of the order of a gyrus cross section.

6.4.1 The classes approach

In contrast to Biswal's approach our experiment does not focus on functional units that are defined by a functional experiment. As extent and location of sensible fibre target regions is not known we first attempted to define regions on the basis of the fluctuation measurement. Contiguous classes of pixels that correlate highly (correlation coefficient above an arbitrary threshold) with each other were formed. Two classes were considered to be functionally connected if the average of the four largest correlation coefficients between pixels in the two classes exceeded an arbitrary threshold. The set of pixel classes was subdivided into "superclasses" of classes that were connected in this sense.

Results

The 7 subjects in the study showed high correlations between various cortical areas. Most of the pixels in white matter did not correlate with any other pixel which was above the threshold. The correlation maps are highly affected by motion and by temporal variations of image ghosts (The ghost image visible in Fig. 5.6 was also apparent in this experiment.) Some sulcal fundi are correlated with a considerably large part of the whole cortical surface. The signal variations for the involved pixels are unusually high. This could indicate that this fundus is a part of a network that is active during some period of the experiment. However, it is more probable that it is due to motion or temporal variations of image artefacts. The effect is not reduced by the four-part correlation.

- In many cases the correlation between topologically equivalent areas in contralateral hemispheres is large which is in accordance with Biswal's results.
- If a cortical region 'A' is correlated with an ipsilateral region 'B' it is in many cases also correlated with the corresponding contralateral area of 'B'. This is in accordance with the anatomical observation that a region 'A' that has an association connection with an ipsilateral region 'B' often also has a commissural connection with a contralateral region 'C' which is homotopic with 'B' [18, p. 370].

- Gyral crowns and sulcal fundi behave differently: The correlation between crowns or between fundi is often higher than the correlation between a crown and a fundus.
- The separate correlation of 4 parts of the time courses revealed that the correlation coefficients vary substantially between the four segments. This can probably be attributed to “real task activation” rather than to fluctuations. The minimum of the correlation coefficient for the 4 time course parts is in many cases considerably lower than the correlation coefficient for the full time courses.
- The classes approach is very sensitive to the choice of the threshold to the correlation coefficient. A slight variation in this threshold can change the superclass a class belongs to.
- Classes often consist of a whole fundus. Contiguous classes on the crowns are rare. This may be attributed to the fact that afferent fibres from subcortical white matter reach the cortex at the crowns rather than at the fundi [217, p. 268]. Crowns are connected to distant brain regions whereas fundi are connected to the rest of the brain predominantly via an adjacent crown. (The connection to the crown can be intracortical.) In task activation the fundi may be triggered by a crown region without causing a measurable haemodynamic response in the crown. If we speculate that fluctuations spread to a significant degree only over direct connections we should expect to observe a correlated haemodynamic response of fluctuations rather between gyri than between sulci. A spontaneous action potential that arises in a fundus would have to be transferred in a crown to another neuron to reach a distant cortical region.

Cell bodies are most densely packed in the fundus [218, p. 26]. This may also contribute to the fact that the correlation between neighbouring pixels tends to be higher at the fundus than on the crown.

- The classes in the fundi of precentral, central, postcentral gyrus often belong to the same superclass. At low thresholds for the correlation coefficient this superclass also includes the crowns in between.
- The typical signal variation is of the order of 3% which is compatible with the variation of 0.5 to 1% observed by Biswal *et al.* at 1.5 T main field strength when the difference in B_0 is taken into account.

6.4.2 The region-of-interest approach

The class/superclass algorithm proved to be inappropriate for the investigation of connectivity between crowns due to the high sensitivity to variations of the threshold for the correlation coefficient in terms of the enormous differences in the number of (super)class elements. To assess how strongly gyral crowns were interconnected we selected gyri on the convex surface of the brain and manually defined regions of interest in the 64×64 matrix situated on the crowns which were defined as the cortical regions at the origin of a fibre tract. Every region also contained subcortical white matter pixels that could serve as starting pixels in the simulation. A typical region of interest consisted of about ten pixels. Three of the seven volunteers in the study did not clearly exhibit U-shaped fibres between adjacent gyri in the DTI maps and were excluded from data evaluation. The starting pixels in the Monte-Carlo simulation were

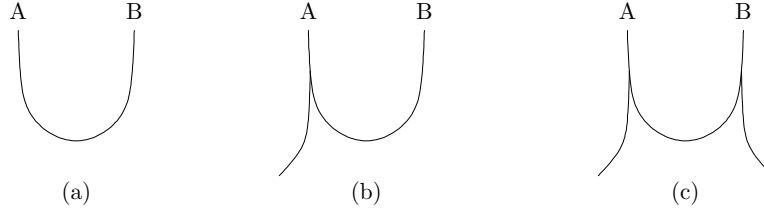


Figure 6.1: Schematic view of different fibre patterns between two regions 'A' and 'B'.

restricted to those 128×128 matrix elements that belonged to one of the regions of interest. Owing to the large voxel size in the 64×64 matrix some regions of interest were directly adjacent to another region. In the simulation, to prevent the virtual particle to jump across the border between regions without having entered white matter, direct jumps between regions were explicitly excluded. The particle paths were terminated if a region of interest other than the starting region was reached. The simulation results were then processed in three steps:

1. The number that was output from the simulation was divided by the value in the start pixel which is usually the number of experiments.⁸ This ratio may be denoted by c_d .
2. The anatomical 128×128 connectivity map obtained from the simulation was converted into the coarser 64×64 matrix format of the functional experiment by taking the maximum over 4 adjacent pixels in the 128×128 matrix.
3. Every ordered pair of regions was assigned an anatomical connectivity value by taking the maximum of c_d over all pixels belonging to a region of interest. The maximum was taken over the start region as well as over the target region. By this procedure a connectivity matrix between regions was created that contains a value between 0 and 1 for each ordered pair of regions.

Similarly, the maximum in the matrix of correlation coefficients between pixels in two regions was used as a correlation measure c_f between the two regions. It has to be pointed out that the generated matrix of anatomical connectivity is not necessarily symmetric, in contrast to the matrix of functional connectivity values. For a comparison of functional and anatomical connectivity between regions it would be desirable to have a symmetric anatomical measure. From the anatomical connectivity matrix C a symmetric matrix C' can be calculated for example by

$$C'_{ij} = \max(C_{ij}, C_{ji}) \quad \text{or by} \quad C'_{ij} = (C_{ij} + C_{ji})/2. \quad (6.5)$$

For two regions 'A' and 'B' this effectively means taking the maximum or the average, respectively, of the c_d value for paths from 'A' to 'B' and the c_d value for paths from 'B' to 'A'. This point merits some discussion.

The two options in (6.5) have different consequences. In the simulation the pathways with fewer bifurcations are privileged since the simulation result for paths from a region 'A' to a region 'B' depends on the number of possibilities encountered on the way between 'A' and 'B'

⁸A difference between the count in the start pixel and the number of experiments can arise from the very rare case where a particle path returns to its origin.

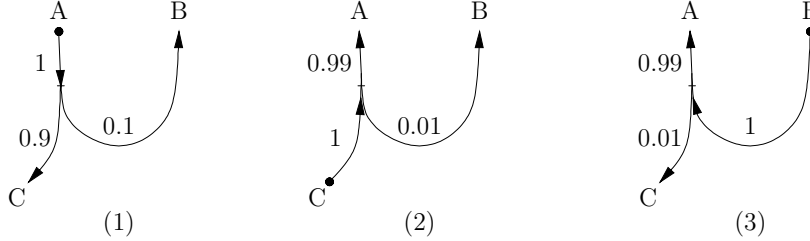


Figure 6.2: Particle path probabilities in the fibre pattern of Fig. 6.1 (b) for different starting regions (marked by a dot).

to divert from the track leading to ‘B’. The calculation for ‘A \rightarrow B’ yields a higher value for the fibre pattern (a) in Fig. 6.1 than for pattern (b) where a part of the fibres emerging from ‘A’ do not reach ‘B’. If we take the maximum over the calculations for ‘A \rightarrow B’ and ‘B \rightarrow A’ we obtain the same anatomical connectivity between ‘A’ and ‘B’ in the situations depicted in Fig. 6.1 (a) and (b), and a lower value in situation (c). By taking instead the average over the two directions we obtain three different connectivity values in the situations (a), (b), and (c).

Another difference of maximum and average approach is revealed when comparing two region pairs in a fibre network. In the situation depicted schematically in Fig. 6.2 (which is equivalent to (b) in Fig. 6.1) where the numbers represent the probability for the jumping particle to move along a path, we obtain with the maximum approach the same value for the pair ‘AC’ as for the pair ‘AB’. This does not account for ‘B’ being hardly reachable from region ‘A’. The direction average however is different for ‘AB’ and ‘AC’.

Which approach makes more sense if we intend to investigate the connectivity hypothesis? In the situation in Fig. 6.1 (b) we would naïvely attempt to obtain a measure of the strength of the connection between ‘A’ and ‘B’ that is independent of the existence of the fibre originating from ‘A’ but not leading to ‘B’. Such a quantity would be generated by taking the maximum in equation (6.5).

One can object against taking the maximum value that it is not reasonable that the connectivity values for (a) and (b) are the same while the values for (b) and (c) differ. In fact, the dependence of the connectivity measure on the number of bifurcations between two points is an inherent property of the simulation. Taking the maximum over directions would artificially remove this dependence in selected cases.

Assume that k axons leave or enter region ‘A’, l axons leave or enter region ‘B’, and n axons connect ‘A’ and ‘B’. We can interpret $c_d(A \rightarrow B)$ as an estimate of n/k , and $c_d(B \rightarrow A)$ as an estimate of n/l . In a mechanistic model of competing influences $c_d(A \rightarrow B)$ represents the relative importance of ‘B’ for the state of ‘A’ provided that all fibres contain an equal number of afferent and efferent axons. This interpretation suggests another way of averaging the two values,

$$C'_{ij} = \frac{n}{(k+l)/2} = 2 \left[\left(\frac{n}{k} \right)^{-1} + \left(\frac{n}{l} \right)^{-1} \right]^{-1} = 2 [(C_{ij})^{-1} + (C_{ji})^{-1}]^{-1}. \quad (6.6)$$

With this “average” we obtain $C'_{ij} \rightarrow 0$ for $C_{ij} \rightarrow 0$, irrespective of the (constant) value of C_{ji} .

It is unclear which choice conveys a better model for the anatomical substrates that might determine the correlation between fluctuations. For these reasons we search for a relationship

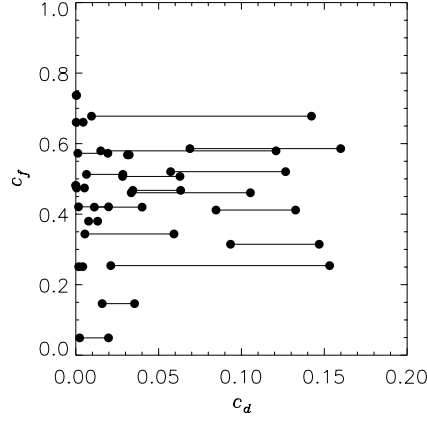


Figure 6.3: Correlation coefficient c_f between regions on adjacent gyri versus the corresponding anatomical connectivity measure c_d for all subjects. Since in the simulation the start pixel can be set in either of the two regions two c_d values per region pair are shown (connected by a horizontal line).

between functional and anatomical connectivity on the basis of the full asymmetric matrix of anatomical connectivities.

Results

Fig. 6.3 shows a plot of the correlation coefficients between regions on adjacent gyri versus the corresponding anatomical connectivity for all subjects. In Table 6.1 the anatomical names of the selected gyri are listed for the data shown in the figure. The following conclusions can be drawn from the plot:

- The value of anatomical connectivity between adjacent gyri in Fig. 6.3 varies by a considerable amount. This is not solely due to interindividual differences since the variation is not less within a single subject (see Table 6.1).
- The difference between the simulation results with start and target region interchanged is large for many region pairs.
- Knowledge of the c_d value(s) is not sufficient to predict the value of c_f .

The data do not clearly contradict the hypothesis that a high anatomical connectivity implies a high functional connectivity. At least high c_d values do not occur in combination with low c_f values. Unfortunately the study does not yield enough data points to test the hypothesis statistically. Fig. 6.4 shows histograms of c_d and c_f values. In Fig. 6.4 (a) all points from Fig. 6.3 are treated as independent data whereas in Fig. 6.4 (b) the c_d values belonging to the same pair of gyri but with start and target region interchanged were combined according to equation (6.6). The impression from Fig. 6.3 that the data points seem to segregate into two groups can be described quantitatively by the dip in the c_d distributions shown in Fig. 6.4. This dip is reduced to a shoulder in a histogram derived from the same data but taking the arithmetic mean over the directions (not shown). It might be an advantage of definition (6.6)

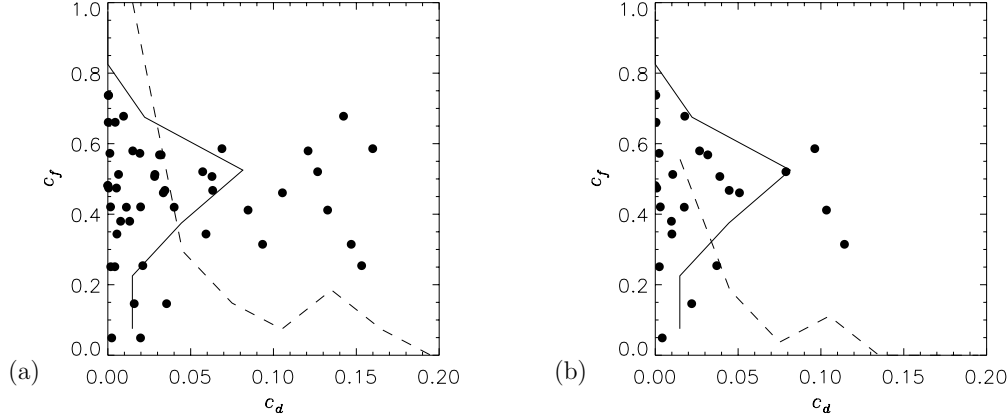


Figure 6.4: Same data as in Fig. 6.3 with histograms of c_f (solid line, occurrence on horizontal axis, bin size 0.15) and c_d values (dashed line, occurrence on vertical axis, bin size 0.03). In (a) the c_d values for opposite path direction were treated as independent data for accidentally the same c_f value whereas in (b) the two values were “averaged” according to the definition in equation (6.6). In all histograms the occurrence axis ranges from 0 to 27 (in (a) the c_f for a pair of c_d values was treated as a single value).

that it preserves the distribution of c_d values. Whether the segregation of data points in Fig. 6.3 is merely incidental or if the situation can be used to classify the connections between adjacent gyri is unclear and remains to be investigated in further experiments including more data.

There are different possible reasons why the experiment failed to show a relationship between functional and anatomical connectivity:

- The connectivity hypothesis is possibly false. Biswal’s results were obtained in the hand area which has relatively few interhemispheric connections. The high interhemispheric correlation may be completely independent of the commissural fibre connection. Friston *et al.* [208] point out that, although (direct or indirect) anatomical connectivity is a prerequisite of functional connectivity, there is no one-to-one mapping between anatomical and functional connectivity. The primary visual cortex (V1, Brodmann’s area 17) exhibits correlation in the signal fluctuations although the commissural fibres between the left and right V1 area are restricted to the border zone to the secondary visual cortex (V2, Brodmann’s area 18) [18, p. 374].
- The measured functional connectivities may not rely on fluctuations analogous to those measured by Golanov *et al.* [215], possibly because they contain too much contamination by uncontrollable task activation.
- The measured anatomical connectivities may be false because they do not account for fibres that are not contained in the image slice.
- The measured anatomical connectivities are possibly false because DTI averages over voxel volumes. The trajectories of single axons cannot be determined. U-shaped fibre tracts seen in DTI fibre orientation maps therefore do not necessarily represent a continuous

anatomical position	Subject 1		Subject 2	Subject 3		Subject 4	
	R	L	R	R	L	R	L
med front g			0.661		0.461		
			0.004 0.000		0.105 0.033		
inf front g					0.737		
					0.000 0.000		
inf front g	0.049	0.481	0.678	0.474		0.344	0.568
	0.020 0.002	0.000 0.000	0.142 0.009	0.005 0.000		0.059 0.005	0.032 0.031
precent g	0.380	0.507	0.513	0.468		0.251	0.586
	0.013 0.008	0.063 0.028	0.028 0.006	0.063 0.034		0.004 0.002	0.160 0.069
postcent g	0.315		0.521	0.254		0.421	0.573
	0.147 0.093		0.127 0.057	0.153 0.021		0.002 0.020	0.019 0.001
supram g				0.580		0.420	0.146
				0.121 0.015		0.040 0.011	0.035 0.016
supram g				0.412			
				0.133 0.085			
inf par lob							

Table 6.1: Assignment of the data for functional and anatomical connectivity in Fig. 6.3 to anatomical structures. The c_f values are given in bold face, c_d values are listed for both directions (maximum first). The numbers in a double line (bold and normal face) are calculated for the U-shaped fibre connecting the gyri named in the lines above and below in the first column. The abbreviations in the first column mean, from top to bottom: medial frontal, inferior frontal (2 \times), precentral, postcentral, supramarginal (2 \times) gyrus, and inferior parietal lobulus, in the right (R) and left (L) hemisphere. A gyrus can appear twice if it has meanderings that make it cross the slice at two points.

fibre connecting the two neighbouring gyri. In the WM within a gyrus radial fibres dominate whereas below the sulcal fundus tangential fibre directions dominate. Radial fibres emerging from the cortex at the sulcus base are scarce and bend at the border to white matter to merge with the tangential fibres [217]. The spatial variation in the relative content of fibre directions in a voxel could lead to a U-shaped fibre pattern while not any of the fibres connects the gyral crowns (false positive result). On the other hand genuine U fibres are constrained to a thin superficial layer of white matter and might be undetectable at the resolution of the DTI experiment (false negative result).

We conclude that it is not possible to directly infer a high correlation in the non-stimulus fMRI experiment from a strong anatomical connection between two cortical regions that is observed in the DTI fibre orientation map. This result is consistent with the observation that a high interhemispheric correlation occurs in brain areas that have no or only few commissural connections. It may however be generated by the limitations of the used DTI measurements. It is questionable whether DTI can be used as a tool to directly investigate functional connectivity. However, it does supply additional information. The results raise the question if the correlation found by Biswal *et al.* [212] and Lowe *et al.* [213] can actually be attributed to the statistical fluctuations found by Golanov *et al.* [215].

Chapter 7

Conclusion

The results of this thesis cover three different fields: a method for spatially resolved *in vivo* measurements of the diffusion tensor, a method to quantify the fibre information contained in a diffusion tensor measurement in brain white matter, and an application to the question as to which knowledge is gained from this fibre information.

The diffusion tensor imaging experiment was set up in two variants based on the imaging sequences EPI, and U-FLARE which has not previously been used for DTI. Both methods can yield an anisotropic diffusion tensor in isotropic substances which is highly undesirable if fibre orientation maps shall be measured *in vivo*. A number of possible causes for inaccuracies in spatially resolved measurements of the diffusion tensor were discussed. Experimental results and calculated estimates led to the conclusion that for *in vivo* applications the image artefacts induced by eddy currents arising from diffusion weighting gradients are the most important cause of errors while the (diffusion) effects of background gradients and non-ideality of the applied gradient fields may be neglected in most cases. In any case carefully adjusted pre-emphasis eddy current suppression must be applied. A further source of error is the presence of flow in CSF-filled compartments, which can influence the tensor measurement in brain tissue by partial volume contribution. With EPI, the reduction of eddy current effects by the double spin-echo approach proposed by Wider *et al.* [155] is about as efficient as the removal of these effects by postprocessing as proposed by Jezzard *et al.* [185]. Further improvement can be achieved by a combination of these two approaches. If in the imaging part of a DTI sequence EPI is replaced by U-FLARE the temporal variation of eddy currents during the echo train is the most important influence. It can lead to spatial signal variation in the image that depends on the diffusion gradient. In this case artificial anisotropy is introduced in the affected image regions. However, U-FLARE based DTI has advantages over EPI whenever limited resolution or image distortions due to a high main field strength are to be avoided. To counteract the SNR disadvantage of U-FLARE as compared with EPI, a U-FLARE based DTI protocol was developed that employs half k-space sampling and TIPE phase encoding. With this sequence diffusion tensor maps of a 5-mm brain slice were obtained in 30 min scan time with about 1.5 mm in-plane resolution.

In order to quantify the strength of a fibre connection between two brain grey matter locations in a fibre orientation map derived from a DTI experiment, a Monte-Carlo based algorithm was developed.

Motivated by the findings of Biswal *et al.* [212] that the T_2^* weighted (BOLD) signal fluctuations in left and right motor cortex are correlated, in an experiment applying both DTI and BOLD imaging the Monte-Carlo algorithm was used for a comparison between the strength

of a fibre connection between two cortical regions and the correlation of T_2^* weighted signal fluctuations in these regions. This comparison was performed for selected regions on adjacent cortical gyri. The anatomical connectivity values calculated by the Monte-Carlo algorithm differed substantially in such a train of gyri, and large interindividual differences were observed. No direct relationship between the two parameters was found. However, a coincidence of high anatomical and low functional connectivity seems to occur rarely.

Future work should include the application of multi-slice DTI measurements to the question of the relationship between functional and anatomical connectivity. This should allow an investigation of the connections between more distant cortical regions. A three-dimensional DTI sequence where spatial resolution in two spatial directions is provided by phase encoding would have a signal-to-noise advantage over multi-slice measurements. Since it must be a multi-shot sequence it is bound to be affected by subject motion, and motion correction methods will be inevitable.

The fibre quantification algorithm should be modified by replacing the path termination in isotropic voxels by a random jump direction in those volume elements.

It is further proposed to compare the correlation results with a BOLD experiment under hypercapnia conditions, where the correlated fluctuations are suppressed [221], in order to investigate the nature of the correlated signal fluctuations. Another promising approach would be to bind the subject's attention during BOLD imaging to a well-defined task that induces activation in well-known sites of the brain. Signal fluctuations in the remaining cortical areas should then be less affected by "real task activation" which may enhance the relationship between BOLD signal correlations and spontaneous neuronal activity.

Work on the integration of DTI results into MEG source localization is in progress. This application would also benefit from the possibility to acquire three-dimensional diffusion tensor data within reasonable scan time.

Appendix A

Colour figures

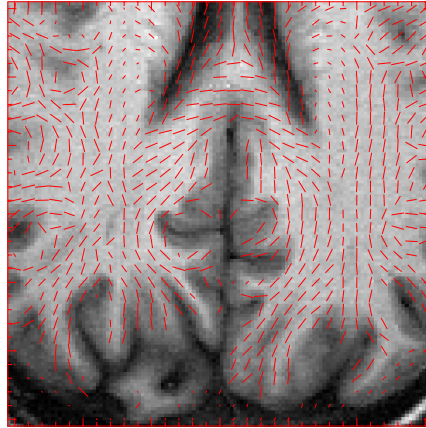


Figure A.1: Fibre orientation map based on EPI sequence. Eigenvector orientations corresponding to the largest eigenvalue are projected onto the imaging plane, and overlaid on a T_1 weighted image. Eigenvector directions were suppressed in voxels with $a_f < 0.2$. (Axial slice, top is anterior, left is subject's left. Double spin-echo EPI (see section 5.6.1), matrix 64×64 , full FOV was 19.2 cm, slice thickness 5 mm, $TE = 140$ ms, $b = 0$ to 600 s mm^{-2} , $\delta = 11$ ms, $\Delta = 70$ ms (symbols defined in Fig. 5.5), whole-body gradient set. Gradient directions as given in (4.1).)

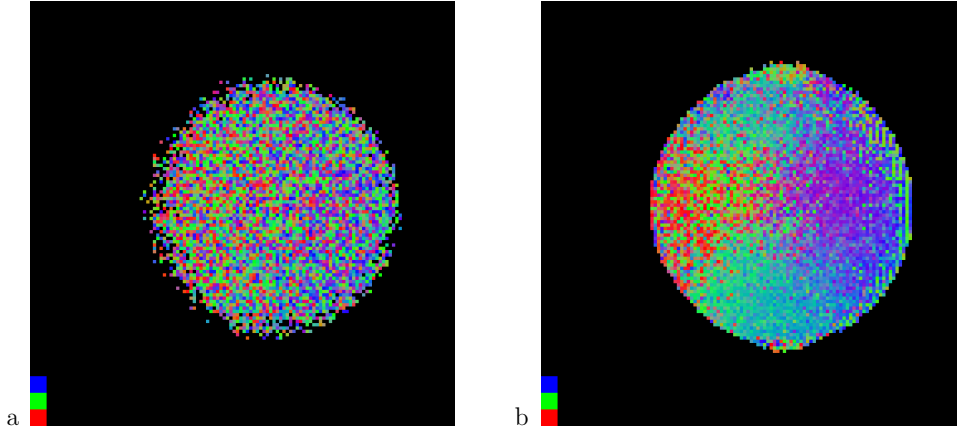


Figure A.2: Noise dependence of the fibre orientation map for an agarose gel phantom. Fibre orientation map with one (a) and 22 (b) repetitions. The pixel colour indicates the “fibre” direction: the magnitude of the horizontal, vertical (phase-encode direction), and through-plane component is indicated by red, green, and blue, respectively. The pure colours for the three axes are shown in the lower left corner. An a_f threshold was not applied. The threshold for the multiple correlation coefficient was set to 0.95 and a high signal intensity threshold was used to suppress signal in the background (see Fig. 5.9). (Phantom diameter approx. 20 cm. Head gradient insert, $b = 20$ to 650 s mm^{-2} , 4 b values, U-FLARE, matrix 128×128 , 5 mm slice thickness, $TE_{\text{prep}} = 70 \text{ ms}$).

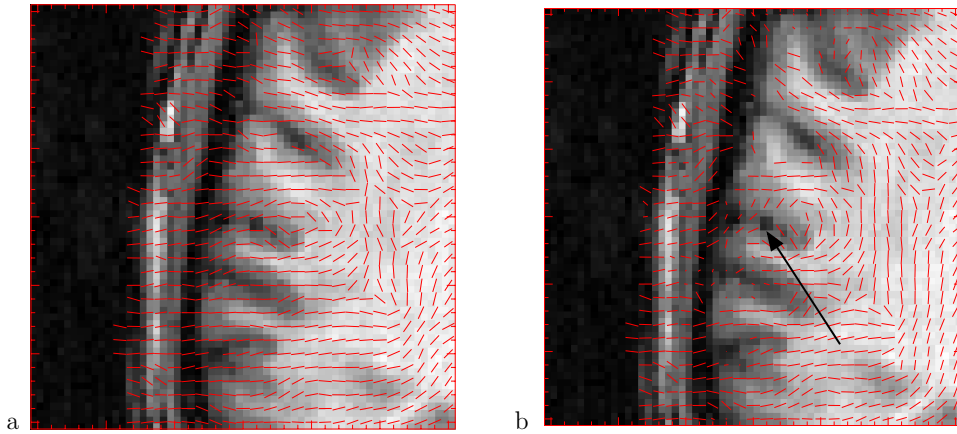


Figure A.3: Fibre orientation map before (a) and after (b) normalization to the tensor in the marked voxel (arrowhead indicates centre of voxel. Fibre orientation lines do not exceed the borders of a voxel.) (Axial slice, top is anterior. Read direction is left-right. Anisotropy threshold $a_f = 0.1$. Whole-body gradients, U-FLARE, matrix 128×128 , full FOV was 25 cm, slice thickness 5 mm, $TE_{\text{prep}} = 80 \text{ ms}$, $TE = 6 \text{ ms}$, $b = 50$ to 800 s mm^{-2} , $\Delta = 40 \text{ ms}$, $\delta = 22 \text{ ms}$.)

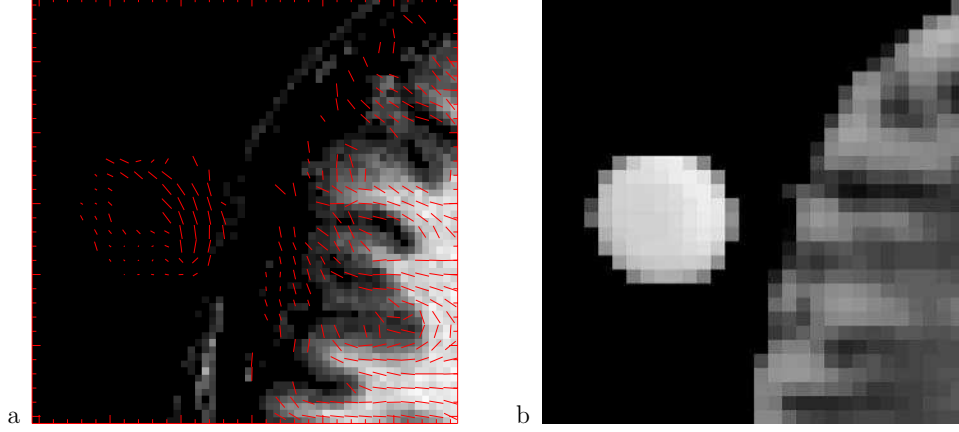


Figure A.4: Anisotropic diffusion in an isotropic water phantom attached to the subject's head. (a) Eigenvector directions (red) corresponding to the largest eigenvalue are projected onto the imaging plane, and overlaid on a T_1 weighted image. Eigenvector directions were suppressed in voxels with $a_f < 0.1$. In the anatomical image a signal threshold was applied such that the phantom disappears due to the large T_1 in water. (b) Corresponding map of Tr D (highest values in white). (Axial slice, top is anterior, left is subject's left. The image vertical is the direction of gravitation. U-FLARE, matrix 128×128 , full FOV 25 cm, slice thickness 3 mm, $TE_{\text{prep}} = 70$ ms, $b = 20$ to 600 s mm^{-2} , whole-body gradient set. Gradient directions as given in (4.1) supplemented by the inverted directions, but no geometric averaging was performed.)

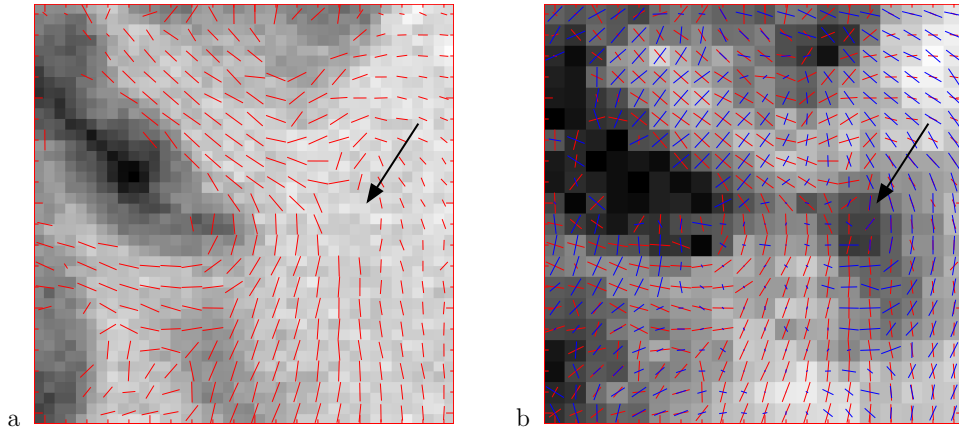


Figure A.5: Reduced anisotropy at fibre crossings. (a) T_1 weighted image with eigenvector directions for the maximum eigenvalue (red), in voxels with $a_f \geq 0.2$ only. The arrow marks a region of ≈ 3 mm diameter where due to fibre averaging the anisotropy is less than the threshold. (b) corresponding map of a_f with eigenvector directions for the largest (red) and smallest (blue) eigenvalue, in voxels with $a_f \geq 0.1$ only. All directions are displayed as projections onto the imaging plane. (Axial slice, top is anterior, left is subject's left. The dark diagonal line in (a) is the central sulcus. Read direction is anterior-posterior. Whole-body gradients, TIPE U-FLARE, experimental parameters as in Fig. A.6.)

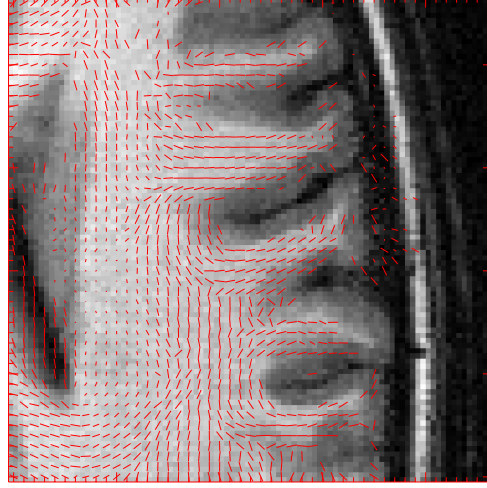


Figure A.6: Fibre orientation map from the DTI experiment overlaid on an anatomical T_1 weighted image (axial slice, top is anterior, right is subject's right). The straight lines indicate the in-plane components of the calculated fibre direction. Fibre directions in voxels with low anisotropy ($a_f < 0.2$) are suppressed. The raw images were also masked to remove the background ghost signal in the phase encode direction. The mask was derived from the EPI data acquired for the fluctuation measurement. Only a $6.75 \text{ cm} \times 6.75 \text{ cm}$ part of the field-of-view is shown. The sulcus at the bottom is the postcentral sulcus. (TIPE U-FLARE, whole-body gradient set, experimental parameters are given in the text.)

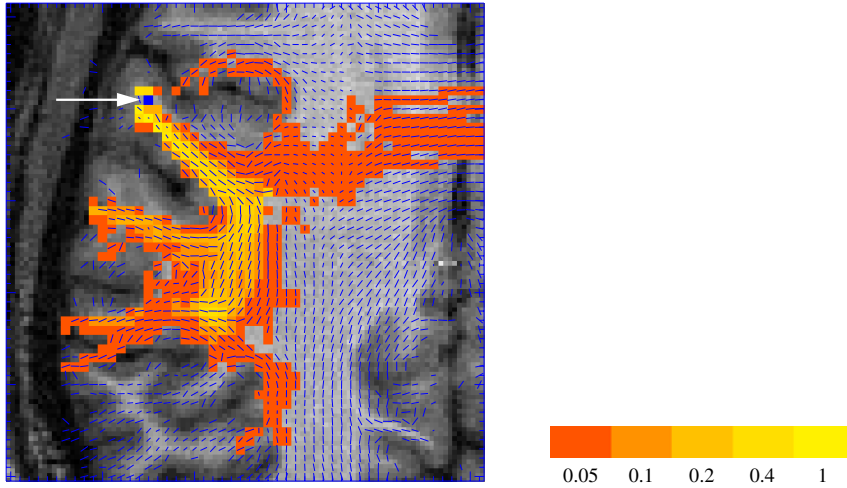


Figure A.7: Example for the result of the particle-jump algorithm. The start pixel is shown in blue and marked with an arrow. c_d values are indicated by red and yellow colours. The colours for five selected c_d values are shown on the right. Uncoloured pixels were never reached by the particle.

Appendix B

Abbreviations

ADC	Apparent Diffusion Coefficient	oxyHb	oxygenated Haemoglobin
BOLD	Blood Oxygenation Level Dependent (contrast)	PFG	Pulsed Field Gradient
CNS	Central Nervous System	PSF	Point Spread Function
CPMG	Carr-Purcell-Meiboom-Gill	RARE	Rapid Acquisition with Relaxation Enhancement
CSF	Cerebrospinal Fluid	rCBF	regional Cerebral Blood Flow
CT	Computed Tomography	RF	Radio Frequency
DC	Direct Current	SAR	Specific Absorption Rate (permissible level of absorbed RF power per unit of body weight)
deoxyHb	deoxygenated haemoglobin	SE	Spin Echo
DSE	Double Spin-Echo	SMA	Supplementary Motor Area
DTI	Diffusion Tensor Imaging	SNR	Signal-to-Noise Ratio
DWI	Diffusion Weighted Imaging	TE	Echo Time
EPI	Echo Planar Imaging	TE_{prep}	Echo Time of Preparation Experiment
FID	Free Induction Decay	TIPE	Template Interactive Phase-Encoding
FLASH	Fast Low-Angle Shot	TR	Repetition Time
fMRI	functional Magnetic Resonance Imaging	U-FLARE	Ultra-Fast Low Angle RARE
FOV	Field of View	V1	primary visual cortex
FT	Fourier Transform	V2	secondary visual cortex
FWHM	Full Width at Half Maximum	WM	White Matter
GM	Grey Matter		
GRASE	Gradient And Spin-Echo		
IDL	Interactive Data Language		
ISMRM	International Society for Magnetic Resonance in Medicine		
IVIM	Intra-Voxel Incoherent Motion		
MDEFT	Modified Driven Equilibrium Fourier Transform		
MEG	Magnetoencephalography, Magnetoencephalogram		
MR	Magnetic Resonance		
MRI	Magnetic Resonance Imaging		
NMR	Nuclear Magnetic Resonance		

Appendix C

Zusammenfassung der wissenschaftlichen Ergebnisse

C.1 Motivation und Einordnung

Seit den achtziger Jahren wird die magnetische Kernresonanz (NMR) bei Wasserstoffkernen für die Bildgebung in der Medizin ausgenutzt. Die Bildgebungsmethoden beruhen in der Regel darauf, dass verschiedene Gewebearten unterschiedliche Relaxationszeiten haben. Für die Untersuchung des Gehirns hat sich die NMR-Bildgebung als besonders leistungsfähig erwiesen. Die Nervenzellen im Gehirn kommunizieren miteinander über lange Fortsätze (Axone), die in der sogenannten weißen Substanz im Innern des Gehirns sehr dicht gepackt sind. Diese Bereiche sind in Bezug auf Relaxationszeiten verhältnismäßig homogen. Obwohl sich in der weißen Substanz in anatomischen Schnitten Bündel von Fasern mit unterschiedlichem Verlauf abgrenzen lassen, ist es deshalb mit herkömmlichen Methoden der NMR-Bildgebung nicht möglich, solche Abgrenzungen am lebenden Menschen vorzunehmen.

Eine Kombination des NMR-Bildgebungsprinzips und der PFG-NMR (Pulsed Field Gradient NMR) ermöglicht die orts aufgelöste nichtinvasive Messung von Diffusionskoeffizienten, die ebenfalls in der biomedizinischen Bildgebung genutzt wird. Seit 1989 [7] ist bekannt, dass die Selbstdiffusion von Wasser in weißer Substanz anisotrop verläuft und deshalb mit einem Tensor beschrieben werden muss. Diese Tatsache beruht auf der geordneten Struktur der weißen Substanz: in vielen Bereichen verlaufen die Axone parallel zueinander und sind von vielen Lagen besonders fetthaltiger Zellmembranen des Stützgewebes (Myelinhüllen) umgeben, die die thermische Bewegung von Wasser quer zur Faser behindern. Basser u. a. [15] stellten 1994 ein Verfahren zur Messung des vollständigen Selbstdiffusionstensors von Wasser vor, das kein A-priori-Wissen über die Lage der Tensorhauptachsen voraussetzt, und bezeichnete es als „Diffusion Tensor Imaging“ (DTI).

Die gewonnene Information kann genutzt werden zur Gewebecharakterisierung in pathologischen Prozessen (z. B. bei Multipler Sklerose oder bei Hirninfarkt), zur Abbildung von Faserbündeln in weißer Substanz vor neurochirurgischen Eingriffen und in der experimentellen Hirnforschung zur Aufklärung der Zusammenhänge zwischen Anatomie und Funktion: Die Zellkörper der Neuronen befinden sich v. a. in der grauen Substanz, die in Gebieten innerhalb der weißen Substanz (Kerngebiete) und auf ihrer Oberfläche (Großhirnrinde, Kortex) konzentriert ist. Es werden große Hoffnungen in die Möglichkeit gesetzt, mit Hilfe von DTI Faserverbindungen zwischen Gebieten grauer Substanz bei Versuchspersonen in neuropsychologischen Experimenten individuell abzubilden. Bei solchen Experimenten kann die Hirnfunktion z. B. mit

Hilfe „funktioneller“ NMR-Bildgebung (fMRI) gemessen werden, welche im Wesentlichen auf dem Nachweis der bei Inanspruchnahme lokal erhöhten Hirndurchblutung beruht. Da Hirngebiete durch viele Axone verknüpft sind, wenn ein hoher Bedarf an Informationsaustausch zwischen ihnen besteht, sollte eine Vermessung der Faserverbindungen (in Verbindung mit fMRI-Experimenten) zur Überprüfung von Modellen der Aufgabenverteilung und der Kommunikation zwischen verschiedenen Hirngebieten beitragen. Ein wichtiges Ziel neuroanatomischer Forschung ist es, anatomische Kriterien zur Definition von funktionellen Einheiten im Gehirn zu finden. Die in einem fMRI-Experiment beobachteten aktivierten Kortextareale haben typischerweise eine Ausdehnung von ca. 1,5 cm. Histologisch definierte Bereiche sind deutlich größer. Damit liegt die Größenordnung von funktionell bedeutsamen Einheiten zwischen der Größe von als „macrocolumns“ bezeichneten Neuronengruppen (unterhalb von 1 mm) und der Größe von histologisch abgegrenzten Bereichen. Bisher steht kein anatomisches Kriterium zur Definition von Einheiten auf dieser „mesoskopischen“ Ebene zur Verfügung. Die Diffusionstensorbildgebung, deren Ortsauflösung bei 1 bis 3 mm liegt, könnte diese Lücke schließen. Sie könnte eine Möglichkeit darstellen, die histologischen Einheiten anhand der zuführenden Fasern in Untereinheiten von funktioneller Bedeutung zu unterteilen.

Für DTI müssen wegen der Bewegungsempfindlichkeit und der hohen Anzahl an erforderlichen Messungen schnelle Bildgebungsmethoden eingesetzt werden. Bislang wurde DTI fast ausschließlich mit der Bildgebungssequenz „Echo Planar Imaging“ (EPI) [63] realisiert. Diese Methode gehört zwar zu den schnellsten Sequenzen in der NMR-Bildgebung, sie hat aber auch gravierende Nachteile: Sie bringt Bildverzerrungen und -auslöschungen mit sich, und eine hohe räumliche Auflösung kann nur mit sehr starken und schnell schaltbaren Gradientenspulen erreicht werden. Beide Probleme machen sich besonders bei hohen Hauptfeldstärken bemerkbar. In dieser Arbeit wird deshalb neben EPI die Bildgebungsmethode U-FLARE (Ultra-Fast Low Angle Rapid Acquisition with Relaxation Enhancement) [159] für die Diffusionstensorbildgebung verwendet. DTI auf der Grundlage von U-FLARE als Bildgebungssequenz wurde bislang nicht beschrieben.

Bei der Realisierung des DTI-Experiments wurde offenbar, dass manche in der Literatur beschriebene Fehlerquellen in der Praxis irrelevant sind, dafür aber andere wichtige Schwierigkeiten bisher wenig behandelt wurden [222]. Die Dissertation befasst sich deshalb zunächst mit einer Analyse der Fehlerquellen bei der Bestimmung des Diffusionstensors und mit der Charakterisierung der verwendeten Methoden hinsichtlich des Einflusses der verschiedenen Fehlerquellen.

Die auf der modifizierten U-FLARE-Sequenz beruhende Messmethode wurde auf eine Fragestellung aus der Neuroanatomie angewandt. Das in Kapitel 6 der Dissertation beschriebene Experiment wurde motiviert durch die Beobachtung von Biswal u. a. [212], dass die Signalfluktuationen im rechten und linken motorischen Kortex bei einer fMRI-Messung der Hirnfunktion zueinander zeitlich korreliert sind, auch wenn keine willkürliche Bewegung ausgeführt wird. Die Autoren führen dies zurück auf spontane Aktivität von Neuronen im motorischen Kortex. Solche Aktivität könnte sich über die ausgeprägten interhemisphärischen Fasern auf die Gegenseite übertragen. Analoge Beobachtungen wurden auch in anderen Hirngebieten beschrieben. Das Experiment in der Dissertation dient der Untersuchung der Hypothese, dass korrelierte Fluktuationen des fMRI-Signals immer zwischen solchen kortikalen Gebieten auftreten, die in der auf DTI beruhenden Faserkarte erkennbar miteinander verbunden sind.

C.2 Methoden

Die Experimente wurden an gesunden Freiwilligen an einem Ganzkörper-Kernspintomographen mit einer Magnetfeldstärke von 3 Tesla durchgeführt.

Pulssequenzen und Tensorberechnung

Das am weitesten verbreitete NMR-Bildgebungsprinzip [58] beruht darauf, eine durch die gewünschte Auflösung bestimmte Anzahl von Echos zu erzeugen, deren Phase durch einen vorangehenden gepulsten Magnetfeldgradienten variabler Stärke systematisch beeinflusst wird (Phasenkodierung). Während der Aufnahme der Echos ist ein weiterer Feldgradient (Auslesegradient) angelegt. Die Phase eines zum Signal beitragenden Spins zu einem bestimmten Zeitpunkt hängt dann von den Koordinaten seiner Position entlang des Auslese- und des Phasenkodiergradienten ab. Mit Hilfe einer zweidimensionalen Fourier-Transformation kann man die Signalbeiträge der verschiedenen Herkunftsorte trennen. Hat man die Anregung der Probe auf eine dünne Schicht beschränkt, erhält man auf diese Weise ein zweidimensionales Bild dieser Objektschicht. Die Echos können mit Hilfe von schaltbaren Feldgradienten oder magnetischen Wechselfeldern (Hochfrequenzimpulsen) erzeugt werden.

Bei EPI [63] wird zur Echoerzeugung das Vorzeichen des Auslesegradienten mehrfach umgekehrt. Die Bildgebungsmethode U-FLARE [159] verwendet stattdessen Hochfrequenzimpulse zur Rephasierung der Spins. Der Präzessionswinkel der Pulse liegt dabei unter 180° , um eine rasche Abfolge von Impulsen zu ermöglichen, ohne zuviel Energie ins Gewebe einzustrahlen. Dies bringt aber Komplikationen mit sich: Die Magnetisierung nach einem Refokussierungsimpuls kann man zerlegen in einen transversalen Anteil, der um die Hauptfeldrichtung \mathbf{B}_0 präzediert, und einen longitudinalen Anteil entlang der Richtung von \mathbf{B}_0 . Die Wirkung des folgenden Impulses kann durch eine erneute Aufteilung der Magnetisierungsvektoren beschrieben werden. Eine solche Betrachtung ermöglicht Aussagen über Zeitpunkt, Amplitude und Phase der bei einer Mehrimpulssequenz entstehenden Echos. Die verschiedenen zu einem Echo beitragenden Anteile sind nur gleichphasig, wenn die Präzessionsachse der Refokussierungsimpulse parallel zum ursprünglichen Magnetisierungsvektor direkt nach der Anregung ist. Andernfalls können die Anteile destruktiv miteinander interferieren. Das hat Auswirkungen auf die Messung von Diffusionskoeffizienten: Eine Translation der Probe zwischen den diffusionswichtigen Gradientenimpulsen führt zu einer globalen Phasenverschiebung, so dass die o.g. Bedingung nicht mehr erfüllt sein muss: Da sich Bewegungen im Mikrometerbereich in der Bildgebung am lebenden Objekt nicht vermeiden lassen, muss man von einer unbekannten Phase der Magnetisierung nach dem diffusionswichtigen Abschnitt des Experiments ausgehen. Der Einfluss von Magnetfeldgradienten ist für die Anteile der Magnetisierung unterschiedlich. In „displaced“ U-FLARE [160] wird dies ausgenutzt, um einen der Beiträge aus dem detektierten Signal auszuschließen und so destruktive Interferenz zu vermeiden. Durch diese Maßnahme wird U-FLARE für diffusionsgewichtete in-vivo-Bildgebung einsetzbar. Erkauft wird diese Möglichkeit durch den Verlust des ausgeschlossenen Signalanteils. Dieser Nachteil muss ausgeglichen werden, um gegenüber EPI eine höhere Auflösung bei gleicher Messzeit zu erreichen. Da eine Signalsteigerung durch Erhöhung des Refokussierungswinkels zu unzulässiger Gewebeerwärmung geführt hätte, wurde die displaced-U-FLARE-Sequenz verändert, um die Anzahl der erforderlichen Refokussierungsimpulse zu minimieren [223]. Die verwendeten Maßnahmen wurden schon zuvor bei anderen Bildgebungsmethoden, nicht jedoch bei U-FLARE verwendet:

- Die Symmetrie der Messdaten wurde ausgenutzt, um die Anzahl der aufgenommenen

Echos (und damit der notwendigen HF-Impulse) ohne Verlust an Auflösung zu verringern. Die für die geforderte Auflösung fehlenden Daten wurden anhand der Symmetriebeziehung berechnet [167].

- Die Phasenkodierschritte (s. o.) wurden auf der Grundlage einer Referenzmessung so umgeordnet, dass die Amplitudenvariation unter den ersten Echos ausgeglichen wird. Damit müssen diese, anders als in [160], nicht von der Datenaufnahme ausgeschlossen werden, und die Anzahl der erforderlichen HF-Impulse verringert sich entsprechend. Dieses Verfahren wurde bereits für andere Bildgebungsmethoden verwendet [168].

Die Bildgebungssequenzen wurden mit Gradientenpulsen zur Diffusionswichtung nach Stejskal und Tanner [91] versehen.

Das An- und Abschalten der zur Diffusionstensormessung erforderlichen verhältnismäßig starken Gradienten verursacht Wirbelströme in leitenden Systemkomponenten, deren Magnetfeld die Messung stören kann. Deshalb wurde die Anfälligkeit von EPI und U-FLARE für durch Wirbelströme verursachte Bildfehler untersucht. Für EPI wurden dabei zwei Maßnahmen zur Vermeidung von Wirbelstromeffekten verglichen: (1) Der diffusionswichtende Teil der Sequenz wurde durch ein Schema ersetzt, das durch die Verwendung von Gradienten unterschiedlicher Orientierung weniger Wirbelströme erzeugt [155]. (2) Eine Messung der Auswirkungen von Wirbelströmen auf die Signalphase wurde zur Korrektur der Bilddaten verwendet [185]. Die Auswirkungen der beiden Maßnahmen für EPI wurden anhand der Korrekturparameter und der Bilddifferenzen zwischen starker und schwacher Diffusionswichtung beurteilt und mit der Wirbelstromanfälligkeit von displaced U-FLARE verglichen.

Mit Hilfe multivariater linearer Regression wurde aus den für verschiedene Gradientenrichtungen und -amplituden gewonnenen Bilddaten für jeden Bildpunkt ein Diffusionstensor errechnet [15]. Eigenwerte und -vektoren des Tensors wurden numerisch berechnet, und der Eigenvektor zum größten Eigenwert, welcher in weißer Hirnsubstanz der Faserrichtung entspricht, als Projektion auf die Bildebene dargestellt („Faserkarte“).

Quantifizierung der Stärke von Faserverbindungen in Tensorkarten

Zur Quantifizierung der in der Faserkarte enthaltenen Information über die Verbindung zwischen zwei Kortexarealen wurde ein Monte-Carlo-Algorithmus entworfen, der ein relatives Maß für die „Stärke“ einer Faserverbindung liefert. Dazu wurden Folgen von Bildelementen erzeugt, die man sich als den zufälligen Weg eines virtuellen, von Element zu Element springenden Teilchens durch die Menge der Bildelemente veranschaulichen kann. Die Wahrscheinlichkeit für den Sprung in ein benachbartes Bildelement war dabei abhängig vom Diffusionstensor und der Richtung des vorhergehenden Sprunges. Die Sprungwahrscheinlichkeit zwischen zwei Volumenelementen (Voxeln) stieg dabei monoton mit der Summe der mittleren quadratischen Verschiebung eines diffundierenden Wassermoleküls in beiden Voxeln, gemessen entlang der Verbindungslinie der Voxelmittelpunkte. Die Elementfolge (der Weg des Teilchens) wurde abgebrochen, sobald ein Voxel erreicht war, in dem die Diffusionsanisotropie unter einem Schwellwert lag. Wie oft ein Bildelement in einer großen Anzahl von Folgen mit demselben Startelement auftaucht, ist ein Maß für die Stärke der Faserverbindung zwischen ihm und dem Startelement. Diese Maß ist nicht invariant unter Vertauschung von Start- und Zielelement. Im Unterschied zu bereits veröffentlichten sogenannten Fibre-Tracking-Verfahren wird bei diesem Algorithmus nicht nur die Richtung der größten Diffusionskonstante, sondern der gesamte Diffusionstensor benutzt.

Das Ziel ist dabei außerdem nicht die Rekonstruktion einer Faser, sondern die Ermittlung der Stärke der Faserverbindung zwischen zwei gegebenen Punkten.

Zusammenhang zwischen Faserstärke und Korrelation hämodynamischer Fluktuationen in den verbundenen Gebieten

Mit Hilfe des modifizierten U-FLARE-Messverfahrens wurde ein Experiment zur Deutung der Ergebnisse von Biswal u. a. (s. o.) durchgeführt. Dabei wurde auf das fMRI-Messprinzip zurückgegriffen, das die Abhängigkeit der Signalintensität in einem T_2^* -gewichteten Bild von der Magnetfeldhomogenität am entsprechenden Ort ausnutzt. Da eine Aktivierung von Kortexarealen mit einer lokalen Erhöhung des Blutflusses verbunden ist und da Oxy- und Desoxy-Hämoglobin unterschiedliche magnetische Suszeptibilitäten besitzen, macht sich eine Aktivitätsänderung in einer Änderung der Signalamplitude in EPI-Bildern bemerkbar. Gemessen wurden die Signalfuktuationen in einer Zeitreihe von 1024 im Abstand von 250 ms aufgenommenen EPI-Bildern an sieben gesunden Versuchspersonen, denen kein äußerer Reiz präsentiert und keine Aufgabe gestellt wurde. Für alle möglichen Paare von Bildelementen wurde der lineare Pearson-Korrelationskoeffizient der Signalverläufe berechnet. Aus einer mit der modifizierten U-FLARE-Sequenz durchgeführten DTI-Messung der Faserstruktur wurde mit Hilfe des in C.2 beschriebenen Algorithmus die Stärke der Faserverbindung zwischen ausgewählten Regionen auf der Krone von benachbarten kortikalen Gyri bestimmt. An solchen Stellen endet der größte Teil der Faserbündel aus der weißen Substanz. Eine Auftragung des Korrelationskoeffizienten zwischen diesen Regionen aus der funktionellen Messung als Funktion der Faserstärke kann darüber Aufschluss geben, ob ein Zusammenhang zwischen diesen Parametern besteht.

C.3 Ergebnisse

Pulssequenzen und Tensorberechnung

- Räumliche Variation und Nichtorthogonalität der Feldgradienten sowie Gradienten anderer Feldkomponenten als der in Hauptfeldrichtung sind vernachlässigbare Fehlerquellen.
- Flussbewegungen im Liquor innerhalb der Seitenventrikel verursachen eine starke künstliche Anisotropie im gemessenen Diffusionstensor, die sich auch auf Volumenelemente auswirken kann, die nur teilweise Liquor enthalten.
- Durch das Schalten der Diffusionsgradienten erzeugte Wirbelströme sind die Hauptursache für Messfehler. Da die Gradientenspulen unterschiedliche Wirbelstromeigenschaften haben, wird in der Regel eine künstliche Anisotropie im Diffusionstensor erzeugt. Ein wichtiger Wirkungsmechanismus ist dabei die Wirbelstromabhängigkeit von Bildartefakten.
- Störungen durch Wirbelströme werden erheblich reduziert durch die Verwendung von zwei refokussierenden Hochfrequenzimpulsen und bipolaren Gradienten zur Diffusionswichtung [155]. Die Verbesserungen durch nachträgliche Bildkorrektur [185] sind etwas geringer [224].

Mit der optimierten U-FLARE-Sequenz [223] konnte innerhalb von 30 min die Tensorkarte einer 5 mm dicken Hirnschicht mit einer Auflösung von ca. 1,5 mm in der Schichtebene aufgenommen

werden. Mit EPI war diese Auflösung (mit der gegebenen Gerätausstattung und ohne Bewegungskorrekturmechanismen) nicht erreichbar. Der Einsatz von U-FLARE kann insbesondere an Tomographen vorteilhaft sein, deren Hauptmagnetfeldstärke oberhalb der klinisch üblichen 1,5 Tesla liegt. Höhere Feldstärken haben zwar Vorteile für die Beobachtung der Hirnfunktion, erschweren aber die Abbildung von Faserstrukturen mit EPI-basiertem DTI.

Quantifizierung der Stärke von Faserverbindungen in Tensorkarten

Der Algorithmus ist leicht so zu modifizieren, dass Gebiete geringer Anisotropie an Faserkreuzungen in weißer Substanz durchquert werden können. Eine Anwendung auf dreidimensionale Tensordaten ist ohne Weiteres möglich. Er trägt besser als veröffentlichte Fibre-Tracking-Verfahren dem Mittelungscharakter von DTI Rechnung, und er benutzt die volle Tensorinformation.

Zusammenhang zwischen Faserstärke und Korrelation hämodynamischer Fluktuationen in den verbundenen Gebieten

- Es konnte kein eindeutiger Zusammenhang zwischen dem Korrelationskoeffizienten der funktionellen Messung ohne Stimulation und der Faserstärke nachgewiesen werden. Der Fall einer starken Faserverbindung zwischen schwach korrelierten Gebieten trat jedoch verhältnismäßig selten auf.
- Setzt man voraus, dass dieses Ergebnis nicht darauf beruht, dass außerhalb der Schicht verlaufende Fasern nicht erfasst werden und nimmt außerdem an, dass die in einer Tensorkarte identifizierten Fasern tatsächlich den Verlauf von Axonen abbilden, muss man den Schluss ziehen, dass entweder (1) die beobachteten Signalkorrelationen nicht auf spontaner neuronaler Aktivität beruhen oder (2) kein kausaler Zusammenhang zwischen der Existenz einer axonalen Verbindung und der Korrelation besteht, d.h. die Korrelation nicht durch axonale Verbindungen vermittelt wird.

C.4 Ausblick

Das Experiment zur Korrelation hämodynamischer Fluktuationen sollte auf Messungen mit dreidimensionaler räumlicher Auflösung ausgedehnt werden, um auch Fasern zu erfassen, die nicht vollständig in einer Schicht verlaufen. Eine dreidimensionale Messmethode, bei der die Ortsauflösung in zwei Raumrichtungen durch Phasenkodierung erfolgt, hätte dabei einen Signal-Rausch-Vorteil gegenüber einer Mehrschichtmessung. Da eine solche Messung nicht mit einer einzigen Anregung durchgeführt werden kann, müssen Bewegungsartefakte durch eine Korrektur der gemessenen Daten verhindert werden. Mit Hilfe der Bewegungskorrektur könnten auch höhere Auflösungen in Einzelschichtmessungen erreicht werden.

Das Korrelationsexperiment sollte außerdem erweitert werden, indem die Aufmerksamkeit der Versuchsperson durch eine gezielte Aufgabe, die bekannte Hirnareale aktiviert, gebunden wird. Das Ergebnis würde weitere Hinweise auf die Herkunft der korrelierten Signalfuktuationen geben.

References

- [1] W. Andrä and H. Nowak, editors, *Magnetism in Medicine*. Wiley-VCH, Berlin, 1st edition, 1998.
- [2] E. R. Kandel and J. H. Schwartz, *Neurowissenschaften. Eine Einführung*. Spektrum Akademischer Verlag, Heidelberg, 1996.
- [3] S. Ogawa, D. W. Tank, R. Menon, J. M. Ellermann, S.-G. Kim, H. Merkle, and K. Ugurbil, Intrinsic signal changes accompanying sensory stimulation: Functional brain mapping with magnetic resonance imaging. *Proc. Natl. Acad. Sci. USA* **89**, 5951–5955 (1992).
- [4] M. S. Cohen and S. Y. Bookheimer, Localization of brain function using magnetic resonance imaging. *Trends Neurosci.* **17**, 268–277 (1994).
- [5] P. A. Bandettini and E. C. Wong, Magnetic Resonance Imaging of Human Brain Function. *Neurosurg. Clin. N. Am.* **8**, 345–371 (1997).
- [6] J. A. Maldjian, A. Gottschalk, J. A. Detre, and D. Alsop, Basal Ganglia And White Matter Activation Using Functional MRI At 4 Tesla. In *Proceedings, ISMRM, 7th Annual Meeting, Philadelphia*, page 444, 1999.
- [7] M. E. Moseley, Y. Cohen, J. Mintorovitch, L. Chileuitt, H. Shimizu, J. Tsuruda, D. Norman, and P. Weinstein, Evidence of Anisotropic Self-Diffusion in Cat Brain. In *Book of Abstracts, 8th Meeting SMRM, Amsterdam*, page 136. Society of Magnetic Resonance in Medicine, Berkeley, California, 1989.
- [8] M. E. Moseley, Y. Cohen, J. Kucharczyk, J. Mintorovitch, H. S. Asgari, M. F. Wendland, J. Tsuruda, and D. Norman, Diffusion-weighted MR Imaging of Anisotropic Water Diffusion in Cat Central Nervous System. *Radiology* **176**, 439–445 (1990).
- [9] M. E. Moseley, Y. Cohen, J. Mintorovitch, L. Chileuitt, H. Shimizu, J. Kucharczyk, M. F. Wendland, and P. R. Weinstein, Early Detection of Regional Cerebral Ischemia in Cats: Comparison of Diffusion- and T2-Weighted MRI and Spectroscopy. *Magn. Reson. Med.* **14**, 330–346 (1990).
- [10] M. Doran, J. V. Hajnal, N. Van Bruggen, M. D. King, I. R. Young, and G. M. Bydder, Normal and Abnormal White Matter Tracts Shown by MR Imaging using Directional Diffusion Weighted Sequences. *J. Comput. Assist. Tomogr.* **14**, 865–873 (1990).
- [11] G. G. Cleveland, D. C. Chang, C. F. Hazlewood, and H. E. Rorschach, Nuclear Magnetic Resonance Measurement of Skeletal Muscle. Anisotropy of the Diffusion Coefficient of the Intracellular Water. *Biophys. J.* **16**, 1043–1053 (1976).
- [12] E. W. Hsu, A. L. Muzikant, S. A. Matulevicius, R. C. Penland, and C. S. Henriquez, Magnetic resonance myocardial fiber-orientation mapping with direct histological correlation. *Am. J. Physiol.* **274**, H1627–H1634 (1998).

- [13] N. Makris, A. J. Worth, A. G. Sorensen, G. M. Papadimitriou, O. Wu, T. G. Reese, V. J. Wedeen, T. L. Davis, J. W. Stakes, V. S. Caviness, E. Kaplan, B. R. Rosen, D. N. Pandya, and D. N. Kennedy, Morphometry of In Vivo Human White Matter Association Pathways with Diffusion-Weighted Magnetic Resonance Imaging. *Ann. Neurol.* **42**, 951–962 (1997).
- [14] T. E. Conturo, N. F. Lori, T. S. Cull, E. Akbudak, A. Z. Snyder, J. S. Shimony, R. C. McKinstry, H. Burton, and M. E. Raichle, Tracking neuronal fiber pathways in the living human brain. *Proc. Natl. Acad. Sci. USA* **96**, 10422–10427 (1999).
- [15] P. J. Basser, J. Mattiello, and D. LeBihan, Estimation of the Effective Self-Diffusion Tensor from the NMR Spin Echo. *J. Magn. Reson. B* **103**, 247–254 (1994).
- [16] P. J. Basser, J. Mattiello, and D. Le Bihan, MR Diffusion Tensor Spectroscopy and Imaging. *Biophys. J.* **66**, 259–267 (1994).
- [17] P. J. Basser, Inferring Microstructural Features and the Physiological State of Tissues from Diffusion-Weighted Images. *NMR Biomed.* **8**, 333–344 (1995).
- [18] R. Nieuwenhuys, J. Voogd, and C. v. Huizen, *The Human Central Nervous System*. Springer-Verlag, Berlin, 3rd edition, 1988.
- [19] V. B. Mountcastle, An organizing principle for cerebral function: The unit module and the distributed system. In G. M. Edelman, editor, *The Mindful Brain*, pages 7–50. Massachusetts Institute of Technology, Cambridge, Massachusetts, 1978.
- [20] U. C. Wieshmann, C. A. Clark, M. R. Symms, F. Franconi, G. J. Barker, and S. D. Shorvon, Reduced Anisotropy of Water Diffusion in Structural Cerebral Abnormalities Demonstrated with Diffusion Tensor Imaging. *Magn. Reson. Imaging* **17**, 1269–1274 (1999).
- [21] T. G. Reese, R. M. Weisskoff, R. N. Smith, B. R. Rosen, R. E. Dinsmore, and V. J. Wedeen, Imaging Myocardial Fiber Architecture in Vivo with Magnetic Resonance. *Magn. Reson. Med.* **34**, 786–791 (1995).
- [22] M. A. Horsfield, H. B. W. Larsson, D. K. Jones, and A. Gass, Diffusion magnetic resonance imaging in multiple sclerosis. *J. Neurol. Neurosurg. Psychiatry* **64**. (Suppl.), S80–S84 (1998).
- [23] P. Mukherjee, M. M. Bahn, R. C. McKinstry, J. S. Shimony, T. S. Cull, E. Akbudak, A. Z. Snyder, and T. E. Conturo, Differences in Water Diffusion between Gray Matter and White Matter in Stroke: Diffusion Tensor MR Imaging Experience in Twelve Patients. In *Proceedings, ISMRM, 7th Annual Meeting, Philadelphia*, page 73, 1999.
- [24] A. G. Sorensen, O. Wu, W. A. Copen, T. L. Davis, R. G. Gonzalez, W. J. Koroshetz, T. G. Reese, B. R. Rosen, V. J. Wedeen, and R. M. Weisskoff, Human Acute Cerebral Ischemia: Detection of Changes in Water Diffusion Anisotropy by Using MR Imaging. *Radiology* **212**, 785–792 (1999).
- [25] M. E. Bastin, M. del Grado, I. R. Whittle, and J. M. Wardlaw, An Investigation into the Effect of Dexamethasone on Intracerebral Tumours using MR Diffusion Tensor Imaging. In *Proceedings, ISMRM, 7th Annual Meeting, Philadelphia*, page 902, 1999.
- [26] J. A. Brunberg, T. L. Chenevert, P. E. McKeever, D. A. Ross, L. R. Junck, K. M. Muraszko, R. Dauser, J. G. Pipe, and A. T. Betley, In vivo MR Determination of Water Diffusion Coefficients and Diffusion Anisotropy: Correlation with Structural Alteration in Gliomas of the Cerebral Hemispheres. *Am. J. Neuroradiol.* **16**, 361–371 (1995).

- [27] M. S. Buchsbaum, C. Y. Tang, S. Peled, H. Gudbjartsson, D. Lu, E. A. Hazlett, J. Downhill, M. Haznedar, J. H. Fallon, and S. W. Atlas, MRI white matter diffusion anisotropy and PET metabolic rate in schizophrenia. *Neuroreport* **9**, 425–430 (1998).
- [28] K. O. Lim, M. Hedehus, M. Moseley, A. de Crespigny, E. V. Sullivan, and A. Pfefferbaum, Compromised white matter tract integrity in schizophrenia inferred from diffusion tensor imaging. *Arch. Gen. Psychiatry* **56**, 367–374 (1999).
- [29] C. Gerthsen, *Physik*. Springer-Verlag, Berlin, 16th edition, 1989.
- [30] F. Bloch, W. W. Hansen, and M. Packard, Nuclear Induction. *Phys. Rev.* **46**, 127 (1946).
- [31] E. M. Purcell, H. C. Torrey, and R. V. Pound, Resonance Absorption by Nuclear Magnetic Moments in a Solid. *Phys. Rev.* **69**, 37 (1946).
- [32] T. Mayer-Kuckuk, *Kernphysik*. B. G. Teubner, Stuttgart, 6th edition, 1994.
- [33] C. P. Slichter, *Principles of Magnetic Resonance*. Springer-Verlag, Berlin, 3rd edition, 1990.
- [34] W. Raith, editor, *Bergmann/Schaefer, Lehrbuch der Experimentalphysik*, volume 4: Teilchen. Walter de Gruyter, Berlin, 1992.
- [35] E. Fick, *Einführung in die Grundlagen der Quantentheorie*. Aula-Verlag, Wiesbaden, 6th edition, 1988.
- [36] P. T. Callaghan, *Principles of Nuclear Magnetic Resonance Microscopy*. Oxford University Press, Oxford, 1993.
- [37] X. R. Li, *Probability, random signals and statistics*. CRC Press, Boca Raton, 1999.
- [38] I. N. Bronstein and K. A. Semendjajew, *Taschenbuch der Mathematik*. BSB B. G. Teubner, Leipzig, 22nd edition, 1985.
- [39] F. Bloch, Nuclear Induction. *Phys. Rev.* **70**, 460–474 (1946).
- [40] H. C. Torrey, Bloch Equations with Diffusion Terms. *Phys. Rev.* **104**, 563–565 (1956).
- [41] T. C. Farrar and E. D. Becker, *Pulse and Fourier Transform NMR. Introduction to Theory and Methods*. Academic Press, Orlando, 1971.
- [42] G. D. Fullerton, Physiologic Basis of Magnetic Relaxation. In D. D. Stark and W. G. Bradley, editors, *Magnetic Resonance Imaging*, chapter 4, pages 88–108. Mosby-Year Book, St. Louis, 2nd edition, 1992.
- [43] A. Abragam, *Principles of Nuclear Magnetism*. Oxford University Press, New York, 1983.
- [44] R. E. Hendrick and U. Raff, Image Contrast and Noise. In D. D. Stark and W. G. Bradley, editors, *Magnetic Resonance Imaging*, chapter 5, pages 109–144. Mosby-Year Book, St. Louis, 2nd edition, 1992.
- [45] J. P. Wansapura, S. K. Holland, R. S. Dunn, and W. S. Ball, Jr., NMR Relaxation Times in the Human Brain at 3.0 Tesla. *J. Magn. Reson. Imag.* **9**, 531–538 (1999).
- [46] C.-N. Chen and D. I. Hoult, *Biomedical Magnetic Resonance Technology*. Adam Hilger, Bristol, 1989.
- [47] D. G. Gadian, *NMR and its applications to living systems*. Oxford University Press, New York, 1995.
- [48] D. Canet, *Nuclear Magnetic Resonance*. John Wiley & Sons, Chichester, 1996.

- [49] E. L. Hahn, Spin Echoes. *Phys. Rev.* **80**, 580–594 (1950).
- [50] H. Y. Carr and E. M. Purcell, Effects of Diffusion on Free Precession in Nuclear Magnetic Resonance Experiments. *Phys. Rev.* **94**, 630–638 (1954).
- [51] S. Meiboom and D. Gill, Modified Spin-Echo Method for Measuring Nuclear Relaxation Times. *Rev. Sci. Instrum.* **29**, 688–691 (1958).
- [52] D. E. Woessner, Effects of Diffusion in Nuclear Magnetic Resonance Spin-Echo Experiments. *J. Chem. Phys.* **34**, 2057–2061 (1961).
- [53] R. Kaiser, E. Bartholdi, and R. R. Ernst, Diffusion and field-gradient effects in NMR Fourier spectroscopy. *J. Chem. Phys.* **60**, 2966–2979 (1974).
- [54] J. Hennig, Multiecho Imaging Sequences with Low Refocusing Flip Angles. *J. Magn. Reson.* **78**, 397–407 (1988).
- [55] G. J. Barker and T. H. Mareci, Suppression of Artifacts in Multiple-Echo Magnetic Resonance. *J. Magn. Reson.* **83**, 11–28 (1989).
- [56] I. I. Rabi, Space Quantization in a Gyating Magnetic Field. *Phys. Rev.* **51**, 652–654 (1937).
- [57] P. C. Lauterbur, Image Formation by Induced Local Interactions: Examples Employing Nuclear Magnetic Resonance. *Nature* **242**, 190–191 (1973).
- [58] W. A. Edelstein, J. M. S. Hutchison, G. Johnson, and T. Redpath, Spin Warp NMR Imaging and Applications to Human Whole-Body Imaging. *Phys. Med. Biol.* **25**, 751–756 (1980).
- [59] D. B. Twieg, The k-trajectory formulation of the NMR imaging process with applications in analysis and synthesis of imaging methods. *Med. Phys.* **10**, 610–621 (1983).
- [60] A. Haase, J. Frahm, D. Matthaei, W. Hänicke, and K.-D. Merboldt, FLASH Imaging. Rapid NMR Imaging Using Low Flip-Angle Pulses. *J. Magn. Reson.* **67**, 258–266 (1986).
- [61] A. Haase, Snapshot FLASH MRI. Applications to T1, T2, and Chemical-Shift Imaging. *Magn. Reson. Med.* **13**, 77–89 (1990).
- [62] J. Hennig, A. Nauerth, and H. Friedburg, RARE Imaging: A Fast Imaging Method for Clinical MR. *Magn. Reson. Med.* **3**, 823–833 (1986).
- [63] P. Mansfield, Multi-planar image formation using NMR spin echoes. *J. Phys. C* **10**, L55–L58 (1977).
- [64] A. M. Howseman, M. K. Stehling, B. Chapman, R. Coxon, R. Turner, R. J. Ordidge, M. G. Cawley, P. Glover, P. Mansfield, and R. E. Coupland, Improvements in snap-shot nuclear magnetic resonance imaging. *Br. J. Radiol.* **61**, 822–828 (1988).
- [65] G. Johnson and J. M. S. Hutchison, The Limitations of NMR Recalled-Echo Imaging Techniques. *J. Magn. Reson.* **63**, 14–30 (1985).
- [66] J. D. Jackson, *Klassische Elektrodynamik*. de Gruyter, Berlin, 1983.
- [67] R. N. Bracewell, *The Fourier Transform and Its Applications*. McGraw-Hill Series in Electrical Engineering. McGraw-Hill, New York, 2nd edition, 1986.
- [68] P. Jezzard and R. S. Balaban, Correction for Geometric Distortion in Echo Planar Images from B_0 Field Variations. *Magn. Reson. Med.* **34**, 65–73 (1995).

- [69] A. A. Feinberg, R. Turner, P. D. Jakab, and M. von Kienlin, Echo-Planar Imaging with Asymmetric Gradient Modulation and Inner-Volume Excitation. *Magn. Reson. Med.* **13**, 162–169 (1990).
- [70] R. J. Ordidge, A. Howseman, R. Coxon, R. Turner, B. Chapman, P. Glover, M. Stehling, and P. Mansfield, Snapshot Imaging at 0.5 T Using Echo-Planar Techniques. *Magn. Reson. Med.* **10**, 227–240 (1989).
- [71] J. Crank, *The Mathematics of Diffusion*. Clarendon Press, Oxford, 2nd edition, 1975.
- [72] A. Fick, Ueber Diffusion. *Annln. Physik Chemie* **170**, 59–86 (1855). 4. Reihe, Band 4 = 94 = 170.
- [73] F. Reif, *Fundamentals of Statistical and Thermal Physics*. McGraw-Hill, Singapore, 1985.
- [74] J. Kärger and D. M. Ruthven, *Diffusion in Zeolites and Other Microporous Solids*. John Wiley & Sons, New York, 1992.
- [75] C. E. Mortimer, *Chemie. Das Basiswissen der Chemie*. Thieme, Stuttgart, 5th edition, 1987.
- [76] A. Einstein, Über die von der molekularkinetischen theorie der wärme geforderte bewegung von in ruhenden flüssigkeiten suspendierten teilchen. *Annalen Physik Chemie (4. Folge)* **17**, 549–560 (1905).
- [77] J. Kärger, H. Pfeifer, and W. Heink, Principles and Application of Self-Diffusion Measurements by Nuclear Magnetic Resonance. *Adv. Magn. Reson.* **12**, 1–89 (1988).
- [78] J. Kärger and W. Heink, The Propagator Representation of Molecular Transport in Microporous Crystallites. *J. Magn. Reson.* **51**, 1–7 (1983).
- [79] P. J. Basser, J. Mattiello, and D. Le Bihan, Anisotropic Diffusion: MR Diffusion Tensor Imaging. In D. Le Bihan, editor, *Diffusion and Perfusion Magnetic Resonance Imaging*, pages 140–149. Raven Press, New York, 1995.
- [80] N. G. van Kampen, *Stochastic Processes in Physics and Chemistry*. Elsevier, Amsterdam, 2nd edition, 1992.
- [81] R. Lenk, *Brownian motion and spin relaxation*. Elsevier, Amsterdam, 1977.
- [82] J. Stepišnik, Analysis of NMR self-diffusion measurements by a density matrix calculation. *Physica B* **104**, 350–364 (1981).
- [83] M. Schachter, R. P. Kennan, A. W. Anderson, and J. C. Gore, Oscillating Field Gradient Measurements of Restricted Diffusion. In *Proceedings, ISMRM, 7th Annual Meeting, Philadelphia*, page 1821, 1999.
- [84] L. D. Landau and E. M. Lifschitz, *Statistische Physik. Teil I*. Akademie-Verlag, Berlin, 7th edition, 1987.
- [85] G. Fischer, *Lineare Algebra*. Friedr. Vieweg & Sohn, Braunschweig, 9th edition, 1989.
- [86] H.-J. Dirschmid, *Tensoren und Felder*. Springer-Verlag, Wien, 1996.
- [87] H. Schade, *Tensoranalysis*. de Gruyter, Berlin, 1997.
- [88] H. Jeffreys and B. Jeffreys, *Methods of Mathematical Physics*. Cambridge University Press, London, 3rd edition, 1972.
- [89] E. O. Stejskal, Use of Spin Echoes in a Pulsed Magnetic-Field Gradient to Study Anisotropic, Restricted Diffusion and Flow. *J. Chem. Phys.* **43**, 3597–3603 (1965).

- [90] P. W. Atkins, *Physical Chemistry*. Oxford University Press, Oxford, 4th edition, 1990.
- [91] E. O. Stejskal and J. E. Tanner, Spin Diffusion Measurements: Spin Echoes in the Presence of a Time-Dependent Field Gradient. *J. Chem. Phys.* **42**, 288–292 (1965).
- [92] D. G. Taylor and M. C. Bushell, The spatial mapping of translational diffusion coefficients by the NMR imaging technique. *Phys. Med. Biol.* **30**, 345–349 (1985).
- [93] J. E. Tanner, Use of the Stimulated Echo in NMR Diffusion Studies. *J. Chem. Phys.* **52**, 2523–2526 (1970). Erratum in *J. Chem. Phys.* **57**, 3586 (1972).
- [94] A. R. Waldeck, P. W. Kuchel, A. J. Lennon, and B. E. Chapman, NMR diffusion measurements to characterise membrane transport and solute binding. *Progr. Nucl. Magn. Reson. Spectrosc.* **30**, 39–68 (1997).
- [95] K.-D. Merboldt, W. Hänicke, and J. Frahm, Diffusion Measurements Using Stimulated Echoes. In D. Le Bihan, editor, *Diffusion and Perfusion Magnetic Resonance Imaging*, pages 28–41. Raven Press, New York, 1995.
- [96] J. Mattiello, P. J. Basser, and D. Le Bihan, Analytical Expressions for the b Matrix in NMR Diffusion Imaging and Spectroscopy. *J. Magn. Reson. A* **108**, 131–141 (1994).
- [97] T. E. Conturo, R. C. McKinsty, E. Akbudak, and B. H. Robinson, Encoding of Anisotropic Diffusion with Tetrahedral Gradients: A General Mathematical Diffusion Formalism and Experimental Results. *Magn. Reson. Med.* **35**, 399–412 (1996).
- [98] T. E. Conturo, R. C. McKinsty, J. A. Aronovitz, and J. J. Neil, Diffusion MRI: Precision, Accuracy and Flow Effects. *NMR Biomed.* **8**, 307–332 (1995).
- [99] E. T. Ahrens, D. H. Laidlaw, C. Readhead, C. F. Brosnan, S. E. Fraser, and R. E. Jacobs, MR Microscopy of Transgenic Mice that Spontaneously Acquire Experimental Allergic Encephalomyelitis. *Magn. Reson. Med.* **40**, 119–132 (1998).
- [100] P. J. Basser, J. Mattiello, and D. LeBihan, Diagonal and off-diagonal components of the self-diffusion tensor: their relation to and estimation from the NMR spin-echo signal. In *Proceedings, SMRM, 11th Annual Meeting, Berlin*, page 1222, 1992.
- [101] U. Sinha and S. Sinha, High Speed Diffusion Imaging in the Presence of Eddy Currents. *J. Magn. Reson. Imaging* **6**, 657–666 (1996).
- [102] J. Coremans, M. Spanoghe, L. Budinsky, J. Sterckx, R. Luypaert, H. Eisendrath, and M. Osteaux, A Comparison between Different Imaging Strategies for Diffusion Measurements with the Centric Phase-Encoded TurboFLASH Sequence. *J. Magn. Reson.* **124**, 323–342 (1997).
- [103] C. Pierpaoli and P. J. Basser, Toward a Quantitative Assessment of Diffusion Anisotropy. *Magn. Reson. Med.* **36**, 893–906 (1996). Erratum in: *Magn. Reson. Med.* **37**, 972 (1997).
- [104] P. J. Basser and C. Pierpaoli, Microstructural and Physiological Features of Tissues Elucidated by Quantitative-Diffusion-Tensor MRI. *J. Magn. Reson. B* **111**, 209–219 (1996).
- [105] D. Le Bihan and R. Turner, Diffusion and Perfusion. In D. D. Stark and W. G. Bradley, editors, *Magnetic Resonance Imaging*, chapter 13, pages 335–371. Mosby-Year Book, St. Louis, 2nd edition, 1992.
- [106] D. G. Norris, The Effects of Microscopic Tissue Parameters on the Diffusion Weighted Magnetic Resonance Imaging Experiment. *NMR Biomed.* in press.

- [107] T. Q. Duong, J. J. H. Ackerman, H. S. Ying, and J. J. Neil, Evaluation of Extra- and Intracellular Apparent Diffusion in Normal and Globally Ischemic Rat Brain via ^{19}F NMR. *Magn. Reson. Med.* **40**, 1–13 (1998).
- [108] D. Le Bihan, Intravoxel Incoherent Motion Imaging. In D. Le Bihan, editor, *Diffusion and Perfusion Magnetic Resonance Imaging*, pages 270–274. Raven Press, New York, 1995.
- [109] D. Le Bihan, E. Breton, D.ALLEMAND, P. Grenier, E. Cabanis, and M. Laval-Jeantet, MR Imaging of Intravoxel Incoherent Motions: Application to Diffusion and Perfusion in Neurologic Disorders. *Radiology* **161**, 401–407 (1986).
- [110] D. Le Bihan, E. Breton, D.ALLEMAND, M.-L. Aubin, J. Vignaud, and M. Laval-Jeantet, Separation of Diffusion and Perfusion in Intravoxel Incoherent Motion MR Imaging. *Radiology* **168**, 497–505 (1988).
- [111] M. Koch, T. Niendorf, and D. G. Norris, Origins of BOLD Contrast — Diffusion and MTC Weighted Functional Imaging of the Human Brain. In *Proceedings, ISMRM, 6th Annual Meeting, Sydney*, page 1407, 1998.
- [112] C. F. Maier, Y. Paran, P. Bendel, B. K. Rutt, and H. Degani, Quantitative Diffusion Imaging in Implanted Human Breast Tumors. *Magn. Reson. Med.* **37**, 576–581 (1997).
- [113] M. R. Verhoye, E. J. 's Gravenmade, E. R. Raman, J. Van Reempts, and A. Van der Linden, In vivo noninvasive determination of abnormal water diffusion in the rat brain studied in an animal model for multiple sclerosis by diffusion-weighted NMR imaging. *Magn. Reson. Imaging* **14**, 521–532 (1996).
- [114] S. Warach, D. Chien, W. Li, M. Ronthal, and R.R. Edelman, Fast magnetic resonance diffusion-weighted imaging of acute human stroke. *Neurology* **42**, 1717–1723 (1992).
- [115] T. Niendorf, R. M. Dijkhuizen, D. G. Norris, M. van Lookeren Campagne, and K. Nicolay, Biexponential Diffusion Attenuation in Various States of Brain Tissue: Implications for Diffusion-Weighted Imaging. *Magn. Reson. Med.* **36**, 847–857 (1996).
- [116] D. G. Norris, T. Niendorf, and D. Leibfritz, Healthy and Infarcted Brain Tissues Studied at Short Diffusion Times: The Origins of Apparent Restriction and the Reduction in Apparent Diffusion Coefficient. *NMR Biomed.* **7**, 304–310 (1994).
- [117] P. van Gelderen, M.H. de Vleeschouwer, D. DesPres, J. Pekar, P.C.M. van Zijl, and C.T. Moonen, Water Diffusion and Acute Stroke. *Magn. Reson. Med.* **31**, 154–163 (1994).
- [118] A. Szafer, J. Zhong, and J.C. Gore, Theoretical Model for Water Diffusion in Tissues. *Magn. Reson. Med.* **33**, 697–712 (1995).
- [119] J. J. Neil, T. Q. Duong, and J. J. H. Ackerman, Evaluation of Intracellular Diffusion in Normal and Globally-Ischemic Rat Brain via ^{133}Cs NMR. *Magn. Reson. Med.* **35**, 329–335 (1996).
- [120] P.A. Barber, D.G. Darby, P.M. Desmond, Q. Yang, R.P. Gerraty, D. Jolley, G.A. Donnan, B.M. Tress, and S.M. Davis, Prediction of stroke outcome with echoplanar perfusion- and diffusion-weighted MRI. *Neurology* **51**, 418–426 (1998).
- [121] K.-A. Hossmann and M. Hoehn-Berlage, Diffusion and Perfusion MR Imaging of Cerebral Ischemia. *Cerebrovasc. Brain Metab. Rev.* **7**, 187–217 (1995).
- [122] K.-O. Lövblad, H.-J. Laubach, A.E. Baird, F. Curtin, G. Schlaug, R.R. Edelman, and S. Warach, Clinical Experience with Diffusion-Weighted MR in Patients with Acute Stroke. *Am. J. Neuroradiol.* **19**, 1061–1066 (1998).

- [123] M. F. Lythgoe, A. L. Busza, F. Calamante, C. H. Sotak, M. D. King, A. C. Bingham, S. R. Williams, and D. G. Gadian, Effects of Diffusion Anisotropy on Lesion Delineation in a Rat Model of Cerebral Ischemia. *Magn. Reson. Med.* **38**, 662–668 (1997).
- [124] E. C. Wong, R. W. Cox, and A. W. Song, Optimized Isotropic Diffusion Weighting. *Magn. Reson. Med.* **34**, 139–143 (1995).
- [125] S. Mori and P. C. M. van Zijl, Diffusion Weighting by the Trace of the Diffusion Tensor within a Single Scan. *Magn. Reson. Med.* **33**, 41–52 (1995).
- [126] K. Butts, J. Pauly, A. de Crespigny, and M. Moseley, Isotropic Diffusion-Weighted and Spiral-Navigated Interleaved EPI for Routine Imaging of Acute Stroke. *Magn. Reson. Med.* **38**, 741–749 (1997).
- [127] T. Chun, A. M. Uluç, and P. C. M. van Zijl, Single-Shot Diffusion-Weighted Trace Imaging on a Clinical Scanner. *Magn. Reson. Med.* **40**, 622–628 (1998).
- [128] M. Trepel, *Neuroanatomie. Eine Einführung*. Urban & Schwarzenberg, München, 1995.
- [129] G. M. Shepherd, *Neurobiologie*. Springer, Berlin, 1993.
- [130] G. Guroff, *Molecular Neurobiology*. Marcel Dekker, New York, 1980.
- [131] K. Zilles and G. Rehkämper, *Funktionelle Neuroanatomie*. Springer-Verlag, Berlin, 1993.
- [132] F. Aboitiz, A. B. Scheibel, R. S. Fisher, and E. Zaidel, Fiber composition of the human corpus callosum. *Brain Res.* **598**, 143–153 (1992).
- [133] M. A. Horsfield, G. J. Barker, and W. I. McDonald, Self-Diffusion in CNS Tissue by Volume-Selective Proton NMR. *Magn. Reson. Med.* **31**, 637–644 (1994).
- [134] C. Beaulieu and P. S. Allen, Determinants of Anisotropic Water Diffusion in Nerves. *Magn. Reson. Med.* **31**, 394–400 (1994).
- [135] C. Beaulieu and P. S. Allen, Water Diffusion in the Giant Axon of the Squid: Implications for Diffusion-Weighted MRI of the Nervous System. *Magn. Reson. Med.* **32**, 579–583 (1994).
- [136] E. W. Hsu, N. R. Aiken, and S. J. Blackband, A Study of Diffusion Isotropy in Single Neurons by Using NMR Microscopy. *Magn. Reson. Med.* **37**, 624–627 (1997).
- [137] C. Beaulieu, F. R. Fenrich, and P. S. Allen, Multicomponent Water Proton Transverse Relaxation and T2-Discriminated Water Diffusion in Myelinated and Nonmyelinated Nerve. *Magn. Reson. Imag.* **16**, 1201–1210 (1998).
- [138] F. Kraemer, A. Darquie, C. A. Clark, and D. Le Bihan, Separation of two diffusion compartments in the human brain. In *Proceedings, ISMRM, 7th Annual Meeting, Philadelphia*, page 1808, 1999.
- [139] G. J. Stanisz, A. Szafer, G. A. Wright, and R. M. Henkelman, An Analytical Model of Restricted Diffusion in Bovine Optic Nerve. *Magn. Reson. Med.* **37**, 103–111 (1997).
- [140] J. C. Ford and D. B. Hackney, Numerical Model for Calculation of Apparent Diffusion Coefficients (ADC) in Permeable Cylinders — Comparison with Measured ADC in Spinal Cord White Matter. *Magn. Reson. Med.* **37**, 387–394 (1997).
- [141] J. S. Shimony, R. C. McKinstry, E. Akbudak, J. A. Aronovitz, A. Z. Snyder, N. F. Lori, T. S. Cull, and T. E. Conturo, Quantitative Diffusion-Tensor Anisotropy Brain Imaging: Normative Human Data and Anatomic Analysis. *Radiology* **212**, 770–784 (1999).

- [142] D. J. Werring, C. A. Clark, G. J. Barker, A. J. Thompson, and D. H. Miller, Diffusion tensor imaging of lesions and normal-appearing white matter in multiple sclerosis. *Neurology* **52**, 1626–1632 (1999).
- [143] H. Igarashi, Y. Katayama, T. Tsuganezawa, M. Yamamuro, A. Terashi, and C. Owan, Three-Dimensional Anisotropy Contrast (3DAC) Magnetic Resonance Imaging of the Human Brain: Application to Assess Wallerian Degeneration. *Intern. Med.* **37**, 662–668 (1998).
- [144] C. Beaulieu, M. D. Does, R. E. Snyder, and P. S. Allen, Changes in Water Diffusion Due to Wallerian Degeneration in Peripheral Nerve. *Magn. Reson. Med.* **36**, 627–631 (1996).
- [145] U. C. Wieshmann, M. R. Symms, C. A. Clark, L. Lemieux, F. Franconi, G. J. M. Parker, G. J. Barker, and S. D. Shorvon, Wallerian Degeneration in the Optic Radiation After Temporal Lobectomy Demonstrated In Vivo with Diffusion Tensor Imaging. *Epilepsia* **40**, 1155–1158 (1999).
- [146] D. J. Werring, C. A. Clark, G. J. Barker, D. H. Miller, G. J. M. Parker, M. J. Brammer, E. T. Bullmore, V. P. Giampietro, and A. J. Thompson, The structural and functional mechanisms of motor recovery: complementary use of diffusion tensor and functional magnetic resonance imaging in a traumatic injury of the internal capsule. *J. Neurol. Neurosurg. Psychiatry* **65**, 863–869 (1998).
- [147] U. C. Wieshmann, C. A. Clark, M. R. Symms, F. Franconi, and S. D. Barker, G. J. Shorvon, Anisotropy of Water Diffusion in Corona Radiata and Cerebral Peduncle in Patients with Hemiparesis. *Neuroimage* **10**, 225–230 (1999).
- [148] W.-Y. Tseng, T. G. Reese, R. M. Weisskoff, and J. Van Wooten, Cardiac Diffusion Tensor MRI In Vivo Without Strain Correction. *Magn. Reson. Med.* **42**, 393–403 (1999).
- [149] W.-Y. I. Tseng, T. G. Reese, R. N. Smith, E. Halpin, and V. J. Wedeen, Histologic correlation of myocardial diffusion tensor MRI: Fibers and sheets both contribute. In *Proceedings, ISMRM, 7th Annual Meeting, Philadelphia*, page 26, 1999.
- [150] L. L. Latour, K. Svoboda, P. P. Mitra, and H. Sotak, Time-dependent diffusion of water in a biological model system. *Proc. Natl. Acad. Sci. USA* **91**, 1229–1233 (1994).
- [151] D. S. Tuch, V. J. Wedeen, A. M. Dale, and J. W. Belliveau, Electrical Conductivity Tensor Map of the Human Brain using NMR Diffusion Imaging: An Effective Medium Approach. In *Proceedings, ISMRM, 6th Annual Meeting, Sydney*, page 527, 1998.
- [152] H. Gudbjartsson, S. E. Maier, R. V. Mulkern, I. Á. Mórocz, S. Patz, and F. A. Jolesz, Line Scan Diffusion Imaging. *Magn. Reson. Med.* **36**, 509–519 (1996).
- [153] H. Gudbjartsson, S. E. Maier, and F. A. Jolesz, Double Line Scan Diffusion Imaging. *Magn. Reson. Med.* **38**, 101–109 (1997).
- [154] G. Liu, P. van Gelderen, J. Duyn, and C. T. Moonen, Single-Shot Diffusion MRI of Human Brain on a Conventional Clinical Instrument. *Magn. Reson. Med.* **35**, 671–677 (1996).
- [155] G. Wider, V. Dötsch, and K. Wüthrich, Self-Compensating Pulsed Magnetic-Field Gradients for Short Recovery Times. *J. Magn. Reson. A* **108**, 255–258 (1994).
- [156] N. G. Papadakis, D. Xing, C. L.-H. Huang, L. D. Hall, and T. A. Carpenter, A Comparative Study of Acquisition Schemes for Diffusion Tensor Imaging Using MRI. *J. Magn. Reson.* **137**, 67–82 (1999).

- [157] D. K. Jones, M. A. Horsfield, and A. Simmons, Optimal Strategies for Measuring Diffusion in Anisotropic Systems by Magnetic Resonance Imaging. *Magn. Reson. Med.* **42**, 515–525 (1999).
- [158] F. Schmitt, M. K. Stehling, and R. Turner, editors, *Echo-Planar Imaging. Theory, Technique and Application*. Springer, Berlin, 1998.
- [159] D. G. Norris, Ultrafast Low-Angle RARE: U-FLARE. *Magn. Reson. Med.* **17**, 539–542 (1991).
- [160] D. G. Norris and P. Börnert, Coherence and Interference in Ultra-Fast RARE Experiments. *J. Magn. Reson. A* **105**, 123–127 (1993).
- [161] D. G. Norris, P. Börnert, T. Reese, and D. Leibfritz, On the Application of Ultra-fast RARE experiments. *Magn. Reson. Med.* **27**, 142–164 (1992).
- [162] D. G. Norris, T. Niendorf, M. Hoehn-Berlage, K. Kohn, E. J. Schneider, P. Hainz, M. Hropot, and D. Leibfritz, Incidence of Apparent Restricted Diffusion in Three Different Models of Cerebral Infarction. *Magn. Reson. Imaging* **12**, 1175–1182 (1994).
- [163] D. C. Alsop, The Sensitivity of Low Flip Angle RARE Imaging. *Magn. Reson. Med.* **37**, 176–184 (1997).
- [164] D. C. Alsop, Phase Insensitive Preparation of Single-Shot RARE: Application to Diffusion Imaging in Humans. *Magn. Reson. Med.* **38**, 527–533 (1997).
- [165] D. G. Norris and D. Böttcher, Leibfritz, A Simple Method of Generating Variable T_1 Contrast Images Using Temporally Reordered Phase Encoding. *Magn. Reson. Med.* **15**, 483–490 (1990).
- [166] R. R. Ernst, G. Bodenhausen, and A. Wokaun, *Principles of Nuclear Magnetic Resonance in One and Two Dimensions*, volume 14 of *The international series of monographs on chemistry*. Oxford University Press, Oxford, reprint edition, 1991.
- [167] A. Jesmanowicz, P. A. Bandettini, and J. S. Hyde, Single-Shot Half k-Space High-Resolution Gradient-Recalled EPI for fMRI at 3 Tesla. *Magn. Reson. Med.* **40**, 754–762 (1998).
- [168] J. Jovicich and D. G. Norris, GRASE Imaging at 3 Tesla with Template Interactive Phase-Encoding. *Magn. Reson. Med.* **39**, 970–979 (1998).
- [169] P. R. Bevington, *Data Reduction and Error Analysis for the Physical Sciences*. McGraw-Hill Series in Electrical Engineering. McGraw-Hill, New York, 1969.
- [170] W. H. Press, S. A. Teukolsky, W. T. Vetterling, and B. P. Flannery, *Numerical Recipes in C. The Art of Scientific Computing*. Cambridge University Press, Cambridge, 2nd edition, 1992.
- [171] J. Hochmann and H. Kellerhals, Proton NMR on Dwoxyhemoglobin: Use of a Modified DEFT Technique. *J. Magn. Reson.* **38**, 23–39 (1980).
- [172] K. Ugurbil, M. Garwood, J. Ellermann, K. Hendrich, R. Hinke, X. Hu, S.-G. Kim, R. Menon, H. Merkle, S. Ogawa, and R. Salmi, Imaging at High Magnetic Fields: Initial Experiences at 4 T. *Magn. Reson. Q.* **9**, 259–277 (1993).
- [173] H. Weingärtner, Self Diffusion in Liquid Water. A Reassessment. *Z. Phys. Chem. Neue Folge* **132**, 129–149 (1982).

- [174] M. E. Bastin, P. A. Armitage, and I. Marshall, The Effect of Experimental Noise on the Calculation of Diffusion Anisotropy in Diffusion Tensor and Diffusion Weighted Imaging. In *Proceedings, ISMRM, 6th Annual Meeting, Sydney*, page 1220, 1998.
- [175] G. J. M. Parker, D. J. Werring, J. A. Schnabel, M. R. Symms, and G. J. Barker, Noise Reduction in Diffusion Tensor Imaging — Reducing Systematic Anisotropy Errors. In *Proceedings, ISMRM, 7th Annual Meeting, Philadelphia*, page 1798, 1999.
- [176] J. Mattiello, P. J. Basser, and D. Le Bihan, The b Matrix in Diffusion Tensor Echo-Planar Imaging. *Magn. Reson. Med.* **37**, 292–300 (1997).
- [177] D. G. Norris and J. M. S. Hutchison, Concomitant magnetic field gradients and their effects on imaging at low magnetic field strengths. *Magn. Reson. Imaging* **8**, 33–37 (1990).
- [178] X. J. Zhou, S G. Tan, and M. A. Bernstein, Artifacts Induced by Concomitant Magnetic Field in Fast Spin-Echo Imaging. *Magn. Reson. Med.* **40**, 582–591 (1998).
- [179] J. P. Basser, A Sensitive Method to Calibrate Magnetic Field Gradients Using the Diffusion Tensor. In *Proceedings, SMR/ESMRMB, 3rd/12th Annual Meeting, Nice*, page 308, 1995.
- [180] Y. Gauthier and I. Cameron, A Phantom Study of Restricted Diffusion of Water in White Matter. In *Proceedings, ISMRM, 7th Annual Meeting, Philadelphia*, page 1802, 1999.
- [181] L. Gates and I. Cameron, Time Dependent Diffusion Coefficients of Water Within Hollow Fibers. In *Proceedings, ISMRM, 6th Annual Meeting, Sydney*, page 1259, 1998.
- [182] S. Großmann, *Mathematischer Einführungskurs für die Physik*. B. G. Teubner, Stuttgart, 5th edition, 1988.
- [183] W. S. Price, Gradient NMR. *Annual Reports on NMR Spectroscopy* **32**, 51–142 (1996).
- [184] A. L. Alexander, J. S. Tsuruda, and D. L. Parker, Elimination of Eddy Current Artifacts in Diffusion-Weighted Echo-Planar Images: The Use of Bipolar Gradients. *Magn. Reson. Med.* **38**, 1016–1021 (1997).
- [185] P. Jezzard, A. S. Barnett, and C. Pierpaoli, Characterization of and Correction for Eddy Current Artifacts in Echo Planar Diffusion Imaging. *Magn. Reson. Med.* **39**, 801–812 (1998).
- [186] B. Aldefeld and P. Börnert, Effects of Gradient Anisotropy in MRI. *Magn. Reson. Med.* **39**, 606–614 (1998).
- [187] J. C. Haselgrove and J. R. Moore, Correction for Distortion of Echo-Planar Images Used to Calculate the Apparent Diffusion Coefficient. *Magn. Reson. Med.* **36**, 960–964 (1996).
- [188] M. E. Bastin, Correction of eddy current-induced artefacts in diffusion tensor imaging using iterative cross-correlation. *Magn. Reson. Imaging* **17**, 1011–1024 (1999).
- [189] S. J. Gibbs and C. S. Johnson, Jr., A PFG NMR Experiment for Accurate Diffusion and Flow Studies in the Presence of Eddy Currents. *J. Magn. Reson.* **93**, 395–402 (1991).
- [190] S. C. Smart, D. A. Porter, F. Calamante, M. A. Hall-Craggs, and A. Connelly, Eddy Current Compensation in Diffusion-Weighted, Stimulated Echo EPI. In *Proceedings, ISMRM, 7th Annual Meeting, Philadelphia*, page 1832, 1999.

- [191] T. G. Reese, R. M. Weisskoff, and V. J. Wedeen, Diffusion NMR facilitated by a refocused eddy-current EPI pulse sequence. In *Proceedings, ISMRM, 6th Annual Meeting, Sydney*, page 663, 1998.
- [192] D. A. Porter, F. Calamante, D. G. Gadian, and A. Connelly, The Effect of Residual Nyquist Ghost in Quantitative Echo-Planar Diffusion Imaging. *Magn. Reson. Med.* **42**, 385–392 (1999).
- [193] R. J. Ordidge, J. A. Helpert, Z. Qing, and R. A. Knight, Correction of motional artifacts in MR diffusion-weighted images. In *Proceedings, SMRM, 11th Annual Meeting, Berlin*, page 1209, 1992.
- [194] R. J. Ordidge, J. A. Helpert, Z. X. Qing, R. A. Knight, and V. Nagesh, Correction of motional artifacts in diffusion-weighted MR images using navigator echoes. *Magn. Reson. Imaging* **12**, 455–460 (1994).
- [195] A. W. Anderson and J. C. Gore, Analysis and Correction of Motion Artifacts in Diffusion Weighted Imaging. *Magn. Reson. Med.* **32**, 379–387 (1994).
- [196] K. Butts, J. M. Pauly, A. de Crespigny, and M. E. Moseley, Isotropic Diffusion-Weighted Interleaved EPI with Two Orthogonal Navigator Echoes. In *Proceedings, ISMRM, 4th Annual Meeting, New York*, page 188, 1996.
- [197] A. W. Anderson and J. C. Gore, Using Spiral Navigator Echoes to Correct for Motion in Diffusion Weighted Imaging. In *Proceedings, SMR/ESMRMB, 3rd/12th Annual Meeting, Nice*, page 743, 1995.
- [198] Z. W. Fu, Y. Wang, R. C. Grimm, P. J. Rossman, J. P. Felmlee, S. J. Riederer, and R. L. Ehman, Orbital Navigator Echoes for Motion Measurements in Magnetic Resonance Imaging. *Magn. Reson. Med.* **34**, 746–753 (1995).
- [199] M. D. Robson, A. W. Anderson, and J. C. Gore, Diffusion-Weighted Multiple Shot Echo Planar Imaging of Humans without Navigation. *Magn. Reson. Med.* **38**, 82–88 (1997).
- [200] T. P. Trouard, Y. Sabharwal, M. I. Altbach, and A. F. Gmitro, Analysis and Comparison of Motion-Correction Techniques in Diffusion-Weighted Imaging. *J. Magn. Reson. Imaging* **6**, 925–935 (1996).
- [201] S. J. Savader, B. L. Savader, F. R. Murtagh, L. P. Clarke, and M. L. Silbiger, MR Evaluation of Flow in a Ventricular Shunt Phantom with In Vivo Correlation. *J. Comput. Assist. Tomogr.* **12**, 765–769 (1988).
- [202] B. De Coene, J. V. Hajnal, P. Gatehouse, D. B. Longmore, S. J. White, A. Oatridge, J. M. Pennock, I. R. Young, and G. M. Bydder, MR of the Brain Using Fluid-Attenuated Inversion Recovery (FLAIR) Pulse Sequences. *Am. J. Neuroradiol.* **13**, 1555–1564 (1992).
- [203] D. S. Tuch, J. W. Belliveau, T. G. Reese, and V. J. Wedeen, Diffusion Imaging at High Angular Resolution Detects Multiple Fiber Populations within a Voxel. *Neuroimage* **7**, S708 (1998).
- [204] D. S. Tuch, R. M. Weisskoff, J. W. Belliveau, and V. J. Wedeen, High Angular Resolution Diffusion Imaging of the Human Brain. In *Proceedings, ISMRM, 7th Annual Meeting, Philadelphia*, page 321, 1999.
- [205] S. Peled, H. Gudbjartsson, C.-F. Westin, R. Kikinis, and F. A. Jolesz, Magnetic resonance imaging shows orientation and asymmetry of white matter fiber tracts. *Brain Res.* **780**, 27–33 (1998).

- [206] D. K. Jones, A. Simmons, S. C. R. Williams, and M. A. Horsfield, Non-Invasive Assessment of Structural Connectivity in White Matter by Diffusion Tensor MRI. In *Proceedings, ISMRM, 6th Annual Meeting, Sydney*, page 531, 1998.
- [207] J. S. Tsuruda, R. B. Burr, and A. L. Alexander, Diffusion Anisotropy of White Matter for Rapid Assessment of the Sensory Motor Cortex. *Int. J. Neuroradiol.* **4**, 277–279 (1998).
- [208] K. J. Friston, C. D. Frith, P. F. Liddle, and R. S. J. Frackowiak, Functional Connectivity: The Principal-Component Analysis of Large (PET) Data Sets. *J. Cereb. Blood Flow Metab.* **13**, 5–14 (1993).
- [209] J. Zhong, O. A. C. Petroff, L. A. Pleban, J. C. Gore, and J. W. Prichard, Reversible, Reproducible Reduction of Brain Water Apparent Diffusion Coefficient by Cortical Electroshocks. *Magn. Reson. Med.* **37**, 1–6 (1997).
- [210] B. R. Ransom, C. L. Yamate, and B. W. Connors, Activity-dependent Shrinkage of Extracellular Space in Rat Optic Nerve: A Developmental Study. *J. Neurosci.* **5**, 532–535 (1985).
- [211] L. Pauling and C. D. Coryell, The Magnetic Properties and Structure of Hemoglobin, Oxyhemoglobin and Carbonmonoxyhemoglobin. *Proc. Natl. Acad. Sci. USA* **22**, 210–216 (1936).
- [212] B. B. Biswal, F. Z. Yetkin, V. M. Haughton, and J. S. Hyde, Functional Connectivity in the Motor Cortex of Resting Human Brain Using Echo-Planar MRI. *Magn. Reson. Med.* **34**, 537–541 (1995).
- [213] M. J. Lowe, B. J. Mock, and J. A. Sorenson, Functional Connectivity in Single and Multislice Echoplanar Imaging Using Resting-State Fluctuations. *Neuroimage* **7**, 119–132 (1998).
- [214] M. Jeannerod, Mental Imagery in the Motor Cortex. *Neuropsychologia* **33**, 1419–1432 (1995).
- [215] E. V. Golanov, S. Yamamoto, and D. J. Reis, Spontaneous waves of cerebral blood flow associated with a pattern of electrocortical activity. *Am. J. Physiol.* **266**, R204–R214 (1994).
- [216] V. Harms, *Biomathematik, Statistik und Dokumentation*. Harms, Kiel, 6th edition, 1992.
- [217] A. Miodoński, The Angioarchitectonics and Cytoarchitectonics (Impregnation Method Golgi-Cox) Structure of the Fissural Frontal Neocortex in Dog. *Folia Biol. (Kraków)* **22**, 237–279 (1974).
- [218] W. Welker, Why Does Cerebral Cortex Fissure and Fold? In A. Peters and E. G. Jones, editors, *Cerebral Cortex*, chapter 10. Plenum Press, New York, 1990.
- [219] R. Xue, P. C. M. van Zijl, B. J. Crain, M. Solaiyappan, and S. Mori, In Vivo Three-Dimensional Reconstruction of Rat Brain Axonal Projections by Diffusion Tensor Imaging. *Magn. Reson. Med.* **42**, 1123–1127 (1999).
- [220] S. Mori, B. J. Crain, V. P. Chacko, and P. C. M. van Zijl, Three-Dimensional Tracking of Axonal Projections in the Brain by Magnetic Resonance Imaging. *Ann. Neurol.* **45**, 265–269 (1999).
- [221] B. Biswal, A. G. Hudetz, F. Z. Yetkin, V. M. Haughton, and J. S. Hyde, Hypercapnia Reversibly Suppresses Low-Frequency Fluctuations in the Human Motor Cortex During Rest Using Echo-Planar MRI. *J. Cereb. Blood Flow Metab.* **17**, 301–308 (1997).

-
- [222] M. Koch and D. G. Norris, Diffusionstensorbildgebung bei 3 T. “1. Jahrestagung der Deutschen Sektion der ISMRM”, Freiburg 1998, contribution no. 10.
 - [223] M. Koch and D. G. Norris, Distortionless diffusion tensor imaging with UFLARE. In *Proceedings, ISMRM, 8th Annual Meeting, Denver*, page 790, 2000.
 - [224] M. Koch and D. G. Norris, An assessment of eddy current sensitivity and correction in single-shot diffusion-weighted imaging. *Phys. Med. Biol.* **45**, 3821–3832 (2000).

Publications

1. M. Koch, R. Fröchtenicht, M. Kaloudis, A. Kulcke, F. Huiskens, Infrared spectroscopy of $(\text{H}_2\text{O})_n$ and $(\text{CH}_3\text{OH})_n$ clusters, free and bound to rare gas clusters. In *Europhysics Conference Abstracts*, vol. **19A**, 5th EPS Conference on Atomic and Molecular Physics, Edinburgh, April 3–7, 1995, p. 589
2. R. Fröchtenicht, M. Kaloudis, M. Koch, F. Huiskens, Vibrational spectroscopy of small water complexes embedded in large liquid helium clusters. *J. Chem. Phys.* **105**, 6128 (1996)
3. F. Huiskens, M. Kaloudis, M. Koch, O. Werhahn, Experimental study of the O–H ring vibrations of the methanol trimer. *J. Chem. Phys.* **105**, 8965 (1996)
4. F. Huiskens, M. Kaloudis, M. Koch, A. Kulcke, Vibrational spectroscopy of size-selected water complexes in gas phase and host clusters. In *Proc. SPIE (International Society for Optical Engineering)*, vol. **3090**, 1997, pp. 33–41
5. M. Koch, T. Niendorf, D. G. Norris, Origins of BOLD Contrast — Diffusion and MTC Weighted Functional Imaging of the Human Brain. In *Proceedings of the International Society for Magnetic Resonance in Medicine, 6th Annual Meeting, Sydney, 1998*, p. 1407
6. M. Koch, D. G. Norris, Diffusionstensorbildgebung bei 3 T. 1. Jahrestagung der Deutschen Sektion der International Society for Magnetic Resonance in Medicine, Freiburg Oct. 5–6, 1998, contribution no. 10
7. D. G. Norris, M. Koch, J. Berrouschot, K. Weih, M. Mengershausen, Diffusion Tensor and Diffusion Weighted Imaging at 3 T. *Physiological Research* **48**, Suppl. 1, S36 (1999). (Talk presented during a workshop at the Second Congress of the Federation of European Physiological Societies, Prague, 1999)
8. C. H. Wolters, U. Hartmann, M. Koch, F. Kruggel, S. Burkhardt, A. Basermann, D. S. Tuch, and J. Haueisen, New Methods for Improved and Accelerated FE-Volume Conductor Modelling in EEG/MEG-Source Reconstruction. Accepted for publication in *Proc. 4th Int. Symp. on Computer Methods in Biomechanics and Biomedical Engineering, Lisboa, Oct. 13–16, 1999*
9. M. Koch, D. G. Norris, Distortionless diffusion tensor imaging with UFLARE. In *Proceedings ISMRM, 8th Annual Meeting, Denver, 2000*, p. 790
10. M. Koch, D. G. Norris, An assessment of eddy current sensitivity and correction in single-shot diffusion-weighted imaging. *Phys. Med. Biol.* **45**, 3821 (2000)

Lebenslauf

Martin Koch
geboren am 21. Oktober 1968 in Dinslaken (Niederrhein)

08/1975–05/1979	Grundschule in Dinslaken
06/1979–06/1988	Theodor-Heuss-Gymnasium Dinslaken
06/1988	Allgemeine Hochschulreife
07/1988–09/1989	Grundwehrdienst
09/1989–11/1995	Studium der Physik an der Georg-August-Universität Göttingen
11/1995	Diplom im wissenschaftlichen Studiengang Physik. Thema der Diplomarbeit: „Infrarotspektroskopie an größenselektierten Ameisensäureclustern“, angefertigt am Max-Planck-Institut für Strömungsforschung, Göttingen
09/1992–09/1993	Studienaufenthalt an der University of Edinburgh, Schottland/U.K.
05/1996–10/1999	Promotionsstipendium am Max-Planck-Institut für neuropsychologische Forschung, Leipzig

Leipzig, den 10. März 2000

Zum Schluss möchte ich mich noch bei allen bedanken, die mir geholfen haben, „es“ zu Ende zu bringen. Zuerst bei Priv.-Doz. David G. Norris PhD, der zu jeder Tageszeit gesprächsbereit war, mir Vieles vermittelt und immer wieder Aufbauhilfe geleistet hat. Prof. Dr. J. Kärger danke ich für die freundliche Begleitung der Arbeit und für die Übernahme der offiziellen Betreuung von Seiten der Universität Leipzig. Dem Direktor am Max-Planck-Institut für neuropsychologische Forschung und Leiter des Arbeitsbereichs Neurologie, Prof. Dr. D.Y. von Cramon, gilt mein Dank für die Unterstützung von neuroanatomischer Seite und für die guten Arbeitsbedingungen am MPI.

Viel Spaß hatte ich mit meinen Mitdoktoranden Jorge Jovicich und Rosie Dymond, und Katrin Weih, die unser Bürobiotop belebt und mich oft aufgerichtet hat. Außerdem ein herzliches Dankeschön an Manfred Weder und Reiner Hertwig für die technische Unterstützung, an unsere unersetzlichen MTAs Anke Mempel, Katrin Wiesner, Mandy Naumann, Grit Wenge und Sabine Busker-Rössig, an H. Dasschaf, P. S. Zbgyev und H. Diku und an alle anderen Mitglieder und Ehemaligen der NMR-Gruppe. Mein Dank geht auch an Alexander Metzler, dem ich den Hinweis auf die Wirbelstromkompensation verdanke, an den MEGler Carsten Wolters, und an unsere EDV-Gruppe und die Grafiker.

Und schließlich und ganz besonders danke ich meinen Eltern und meinem Manfred.

MPI SERIES IN COGNITIVE NEUROSCIENCE

1 Anja Hahne

Charakteristika syntaktischer und semantischer Prozesse bei der auditiven Sprachverarbeitung: Evidenz aus ereigniskorrelierten Potentialstudien

2 Ricarda Schubotz

Erinnern kurzer Zeitdauern: Behaviorale und neurophysiologische Korrelate einer Arbeitsgedächtnisfunktion

3 Volker Bosch

Das Halten von Information im Arbeitsgedächtnis: Dissoziationen langsamer corticaler Potentiale

4 Jorge Jovicich

An investigation of the use of Gradient- and Spin-Echo (GRASE) imaging for functional MRI of the human brain

5 Rosemary C. Dymond

Spatial Specificity and Temporal Accuracy in Functional Magnetic Resonance Investigations

6 Stefan Zysset

Eine experimentalpsychologische Studie zu Gedächtnisabrufprozessen unter Verwendung der funktionellen Magnetresonanztomographie

7 Ulrich Hartmann

Ein mechanisches Finite-Elemente-Modell des menschlichen Kopfes

8 Bertram Opitz

Funktionelle Neuroanatomie der Verarbeitung einfacher und komplexer akustischer Reize: Integration haemodynamischer und elektrophysiologischer Maße

9 Gisela Müller-Plath

Formale Modellierung visueller Suchstrategien mit Anwendungen bei der Lokalisation von Hirnfunktionen und in der Diagnostik von Aufmerksamkeitsstörungen

10 Thomas Jacobsen

Characteristics of processing morphological structural and inherent case in language comprehension

11 Stefan Kölsch

Brain and Music

A contribution to the investigation of central auditory processing with a new electrophysiological approach

12 Stefan Frisch

Verb-Argument-Struktur, Kasus und thematische Interpretation beim Sprachverstehen

13 Markus Ullsperger

The role of retrieval inhibition in directed forgetting — an event-related brain potential analysis

14 Martin Koch

Measurement of the Self-Diffusion Tensor of Water in the Human Brain

